THE UNIVERSITY OF CHICAGO

BARYOGENESIS: MODELS AND COMPUTATIONS

A DISSERTATION SUBMITTED TO
THE FACULTY OF THE DIVISION OF THE PHYSICAL SCIENCES
IN CANDIDACY FOR THE DEGREE OF
DOCTOR OF PHILOSOPHY

DEPARTMENT OF PHYSICS

BY
TONG OU

CHICAGO, ILLINOIS
JUNE 2026

© 2026 by Tong Ou

ORCID iD: https://orcid.org/0000-0002-3245-4328

TABLE OF CONTENTS

LIST OF FIGURES vi

LIST OF TABLES xii

ACKNOWLEDGMENTS xiii

ABSTRACT xv

1 INTRODUCTION TO BARYOGENESIS 1

2 PHASE TRANSITION AND BUBBLE WALL DYNAMICS 5
2.1 Basics of Phase Transition Calculation 5
2.1.1 Effective potential 5
2.1.2 Bubble nucleation 7
2.2 Bubble Wall Dynamics 8
2.2.1 Energy-Momentum Conservation 9
2.2.2 Matching Conditions in LTE 12
2.2.3 Equation of State 14
2.2.4 Fluid Profiles 18
2.2.5 Determining v_w in LTE 23
2.3 Wall Velocity Calculation in a Benchmark Model 25
2.4 Summary 28

3 ELECTROWEAK BARYOGENESIS WITH DARK CP VIOLATION 30
3.1 The EWBG model 31
3.2 Anatomy of the electroweak phase transition 35
3.2.1 The one-loop order scalar potential 36
3.2.2 Zero temperature boundary conditions 37
3.2.3 Thermal history 40
3.2.4 Critical conditions with light scalars 47
3.2.5 Nucleation 50
3.2.6 Numerical scan 51
3.3 Discriminant Power of Wall Velocity: Baryon Number and Gravitational Waves in DarkCPV 53
3.3.1 Wall Velocity 53
3.3.2 Baryon number generation and its v_w dependence 56
3.3.3 Gravitational Waves 62
3.4 Summary 64

4 TOWARDS REAL-TIME SIMULATION OF BARYOGENESIS 68
4.1 Limitations of conventional calculations for EWBG 69
4.2 Prototype study: Real-time simulation of CP violation in electroweak baryogenesis 71
4.2.1 Simulation setup in the continuum and infinite volume 73
4.2.2 Observables 75
4.2.3 Mass profiles 80
4.2.4 Lattice Simulations 81
4.2.5 Simulation results: real mass ($\theta_0 = 0$) 86
4.2.6 Simulation results: complex mass ($\theta_0 \neq 0$) 92
4.3 Discussion and outlooks 95

5 POST-SPHALERON BARYOGENESIS AND DETECTION 98
5.1 Baryon and lepton number violation at low energy scale 98
5.2 Model and effective operators 102
5.3 Baryogenesis model 105
5.4 Baryon Number Violation at the LHC and HL-LHC 109
5.5 Summary 114

A APPENDICES FOR CHAPTER 2 116
A.1 Out-of-Equilibrium Bubble Wall 116
A.1.1 Dynamics of the Expanding Bubble 117
A.1.2 Wall Velocity and Thickness from EOM 120
A.2 Free Energy 125
A.3 Reference Frames 127
A.4 Relativistic Fluid Equations 129

B APPENDICES FOR CHAPTER 3 131
B.1 Baryon Number Calculation 131
B.2 Gravitational Wave Spectrum from different sources 135
B.2.1 Scalar Field Contribution 135
B.2.2 Sound Waves 137
B.2.3 Magnetohydrodynamic Turbulence 139

C APPENDICES FOR CHAPTER 4 140
C.1 Symmetries 140
C.1.1 Continuum 140
C.1.2 Lattice 142
C.2 Phase asymmetry for Gaussian wave packets 143
C.3 Wave packets on the lattice and time evolution 147
C.4 Systematic Uncertainties 150
C.4.1 Charge asymmetry of the initial state 151
C.4.2 Asymmetry generation from scattering with step-function complex mass profile 152

D APPENDICES FOR CHAPTER 5 155
D.1 Existing constraints 155
D.1.1 Proton Decay 155
D.1.2 Baryon Number Conserving Constraints 157

REFERENCES 161

LIST OF FIGURES

2.1 Fluid profiles for deflagration, hybrid, and detonation solutions. The blue shaded region indicates non-zero fluid velocity. 18

2.2 $\Delta(s\gamma v)$ as a function of v_w in arbitrary unit for the $\mathbb{Z}_2$ symmetric real singlet extension model (discussed in Sec. 2.3) for two types of bubbles. Left: Deflagration/hybrid-type bubble with a positive peak of $\Delta(s\gamma v)$ at v_J. Right: Detonation-type bubble with a negative peak of $\Delta(s\gamma v)$. We truncate the plot at $v_w < 1$, since for $v_w \sim 1$, out-of-equilibrium effects become dominant and LTE is not justified [1]. 23

2.3 Strong first-order EWPT points and wall velocities calculated under the LTE approximation, using the entropy conservation approach for the $\mathbb{Z}_2$ symmetric real scalar singlet extended SM. We fix $\lambda_S = 1$, and vary λ_{SH} and m_S in the scanning. Panel (a) shows detonation and deflagration/hybrid solutions in the m_S-λ_{SH} plane, with wall velocities depicted by the color gradient. Panel (b) shows the histogram of α_n for the detonation and deflagration/hybrid solutions. Panel (c) shows all the deflagration/hybrid points in the α_n-v_w plane. The points highlighted in blue, green, and red have one of the model parameters m_S restricted to a narrow range as indicated by the legend. The solid lines of the same colors are the fitting of the scatter points with the function $f(x) = a\ln(x) + b + cx + dx^2$, with fitted parameters listed in Table 2.2. Panel (d) shows all the strong first-order EWPT points (in gray), including detonation bubbles, in the α_n-v_n/T_n plane. The blue, green, and red points and lines have the same meaning as those in panel (c). 27

3.1 Low energy sector of the model and probes for EWBG and a dark matter candidate. 31

3.2 Tree-level annihilations of the dark fermion χ. 35

3.3 Results of the zero temperature numerical scans at one loop level on the $v_S' - \lambda_{SH}$ plane with fixed parameters (a) $m_a = 10$ GeV, $m_0 = 20\,\text{GeV}$, $\lambda = 0.17$ and (b) $m_a = 150$ GeV, $m_0 = 200\,\text{GeV}$, $\lambda = 0.4$. The benchmarks satisfying zero temperature boundary conditions are shown in red, benchmarks not satisfying BFB are shown in blue and benchmarks where the EW vacuum is not the global minimum are shown in gray. Analytical conditions **C1** (loop-level, BFB) and **C2** (tree-level, global minimum) are shown by the blue and gray lines. The gray points below the blue line, which should also be colored blue, in the right plot have a global minimum different from the EW minimum, despite satisfying **C2**, due to the significant one loop effects to the small quartic coupling. 38

3.4 Patterns of symmetry breaking at different temperatures on the a–h plane with $\langle s \rangle = 0$. We use $\times$ to denote a minimum, $\otimes$ to denote a saddle point, $\bullet$ to denote a maximum, and $\times$ ($\bigcirc$) to denote a stationary point that may be minimum (maximum). (a) $T \gg T_{\rm EW}$: The dark Yukawa coupling breaks the Z_2 symmetry and induces a non-zero vev for the a field at temperatures much higher than $T_{\rm EW} \approx 140\,{\rm GeV}$. (b) Below T_a, the temperature where two additional solutions for the vev of the a field arise, there are three branches along the direction $h = 0$, two of which are minima and one is a saddle point, with the global minimum being $(0, 0, a_S)$. When the temperature drops to T_h, a new minimum $(h_{\rm EW}, 0, a_{\rm EW})$ starts to develop from $(0, 0, a_2)$. (c) At the critical temperature, the new minimum $(h_{\rm EW}, 0, a_{\rm EW})$ becomes degenerate with $(0, 0, a_S)$. a_2 has transformed into a maximum at this temperature. a_1 could be a minimum or saddle point depending on the relation between the temperature and the model parameters. (d) At $T = 0$, $(v_H, 0, 0)$ becomes the global minimum and the origin becomes a maximum. There are other potential minima or maxima given by Eq. (3.18): a_2, a_1 and a_S in the plot are the values for the singlet vev at the three stationary points p_3 and $\mp p_2$ respectively. Note that we use $-p_i$ to denote the negative solutions. 42

3.5 Results of phase transitions on the $v_S' - \lambda_{SH}$ plane for points satisfying the zero temperature boundary conditions for the same two benchmark scenarios as in Fig. (3.3): (a) $m_a = 10$ GeV, $m_0 = 20\,{\rm GeV}$, $\lambda = 0.17$ and (b) $m_a = 150$ GeV, $m_0 = 200\,{\rm GeV}$, $\lambda = 0.4$. Points satisfying the nucleation and SFOEWPT conditions, $S_3/T \lesssim 140$ and $h_{\rm EW}(T_n)/T_n > 1$, are shown as red solid circles, and points satisfying the condition $h_{\rm EW}(T_c)/T_c > 1$ are shown as red open circles. The analytical bounds derived in Sec. 3.2, **C1-C4** are shown by the lines. The shaded regions are excluded by the corresponding conditions. **C3'**, the condition derived at T_c, is shown for $m_a = 10\,{\rm GeV}$ only, since the derivation for T_c only applies to the case with $m_a < m_h/2$. The perturbativity requirement $\lambda_S < 4\pi$ is shown for $m_a = 150\,{\rm GeV}$, while the λ_S for $m_a = 10\,{\rm GeV}$ is always small enough to satisfy this requirement. The lowest y-axis value for λ_{SH} for these figures is set by Eq. (3.30). 51

3.6 Strong first-order EWPT points and v_w calculated under LTE using the entropy conservation approach for the DarkCPV model. There are two free parameters varying in the scanning: v_S' and λ_{SH}. Other parameters are fixed as given in the plot title. (a) Detonation and deflagration/hybrid points in the v_S'-λ_{SH} plane. Wall velocities for the deflagration/hybrid points are depicted by the color gradient. (b) Histogram of α_n for the detonation and deflagration/hybrid solutions. (c) α_n and v_w of the deflagration/hybrid points. The red line is a fitting of the scatter points with the function indicated by the legend. (d) α_n and v_n/T_n of all the strong first-order EWPT points. The red line is again a fitting with the same function as in panel (c). 54

3.7 Baryon number to photon ratio η_B normalized to the observed value $\eta_{B,\mathrm{obs}}$ as a function of v_w in the DarkCPV model. The terminal v_w obtained using the entropy conservation approach is labeled by the black dashed line. The gray dashed line denotes the Jouguet velocity. The green solid curve shows the result of the all orders calculation, retaining full v_w-dependence. The gray dot-dashed line is the result of the L.O. approximation, which truncates the transport equation at leading order in v_w and so is valid only for small $v_w \ll 1$. This approximation introduces an unphysical divergence when $v_w \sim 0.5$ crosses the sound speed. Clearly, the all orders treatment is necessary in such a regime. 60
3.8 GW spectrum for the DarkCPV model, with v_w depicted by the color gradient. Orange curves are detonation bubbles. 65

4.1 Schematic for our simulations of fermion-bubble scattering. *Top*: local charge density for a fermion (or antifermion) wave packet in position space. The region around $x = 0$ with the color gradient represents the bubble wall. *Bottom:* the wave packet in momentum space. 72
4.2 The phase-asymmetry observable Φ [Eq. (4.26)] captures the relative spatial displacement between the particle and antiparticle wave packets, while the magnitude asymmetry $\mathcal{Q}_\infty$ [Eq. (4.21)] captures the asymmetry between the total amount of charge reflected. In this picture of the local charge densities $\rho_\pm(x)$ for the particle (blue) and antiparticle (red) wave packets, Φ is the distance between the peaks of the Gaussian wave packets, and $\mathcal{Q}_\infty$ is the sum of (signed) areas enclosed by the wave packets. 78
4.3 Simulation results for a fermion wave packet with $\sigma_k = 0.5$ scattering off a real mass profile with wall width $L_w = 0.6$ in a lattice box of size $L = 28$. (a) Evolution of the particle number density over the lattice for $k_0 = 1.0$ and $a = 1/8$. (b) Particle number in the symmetric phase $\hat{\mathcal{Q}}_{t,+}$ as function of time at different lattice spacings. The vertical dotted line shows the time $t = 3T/4$. The yellow highlighted band in (a) and (b) shows the time window $(\Delta t)_{\mathcal{Q}}$ used for the asymptotic value $\hat{\mathcal{Q}}_{\infty,+}$. (c) Continuum limit extrapolations for $\hat{\mathcal{Q}}_{\infty,+}$ using linear fit for various values k_0. The measurement errors are too small to be visible on this scale. (d) Continuum limit of $\hat{\mathcal{Q}}_{\infty,+}$ as a function of k_0, compared with the analytic prediction (black line) $R_f(k_0)$ [Eq. (4.42)]. The result for $k_0 = 1$, corresponding to (a) and (b), is highlighted by a yellow circle. 87

4.4 Magnitude asymmetry as a measure of C-asymmetry generated during fermion and antifermion scattering with a complex mass profile for fixed wave packet with $k_0 = 2\sigma_k = 1.0$ and physical volume of $L = 28$. For two parameters $\theta_0 = \pi/12, 3\pi/12$, (a) shows the net charge density in spacetime and (b) the evolution of the net charge density in the symmetric phase $\hat{\mathcal{Q}}_t$ at different lattice spacings a. The yellow band marks the time window $(\Delta t)_{\mathcal{Q}}$ used to measure the asymptotic value $\hat{\mathcal{Q}}_\infty$ and estimate the systematic uncertainties, as described in Sec. 4.2.4. (c) Continuum limit extrapolations for $\hat{\mathcal{Q}}_\infty$ using linear fit for various values of θ_0. The errors on the measurements are too small to be seen on this scale, and the 1σ errors from the fitting are shown for the extrapolated $a \to 0$ points. (d) Finally, $\hat{\mathcal{Q}}_\infty$ as function of θ_0. The error bars are 1σ uncertainties computed in $a \to 0$ fits of (c). 90

4.5 Phase asymmetry as a measure of C-asymmetry generated during fermion and antifermion scattering with a complex mass profile for fixed wave packet with $k_0 = 2\sigma_k = 1.0$ and physical volume of $L = 28$. For two parameters $\theta_0 = \pi/12, 3\pi/12$, (a) shows the net charge density in spacetime and (b) the evolution of the phase asymmetry in the symmetric phase $\hat{\Phi}_t$ at different lattice spacings a. The yellow band marks the time window $(\Delta t)_\Phi$ used to measure the asymptotic value $\hat{\Phi}_\infty$ and estimate the systematic uncertainties. (c) Continuum limit extrapolations for $\hat{\Phi}_\infty$ using linear fit for various values of θ_0. The errors from the measurements and the 1σ errors from the fitting are shown for the finite a points and the extrapolated $a \to 0$ point, respectively. (d) Finally, $\hat{\Phi}_\infty$ as function of θ_0. The error bars are the 1σ uncertainties computed in $a \to 0$ fits of (c). 91

5.1 Tree and one-loop diagrams of Φ_r decay that would interfere and violate CP symmetry. We use $i, j, k, ...$ for the flavour indices, and $\alpha, \beta, \gamma, ...$ for the $SU(2)_L$ indices. 109

5.2 Parton level description of the distinctive hadron collider signature we propose for our model. An up and a charm quark from the protons annihilate to produce a diquark, a process which benefits from an s channel enhancement. It then decays to a leptoquark and a dilepton singlet. These in turn decay to an anti-top quark and an anti-muon, and an anti-muon and an anti-neutrino. The anti-top in the final state makes it possible to identify the charge — and hence baryon number of the outgoing particle and establish that baryon number violation by one unit, $\Delta\mathrm{B} = -1$, has occurred. However, due to the anti-neutrino in the final state, it is not possible to identify whether lepton number has bee violated by one, $\Delta\mathrm{L} = -1$, or three, $\Delta\mathrm{L} = -3$, units. 110

5.3 Missing transverse energy distributions for signal and background events for the current LHC and HL-LHC cases. The signal to background ratios for each bin are given in the subplots. 113

5.4 Parameter space showing existing constraints (blue), proton lifetime contours (dark gray contours), and BNV cross sections at $\sqrt{s} = 14$ TeV observable at the HL-LHC (green) while varying the scalar diquark mass and Yukawa coupling to up quark and charm quark. The shaded blue region is ruled out by existing dijet searches at the LHC [2, 3]. The proton lifetimes in this region span from $\tau_p \gtrsim 10^{43}$ years, well above the current Super-K bound ($\sim 10^{32}$ years) and projected Hyper-K bound ($\sim 10^{35}$ years). The green contours show the BNV cross section times branching ratio for the final state of Eq. (5.12) after applying the cuts of Eq. (5.13). They correspond to 10^{-4} pb (solid), 10^{-5} pb (dashed), and 10^{-6} pb (dotted), accessible at the (HL-)LHC. The solid contour corresponds to $\mathcal{O}(300)$ events with HL-LHC luminosity $\mathcal{L} = 3 \times 10^6$ pb^{-1}. The dark red and dark blue circles represent the benchmark points shown in Fig. 5.3. 114

A.1 Left: Total pressure on the wall $\mathcal{P}_{\text{tot}}$ as a function of v_w in arbitrary units. Right: Entropy difference $\Delta(s\gamma v)$ between plasmas on either side of the wall (arbitrary units). Note that both display qualitatively identical behavior and cross zero at the same value of v_w. We do not plot v_w up to 1 since LTE is not justified in that range. 124

A.2 The two main reference frames and their coordinate systems. The left panel shows a spherically symmetric bubble expanding radially outwards in the cosmic frame, with $\xi = r/t$ labeling an arbitrary point in the wave profile. The bubble wall itself is shown in blue; note the thickness has been greatly exaggerated for illustrative purposes. The gradient represents how the scalar profile interpolates between false and true vacua, as shown more explicitly in the right panel as a function of z, the wall frame coordinate. 128

C.1 Magnitude asymmetry of the initial state $\hat{\mathcal{Q}}_0$ for various lattice spacings and physical volumes. The mass profile is chosen to be the same one used for Figs. 4.4 and 4.5, with $\theta_0 = \pi/3$. For each physical volume L, we calculate the continuum limits by fitting $\hat{\mathcal{Q}}_0$ as a linear function of the lattice spacings a and extrapolating to $a = 0$. The continuum limits are then fitted as a linear function of the inverse lattice volume $1/L$ and extrapolated to the infinite-volume limit $1/L \to 0$. The deviation of the infinite-volume limit of $\hat{\mathcal{Q}}_0$ from zero measures the systematic uncertainty of the charge asymmetry in the initial state. 153

C.2 Same as Fig. C.1 but for the phase asymmetry $\hat{\Phi}_0$ of the initial state. 153

C.3 The continuum limits at the largest physical volume $L = 28$ and the infinite-volume limits of $\hat{\mathcal{Q}}_\infty$ and $\hat{\Phi}_\infty$ generated from scattering with the step mass profiles with $m_0 = 1$ and θ_0 varying in the range $[0, \pi/2]$. The error bars represent the 1σ fitting errors. 154

D.1 Feynman diagrams for loop level proton decay, where j, k, l, m, n are flavour indices. A chirality flip along the u_k propagator is necessary to ensure the correct chirality on both vertices, which is induced by a mass insertion denoted by the $\times$. When the two antineutrinos are of the same flavour, $l = m$, each of these diagrams has a companion with $k_1 \leftrightarrow k_2$. On the upper panel, the W boson couples an incoming up quark and a virtual down type quark of flavour j. On the lower panel it couples an outgoing antineutrino and a virtual lepton of flavour j. Because of the $SU(2)$ index contraction of the leptoquark couplings, these two diagrams carry a relative minus sign between them and interfere destructively. 156

LIST OF TABLES

2.1 Summary of boundary conditions for deflagration, hybrid, and detonation solutions. 22
2.2 Fitted parameters for v_w and v_n/T_n as function $f(\alpha_n) = a\ln(\alpha_n) + b + c\,\alpha_n + d\,\alpha_n^2$ for m_S in the given ranges. 28

5.1 Quantum Numbers of the three new scalars of the $B - L/3$ conserving model considered in this work. 102
5.2 Cut flow of the signal at each benchmark point (BP) and dominant SM background $t\bar{t}W$. The cuts applied are given in Eq. (5.13). 111

A.1 Summary of different algorithms to solve for the wall velocity. 123

C.1 Charge-conjugation C_ϵ and parity P transformation properties of various fermion bilinears $\overline{\psi}\Gamma\psi$. The two definitions of charge conjugation correspond to $\epsilon = \pm$, as defined in Eqs. (C.3) and (C.5). The action of charge conjugation on γ_5 depends on the dimension and is given by $\eta_5 = (-1)^{\frac{D}{2}}$ in D spacetime dimensions. We use the notation where $(-1)^\mu = 1$ for $\mu = 0$ and -1 otherwise. 142

D.1 Summary of existing constraints on the leptoquark reproduced from [4]. Cross-generational couplings of light quarks to light leptons are set to zero to avoid lepton flavour violation constraints such as the $\mu \to e\gamma$ process discussed previously. Top quark couplings to the muon and τ leptons are set to unity while that to the electrons is set to zero for consistency with $\mu \to e\gamma$ limits. See the text for more details. 159
D.2 Summary of existing constraints on the dilepton singlet from [5]. See the text for more details. 159

ACKNOWLEDGMENTS

This dissertation would have been impossible without the supports I received. First, I would like to thank my advisor, Professor Marcela Carena. I am deeply grateful for having such a great advisor, who has always been supportive and caring. She has been patiently guiding me through some of the most challenging projects, constantly inspiring me to explore cutting-edge research ideas, and unconditionally supporting me for my personal development. Her success as a distinguished female scientist has greatly encouraged me to pursue my own academic career. Over the years, she has also become like family to me, making life far from my original family much easier.

I would like to thank my thesis committee members: Professors Carlos Wagner, David Miller and Michael Levin, for evaluating my academic progress and thesis defense. In addition, I want to thank Professor Peisi Huang for helpful comments on the thesis.

I would like to thank the Department of Physics at the University of Chicago for its financial and academic support throughout my PhD program. I would also like to thank the Fermilab Theory Division and Perimeter Institute for Theoretical Physics for hosting my visits, during which a significant amount of work in this dissertation was completed.

I would like to thank my collaborators for the research projects presented in this dissertation: Ying-Ying Li, Yikun Wang, Isaac Ruoquan Wang, Aurora Ireland, Hersh Singh, Amit Bhoonah, Da Liu, Deepak Sathyan and Francis Marston Burk. Discussions with them have always been fruitful and inspiring, greatly enhancing my research skills and broadening my perspective.

Last but not least, I would like to thank my family and friends. I am deeply grateful to my family for supporting my decision to study abroad and for their understanding during our time apart. Graduate school would have been much more difficult without friends. I am incredibly fortunate to have a wonderful group of friends who have accompanied me through the difficult moments, shared in the joys of life, and inspired me to embark on new

adventures. Thanks for making Chicago feel like home to me.

ABSTRACT

The observed asymmetry between baryons and antibaryons in the Universe is one of the most outstanding mysteries of particle physics, as it cannot be explained by the Standard Model. Baryogenesis offers a compelling framework in which the Universe, initially symmetric in baryons and antibaryons, dynamically generates the observed asymmetry during its evolution. In this thesis, I investigate various baryogenesis models, develop precise theoretical computations of the underlying dynamics, and examine as well as propose experimental probes of the new physics relevant to baryogenesis.

Among the existing baryogenesis mechanisms, Electroweak Baryogenesis is of particular interest since it directly links the origin of the baryon asymmetry to the generation of the Higgs vacuum expectation value (VEV). In this framework, the asymmetry can be produced during a first-order electroweak phase transition, through which the Higgs field acquires its nonzero VEV, provided certain conditions are satisfied. Quantitative studies of this scenario require precise determination of the phase transition pattern and the associated bubble dynamics in a first-order phase transition. In Chapter 2, I analyze the physics governing the bubble wall velocity and develop a practical algorithm to compute it based on entropy conservation in local thermal equilibrium.

A major challenge in electroweak baryogenesis model building is to introduce a source of CP violation that is sufficiently large to account for the observed baryon asymmetry while remaining consistent with the stringent bounds from measurements of electron electric dipole moment. In Chapter 3, I present a model in which CP violation originates from a dark sector and is transmitted to the visible sector during the electroweak phase transition, enabling baryon asymmetry generation while evading present-day constraints. I analyze the phase transition pattern of this model in detail and compute the bubble wall velocities using the method developed in Chapter 2. These results are then employed to evaluate the resulting baryon asymmetry and the associated gravitational wave signals, allowing me to

assess the prospects for probing this scenario with current and near-future gravitational wave observatories.

Baryogenesis is intrinsically a nonequilibrium, real-time process that is intractable for classical computational methods. The rapid development of quantum technologies enables a reformulation of these dynamics in real time, allowing nonequilibrium effects to be treated consistently. As a prototype study, in Chapter 4 I perform a real-time simulation of the CP violating dynamics relevant for electroweak baryogenesis and construct suitable observables to quantify asymmetry generation. The simulation is implemented using tensor network techniques and can be naturally extended to quantum hardware. This study serves as the first step toward a fully nonperturbative *ab initio* simulation of baryogenesis.

Baryon number violation is a necessary ingredient for baryogenesis and is typically provided by the Standard Model process—weak sphaleron. In Chapter 5, I explore an alternative scenario in which baryon number violation arises from new interactions beyond the Standard Model, leading to a post-sphaleron baryogenesis framework. By imposing a specific pattern of baryon and lepton number violation, the masses of the new particles can be of TeV scale while remaining consistent with the non-observation of proton decay. This feature opens the exciting possibility of directly producing and detecting these new particles at colliders.

CHAPTER 1

INTRODUCTION TO BARYOGENESIS

It is obvious from everyday experience that there is more matter than antimatter in our Universe. This asymmetry is quantified by the ratio of the number density of baryons to photons[1] and is measured most precisely in the cosmic microwave background (CMB) by *Planck* [6]:

$$\eta_B \equiv \frac{n_B}{n_\gamma} = (6.12 \pm 0.04) \times 10^{-10}, \tag{1.1}$$

which is consistent with the most recent analysis of primordial nucleosynthesis apart from the "lithium problem" [7–9]. Another commonly used quantity for baryon asymmetry is the baryon to entropy (s) ratio. Using $s/n_\gamma = 7.04$, we have

$$Y_B \equiv \frac{n_B}{s} \approx 8.7 \times 10^{-11}. \tag{1.2}$$

A possible explanation for the baryon asymmetry is that it was present as an initial condition of the Universe. However, this possibility is disfavored by inflation, which would dilute any primordial asymmetry to a negligible amount. A more plausible scenario is that the Universe began in a state with equal numbers of baryons and antibaryons ($B = 0$), and that the observed baryon asymmetry ($B > 0$) was subsequently generated through dynamical processes. This latter scenario is known as **Baryogenesis**, and is first studied by A. D. Sakharov in Ref. [10]. Baryogenesis mechanisms must satisfy the following three **Sakharov conditions**:

1. Baryon number (B) violation — Processes that violate baryon number ($\Delta B \neq 0$) must

1. Due to the absence of antimatter in the Universe, the baryon number density n_B is equal to the number density difference ($n_B - n_{\bar{B}}$). Therefore, the ratio of baryon to photon (entropy) is also the ratio for the matter-antimatter asymmetry.

exist so that a net baryon number can be generated from an initial state with $B = 0$.

2. C, CP violation — If the fundamental interactions were invariant under charge conjugation (C) and charge–parity conjugation (CP), baryons and antibaryons would be produced at identical rates. Violations of these symmetries are therefore required to preferentially produce baryons over antibaryons.

3. Departure from thermal equilibrium — In thermal equilibrium, baryon-number-producing processes are balanced by their inverse reactions, preventing the generation of a net baryon asymmetry. A departure from thermal equilibrium is therefore necessary to avoid this cancellation and allow a net baryon number to develop.

A natural question to ask is whether baryogenesis can be realized purely within the Standard Model (SM). It is known that the SM has a source of baryon number violation—the weak sphaleron processes associated with the chiral anomaly violate baryon and lepton numbers respectively while preserve $B - L$ [11]. Since only the left-handed fermions and antifermions—rather than their right-handed C conjugates—participate in the weak interactions, the weak sphalerons violate C symmetry as well. There is also available source of CP violation within the SM—the Cabibbo–Kobayashi–Maskawa (CKM) matrix in the quark sector. The strength of this CP-violating effect can be quantified by the Jarlskog invariant, which can be expressed as the determinant of the commutator of the up- and down-type quark (squared) mass matrices [12, 13]:

$$J = \det\left[m_u^2, m_d^2\right]. \tag{1.3}$$

For the weak sphalerons to operate, the temperature of the Universe must be above the electroweak (EW) scale, $T_{\mathrm{EW}} \sim 100\,\mathrm{GeV}$. At this energy scale, a dimensionless measure of

the CP-violating effect can be estimated as:

$$\frac{J}{T_{\rm EW}^{12}} \sim 10^{-20}. \tag{1.4}$$

This extremely small value is commonly taken as an indication that the amount of CP violation present in the SM is insufficient to account for the observed baryon asymmetry of the Universe [14]. Therefore, it is not evident that the SM by itself provides all the necessary ingredients for successful baryogenesis, suggesting that additional sources of new physics may be required. In the following, we briefly review several baryogenesis mechanisms that utilize ingredients both within and beyond the SM:

Electroweak Baryogenesis Electroweak Baryogenesis (EWBG) is an elegant mechanism that generates the observed baryon asymmetry in the Universe (BAU) at the Electroweak Phase Transition (EWPT), during which the Higgs field acquires a nonzero vacuum expectation value (VEV) [15, 16]. Specifically, this mechanism requires a first-order EWPT that proceeds through bubble nucleation and expansion to create an out-of-equilibrium environment and facilitate the generation of baryon asymmetry by the weak sphalerons. While nonperturbative studies have established that, within the pure SM, the EWPT is a smooth crossover [17–28], simple extensions of the SM can readily render the EWPT first order (see e.g., [29–38]). With CP violation introduced by a complex coupling between the fermion and the Higgs boson, the fermions are reflected and transmitted at different rates on the bubble walls, generating an amount of chiral asymmetry that acts as a chemical potential and biases the sphalerons to generate more baryons than antibaryons. If the EWPT is sufficiently strong, the sphalerons would be suppressed in the broken phase inside the bubble, while remain active in the symmetric phase outside the bubble. As a result, the baryon asymmetry would be generated outside the bubble and subsequently transported into the broken phase as the bubble expands, where the sphalerons are inactive and the asymmetry is preserved.

Leptogenesis Leptogenesis is a class of models that generate the BAU from a lepton asymmetry produced from the decay of a heavy sterile neutrino [39–44]. This is a motivating mechanism since the existence of the heavy sterile neutrino may also explain the small but nonvanishing masses of the SM neutrinos via the seesaw mechanism. The Majorana mass term involved in the seesaw mechanism necessarily breaks lepton number symmetry, and the complex phases in the Yukawa couplings generally break CP symmetry. By requiring that the decay of the sterile neutrino occurs out of equilibrium, all the Sakharov conditions are satisfied and a lepton asymmetry can be generated which is then converted to baryon asymmetry by the weak sphalerons.

Post-Sphaleron Baryogenesis Weak sphalerons, as a process within the SM, remain the dominant source of baryon number violation (BNV) in baryogenesis model building. However, they are only active above the EW scale and therefore impose a lower bound on the energy scale at which baryogenesis can occur. This constraint can be alleviated if BNV processes beyond the SM are invoked to generate the baryon asymmetry—post-sphaleron baryogenesis is one such mechanism. The main challenge for introducing new BNV interactions arises from the non-observation of proton decay in experiments (see the latest results in [45–49]). In the original proposal of post-sphaleron baryogenesis by [50], a six-quark $\Delta B = 2$ operator was considered that is consistent with current experimental constraints. In this scenario, the baryon asymmetry is generated through the decay of a heavy particle mediated by the BNV operator at temperatures well below the EW scale, with CP violation sourced from the CKM matrix[2]. In Chapter 5, we introduce a different model based on an operator that violates baryon number by one unit and lepton number by three units, which is the main result of our publication [51].

2. The CP-violating effect can be estimated as Eq. (1.4) with $T_{\rm EW}$ replaced by a much lower decay temperature, yielding a much stronger effect.

CHAPTER 2

PHASE TRANSITION AND BUBBLE WALL DYNAMICS

Phase transitions in the early Universe play an important role in particle physics and cosmology. In particular, the nature of the electroweak phase transition (EWPT) that led to the Higgs VEV and mass observed today is of great interest and remains to be fully understood. While the EWPT in the pure SM is known to be a smooth crossover, a first-order EWPT, that is relevant for many beyond the Standard Model (BSM) theories such as electroweak baryogenesis, can be readily realized in simple extensions of the SM (see discussions in Chapter 1). To guide experimental searches for such new physics scenarios, it is therefore essential to compute the phase transition properties precisely and to identify the parameter regions that yield a first-order EWPT.

In this chapter, we begin by reviewing the basics of (perturbative) calculations of phase transitions (Sec. 2.1), introducing the one-loop finite-temperature effective potential for the scalar field and the nucleation condition required for the phase transition to occur. We then discuss the hydrodynamics of an expanding bubble wall during the phase transition, deriving the matching conditions and equations of state for the quantities on either side of the wall and classifying the possible fluid profiles in its vicinity (Sec. 2.2). Building on this framework, we develop a convenient algorithm for computing the bubble wall velocity under the assumption of local thermal equilibrium (Sec. 2.2.5). This is one of the main results of our work [52]. In Sec. 2.3, we apply this algorithm to a benchmark model and examine its validity.

2.1 Basics of Phase Transition Calculation

2.1.1 Effective potential

The VEV of the Higgs field (or a general scalar field) is determined by the global minimum of its effective potential—which receives loop corrections from radiative effects and thermal effects

in the early Universe. While the tree-level potential is model-dependent, the formulation of the one-loop order corrections is universal as discussed below. In this section, we focus on a single scalar field scenario for the simplification of notations and denote the scalar field undergoing phase transitions as ϕ. The generalization to multi-field scenarios can be straightforwardly implemented by adding the corresponding field variables.

The one-loop order radiative corrections to the scalar potential can be calculated via the Coleman-Weinberg (CW) potential in the $\overline{\text{MS}}$ scheme using dimensional regularization as [53]

$$V_{\text{CW}}(\phi) = \frac{1}{64\pi^2}\left\{ \sum_B n_B |m_B(\phi)|^4 \left[\log\left(\frac{|m_B(\phi)|^2}{Q^2}\right) - c_B\right] - \sum_F n_F |m_F(\phi)|^4 \left[\log\left(\frac{|m_F(\phi)|^2}{Q^2}\right) - c_F\right]\right\}, \tag{2.1}$$

where Q is the renormalization scale, m_B and m_F are the field-dependent masses of bosons and fermions [54], n_B and n_F are the degrees of freedom (dof), $c_B = 3/2$ (5/6) for scalar (vector) bosons, and $c_F = 3/2$.

At a finite temperature T, one has to include the thermal correction, which at the one-loop order is of the following form [55]:

$$V_T(\phi, T) = \frac{T^4}{2\pi^2}\left[\sum_B n_B J_B\left(\frac{|m_B(\phi)|^2}{T^2}\right) - \sum_F n_F J_F\left(\frac{|m_F(\phi)|^2}{T^2}\right)\right], \tag{2.2}$$

where J_B and J_F are bosonic and fermionic thermal functions defined as

$$J_B(\alpha) = \int_0^\infty dx x^2 \log\left[1 - e^{-\sqrt{x^2+\alpha}}\right], \quad J_F(\alpha) = \int_0^\infty dx x^2 \log\left[1 + e^{-\sqrt{x^2+\alpha}}\right], \tag{2.3}$$

with $\alpha = |m|^2/T^2$. It is useful for analytic studies to consider the expansions of J_B and J_F to the leading orders of α, which is a good approximation at the high temperature (HT) limit

with $|m| \ll T$:

$$J_B^{\rm HT}(\alpha) \approx -\frac{\pi^4}{45} + \frac{\pi^2}{12}\alpha - \frac{\pi}{6}\alpha^{3/2} - \frac{1}{32}\alpha^2 \log\left(\frac{\alpha}{a_B}\right) + \mathcal{O}(\alpha^3), \tag{2.4}$$

$$J_F^{\rm HT}(\alpha) \approx \frac{7\pi^4}{360} - \frac{\pi^2}{24}\alpha - \frac{1}{32}\alpha^2 \log\left(\frac{\alpha}{a_F}\right) + \mathcal{O}(\alpha^3), \tag{2.5}$$

where $a_B = 16\pi^2 \exp(3/2 - 2\gamma_E)$ and $a_F = \pi^2 \exp(3/2 - 2\gamma_E)$, with $\gamma_E \approx 0.577$ being the Euler-Mascheroni constant.

To ensure the validity of perturbative expansion near the critical temperature of the phase transition and prevent infrared divergences, one needs to include the resummation of higher-loop daisy diagrams into the full one-loop potential. There are two commonly employed resummation schemes: Parwani scheme [56] and Arnold-Espinosa scheme [57]. The Parwani scheme involves replacing the tree-level bosonic squared masses $|m_B(\phi)|^2$ with the thermal corrected squared masses $|m_B(\phi)|^2 + \Pi_i(T)$ in Eq. (2.1) and Eq. (2.2), where $\Pi_i(T)$ is the self-energy induced by thermal corrections and is usually estimated with the leading-order term of $J_B^{\rm HT}(\alpha)$ in Eq. (2.4). The Arnold-Espinosa scheme involves modifying the cubic term of the potential, which originates from the Matsubara zero modes of the bosonic dof and is associated with the infrared divergence problem. Specifically, the resummation is implemented by replacing the mass in the cubic term with the thermally corrected one, while leaving the masses in other terms unchanged. Comparison of these two schemes and development of more refined resummation prescriptions can be found in e.g., [58, 59].

2.1.2 Bubble nucleation

The effective potential that allows for first-order phase transitions would have multiple minima coexisting at certain temperatures. The temperature at which the two lowest minima become degenerate is defined as the critical temperature. As the temperature falls below the critical temperature, the phase in which the Universe initially resides becomes metastable (a false

vacuum), and bubbles of the true vacuum can nucleate within this background. From the field theory point of view, the bubbles are scalar field configurations in the spacetime that connect the true and false vacua, which are determined by the minimization of the field configuration action. Assuming thermal equilibrium, the periodicity in the Euclidean time with period $1/T$[1] allows for factorizing the time and space integrals in the Euclidean action, which can then be written as $S_E = S_3/T$, with S_3 being the three-dimensional action defined as

$$S_3 = \int d^3x \left[\frac{1}{2}(\nabla\phi)^2 + V(\phi, T)\right]. \tag{2.6}$$

The field configuration that minimizes this action can then be solved from the Euler-Lagrange equation of motion:

$$\Box\phi + \frac{\partial V(\phi, T)}{\partial\phi} = 0. \tag{2.7}$$

The onset of nucleation is conventionally defined as the time at which the probability for a single bubble to be nucleated within one Hubble volume is $\mathcal{O}(1)$ — this is known as the nucleation condition. With the nucleation rate scaling as $\Gamma_{\text{nuc}} \sim \exp(-S_3/T)$, the nucleation condition corresponds to $S_3/T \simeq 140$ around the electroweak scale.

2.2 Bubble Wall Dynamics

Following bubble nucleation, the potential energy differential drives the bubble wall to accelerate into the false vacuum. As it does so, it perturbs and heats the surrounding plasma, which in turn exerts a frictional force on the wall. Once this frictional force balances the driving force, the bubble wall reaches a terminal velocity v_w.

1. This periodicity is known as the Kubo-Martin-Schwinger relation [60, 61].

The terminal bubble wall velocity v_w can be computed from first principles. In the bubble wall frame, one defines the fluid velocity near the bubble wall both in the false and true vacua, v_+ and v_-, respectively, and relates these quantities through matching conditions. We then relate the fluid velocities with the instantaneous bubble wall velocity depending on the type of plasma motion. The matching conditions are derived by means of energy-momentum conservation, considering the plasma and scalar field as a closed system. The scalar field equation of motion (EOM) also provides an independent matching condition. As we will explicitly show, for a system in local thermal equilibrium (LTE), one can equivalently use entropy conservation as a matching condition in place of EOM. This approach provides a much more efficient way of performing numerical calculations.

2.2.1 Energy-Momentum Conservation

Energy-momentum conservation in the closed scalar-fluid system is expressed through the following conservation law,

$$\partial_\mu T^{\mu\nu} = \partial_\mu \left(T^{\mu\nu}_\phi + T^{\mu\nu}_f \right) = 0 \,, \tag{2.8}$$

where in the second term we have decomposed the energy-momentum tensor (EMT) into scalar ϕ and fluid f contributions. The scalar field EMT with zero-temperature potential $V_0(\phi)$[2] is given by[3]

$$T^{\mu\nu}_\phi = \partial^\mu \phi \partial^\nu \phi - \eta^{\mu\nu} \left(\frac{1}{2} (\partial\phi)^2 - V_0 \right) \,, \tag{2.9}$$

2. V_0 includes both the tree-level potential $V_{\rm tree}$ and quantum corrections, most notably the 1-loop Coleman Weinberg potential $V_{\rm CW}$.

3. We presume the phase transition proceeds sufficiently quickly relative to the Hubble rate that the spacetime is approximately Minkowski $\eta^{\mu\nu}$. We use the mostly-negative signature $(+,-,-,-)$ to match the convention in the literature.

while the fluid contribution is

$$T_f^{\mu\nu} = \sum_i n_i \int \frac{d^3k}{(2\pi)^3} \frac{k^\mu k^\nu}{E_{i,k}} f_i(k,x)\,, \tag{2.10}$$

where the sum runs over all dynamical particle species in the plasma, n_i is the particle degrees of freedom for species i, and $f_i(k,x)$ is the phase space distribution function for species i. Eq. (2.10) is the most general expression for the fluid EMT and can be used for general out-of-equilibrium calculations of bubble wall dynamics, which we review in Appendix A.1.

In what follows, we will assume the fluid is in local thermal equilibrium (LTE), i.e. $f_i(k,x) = f_i^{\rm eq}(k,x)$, with equilibrium distribution

$$f_i^{\rm eq}(k,x) = \frac{1}{e^{E_i/T} \mp 1}\,, \tag{2.11}$$

where the $-$ $(+)$ sign is for bosons (fermions) and $E_i = \sqrt{\vec{k}^2 + m_i^2}$. This approximation is justified for sub-luminal wall velocities $v_w < 1$, for which equilibrium effects give the dominant contribution to the net pressure controlling bubble expansion. As shown in Ref. [1], as well as in this work, the LTE approximation can accurately reproduce the full out-of-equilibrium result for the terminal wall velocity in this regime. Although out-of-equilibrium contributions may become important for ultra-relativistic bubbles with $v_w \sim 1$, this scenario is beyond the scope of this work[4].

In LTE, we can equivalently formulate the fluid EMT of Eq. (2.10) in terms of local thermodynamic quantities. To do so, we first identify the fluid pressure as the (negative of the) fluid free energy $\mathcal{F}_f$, which coincides with the finite temperature contribution to the

4. It was previously thought that the frictive force from the thermal plasma, important for preventing runaway bubble walls, arose only when there was a departure from thermal equilibrium in the plasma. This is now known not to be the case [62, 63].

effective potential for the scalar field V_T as discussed in Appendix A.2,

$$p_f = -\mathcal{F}_f = -V_T \,. \tag{2.12}$$

The fluid enthalpy density w_f, entropy density s_f, and energy density e_f are defined in terms of the pressure as

$$w_f = T\frac{\partial p_f}{\partial T}\,, \quad s_f = \frac{\partial p_f}{\partial T}\,, \quad e_f = T\frac{\partial p_f}{\partial T} - p_f\,, \tag{2.13}$$

such that $w_f = e_f + p_f$. It is also useful to note that the energy density and pressure for the scalar field are $e_\phi = V_0(\phi)$ and $p_\phi = -V_0(\phi)$, satisfying the vacuum equation of state. Hence the total pressure $p = p_f + p_\phi$ and energy density $e = e_f + e_\phi$ are,

$$p = p_f - V_0\,, \quad e = e_f + V_0\,. \tag{2.14}$$

The enthalpy and entropy densities receive contributions only from the fluid, such that $w = w_f$ and $s = s_f$. Using these quantities, the fluid EMT in LTE can be written in a perfect fluid form

$$T^{\mu\nu}_{f,\mathrm{LTE}} = w_f\, u^\mu u^\nu - p_f\, \eta^{\mu\nu}\,, \tag{2.15}$$

with u_μ the fluid 4-velocity, which is normalized as $u^\mu u_\mu = 1$. The divergence entering the EMT conservation law is then

$$\partial_\mu T^{\mu\nu}_{f,\mathrm{LTE}} = \partial_\mu(w_f u^\mu u^\nu) - \partial^\nu\phi\frac{\partial p_f}{\partial\phi} - s_f\partial^\nu T\,, \tag{2.16}$$

where we have allowed for the temperature to have a non-trivial profile in spacetime and used the definition of the entropy density above. Combining this result with the scalar field contribution,

$$\partial_\mu T^{\mu\nu}_\phi = \partial^\nu\phi\left(\Box\phi + \frac{\partial V_0}{\partial\phi}\right)\,, \tag{2.17}$$

the statement of EMT conservation becomes

$$\partial^\nu \phi \left(\Box\phi + \frac{\partial V_{\text{eff}}}{\partial \phi} \right) + \partial_\mu (w u^\mu u^\nu) - s \partial^\nu T = 0 \,, \tag{2.18}$$

where we have used the fact that $p_f = -V_T$ and combined $V_0 + V_T = V_{\text{eff}}$. We will return to this expression shortly when we turn to derive the condition for entropy conservation.

2.2.2 Matching Conditions in LTE

In this subsection, we focus on the steady state where the bubble wall expands at constant velocity, and derive the matching conditions for the fluid velocities ($v_\pm$, $+/-$ for false/true vacuum) and temperatures ($T_\pm$) on each side of the bubble wall under the LTE approximation. There are two matching conditions coming from the EMT conservation, and a third one from the combination of the scalar field EOM and EMT conservation. The third condition is also identified as the entropy conservation condition, which will be shown to be equivalent to the scalar field EOM in LTE.

We choose to work in the wall rest frame, which is an inertial frame for a steady-state bubble[5]. This reference frame has the benefit that all quantities are time-independent and depend only on the coordinate corresponding to the direction of bubble expansion, which is taken to be the z-direction. Thus, in the wall frame, EMT conservation Eq. (2.8) leads to just two independent equations

$$\partial_z T^{z0} = 0 \,, \quad \partial_z T^{zz} = 0 \,. \tag{2.19}$$

We also note that in the wall frame, the fluid 4-velocity u^μ can be parameterized as

$$u^\mu(z) = \gamma(z) \left(1, 0, 0, -v(z)\right) , \tag{2.20}$$

5. See Appendix A.3 for a general review of the reference frames for the scalar-fluid system.

with v the physical velocity in the z-direction and $\gamma = 1/\sqrt{1-v^2}$ the Lorentz factor, so that it satisfies the normalization condition $u^\mu u_\mu = 1$.

Eq. (2.19) leads to two matching conditions as follows. Expanding the scalar and fluid contributions explicitly using Eqs. (2.9) and (2.15), we have[6]

$$\partial_z \left(w\gamma^2 v \right) = 0 \,, \tag{2.21a}$$

$$\partial_z \left(\frac{1}{2}(\partial_z \phi)^2 + w\gamma^2 v^2 + p \right) = 0 \,. \tag{2.21b}$$

Integrating over z, we obtain the following matching conditions[7]

$$\boxed{\text{Condition 1:} \quad w_+ \gamma_+^2 v_+ = w_- \gamma_-^2 v_-} \,, \tag{2.22a}$$

$$\boxed{\text{Condition 2:} \quad w_+ \gamma_+^2 v_+^2 + p_+ = w_- \gamma_-^2 v_-^2 + p_-} \,, \tag{2.22b}$$

where we denote quantities in the false/true vacuum with $+/-$. This system of equations can be equivalently formulated as [64]

$$v_+ v_- = \frac{p_+ - p_-}{e_+ - e_-} \,, \tag{2.23a}$$

$$\frac{v_+}{v_-} = \frac{e_- + p_+}{e_+ + p_-} \,. \tag{2.23b}$$

A third matching condition can be derived by imposing scalar field EOM on top of EMT conservation. Returning to the condition of EMT conservation in Eq. (2.18), we multiply both sides by u_ν. From the normalization condition $u_\mu u^\mu = 1$, it follows that $u_\nu \partial_\mu u^\nu = 0$,

6. Note that the thermodynamic quantities appearing here correspond to the total scalar-fluid system and are defined in Eq. (2.14).

7. In deriving Eq. (2.22b), we have used the fact that $\partial_z \phi = 0$ away from the wall.

and so one can show that

$$u_\nu \partial^\nu \phi \left(\Box\phi + \frac{\partial V_{\text{eff}}}{\partial \phi} \right) + T \partial_\mu S^\mu = 0 \,, \tag{2.24}$$

where we have defined the entropy current $S^\mu = u^\mu s$. The quantity in parenthesis can be identified as the scalar field EOM in LTE, which should vanish independently: $\Box\phi + \partial_\phi V_{\text{eff}} = 0$, leaving us the conservation condition for the entropy

$$\partial_\mu S^\mu = 0 \,. \tag{2.25}$$

This demonstrates the equivalence of the scalar EOM with entropy conservation in LTE under EMT conservation, which was first identified in Ref. [63] as a useful matching condition for calculating the bubble wall velocity. Entropy conservation is also generally expected for systems in thermal equilibrium based on the second law of thermodynamics. In the wall frame, Eq. (2.25) reads

$$\partial_z \left(s \gamma v \right) = 0 \,, \tag{2.26}$$

which upon integrating over the wall becomes

$$\boxed{\text{Condition 3:} \quad s_+ \gamma_+ v_+ = s_- \gamma_- v_-} \,. \tag{2.27}$$

Using $s = w/T$ and Eq. (2.22a), this condition can equivalently be written as

$$\gamma_+ T_+ = \gamma_- T_- \,. \tag{2.28}$$

2.2.3 Equation of State

It would be useful to connect the matching conditions to the strength and temperature of the phase transition. For this we must specify the equations of state (EOS) for the fluid and

the scalar field that express the thermodynamic quantities in terms of the temperature and other variables entering the effective potential.

We start from the simplest "bag" approximation where the fluid and scalar contributions are separable. In this case, the fluid can be well modeled as a relativistic gas, with pressure and energy given by

$$p_{\pm}^{f} = \frac{1}{3} a_{\pm} T_{\pm}^{4}, \quad e_{\pm}^{f} = a_{\pm} T_{\pm}^{4}. \tag{2.29}$$

In the bag model, all the species lighter than the temperature are counted into the relativistic degrees of freedom $a_{\pm}$, while the species heavier than the temperature are considered to be Boltzmann suppressed and have negligible contributions. Since the fluid pressure is directly related to the free energy as given by Eq. (2.12), $a_{\pm}$ is given by

$$a_{\pm} = \frac{\pi^2}{30} \left(\sum_{B \in \pm} n_B + \frac{7}{8} \sum_{F \in \pm} n_F \right) , \tag{2.30}$$

such that $(-p_{\pm}^{f})$ is equal to the zeroth-order term of the high-temperature expansion of the free energy (or the thermal potential) given by Eq. (2.4) and Eq. (2.5) (see detailed derivations in Appendix A.2). Meanwhile, the scalar field energy is denoted as $e_{\pm}^{\phi} = \epsilon_{\pm}$, and its pressure satisfies the vacuum EOS: $p_{\pm}^{\phi} = -e_{\pm}^{\phi} = -\epsilon_{\pm}$. In the bag model, the scalar field contribution is independent of the fluid, and thus is determined by the zero-temperature scalar potential $V_0(\phi)$, which is conventionally normalized such that the scalar field energy in the true vacuum vanishes, $\epsilon_{-} = V_0(\phi_{-}) = 0$. Summing the fluid and scalar field contributions, we get the EOS for the total pressure and energy of the scalar-fluid system as

$$p_{\pm} = \frac{1}{3} a_{\pm} T_{\pm}^{4} - \epsilon_{\pm} , \quad e_{\pm} = a_{\pm} T_{\pm}^{4} + \epsilon_{\pm} . \tag{2.31}$$

Comparing the bag model expression for $p_{\pm} = -V_{\rm eff}(\phi_{\pm}, T_{\pm})$ in Eq. (2.31) to the general

form of V_{eff} in Eq. (A.29), one can easily see that the bag EOS neglects contributions from finite particle masses. This is problematic when there exist particles in the plasma with masses comparable to the temperature $m \sim T$, as is the case for many realistic particle models. In particular, there exist several such particles in the SM EWPT, for example the massive gauge bosons $W^{\pm}$ and Z^0. Systems with such intermediate-mass particles can still be described by the EOS given by Eq. (2.31), but with generalized temperature-dependent definitions of $a_{\pm}$ and $\epsilon_{\pm}$ [64]:

$$a_{\pm} \equiv \frac{3}{4T_{\pm}^3}\frac{\partial p_{\pm}}{\partial T_{\pm}} = \frac{3w_{\pm}}{4T_{\pm}^4}\,, \quad \epsilon_{\pm} \equiv \frac{1}{4}(e_{\pm} - 3p_{\pm})\,. \tag{2.32}$$

We note here that $a_{\pm}$ still serves as the coefficient of T^4 by this definition. In this general definition, however, $a_{\pm}$ depends on field value and temperature. $\epsilon_{\pm}$ is now defined to contain all the remaining things in $p_{\pm}$ other than $a_{\pm}T^4/3$. The physical meaning of $\epsilon_{\pm}$ is apparent by identifying it with the trace of stress-energy tensor, $\epsilon_{\pm} = \eta_{\mu\nu}T^{\mu\nu}(\phi_{\pm}, T_{\pm})$. One can easily check that Eq. (2.32) reduces to the bag model once only zeroth-order terms of T in V_{eff} is kept.

Now we apply the EOS to the matching conditions derived in the previous section. For convenience, we introduce the following two parameters

$$r = \frac{w_+}{w_-}\,, \tag{2.33}$$

$$\alpha_+ = \frac{4(\epsilon_+ - \epsilon_-)}{3w_+}\,. \tag{2.34}$$

where r represents the enthalpy ratio between the false and true vacua. The α_+ is defined as the difference of the trace of stress-energy tensor normalized by 3/4 of the enthalpy, and is widely used in gravitational wave calculation. α_+ reduces to the released vacuum energy density normalized by the radiation energy in the bag model. α_+ is commonly used to

characterize the phase transition strength, especially in the GW calculations. In the following sections, we will study its correlation with another phase transition strength parameter commonly used in the EWBG studies, v_n/T_n, which characterizes the degree to which the electroweak sphaleron process is suppressed in the broken phase.

Substituting the general EOS into the two matching conditions of Eq. (2.23) and using these new parameters yields the relations

$$v_+ v_- = \frac{1-(1-3\alpha_+)r}{3-3(1+\alpha_+)r}\,, \tag{2.35a}$$

$$\frac{v_+}{v_-} = \frac{3+(1-3\alpha_+)r}{1+3(1+\alpha_+)r}\,. \tag{2.35b}$$

These can be combined by eliminating r to give [64]

$$v_+ = \frac{1}{6(1+\alpha_+)v_-}\left(1+3v_-^2 \pm \sqrt{1+6(6\alpha_+^2+4\alpha_+-1)v_-^2+9v_-^4}\right)\,, \tag{2.36}$$

which relates the fluid velocities on either side of the wall $v_\pm$ as a function of the phase transition strength α_+.

Here we comment on the value of the sound speed, which is defined as

$$c_{s,\pm} \equiv \sqrt{\frac{dp_\pm/dT_\pm}{de_\pm/dT_\pm}}\,. \tag{2.37}$$

Specifically, in the bag model where $a_\pm$ are temperature-independent constants, the sound speed is also a constant $c_{s,\pm} = 1/\sqrt{3}$. While for the general definitions Eq. (2.32), $a_\pm$ become temperature-dependent, and so does the sound speed. The deviation from $1/\sqrt{3}$, however, is typically not too large. Sound speed plays a crucial role in the fluid profile induced by the bubble expansion, as one will see in Sec. 2.2.4.

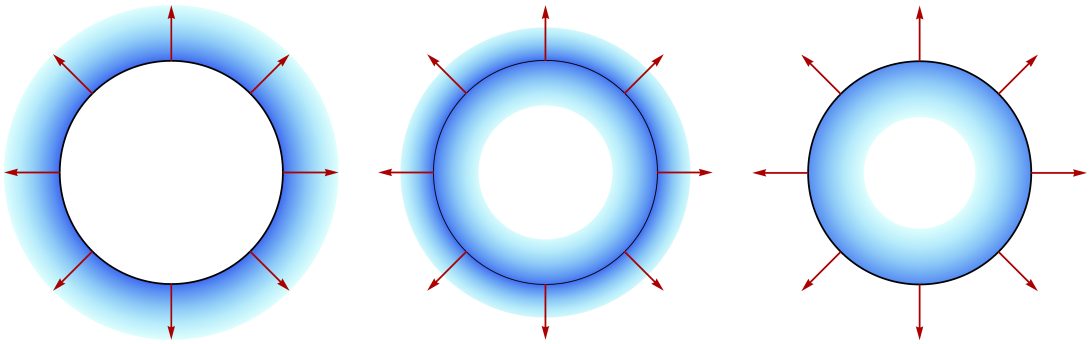


Figure 2.1: Fluid profiles for deflagration, hybrid, and detonation solutions. The blue shaded region indicates non-zero fluid velocity.

2.2.4 Fluid Profiles

The matching conditions for the asymptotic fluid velocities $v_\pm$ and temperatures $T_\pm$ are provided by Eqs. (2.27), (2.35a) and (2.35b), yet the relationship between these quantities and v_w remains undetermined. As we will see in this subsection, this relationship depends on the global fluid profiles induced by the bubble expansion. In the following, we review the three types of fluid profile, and how v_w enters the matching conditions in each case. We summarize the results in Table 2.1 for the readers' convenience.

To solve for the fluid profiles around the bubble, it is more convenient to work in the cosmic frame where the center of the bubble is at rest. We define a dimensionless quantity $\xi \equiv R/t$, assuming spherical symmetry, with R being the radial distance from the bubble center, and t being the time since nucleation. The profile of the disturbed plasma is then described by the local fluid velocity $v_{\rm cf}(\xi)$ and temperature $T(\xi)$.

In Appendix A.4, we derive the following master equation for the velocity profile[8]

$$2\frac{v_{\rm cf}(\xi)}{\xi} = \gamma_{\rm cf}^2(1 - v_{\rm cf}(\xi)\,\xi)\left(\frac{\mathfrak{v}(\xi, v_{\rm cf}(\xi))^2}{c_s^2(\xi)} - 1\right)\frac{\partial v_{\rm cf}(\xi)}{\partial \xi}\,, \tag{2.38}$$

8. Appendix A.4 also contains the derivation for the master equation for the temperature profile $T(\xi)$.

where we have defined the Lorentz boost as

$$\mathfrak{v}(\xi, v) = \frac{\xi - v}{1 - \xi\, v}\,. \tag{2.39}$$

One property of Eq. (2.38) is that ($\xi = c_s, v_{\rm cf} = 0$) is a stationary point of this equation, indicating a vanishing fluid velocity at $\xi = c_s$. Eq. (2.38) admits three broad classes of solutions for the fluid profile [64] — detonation, deflagration, and hybrid — which we depict schematically in Fig. 2.1. In the remainder of this subsection, we discuss each of these solutions.

Detonation

A detonation solution occurs for fast-moving bubble walls and is characterized by a fluid at rest in front of the wall and a rarefaction wave of the perturbed fluid behind the wall. Since the fluid in front of the bubble wall remains unperturbed, in the wall frame we can identify

$$v_+ = v_w\,,\;\; T_+ = T_n\,, \tag{2.40}$$

where T_n is the nucleation temperature, defined as the temperature when the bubble nucleation rate reaches the Hubble rate. v_- and T_- can then be directly solved from Eqs. (2.22a) and (2.22b).

Such a type of fluid profile only exists when the bubble wall moves fast enough so that the disturbed plasma falls behind. We now derive the allowed lowest value of v_w consistent with a detonation profile. Working in the cosmic frame, we denote the velocity of a fluid element at a point ξ in the wave profile of the rarefaction wave behind the wall by $v_{\rm cf}(\xi)$, with $\xi < v_w$. This velocity is largest right behind the wall at $\xi_w = v_w$, where $v_{\rm cf}(\xi_w) = \mathfrak{v}(v_w, v_-)$, and decreases monotonically as one moves further towards the interior of the bubble, i.e. along negative ξ direction, eventually vanishing at $\xi = c_s^-$. In other words, $v_w \geq c_s^-$ is a necessary

condition for a rarefaction wave to exist behind the wall. A consistent solution for $v_{\rm cf}(\xi)$ in the regime $c_s^- < \xi < \xi_w$ requires $\partial_\xi v_{\rm cf} > 0$. Considering Eq. (2.38) with such a requirement, we see that the boosted fluid velocity must exceed the sound speed in the bubble interior, $\mathfrak{v}(\xi, v_{\rm cf}(\xi)) \geq c_s^-$. At the location of the wall, this implies $v_- \geq c_s^-$. This condition allows us to define the *Jouguet velocity* v_J as the smallest value of v_w compatible with a detonation profile,

$$v_J \equiv v_w \;\; \text{such that} \;\; v_- = c_s^- \text{ under detonation profile}\,. \tag{2.41}$$

For values of $v_- \geq c_s^-$, we have $v_w \geq v_J$ and the detonation profile is allowed.

Deflagration

For $v_w < c_s^-$, we have deflagration solutions, for which the plasma behind the wall is at rest and a shockwave precedes the wall. The upper bound on v_w comes from the following counter-argument: if $v_w > c_s^-$, a solution with $dv_{\rm cf}(\xi)/d\xi > 0$ would be allowed in the range $c_s^- < \xi < \xi_w$, as can be seen from Eq. (2.38). Therefore, a rarefaction wave would exist, and the bubble wall would no longer be deflagration-type. Hence, when $v_w < c_s^-$, the plasma behind the wall is at rest, and we can identify

$$v_- = v_w\,. \tag{2.42}$$

Moreover, in the deflagration case, the thermodynamic quantities evolve in the perturbed region in front of the wall. This perturbation starts from the bubble wall and ends at a distance in front of it, known as the shock wave front, whose location is denoted as $\xi_{\rm sh}$. The fluid outside of $\xi_{\rm sh}$ is at rest, and we have

$$T_{\rm sh,+} = T_n\,, \tag{2.43}$$

where the + labels the symmetric side of the shock wave front.

The boundary conditions Eqs. (2.42) and (2.43) are not at the same location. To solve for T_- and v_+, T_+, we need to connect the bubble wall and the shock wave front. As before, we move to the cosmic frame and analyze the fluid profile $v_{\rm cf}(\xi)$. The fluid velocity is fastest immediately outside the wall, where $v_{\rm cf}(\xi_w) = \mathfrak{v}(\xi_w, v_+)$. Moving outward along ξ, it decreases monotonically until arriving at the shock wave front, where the temperature and velocity of the plasma are discontinuous. The decreasing $v(\xi)$ implies that $\mathfrak{v}(\xi, v_{\rm cf}(\xi)) \leq c_s^+$, as can be inferred from Eq. (2.38). At the wall, this becomes $v_+ \leq c_s^+$. The matching conditions Eqs. (2.23a) and (2.23b) can be directly applied at the shock wave front, with no discontinuity of the scalar field value. In terms of the cosmic frame velocities, we identify $v_{\rm sh,-} = \mathfrak{v}(\xi_{\rm sh}, v_{\rm cf}(\xi_{\rm sh}))$, and $v_{\rm sh,+} = \mathfrak{v}(\xi_{\rm sh}, 0) = \xi_{\rm sh}$. Here, $v_{\rm sh,\pm}$ is the fluid velocity on both sides of the shock wave front, measured in the shock wave frame. Recall the definition of the sound speed, the first matching condition (2.23a) becomes

$$\mathfrak{v}(\xi_{\rm sh}, v_{\rm cf}(\xi_{\rm sh}))\xi_{\rm sh} = (c_s^+)^2\,, \tag{2.44}$$

which is used to determine the location of the shock wave front, $\xi_{\rm sh}$. The velocity profile $v_{\rm cf}(\xi)$ applied here can be solved together with the temperature profile $T(\xi)$ from Eqs. (2.38) and (A.37b). The corresponding boundary condition is $v_{\rm cf}(\xi_w) = \mathfrak{v}(\xi_w, v_+)$ and $T(\xi_w) = T_+$. Specifically, $T(\xi_{\rm sh})$ should be regarded as $T_{\rm sh,-}$, which is related to $T_{\rm sh,+}$ by Eq. (2.23b).

Based on the discussion above, the relationship between v_+, T_+ and $T_{\rm sh,+}$ is established. Since $T_\pm$ and v_+ are still unknown, the following shooting method can be applied to solve for them,

1. Set $v_- = v_w$ and make an initial guess for T_-.

2. Solve for v_+ and T_+ using the matching conditions Eqs. (2.35a), (2.35b).

3. Solve Eqs. (2.38) and (A.37b) with boundary condition $v(\xi_w) = \mathfrak{v}(\xi_w, v_+)$ and $T(\xi_w) =$

T_+ for the velocity and temperature profiles $v(\xi)$ and $T(\xi)$.

4. Using $v(\xi)$ and $T(\xi)$, solve Eq. (2.44) for the location of the shockwave front. Identify $v_{\mathrm{sh},-} = \mathfrak{v}(\xi_{\mathrm{sh}}, v_{\mathrm{cf}}(\xi_{\mathrm{sh}}))$ and $T_{\mathrm{sh},-} = T(\xi_{\mathrm{sh}})$.

5. Use the matching conditions at ξ_{sh} to solve for $T_{\mathrm{sh},+}$.

6. Check whether $T_{\mathrm{sh},+} = T_n$. If not, modify T_- and continue iteration.

Hybrid

The remaining range of v_w to be discussed is now $c_s^- < v_w < v_J$, which is known as the hybrid solution, characterized by the existence of both rarefaction wave behind the wall and preceding shock wave between the wall and the shock wave front. Since deflagration requires $v_- \leq c_s^-$ while detonation requires $v_- \geq c_s^-$, the hybrid solution, as an intermediate range, must require

$$v_- = c_s^- < v_w \,. \tag{2.45}$$

As in the deflagration case, the nucleation temperature is identified with the temperature at the shock wave front

$$T_{\mathrm{sh},+} = T_n \,. \tag{2.46}$$

Due to the nature of these boundary conditions, one must again use the shooting method algorithm to determine $T_{\mathrm{sh},+}$. This procedure is completely analogous to the deflagration case except that the initial v_- is set by c_s^-. Hybrid solutions are sometimes referred to as "supersonic deflagrations" given their similarity to deflagrations whilst having $v_w > c_s^-$.

	Deflagration	Hybrid	Detonation
v_w	$v_w < c_s^-$	$c_s^- < v_w < v_J$	$v_J < v_w$
Boundary Conditions	$v_- = v_w$, $T_{\mathrm{sh},+} = T_n$, $\mathfrak{v}(\xi_{\mathrm{sh}}, v(\xi_{\mathrm{sh}}))\xi_{\mathrm{sh}} = (c_s^+)^2$	$v_- = c_s^-$, $T_{\mathrm{sh},+} = T_n$, $\mathfrak{v}(\xi_{\mathrm{sh}}, v(\xi_{\mathrm{sh}}))\xi_{\mathrm{sh}} = (c_s^+)^2$	$v_+ = v_w$, $T_+ = T_n$

Table 2.1: Summary of boundary conditions for deflagration, hybrid, and detonation solutions.

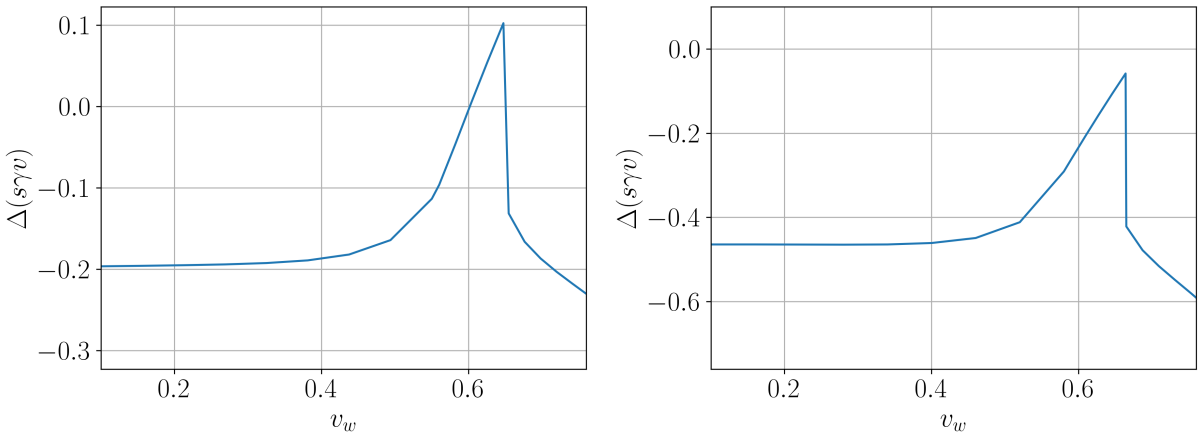


Figure 2.2: $\Delta(s\gamma v)$ as a function of v_w in arbitrary unit for the $\mathbb{Z}_2$ symmetric real singlet extension model (discussed in Sec. 2.3) for two types of bubbles. Left: Deflagration/hybrid-type bubble with a positive peak of $\Delta(s\gamma v)$ at v_J. Right: Detonation-type bubble with a negative peak of $\Delta(s\gamma v)$. We truncate the plot at $v_w < 1$, since for $v_w \sim 1$, out-of-equilibrium effects become dominant and LTE is not justified [1].

2.2.5 Determining v_w in LTE

In summary, for a given v_w and phase transition dynamics, the fluid velocity and temperature near the wall, i.e. $v_\pm$ and $T_\pm$, can be solved based on the two matching conditions, Eqs. (2.22a) and (2.22b), derived from EMT conservation, as well as the boundary conditions depending on the type of solutions as summarized in Table 2.1. The remaining matching condition demanding entropy conservation in the steady state, $\Delta(s\gamma v) \equiv (s\gamma v)|_-^+ = 0$, Eq. (2.27), can then be used to determine the true terminal velocity.

Fig. 2.2 shows $\Delta(s\gamma v)$ as a function of v_w in the cases of deflagration/hybrid and detonation for the $\mathbb{Z}_2$ symmetric real singlet extension model, which is used as the test model and discussed in detail in Sec. 2.3. We observe that $\Delta(s\gamma v)$ peaks at $v_w = v_J$ for both deflagration/hybrid and detonation. This can be intuitively understood recalling that the scalar field EOM is equivalent to entropy conservation in satisfying the condition of EMT conservation, see Eq. (2.24). When $v_w > v_J$, there is no heated plasma in front of the wall, eliminating the friction on the bubble wall and altering the net pressure defined in Appendix A.1. This lack of friction, whenever $v_w > v_J$, is responsible for the peak in

the total net pressure on the wall at v_J. Such a phenomenon is known as hydrodynamic obstruction [65]. If $\Delta(s\gamma v)$ at v_J is positive, there are two solutions of v_w on both sides of v_J satisfying $\Delta(s\gamma v) = 0$, see the left panel of Fig. 2.2. The solution with smaller v_w of $\Delta(s\gamma v) = 0$ gives the true terminal velocity that corresponds to a deflagration/hybrid solution. If $\Delta(s\gamma v)$ at v_J is negative, there is no solution of v_w satisfying $\Delta(s\gamma v) = 0$, as shown in the right panel of Fig. 2.2. In this case, no terminal velocity is predicted under LTE, and the bubble wall is detonation-type. Despite the lack of friction for $v_w > v_J$ in LTE, the out-of-equilibrium effects can still contribute to the friction on the bubble wall, which increases with v_w [66] and only becomes significant when $v_w \to 1$ [1]. This friction generated from the out-of-equilibrium contribution would eventually balance the driving pressure and stop the bubble wall from accelerating when $v_w \to 1$. Such an effect is crucial when discussing the scalar field contribution to the GW signal, and will be discussed further in Appendix B.2.

We design the following algorithm utilizing the entropy conservation condition first considered in [63, 67, 68] as:

1. Start from a high value of $v_w \to 1$. Solve for v_- and T_- assuming a detonation solution. Decrease v_w until we find $v_- = c_s^-$. Identify such v_w as v_J.

2. Compute the peak of $\Delta(s\gamma v)$ at $v_w \to v_J$ assuming hybrid-type bubble wall. If $\Delta(s\gamma v) < 0$ at this peak, conclude the bubble is detonation-type. If not, the bubble wall is deflagration/hybrid type, and proceed to the next step.

3. Solve for the true terminal velocity v_w between 0 and v_J satisfying $\Delta(s\gamma v) = 0$ using the deflagration or hybrid boundary conditions as appropriate.

It is worth noting that some recent studies taking the time dependency of the wall velocity into account find that in a large region of parameter space, the steady-state solution of the fluid profile is not fully established during deflagration/hybrid wall expansion [69, 70]. Consequently, bubble walls are more likely to enter the detonation regime. The above recent

works offer a challenge to results using the LTE approximation in the existing literature, and we intend to explore this issue in more detail in a future work.

2.3 Wall Velocity Calculation in a Benchmark Model

We apply the method introduced in Sec. 2.2.5 for computing wall velocity to a $\mathbb{Z}_2$-symmetric real singlet scalar extension of the SM, which is regarded as the most minimal extension capable of rendering a strong first-order EWPT, and has been studied extensively in the literature [33, 71–80]. In particular, Ref. [1] has studied the terminal wall velocity under the general conditions including the out-of-equilibrium effect (see Appendix A of [52] for a review). Hence, we study this model as a test case to verify explicitly the validity of the LTE approximation and the entropy conservation condition approach.

Consider supplementing the SM with a real scalar singlet S and a discrete $\mathbb{Z}_2$ symmetry under which $S \to -S$ while the rest of the SM fields remain unchanged. Letting H be the SM Higgs doublet and working in the unitary gauge, the tree-level potential of the scalar sector reads [33, 71–78]

$$V_{\text{tree}} = -\mu_H^2 (H^\dagger H)^2 + \lambda_H (H^\dagger H)^4 + \frac{\mu_S^2}{2} S^2 + \frac{\lambda_S}{4} S^4 + \frac{\lambda_{SH}}{2} S^2 (H^\dagger H)\,. \tag{2.47}$$

The finite-temperature effective potential V_{eff} is the sum of this tree level potential with the Coleman-Weinberg and finite-temperature corrections, $V_{\text{eff}} = V_{\text{tree}} + V_{\text{CW}} + V_T$, see Appendix E of [52] for details. Among the five parameters in the tree-level potential, two of them are fixed by the SM Higgs mass and VEV, while the other three remain free. In the following, we parameterize the model as a function of: λ_S, λ_{SH}, and the physical mass of the real scalar singlet m_S.

To verify explicitly the validity of the LTE approximation and the entropy conservation approach, we use this formalism to compute v_w and compare the results with those in Ref. [1].

Fig. 2.3 presents the results for 394 benchmark points that have strong first-order EWPT, with fixed $\lambda_S = 1$ and varying m_S and λ_{SH}. In the parameter region being considered, the EWPT proceeds in two steps in the (h, S) field configuration space: $(0, 0) \to (0, w') \to (v_n, 0)$. Fig. 2.3(a) shows the detonation and deflagration/hybrid solutions in the m_S-λ_{SH} plane, with the wall velocities of the deflagration/hybrid points depicted by the color gradient. The wall velocity falls into the range from $\sim 0.53 - 0.68$, slightly narrower than that in Ref. [1] due to lower statistics[9]. Fig. 2.3(b) shows the histogram of α_n for the detonation and deflagration/hybrid solutions. Comparing Fig. 2.3(a) and Fig. 2.3(b) with Fig. 3 and 4 of Ref. [1] (see also Fig. 5 of Ref. [82]), we see that the distribution of the detonation and deflagration/hybrid solutions displays the same pattern. This adds credence to the claim that the leading-order effects are already present in LTE. Most importantly, our results prove that the entropy conservation algorithm provides a reliable method of computing v_w. In Fig. 2.3(c) and Fig. 2.3(d), we show scatter plots in the α_n-v_w plane (for the deflagration/hybrid points), and in the α_n-v_n/T_n plane (for all the benchmark points, same as Fig. 2.3(a) and Fig. 2.3(b)). We observe positive correlations between α_n and v_w, α_n and v_n/T_n, respectively, although with two varying parameters (m_S, λ_{SH}), there is no 1-to-1 correspondence between them in either case. When one parameter is fixed, or restricted to a narrow range, α_n (nearly) uniquely determines v_w and v_n/T_n. In Fig. 2.3(c) and Fig. 2.3(d), the blue, green, and red points have $m_S \in [60, 70]\,\text{GeV}$, $m_S \in [90, 100]\,\text{GeV}$ and $m_S \in [110, 120]\,\text{GeV}$, respectively, with λ_{SH} varying in the range illustrated in Fig. 2.3(a). The blue, green, and red lines are the fitting of the corresponding points with the function $f(x) = a\ln(x) + b + cx + dx^2$, with the fitted parameters summarized in Table 2.2. Although the fitting coefficient accompanying the $\ln(x)$ term is rather small, we emphasize that this term dominates in the low-α_n regime and therefore is essential for the fit.

We would like to further comment on the fact that Fig. 2.3(b) shows a notable overlap

9. Our results, similar to Ref. [1], are at variance with simple approximations yielding a very small value of v_w, e.g. $v_w \simeq (T_c - T_n)/T_n$ [81].

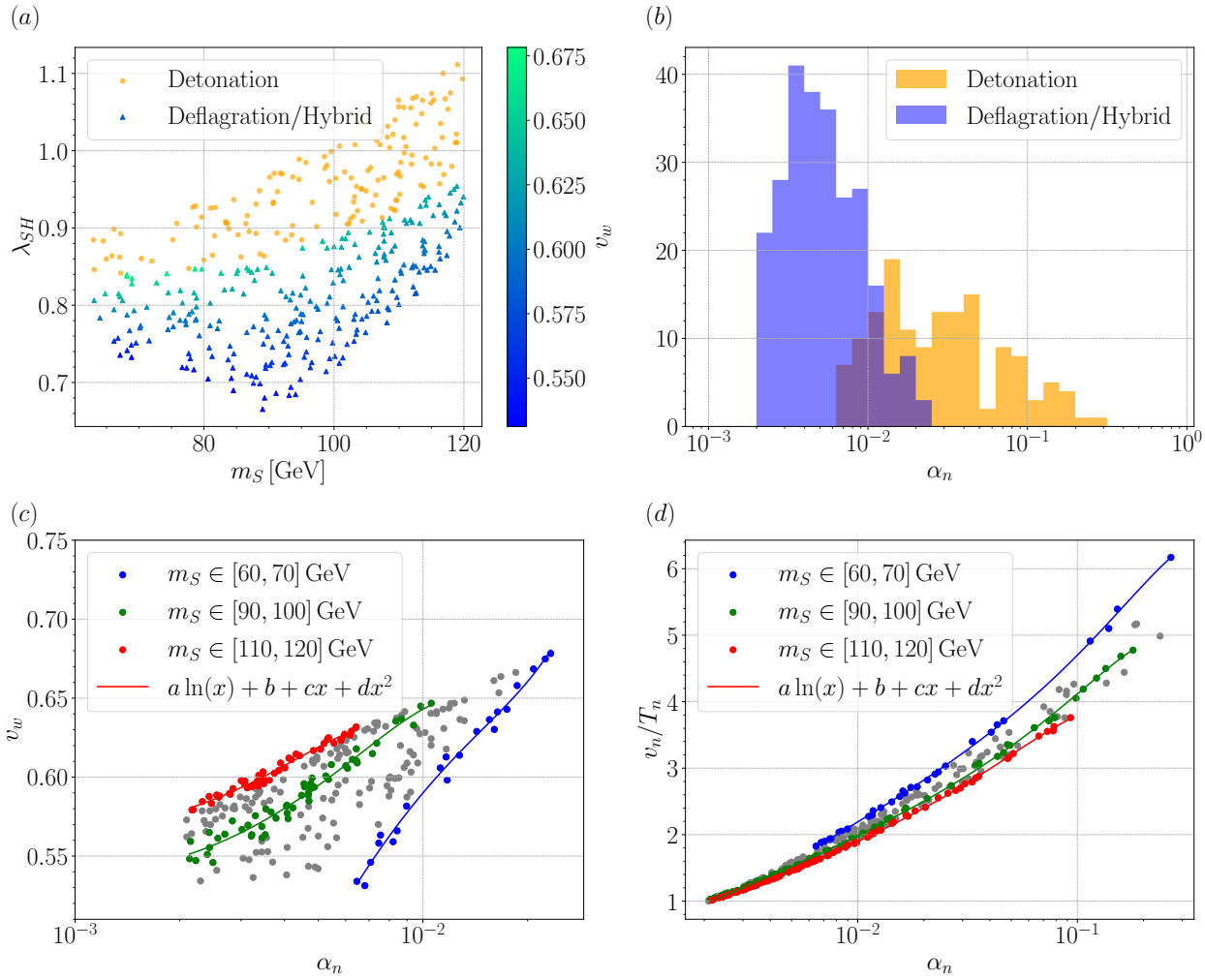


Figure 2.3: Strong first-order EWPT points and wall velocities calculated under the LTE approximation, using the entropy conservation approach for the $\mathbb{Z}_2$ symmetric real scalar singlet extended SM. We fix $\lambda_S = 1$, and vary λ_{SH} and m_S in the scanning. Panel (a) shows detonation and deflagration/hybrid solutions in the m_S-λ_{SH} plane, with wall velocities depicted by the color gradient. Panel (b) shows the histogram of α_n for the detonation and deflagration/hybrid solutions. Panel (c) shows all the deflagration/hybrid points in the α_n-v_w plane. The points highlighted in blue, green, and red have one of the model parameters m_S restricted to a narrow range as indicated by the legend. The solid lines of the same colors are the fitting of the scatter points with the function $f(x) = a\ln(x) + b + cx + dx^2$, with fitted parameters listed in Table 2.2. Panel (d) shows all the strong first-order EWPT points (in gray), including detonation bubbles, in the α_n-v_n/T_n plane. The blue, green, and red points and lines have the same meaning as those in panel (c).

m_S range (GeV)	(a, b, c, d) for $v_w = f(\alpha_n)$	(a, b, c, d) for $v_n/T_n = f(\alpha_n)$
$60 - 70$	$(0.27, 2.00, -22.83, 382.07)$	$(0.78, 5.68, 9.59, -14.60)$
$90 - 100$	$(-0.016, 0.40, 27.24, -1021.60)$	$(0.59, 4.60, 11.48, -26.61)$
$110 - 120$	$(-0.028, 0.34, 36.93, -2114.66)$	$(0.52, 4.13, 16.41, -78.95)$

Table 2.2: Fitted parameters for v_w and v_n/T_n as function $f(\alpha_n) = a\ln(\alpha_n) + b + c\,\alpha_n + d\,\alpha_n^2$ for m_S in the given ranges.

between the detonation and deflagration/hybrid solutions. This is at variance with the results of the analytic treatment of Ref. [68], which demonstrate the existence of a critical value of $\alpha_n^{\max}$ defining the boundary between the deflagration/hybrid and detonation regimes. The derivation assumes the bag equation of state, and relies on the fact that the height of the pressure peak is a monotonic function of α_n. It solves for the critical value $\alpha_n^{\max}$ as the value at which the height of the peak in Fig. 2.2 is at zero. The result is an expression for $\alpha_n^{\max}$ which depends solely on the number of light degrees of freedom in the model. Applying this formula to the $\mathbb{Z}_2$-symmetric scalar singlet extension, one finds the critical value $\alpha_n^{\max} \simeq 0.05$. However, Fig. 2.3(b) shows a more complicated pattern, implying a deviation from the bag equation of state. Nevertheless, the results in [68] still provide guidance for the maximal value of α_n for deflagration/hybrid solutions in EWPT.

2.4 Summary

In this chapter, we review the basics of phase transition calculations, including the formulation of effective potential and the evaluation of nucleation rate. We then analyze the bubble wall dynamics in detail, deriving two matching conditions for the fluid velocities and temperatures on either side of the bubble wall. Assuming local thermal equilibrium, a third matching condition can be identified as entropy conservation across the bubble wall. These three matching conditions, together with the boundary conditions determined by the fluid profiles near the bubble wall, uniquely fix the bubble wall velocity. The corresponding procedure is outlined in Sec. 2.2.5. We then apply such procedure to the $\mathbb{Z}_2$-symmetric scalar singlet

extension model and compare the results with those obtained from a full nonequilibrium calculation, finding good agreement between the two. This explicitly verifies the validity of the LTE approximation and the entropy conservation approach.

CHAPTER 3

ELECTROWEAK BARYOGENESIS WITH DARK CP VIOLATION

EWBG is an elegant mechanism that generates the observed BAU at the Electroweak Phase Transition (EWPT) [15, 16]. The Standard Model (SM), however, can not account for successful EWBG: the Higgs mass is too heavy to allow for a strong first order phase transition and the CP violation source is not sufficient, hence new physics is required. However, new sources of CP violation from particles charged under the SM are strongly constrained by the remarkable results from electric dipole moment (EDM) experiments [83, 84]. In this chapter, we focus on a new EWBG mechanism in which CP violation occurs in the dark sector and is transmitted to the visible sector via a vector gauge boson Z' from a $U(1)_l$ gauge lepton symmetry first proposed in Refs. [85, 86]. In such a scenario, a complex scalar singlet S provides the source of CP violation through its Yukawa coupling to a dark fermion χ charged under $U(1)_l$ as well as leads to a strongly first order electroweak phase transition (SFOEWPT) via its coupling with the Higgs boson field. In this way, the contribution to EDM is suppressed to beyond two-loop level and compatible with current experiments. The dark fermion χ can also serve as an ideal dark matter candidate.

In the following, we first introduce the model (Sec. 3.1), and then present a detailed analysis of the EWPT pattern of this model (Sec. 3.2). Focusing on the phase transition points that allow for EWBG, we calculate in Sec. 3.3.1 the corresponding wall velocities under the local thermal equilibrium (LTE) approximation using the method introduced in Sec. 2.2.5. We will find that the typical wall velocities are much higher than the commonly assumed values for EWBG, and so in Sec. 3.3.2 we examine the implications for baryogenesis in this model. We compute the BAU in different computational frameworks and comment on their applicability depending on the value of v_w. Finally in Sec. 3.3.3 we examine the consequences for the gravitational waves (GW) signal. The calculations and results presented

in this chapter are based on my publications [52, 87] in collaboration with others.

3.1 The EWBG model

In this section, we briefly introduce the model for EWBG as schematically shown in Fig. (3.1), with CP violation sourced from the dark sector, and an SFOEWPT where the barrier is provided by the tree-level coupling between the complex singlet and the SM Higgs. In the following, we would present the Lagrangian terms that define the Higgs and gauge boson portals between the SM sector and the dark sector of the theory. Readers can find more specific details of the model in [85, 86]. In this work, we focus on the EW-scale low energy

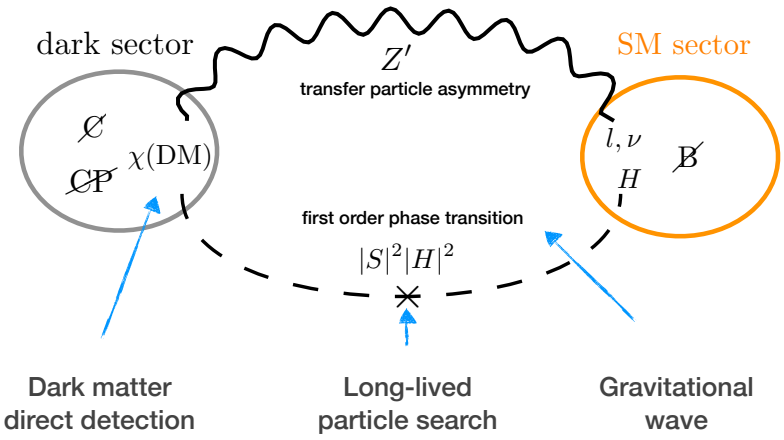


Figure 3.1: Low energy sector of the model and probes for EWBG and a dark matter candidate.

effective theory of the UV complete model for baryogenesis presented in [85], where the $U(1)_l$ symmetry, the gauge symmetry promoted from the lepton number, has been spontaneously broken by a heavy singlet field Φ. Integrating out various anomalon fields, the low energy sector of the model contains the SM fields plus the new fields

$$Z'_\mu, \quad S, \quad \chi_L, \quad \chi_R. \tag{3.1}$$

The complex singlet S couples to the SM Higgs to provide a barrier for the EWPT. At zero temperature, the tree level effective scalar potential reads

$$V_0 = \lambda_H(|H|^2 - v_H^2)^2 + \lambda_S(|S|^2 - v_S^2)^2 + \lambda_{SH}|S|^2|H|^2 + \delta V, \tag{3.2}$$

where H is the Higgs doublet and

$$\delta V = \rho_S S + \kappa_S^2 S^2 + \lambda_{3S}|S|^2 S + \text{h.c.} \tag{3.3}$$

Observe that apart from the δV the tree level potential only depends on $|S|$. Hence, to accommodate a CP violating effect, additional terms depending on S are needed . Such terms can arise from renormalizable, $U(1)_l$ invariant terms, involving the heavy singlet field Φ. For this work, we study the case where S has a zero vacuum expectation value (vev) at the EW vacuum, that implies no tadpole at zero temperature. This can be achieved by adjusting the coefficient for the tadpole term to be zero at one-loop order, as will be discussed later. For simplicity, we will turn off the cubic term. The coefficient of the quadratic term, κ_S^2, is a free parameter for scanning and is in general complex.

The complex SM $SU(2)$ Higgs doublet H and the complex SM scalar singlet S can be expressed in terms of real fields as follows

$$H = \frac{1}{\sqrt{2}}\begin{pmatrix} G_1 + iG_2 \\ h + iG_3 \end{pmatrix}, \quad S = \frac{1}{\sqrt{2}}(s + ia). \tag{3.4}$$

Using unitary gauge to eliminate the Goldstone fields G_i's, we can rewrite the potential in Eq. (3.2) in terms of (h, s, a) as

$$\begin{aligned} V_0 = \quad & -\frac{1}{2}\mu_H^2 h^2 + \frac{1}{4}\lambda_H h^4 + \frac{1}{4}\lambda_{SH} h^2(s^2 + a^2) \\ & -\frac{1}{2}\mu_S^2(s^2 + a^2) + \frac{1}{4}\lambda_S(s^2 + a^2)^2 + \kappa_S^2(s^2 - a^2), \end{aligned} \tag{3.5}$$

where $\mu^2_{H(S)} = \lambda_{H(S)} v^2_{H(S)}$. The Higgs quartic coupling and the Higgs vev at $T = 0$ are fixed by Higgs boson measurements to be $\lambda_H = 0.129$ and $v_H = 246$ GeV. For convenience, we rewrite the singlet quartic coupling λ_S and the coefficient of the CP violating term κ^2_S in Eq. (3.5) in terms of physical parameters, i.e., the masses of the scalars a, s at $T = 0$, $m_{a,s}$:

$$m_a^2 = \frac{1}{2}\lambda_{SH} v_H^2 - \lambda_S v_S'^2, \quad m_s^2 = m_a^2 + 4\kappa_S^2, \tag{3.6}$$

with $v_S'^2 \equiv v_S^2 + 2\kappa_S^2/\lambda_S$. As will be shown in Sec. 3.2.2 and Sec. 3.2.4, v_S' is the value of the singlet field in the a-direction at a zero temperature EW symmetric stationary point of the scalar potential. The existence of this stationary point facilities a SFOEWPT.

The fermion fields χ_L and χ_R are SM singlets that couple to the singlet composite scalar S. The Yukawa coupling between S and χ is given by

$$\bar{\chi}_L(m_0 + \lambda_c S)\chi_R + \text{h.c.}\,, \tag{3.7}$$

and the mass of χ reads

$$M_\chi = m_0 + \lambda \exp(i[\theta + \arg(S)])|S|, \tag{3.8}$$

where $\lambda = |\lambda_c|$ and $\theta = \arg(\lambda_c)$[1]. Note that m_0 is induced by the coupling of χ to the heavy singlet scalar field Φ, when it acquires a non-zero vev at the UV. The corresponding Yukawa coupling is assumed to be small such that m_0 is much lighter than the vev $\langle\Phi\rangle$ and the dark fermions remain dynamical at low energies. We use the freedom of field redefinition to make κ_S^2 and m_0 real and positive, leaving λ_c complex in general. During the EWPT, the phase of M_χ varying in the direction of the expanding bubble wall, can be derived from m_0, the phases of λ_c and the S vev. This is the physical source of CP violation, that will then induce

1. Observe that in [85], θ is defined as $\arg(\lambda_c) + \arg(S)$ with $\arg(S)$ fixed to $\pi/2$.

a chiral asymmetry in the χ particles.

As has been mentioned above, the lepton number is promoted to a $U(1)_l$ gauge symmetry with an associated Z' gauge boson, and the dark fermion χ and the singlet S are assigned certain lepton number charges. Possible anomaly-free UV completions can be found in [88–93]. The new interactions introduced at low energy are:

$$\mathcal{L} \supset g' Z'_\mu \left[(N_g + q)\bar{\chi}_L \gamma^\mu \chi_L + q\bar{\chi}_R \gamma^\mu \chi_R + \bar{L}\gamma^\mu L + \bar{e}_R \gamma^\mu e_R \right] . \tag{3.9}$$

We assume $U(1)_l$ with $l = e, \mu, \tau$ and thus $N_g = 3$, and the charge $q \sim \mathcal{O}(1)$ throughout this study. Given that χ_L and χ_R carry different $U(1)_l$ charges, the chiral asymmetry in the χ sector will give a net $U(1)_l$ charge density near the bubble wall, that generates a background for the Z'_0 component. Because of the coupling of the SM leptons with the Z', this background further generates a chemical potential for the SM leptons and consequently a net chiral asymmetry for them. As will be discussed in detail later on, solving the corresponding Boltzmann equation, considering the EW sphaleron rate suppressed inside the bubble wall, one obtains a lepton asymmetry. Ultimately, a baryon asymmetry will be generated by the sphaleron processes which preserve $B - L$.

Protected by a Z_2 symmetry in the Lagrangian, $\chi \to -\chi$, the dark fermion χ is stable and could be a dark matter candidate. The annihilation channels for χ at tree level include annihilating to $Z'Z'$, SM lepton pairs, ss, aa and sa. The corresponding Feynman diagrams are shown in Fig. (3.2). Given the LEP constraints on Z' search, the dominant annihilation channel to achieve the correct relic density is $\chi\bar{\chi} \to ss, aa, sa$, which requires [86]

$$\sqrt{\frac{m_0}{1.4\text{TeV}}} < \lambda < \sqrt{\frac{m_0}{1\text{TeV}}}. \tag{3.10}$$

The range for λ is due to the θ dependence of the annihilation cross section. We will implement this relation in the numerical scanning to generate the observed dark matter relic abundance.

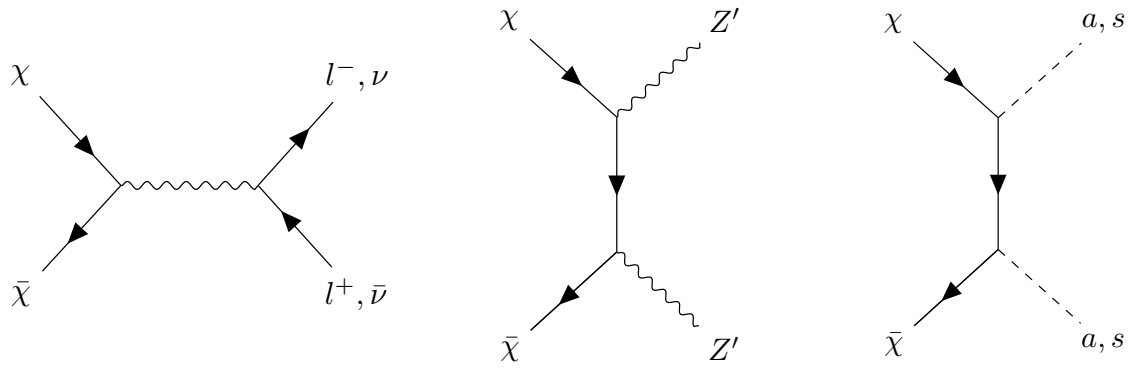


Figure 3.2: Tree-level annihilations of the dark fermion χ.

To conclude this section, we categorize our model parameters through the following groups:

$$\begin{aligned} \text{fixed parameters}: &\quad \{\lambda_H, v_H\}, \\ \text{scalar sector parameters}: &\quad \{\lambda_S, v_S', \lambda_{SH}, m_a, m_s\}, \\ \text{dark fermion parameters}: &\quad \{m_0, \lambda, \theta\}, \\ Z\text{' parameters}: &\quad \{g', M_{Z'}\}. \end{aligned}$$

The stability of the scalar potential and the EW thermal history would be affected by the fixed parameters and the scalar potential parameters at tree level, as well as by the dark fermion parameters at loop level. The Z' parameters do not enter the scalar potential but would be crucial for the transmission of the baryon asymmetry and thus are relevant for the BAU. They are also of great importance for the phenomenology associated to the Z' searches. The scalar singlet phenomenology and the dark matter direct detection constraints involve parameters across the model and will be discussed in detail in later sections.

3.2 Anatomy of the electroweak phase transition

In this section, we introduce the one loop order scalar potential, based on which, we analyze the thermal history, the phase transition patterns, and the nucleation requirement. With

various boundary conditions, derived at zero and finite temperatures, we identify the viable parameter space that can be compatible with the desired thermal history for EWBG. Towards the end of this section, we show numerical results from parameter scannings to support our analytical calculations for the phase transitions.

3.2.1 The one-loop order scalar potential

The one-loop order scalar potential is composed of the following terms:

$$V(h, s, a, T) = V_0 + V_{\rm CW} + V_{\rm ct} + V^T_{\text{1-loop}}, \tag{3.11}$$

where $V_{\rm CW}$ is the Coleman-Weinberg potential and $V^T_{\text{1-loop}}$ is the one-loop thermal correction, which can be calculated following the discussions in Sec. 2.1. $V_{\rm ct}$ is the counterterm potential added to fix the vevs and masses as their tree-level values at the physical vacuum at $T = 0$. To achieve this, the first and second derivatives of $V_{\rm ct}$ should counteract those of $V_{\rm CW}$ at the physical vacuum, which is taken to be $(h, s, a)_{T=0} = (v_H, 0, 0)$:

$$\begin{cases} \partial V_{\rm CW} + \partial V_{\rm ct}|_{T=0,(v_H,0,0)} = 0 \\ \partial^2 V_{\rm CW} + \partial^2 V_{\rm ct}|_{T=0,(v_H,0,0)} = 0 \end{cases} . \tag{3.12}$$

The counterterm potential is chosen to be the following form:

$$V_{\rm ct} = -\frac{1}{2}\delta_{\mu_H^2} h^2 - \frac{1}{2}\delta_{\mu_s^2} s^2 - \frac{1}{2}\delta_{\mu_a^2} a^2 + \frac{1}{4}\delta_{\lambda_H} h^4 + (\delta_{\rho_S} S + \text{h.c.}), \tag{3.13}$$

with coefficients fixed by Eq. (3.12). Note that the Hessian matrix evaluated at the EW vacuum contains an off-diagonal term between s and a due to the dark fermion loop. We would ignore this loop-suppressed off-diagonal term when fixing the counterterms, and thus the small mixing effect in the singlet sector on singlet phenomenology.

For the thermal correction, we employ the Parwani scheme [56] for daisy resummation, replacing the tree-level bosonic squared masses $|m_B(h,s,a)|^2$ with the thermal corrected squared masses $|m_B(h,s,a)|^2 + \Pi_i(T)$ in $V_{\rm CW}$ and $V^T_{\text{1-loop}}$. In our model, the self-energy $\Pi_i(T)$ functions for the bosonic fields are as follows

$$\begin{aligned}
\Pi_h(T) = \Pi_G(T) &= \left(\frac{3}{16}g_2^2 + \frac{1}{16}g_1^2 + \frac{1}{4}y_t^2 + \frac{1}{2}\lambda_H + \frac{1}{12}\lambda_{SH}\right)T^2, \\
\Pi_s(T) = \Pi_a(T) &= \left(\frac{1}{12}\lambda^2 + \frac{1}{3}\lambda_S + \frac{1}{6}\lambda_{SH}\right)T^2, \\
\Pi^L_{W^{\pm,3},B}(T) &= \frac{11}{6}T^2 \text{diag}(g_2^2, g_2^2, g_2^2, g_1^2),
\end{aligned} \tag{3.14}$$

where g_2 and g_1 are the SM $SU(2)$ and $U(1)$ gauge couplings, and y_t is the Yukawa coupling of the top quark with the SM Higgs boson.

3.2.2 Zero temperature boundary conditions

At zero temperature, the Universe should arrive at the physical vacuum, $(h,s,a)_{T=0} = (v_H, 0, 0)$, implicating that such a minimum should be the global minimum of the bounded-from-below (BFB) scalar potential. Such requirements imply several boundary conditions on the zero temperature scalar potential, that we summarize here:

1. The stationary point $(v_H, 0, 0)$ is non-tachyonic;

   On top of requiring a physical Higgs mass m_h, this additionally requires non-tachyonic scalar masses $m_s^2 > 0$ and $m_a^2 > 0$. According to Eq. (3.6), this at tree level requires

   $$\frac{1}{2}\lambda_{SH} v_H^2 > \lambda_S v_S'^2 \tag{3.15}$$

   while at one loop level, this is guaranteed by the counterterms;

2. The potential is bounded from below;

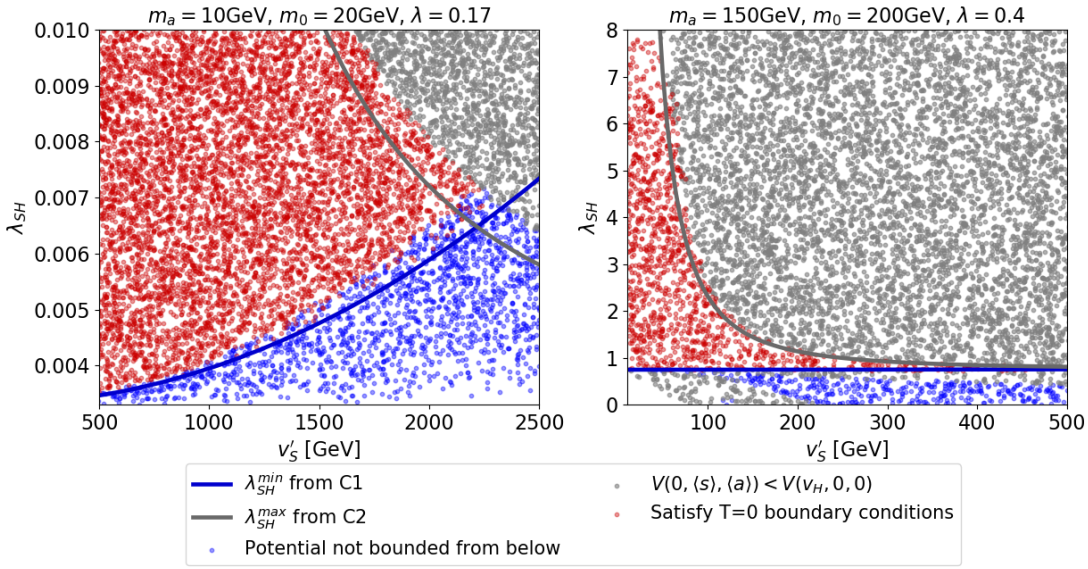


Figure 3.3: Results of the zero temperature numerical scans at one loop level on the $v'_S - \lambda_{SH}$ plane with fixed parameters (a) $m_a = 10$ GeV, $m_0 = 20$ GeV, $\lambda = 0.17$ and (b) $m_a = 150$ GeV, $m_0 = 200$ GeV, $\lambda = 0.4$. The benchmarks satisfying zero temperature boundary conditions are shown in red, benchmarks not satisfying BFB are shown in blue and benchmarks where the EW vacuum is not the global minimum are shown in gray. Analytical conditions **C1** (loop-level, BFB) and **C2** (tree-level, global minimum) are shown by the blue and gray lines. The gray points below the blue line, which should also be colored blue, in the right plot have a global minimum different from the EW minimum, despite satisfying **C2**, due to the significant one loop effects to the small quartic coupling.

At tree level, this is satisfied as we consider the region where all quartic couplings are positive. At one loop level, the quartic coupling for the singlet receives negative correction from the dark fermion loop. A necessary condition for the one loop potential to be BFB, can be derived by requiring the tree level coupling being larger than the one loop contribution from the dark Yukawa coupling:

$$\lambda_S \gtrsim \lambda_{S,\mathrm{BFB}} \equiv \frac{\lambda^4}{16\pi^2}\left[\log\left(\frac{|M_\chi|^2}{Q^2}\right) - \frac{3}{2}\right], \tag{3.16}$$

which can be converted to a lower bound on λ_{SH} via Eq. (3.6):

$$\mathbf{C1}: \lambda_{SH} \gtrsim \lambda_{SH}^{\min} \equiv \frac{2}{v_H^2}\left(\lambda_{S,\mathrm{BFB}} \cdot v_S'^2 + m_a^2\right). \tag{3.17}$$

In this work we mainly investigate the low energy part of the model, that is related to the EWPT, around the EW scale. Therefore we check numerically that the potential is BFB up to 10 TeV before the UV sector of the complete model factors in.

3. The physical vacuum at $(v_H, 0, 0)$ is the global minimum of the potential;

Analysing the stationary points structure of the potential, we start with the tree-level potential given in Eq. (3.5), focusing on the relations among m_a, v_S' and λ_{SH}, neglecting the one loop corrections and hence any constraints on the dark fermion parameters. There are four stationary points $(h, s, a) = p_i$ for $i = 1, \cdots, 4$ (considering only the positive solutions due to Z_2 symmetry of the scalar potential at zero temperature), which read

$$\begin{aligned} &p_1 = (v_H, 0, 0), \qquad p_2 = (0, 0, v_S'), \qquad p_3 = (0, 0, 0), \\ &p_4 = \left(\sqrt{\frac{2(2\kappa_S^2\lambda_{SH} + \lambda_S\lambda_{SH}v_S^2 - 2\lambda_S\lambda_H v_H^2)}{\lambda_{SH}^2 - 4\lambda_S\lambda_H}}, 0, \sqrt{\frac{2\lambda_H(\lambda_{SH}v_H^2 - 2\lambda_S v_S^2 - 4\kappa_S^2)}{\lambda_{SH}^2 - 4\lambda_S\lambda_H}}\right). \end{aligned} \tag{3.18}$$

For p_1 to be the global minimum, the potential values at p_2–p_4 must be greater than

that at p_1. Requiring $V(p_1) < V(p_2)$, we get the following condition:

$$\mathbf{C2}: \lambda_{SH} < \lambda_{SH}^{\max} \equiv 2\left(\frac{m_a^2}{v_H^2} + \frac{\lambda_H v_H^2}{v_S'^2}\right). \tag{3.19}$$

$V(p_1) < V(p_3) \Rightarrow -\frac{1}{4}\lambda_H v_H^4 < 0$ which is automatically satisfied. One can check analytically that, the necessary condition for the existence of p_4: $\lambda_{SH}^2 - 4\lambda_S\lambda_H > 0$, given the fact that $2\lambda_H(\lambda_{SH}v_H^2 - 2\lambda_S v_S^2 - 4\kappa_S^2) = 4\lambda_H m_a^2 > 0$, guarantees $V(p_1) < V(p_4)$.

The analytical conditions **C1** and **C2** are derived either at tree level or estimated at loop level. In the numerical calculations we impose the above requirements at one loop level. The benchmarks satisfying all conditions will be the ones used for phase transition and EWBG studies. Fig. (3.3) shows the numerical scanning results at one loop level at $T = 0$ for two benchmark points with the parameters:
(a) $m_a = 10$ GeV, $m_0 = 20\,\text{GeV}$, $\lambda = 0.17$, $\theta \in (0, \pi/2)$, $m_s \in (70, 200)$ GeV, $v_S' \in (500, 2500)$ GeV, $\lambda_{SH} \in (10^{-5}, 10^{-2})$.
(b) $m_a = 150$ GeV, $m_0 = 200\,\text{GeV}$, $\lambda = 0.4$, $\theta \in (0, \pi/2)$, $m_s \in (155, 200)$ GeV, $v_S' \in (10, 500)$ GeV, $\lambda_{SH} \in (10^{-4}, 8)$.
The analytical conditions **C1** and **C2** are shown as blue and gray lines, respectively. We see that the boundaries set by the analytical conditions agree well with the numerical results, with a few exceptions caused by loop effects.

3.2.3 Thermal history

As a starting point, to analyze the thermal history, we use the high-temperature expansion of the thermal functions in Eq. (2.4) and Eq. (2.5) to the lowest order of α given by

$$J_B^{\text{high-T}}(\alpha) \approx -\frac{\pi^4}{45} + \frac{\pi^2}{12}\alpha, \quad J_F^{\text{high-T}}(\alpha) \approx \frac{7\pi^4}{360} - \frac{\pi^2}{24}\alpha. \tag{3.20}$$

Such a leading order approximation is sufficient for analytical purposes, as will be shown in the following: a first order phase transition is guaranteed by a tree-level barrier, and the thermal barrier arising from the next-to-leading order in the high-temperature expansion is negligible for achieving a SFOEWPT.

With this expansion, the finite temperature potential can be written as

$$V(h,s,a,T) = V_0 + \frac{1}{2}T^2\left[c_H h^2 + c_S(s^2+a^2) + A_s s - A_a a\right] + \text{field-independent terms}, \tag{3.21}$$

where coefficients c_H, c_S, A_s and A_a read

$$\begin{aligned} c_H &= \frac{3}{16}g_2^2 + \frac{1}{16}g_1^2 + \frac{1}{4}y_t^2 + \frac{1}{2}\lambda_H + \frac{1}{12}\lambda_{SH}, \\ c_S &= \frac{1}{12}\lambda^2 + \frac{1}{3}\lambda_S + \frac{1}{6}\lambda_{SH}, \\ A_s &= \frac{\sqrt{2}}{6}m_0\,\mathrm{Re}(\lambda_c), \\ A_a &= \frac{\sqrt{2}}{6}m_0\,\mathrm{Im}(\lambda_c). \end{aligned} \tag{3.22}$$

The first derivatives of the effective potential at finite temperature, considering the high temperature expansion in Eq. (3.21), read

$$\frac{\partial V}{\partial h} = h\left[-\mu_H^2 + \lambda_H h^2 + \frac{1}{2}\lambda_{SH}(s^2+a^2) + c_H T^2\right], \tag{3.23}$$

$$\frac{\partial V}{\partial s} = s\left[-\mu_S^2 + \lambda_S(s^2+a^2) + \frac{1}{2}\lambda_{SH}h^2 + 2\kappa_S^2 + c_S T^2\right] + \frac{1}{2}A_s T^2, \tag{3.24}$$

$$\frac{\partial V}{\partial a} = a\left[-\mu_S^2 + \lambda_S(s^2+a^2) + \frac{1}{2}\lambda_{SH}h^2 - 2\kappa_S^2 + c_S T^2\right] - \frac{1}{2}A_a T^2. \tag{3.25}$$

The above equations vanish at the stationary points. For the analytical understanding of the thermal history that follows, we will fix $\theta = \pi/2$ so that the tadpole coefficients $A_s = 0$ and $A_a = \sqrt{2}m_0\lambda/6$. With this simplification, one can prove that all local minima have $s = 0$

at arbitrary temperatures, see calculations in Appendix B of Ref. [86] [2]. Solving for the minima, the thermal history typically goes through several stages as shown by Fig. (3.4) and described below:

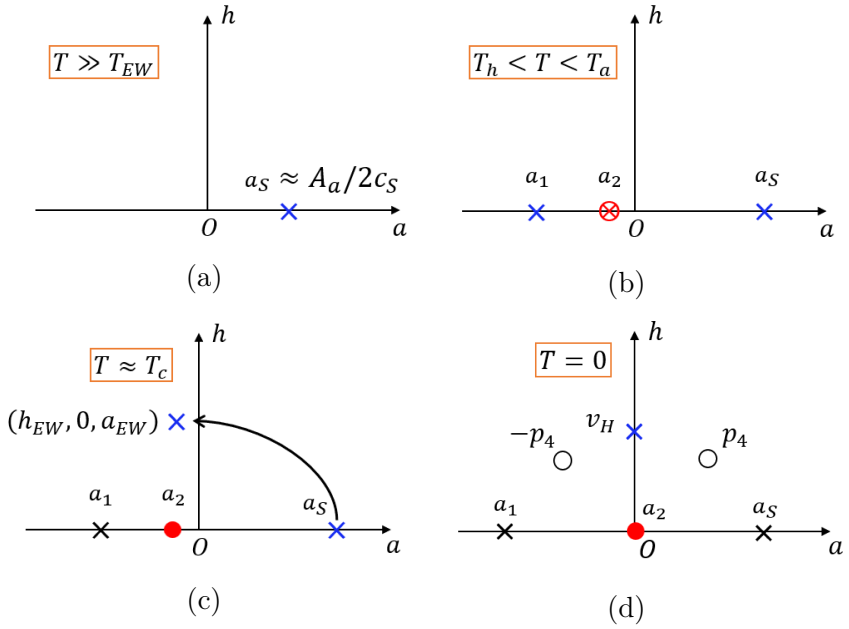


Figure 3.4: Patterns of symmetry breaking at different temperatures on the a–h plane with $\langle s \rangle = 0$. We use $\times$ to denote a minimum, $\otimes$ to denote a saddle point, $\bullet$ to denote a maximum, and $\times$ ($\bigcirc$) to denote a stationary point that may be minimum (maximum). (a) $T \gg T_{\rm EW}$: The dark Yukawa coupling breaks the Z_2 symmetry and induces a non-zero vev for the a field at temperatures much higher than $T_{\rm EW} \approx 140\,{\rm GeV}$. (b) Below T_a, the temperature where two additional solutions for the vev of the a field arise, there are three branches along the direction $h = 0$, two of which are minima and one is a saddle point, with the global minimum being $(0, 0, a_S)$. When the temperature drops to T_h, a new minimum $(h_{\rm EW}, 0, a_{\rm EW})$ starts to develop from $(0, 0, a_2)$. (c) At the critical temperature, the new minimum $(h_{\rm EW}, 0, a_{\rm EW})$ becomes degenerate with $(0, 0, a_S)$. a_2 has transformed into a maximum at this temperature. a_1 could be a minimum or saddle point depending on the relation between the temperature and the model parameters. (d) At $T = 0$, $(v_H, 0, 0)$ becomes the global minimum and the origin becomes a maximum. There are other potential minima or maxima given by Eq. (3.18): a_2, a_1 and a_S in the plot are the values for the singlet vev at the three stationary points p_3 and $\mp p_2$ respectively. Note that we use $-p_i$ to denote the negative solutions.

1. At sufficiently high temperatures — well above the EW scale and below the $U(1)_l$

2. The thermal history with a general value of θ follows the same analytic features as $\theta = \pi/2$ since the vev of s is always suppressed by the term $\kappa_S^2(s^2 - a^2)$ in the tree-level potential.

symmetry breaking scale, the thermal corrections dominate, and the symmetry is restored for h and s, while a has a non-zero vev that minimizes the effective potential. Hence, the thermal history starts from the vacuum

$$T \gg T_{\rm EW}: \quad (0,0,a_S) = \left(0,0,\frac{A_a}{2c_S}\right) \tag{3.26}$$

as shown in Fig. (3.4a). We introduce the notation a_S to denote the vev of a at the EW symmetry preserving global minimum. The non-restoration of Z_2 symmetry for a is induced by the non-zero A_a from the Yukawa interaction in the dark sector and is an important signature of our model.

2. As the Universe cools down but still with the vev along the h direction being zero, the equation for a can be written in the form of a depressed cubic equation

$$a^3 + p(T)a - q(T) = 0, \tag{3.27}$$

with

$$p(T) = \frac{1}{\lambda_S}\left(c_S T^2 + m_a^2 - \frac{1}{2}\lambda_{SH} v_H^2\right), \quad q(T) \ = \frac{A_a T^2}{2\lambda_S}. \tag{3.28}$$

Here we have replaced $(-\mu_S^2 - 2\kappa_S^2)$ with $(m_a^2 - \frac{1}{2}\lambda_{SH} v_H^2)$ using Eq. (3.6). The number of real solutions to Eq. (3.27) is determined by the sign of its discriminant $D(T)$ defined as:

$$D(T) \equiv 4p^3(T) + 27q^2(T). \tag{3.29}$$

If $D(T)$ is positive, there will be only one real solution, while, if it is negative, there will be three real solutions to Eq. (3.27).

For the model parameter space we investigate, all the quartic couplings are positive, rendering $c_S > 0$. Hence, in the case where $\lambda_{SH} < 2m_a^2/v_H^2$, $p(T)$ is always positive, and so is the discriminant $D(T)$, implying there is only one real solution to a throughout the thermal history. Because of the Z_2 symmetry of the potential in the Higgs direction, i.e. $h \to -h$, once an EW broken stationary point develops, the stationary point $(0, 0, a_S)$ necessarily becomes a maximum in the h direction, and a roll-over to the EW broken stationary point would happen. Note that the inclusion of the thermal cubic term beyond Eq. (3.21) introduces a thermal barrier and the roll-over is promoted to a first-order phase transition, which however is generically weak given the loop-suppression nature of the barrier. We do not investigate this case further. Thus,

$$\lambda_{SH} > \frac{2m_a^2}{v_H^2}. \tag{3.30}$$

is a necessary condition for a SFOEWPT to be induced by a sizable tree-level barrier. This is a weaker constraint than **C1**, however can be used to down-select the parameter space for the numerical scan.

With Eq. (3.30), $p(T)$ starts out to be positive at high temperatures, and turns negative at sufficiently low temperatures, rendering a negative discriminant $D(T)$ and more than one solution to Eq. (3.27). We define T_a as the temperature at which

$$D(T_a) = 0. \tag{3.31}$$

T_a can be solved analytically. To forbid a roll-over to the EW broken direction until T_a, the stationary point $(0, 0, a_S)$ needs to be a minimum along the h direction, leading to the necessary condition

$$\textbf{C3}: \frac{\partial^2 V}{\partial h^2}|_{T_a,(0,0,a_S)} = -\mu_H^2 + \frac{1}{2}\lambda_{SH} a_S(T_a)^2 + c_H T_a^2 > 0, \tag{3.32}$$

with $a_S(T_a) = \sqrt[3]{4q(T_a)}$. This condition provides a lower bound on λ_{SH} as a function of v'_S. Notice that **C3** also guarantees that the term inside the bracket of Eq. (3.23) is positive before or at T_a and thus no EW broken stationary point is developed.

3. Below T_a but above the temperature T_h, at which h starts to develop a non-zero vev, two more solutions for a arise, as shown in Fig. (3.4b). The second derivative

$$\frac{\partial^2 V}{\partial a^2} = 3a^2 + p(T) \tag{3.33}$$

vanish at $a_\pm = \pm\sqrt{\frac{|p|}{3}}$ which are the stationary points of the first derivative $\frac{\partial V}{\partial a}$. Thus the three real solutions to Eq. (3.27) where $\frac{\partial V}{\partial a} = 0$, denoted as $a_{1,2,3}$ with $a_3 > a_2 > a_1$ should satisfy $a_3 > a_+ > a_2 > a_- > a_1$. This also implies that $\partial^2 V/\partial a^2$ is positive for both a_1 and a_3 and negative for a_2. To determine the global minimum, we need to compare the potentials at $(0, 0, a_1)$ and $(0, 0, a_3)$. For the solutions given above, we find that

$$V(0,0,a_3) - V(0,0,a_1) = q(T)\lambda_S(a_3 - a_1)\left[\frac{(a_1+a_3)^2}{4a_1a_3} - 1\right] < 0. \tag{3.34}$$

Thus right below T_a, the Universe would be at the $(0, 0, a_3)$, identified as $(0, 0, a_S)$, i.e. the global minimum where the EW symmetry is preserved.

4. From Eq. (3.23), in order to allow for a non-zero h, the following condition should be satisfied as temperature drops:

$$-\mu_H^2 + \frac{1}{2}\lambda_{SH}(s^2 + a^2) + c_H T^2 < 0. \tag{3.35}$$

We define T_h as the temperature at which the left-handed side above equals to zero, below which a non-zero h vev starts to develop. The stationary point $(0, 0, a_2)$ is the first one to satisfy the above condition as the Universe cools down and it smoothly

transforms into an EW broken stationary point. As the left-hand side of Eq. (3.35) also equals to $\partial^2 V/\partial h^2|_{(0,0,a_2)}$, T_h is also the temperature at which $\partial^2 V/\partial h^2|_{(0,0,a_2)}$ starts to be negative. Thus the stationary point $(0,0,a_2)$ transforms from a minimum along the h direction to a maximum as temperature drops below T_h. The new stationary point with non-vanishing h will be denoted as $(h_{\rm EW},0,a_{\rm EW})$. The second derivative in the h direction is guaranteed to be positive for any EW breaking stationary points given that:

$$\frac{\partial^2 V}{\partial h^2}|_{(h_{\rm EW},0,a_{\rm EW})} = 2\lambda_H h^2 > 0 \text{ for } h \neq 0. \tag{3.36}$$

We expect $(h_{\rm EW},0,a_{\rm EW})$ to be the minimum where the Universe settles in after the phase transition. The critical temperature T_c is defined as the temperature at which $V(h_{\rm EW},0,a_{\rm EW}) = V(0,0,a_S)$. The SFOEWPT from $(0,0,a_S)$ to $(h_{\rm EW},0,a_{\rm EW})$ (Fig. (3.4c)) proceeds through bubble nucleation at a slightly lower temperature T_n. Since the start and end local minima are separated by a region with $|H| \neq 0$ and $|S| \neq 0$, a barrier is guaranteed by the tree level coupling between H and S proportional to λ_{SH}. More details on the nucleation condition are to be discussed in Sec. 3.2.5.

5. Finally, the Universe smoothly deforms into the EW vacuum $(v_H,0,0)$ from $(h_{\rm EW},0,a_{\rm EW})$ as the temperature drops to zero, with $a_{\rm EW}$ and a_2 go to zero, shown in Fig. (3.4d).

Analysing the thermal history, in the case of a SFOEWPT, there should be more than one branch of the stationary point solutions in the singlet direction above the phase transition temperature, as shown in Fig. (3.4). At the nucleation temperature T_n, the false singlet vacuum resides at one branch and tunnels to the true EW vacuum, which develops from another branch. Thus, between the false and the true vacuum, a barrier forms in the region where both $|S|$ and $|H|$ are non-zero. Accordingly, we identify the most relevant condition **C3** for a SFOEWPT, i.e. Eq. (3.32). Numerical study to be shown later agrees very well with such a condition, together with zero temperature boundary conditions, **C1** and **C2**

we have derived. Notice that due to the difficulties in solving the cubic equations for the stationary points, we do not present an analytical solution for the critical temperature T_c - the temperature at which to impose the SFOEWPT condition. However, for light scalar a with mass $m_a < m_h/2$, the coupling λ_{SH} is constrained by experiments to be $\lambda_{SH} \lesssim 10^{-2}$. In this scenario, various approximations can be reliably applied on top of the high temperature expansion, which results in an approximate analytic form for T_c. With T_c estimated this way, we could provide a lower bound for λ_{SH} that agrees better with the numerical results for $m_a < m_h/2$. We describe such an approach and the derived conditions in the following.

3.2.4 Critical conditions with light scalars

For the light singlet scalar with $m_a < m_h/2$, the minimal requirement from Higgs invisible decays imposes that $\lambda_{SH} \lesssim 10^{-2}$. Considering the lower bound for λ_{SH} imposed by Eq. (3.30), m_a is bounded to be $m_a \lesssim 17\,\text{GeV}$. The orders of λ_S and v'_S consistent with the conditions **C1-C3** are estimated to be $\lambda_S \lesssim 10^{-2}$ and $v'_S \sim 10^3\,\text{GeV}$. Given that we are mainly interested in SFOEWPT, where $h_{\text{EW}}(T_c)/T_c > 1$, the temperature involved in the following calculation is bounded to be $T < v_H$. We can solve for T_c analytically with reliable approximations, by evolving the field vevs from their $T = 0$ values to higher temperatures. We consider the potential of the form given by Eq. (3.21) to get analytical insights. Based on our analysis above, the SFOEWPT takes place between the two minima $(0, 0, a_S)$ and $(h_{\text{EW}}, 0, a_{\text{EW}})$, which are smooth deformations of the two stationary points at $T = 0$: $p_2 = (0, 0, v'_S)$ and $p_1 = (v_H, 0, 0)$ as in Eq. (3.18). The first derivatives of the potential at finite temperatures can be written as Taylor expansions around the stationary points at $T = 0$. Expanding around the EW vacuum $(v_H, 0, 0)$, we have

$$\begin{aligned}\partial_h V(h,0,a,T) =& m_h^2(h-v_H) + 3\lambda_H v_H (h-v_H)^2 + \frac{1}{2}\lambda_{SH} v_H a^2 + c_H v_H T^2 \\ &+ \sum_{m+n+p=3} \frac{1}{m!n!p!}\partial_h^{1+m}\partial_a^n \partial_T^p V|_{(v_H,0,0,T=0)} (h-v_H)^m a^n T^p,\end{aligned} \tag{3.37}$$

$$\begin{aligned}\partial_a V(h,0,a,T) =& m_a^2 a - \frac{1}{2}A_a T^2 + \lambda_{SH} v_H a(h - v_H) \\ &+ \sum_{m+n+p=3} \frac{1}{m!n!p!}\partial_h^m \partial_a^{1+n} \partial_T^p V|_{(v_H,0,0,T=0)} (h - v_H)^m a^n T^p,\end{aligned} \tag{3.38}$$

where m_h^2 and m_a^2 both take their $T = 0$ values at the EW vacuum, and the last term in both equations sums over all non-negative integers satisfying $m + n + p = 3$. Solving Eq. (3.37)=0 and keeping only the leading-order terms (see the validity argument in Appendix. **??**), we get the finite temperature vev of the h field at the EW vacuum

$$h_{\rm EW}(T) \approx v_H \left(1 - \frac{c_H T^2}{2\lambda_H v_H^2}\right). \tag{3.39}$$

Substituting this into Eq. (3.38), the leading-order contribution to the finite temperature vev of a at the EW vacuum is found to be

$$a_{\rm EW}(T) \approx \frac{A_a T^2}{2m_a^2}. \tag{3.40}$$

Expanding around the singlet vacuum $(0, 0, v_S')$, the first-order derivative along the a direction with $h = s = 0$ reads

$$\begin{aligned}\partial_a V(0,0,a,T) =& 2\lambda_S (v_S')^2 (a - v_S') + 3\lambda_S v_S' (a - v_S')^2 + \left(c_S v_S' - \frac{1}{2}A_a\right) T^2 \\ &+ \sum_{n+p=3} \frac{1}{n!p!}\partial_a^{1+n} \partial_T^p V|_{(0,0,v_S',T=0)} (a - v_S')^n T^p,\end{aligned} \tag{3.41}$$

with the last term being a summation over all non-negative integers satisfying $n + p = 3$. Solving for the roots and keeping the leading-order terms, we get the finite temperature vev of a at the singlet vacuum (See details in Appendix. **??**)

$$a_S(T) \approx v_S' + \frac{T^2}{4\lambda_S v_S'^2}\left(A_a - 2c_S v_S'\right). \tag{3.42}$$

The critical temperature T_c is when the two stationary points are degenerate

$$V(h_{\rm EW}, 0, a_{\rm EW}, T_c) = V(0, 0, a_S, T_c), \tag{3.43}$$

which can be written as an expansion around $T = 0$ to the second order of the field vevs and temperature:

$$\begin{aligned} &V(v_H, 0, 0, 0) + \frac{1}{2} m_h^2|_{(v_H,0,0)} (h_{\rm EW} - v_H)^2 + \frac{1}{2} m_a^2|_{(v_H,0,0)} a_{\rm EW}^2 + \frac{1}{2} c_H v_H^2 T_c^2 \\ &= V(0, 0, v'_S, 0) + \frac{1}{2} m_a^2|_{(0,0,v'_S)} (a_S - v'_S)^2 + \frac{1}{2} (c_S v_S'^2 - A_a v'_S) T_c^2. \end{aligned} \tag{3.44}$$

Substituting the field vevs derived above, we get a quadratic equation of T_c^2:

$$\alpha T_c^4 + \beta T_c^2 + \gamma = 0, \tag{3.45}$$

with

$$\begin{aligned} \alpha &= \frac{v_H^2 c_H^2}{2 m_h^2|_{(v_H,0,0)}} + \frac{A_a^2}{4\lambda_{SH} v_H^2 - 8\lambda_S v_S'^2} - \frac{\left(A_a - 2 c_S v'_S\right)^2}{16 \lambda_S v_S'^2} \\ \beta &= \frac{1}{2} \left(c_H v_H^2 - c_S v_S'^2 + A_a v'_S \right) \\ \gamma &= \frac{1}{4} \left(-\lambda_H v_H^4 + \lambda_S v_S'^4 \right). \end{aligned} \tag{3.46}$$

T_c can be solved as

$$T_c = \sqrt{\frac{-\beta + \sqrt{\beta^2 - 4\alpha\gamma}}{2\alpha}}. \tag{3.47}$$

Similar to condition **C3**, a necessary condition for SFOEWPT with light singlet scalars at the critical temperature given by Eq. (3.47) reads

$$\textbf{C3'}: \frac{\partial^2 V}{\partial h^2}|_{T_c,(0,0,a_S)} > 0, \tag{3.48}$$

where a_S at T_c can be estimated by Eq. (3.42). However, as the temperature dependent term in Eq. (3.42) is found to be negligible for light singlets, we will use $a_S(T_c) \approx v'_S$ for the following calculations. Both **C3** and **C3'** would give a lower bound for λ_{SH} as a function of v'_S as shown in Fig. (3.5), while **C3'** is expected to give a more restrictive bound since T_c is supposed to be lower than T_a for a SFOEWPT.

3.2.5 Nucleation

In this section, we derive a semi-analytical condition for nucleation to proceed. The potential must be away from the "thin wall limit" for the tunneling to happen. The thin wall limit refers to the case where the energy difference between the minima of the potential is significantly smaller than the height of the barrier separating the two phases. The tunneling rate is known to be highly suppressed in such cases. Denoting the singlet phase as ϕ_s, the EW phase as ϕ_h and the barrier as ϕ_b, this requirement could be formulated as

$$\textbf{C4}: \frac{V(\phi_s) - V(\phi_h)}{V(\phi_b) - V(\phi_h)} > \Delta, \tag{3.49}$$

where $\mathcal{O}(0.1) < \Delta < 1$ can be chosen empirically to be consistent with the numerical results [94]. This condition should be checked at the temperature where the phase transition completes. Since this is only an approximate condition, we would check this condition at $T = 0$ to gain analytical insights. In this case, ϕ_s, ϕ_h and ϕ_b would be zero temperature stationary points p_2, p_1 and p_4 given in Sec. 3.2.2. The ratio Δ is chosen to be 0.7 to be consistent with the numerical results.

To summarize, we have derived four necessary conditions (five for $m_a < m_h/2$) analytically from requiring $T = 0$ boundary conditions, first order phase transtion and nucleation. These requirements, which should be checked by numerical calculations at one loop level, will be discussed in the following section.

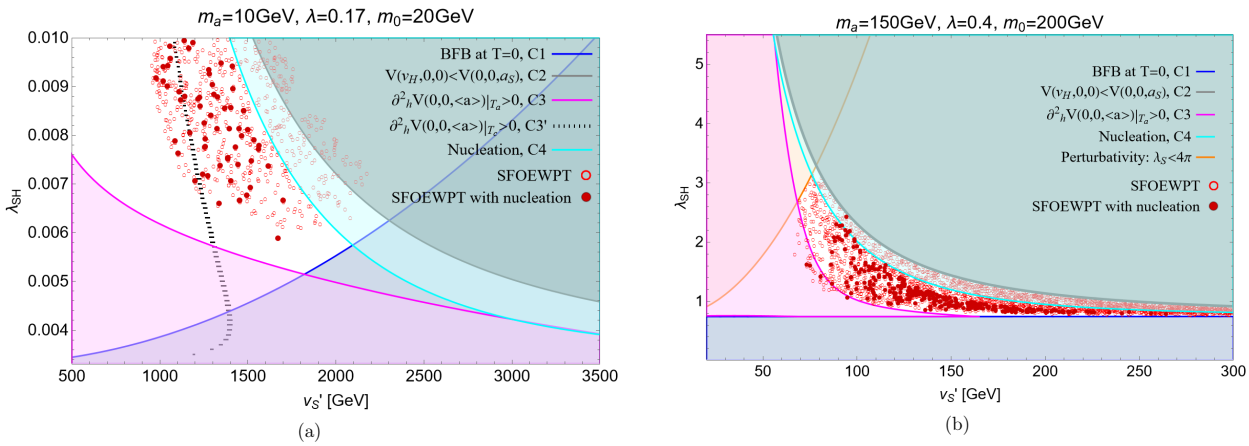


Figure 3.5: Results of phase transitions on the $v'_S - \lambda_{SH}$ plane for points satisfying the zero temperature boundary conditions for the same two benchmark scenarios as in Fig. (3.3): (a) $m_a = 10\,\text{GeV}$, $m_0 = 20\,\text{GeV}$, $\lambda = 0.17$ and (b) $m_a = 150\,\text{GeV}$, $m_0 = 200\,\text{GeV}$, $\lambda = 0.4$. Points satisfying the nucleation and SFOEWPT conditions, $S_3/T \lesssim 140$ and $h_{\text{EW}}(T_n)/T_n > 1$, are shown as red solid circles, and points satisfying the condition $h_{\text{EW}}(T_c)/T_c > 1$ are shown as red open circles. The analytical bounds derived in Sec. 3.2, **C1-C4** are shown by the lines. The shaded regions are excluded by the corresponding conditions. **C3'**, the condition derived at T_c, is shown for $m_a = 10\,\text{GeV}$ only, since the derivation for T_c only applies to the case with $m_a < m_h/2$. The perturbativity requirement $\lambda_S < 4\pi$ is shown for $m_a = 150\,\text{GeV}$, while the λ_S for $m_a = 10\,\text{GeV}$ is always small enough to satisfy this requirement. The lowest y-axis value for λ_{SH} for these figures is set by Eq. (3.30).

3.2.6 Numerical scan

We use `CosmoTransitions` [95] for numerical studies of the phase transitions. This tool starts from the local minima of the scalar potential at zero temperature, tracing the evolution of these minima as temperature increases until it hits some saddle point, which indicates the possible existence of other local minima. At such temperatures, the tool will check the existence of other local minima in the field space close to the saddle point. If it finds one, it will trace back in temperature the evolution of this new minimum until its appearance. With this procedure, the tool can locate all local minima in field space at different temperatures, and thus determine all critical temperatures at which phase transitions may happen. However, the phase transitions identified this way by `CosmoTransitions` are not physically allowed to happen unless they satisfy the following conditions:

- First order phase transition should proceed via bubble nucleation. By requiring that the probability for one bubble to nucleate per Hubble volume is $\sim \mathcal{O}(1)$, one can define the bubble nucleation temperature T_n at which $S_3(T)/T \sim 140$, with S_3 being the 3-dimensional Euclidean action of the instanton integrated over the bubble wall [95]. Around T_n, when temperature drops, $S_3(T)/T$ typically drops, and the nucleation will be more efficient. A first order phase transition can happen only if the nucleation condition given above is satisfied at some point within the phase transition temperature window.

- For a specific starting phase (the global minimum at higher temperature), if there are more than one eligible ending phases for it to transit to, only the transition occurring at the highest temperature can actually happen, since it occurs earlier than all others in the cooling-down history of the Universe.

For a successful EWBG, the first order EWPT needs to be strong enough such that the sphaleron rate inside the bubble is suppressed to preserve the produced baryon asymmetry. The strength of the phase transition could be measured by the order parameter $h_{\rm EW}(T)/T$ at the phase transition temperature. We use the following criterion for a SFOEWPT in our numerical scan:

$$\frac{h_S(T)}{T} < 0.5 \text{ and } \frac{h_{\rm EW}(T)}{T} > 1, \tag{3.50}$$

where $h_{\rm EW}(T)$ and $h_S(T)$ are the Higgs vevs inside and outside the bubble at T_c or T_n. Note that the requirement $h_S(T)/T < 0.5$ is to ensure the sphaleron process is efficient outside the bubble.

We use `CosmoTransitions` to numerically study the thermal history of the parameter space satisfying zero temperature boundary conditions for the two benchmarks presented in Fig. (3.3). Fig. (3.5) shows the parameter space that gives SFOEWPT (○) as defined

by $h_{\rm EW}(T_c)/T_c > 1$ as well as the parameter space that satisfies the nucleation condition $S_3/T \lesssim 140$ and SFOEWPT defined by $h_{\rm EW}(T_n)/T_n > 1$ (•). We also show the analytical conditions **C1**-**C4** (**C3'** included for light singlet) in Fig. (3.5). For the nucleation condition **C4**, the empirical parameter Δ is chosen to be 0.7. Our numerical results agree well with the analytical conditions with only a few exceptions on the boundary. This is due to the difference between the scalar potentials used for the analytical and numerical calculations (**C2** and **C3**) as explained in the following, or the approximate nature of the analytical conditions (**C3'** and **C4**). For analytical calculations, we use the high temperature expanded thermal potential up to the leading order plus tree-level zero-temperature potential, while for the numerical calculation, we use the full expression for the thermal potential plus one-loop order zero-temperature potential and daisy resummation in the Parwani scheme.

3.3 Discriminant Power of Wall Velocity: Baryon Number and Gravitational Waves in DarkCPV

Precise calculation of wall velocity is crucial for a precise determination of the baryon number generation and the gravitational wave signals. In this section, we compute the wall velocities for the EWBG model introduced in Sec. 3.1 (referred to as "DarkCPV" model in the following), and examine its impacts on the predictions of baryon number and gravitational waves.

3.3.1 Wall Velocity

We now proceed to compute v_w for the SFOEWPT points in the DarkCPV model presented above in the LTE approximation and using the entropy conservation approach introduced in Sec. 2.2.5. As discussed in Ref. [87], if both the masses of s and a are lighter than half of the Higgs mass, searches for Higgs exotic decays on the LHC constrains $\lambda_{SH} \lesssim 10^{-4}$ — which is too small to allow for a SFOEWPT. In addition, considering that the observed dark matter

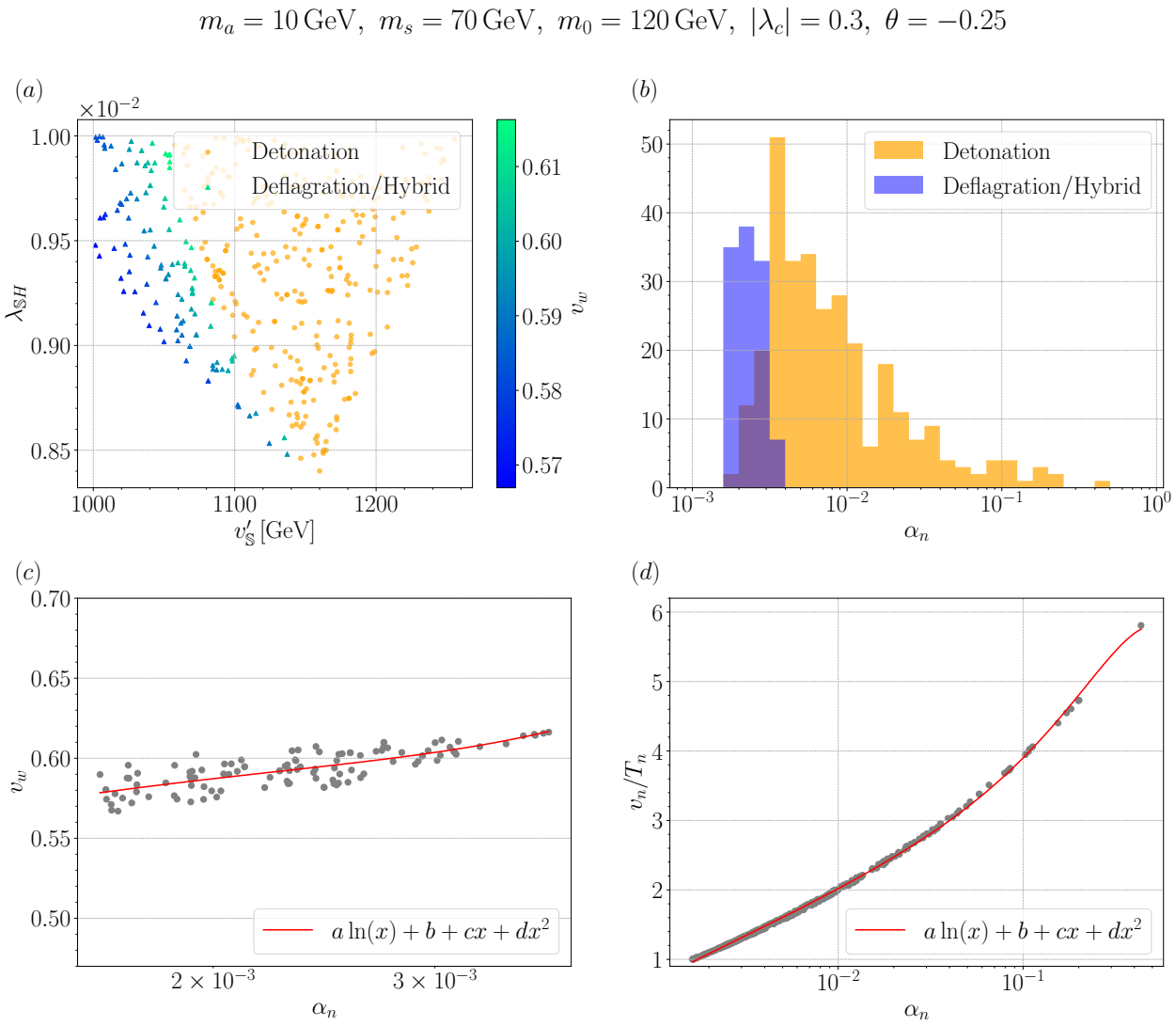


Figure 3.6: Strong first-order EWPT points and v_w calculated under LTE using the entropy conservation approach for the DarkCPV model. There are two free parameters varying in the scanning: v'_S and λ_{SH}. Other parameters are fixed as given in the plot title. (a) Detonation and deflagration/hybrid points in the v'_S-λ_{SH} plane. Wall velocities for the deflagration/hybrid points are depicted by the color gradient. (b) Histogram of α_n for the detonation and deflagration/hybrid solutions. (c) α_n and v_w of the deflagration/hybrid points. The red line is a fitting of the scatter points with the function indicated by the legend. (d) α_n and v_n/T_n of all the strong first-order EWPT points. The red line is again a fitting with the same function as in panel (c).

relic density is mainly determined by the annihilation channel $\bar{\chi}\chi$ into scalars, m_0 should be appreciably larger than m_a or m_s. On the other hand, a too heavy m_0 leads to too strong baryon number washout based on the baryon number generation calculation discussed in Sec. 3.3.2. Considering all the above, we choose the parameter region for which $m_a < m_h/2$, $m_s > m_h/2$, $m_0 > m_{a,s}$, and $\lambda_{SH} \lesssim 0.01$, the latter to avoid collider bounds from Higgs invisible decay.

Fig. 3.6 shows 417 benchmark points with a strong first-order phase transition for fixed values of $m_a = 10\,\text{GeV}$, $m_s = 70\,\text{GeV}$, $m_0 = 120\,\text{GeV}$, $|\lambda_c| = 0.3$, $\theta = -0.25$. Only two free parameters then remain in the scanning: v_S' and λ_{SH}, as depicted in Fig. 3.6(a). The wall velocities for the deflagration/hybrid walls are in the range $\sim 0.56 - 0.62$. A histogram of α_n for the detonation and deflagration/hybrid solutions is shown in Fig. 3.6(b), from which we observe an upper bound of α_n for the deflagration/hybrid bubbles at around 4×10^{-3}. For these results we adopt the α_n widely used in the literature as given below, which matches Eq. (2.34) at T_n, ignoring the temperature difference between the two phases:

$$\alpha_n = \frac{1}{g_* T^4 \pi^2/30} \left(\Delta V_{\text{eff}} - \frac{T}{4} \frac{\partial \Delta V_{\text{eff}}}{\partial T} \right) \Bigg|_{T_n} \tag{3.51}$$

where $g_* = 106.75$ is the number of the light degrees of freedom in the SM and ΔV_{eff} refers to the difference of V_{eff} between the false vev and the true vev. Fig. 3.6(c) and Fig. 3.6(d) show the deflagration/hybrid points in the α_n-v_w plane and all the SFOEWPT points in the α_n-v_n/T_n plane, respectively. We observe positive correlations between α_n and v_w, α_n and v_n/T_n, respectively. To quantify these correlations, we perform a fitting over the points in Fig. 3.6(c) and Fig. 3.6(d) with the same functional form $f(x) = a\ln(x) + b + cx + dx^2$. The

fitting results are shown by the red lines, with the fitted parameters being:

$$v_w = f(\alpha_n): \ a = 0.15, \ b = 1.64, \ c = -95.07, \ d = 1.05 \times 10^4.$$
$$\frac{v_n}{T_n} = f(\alpha_n): \ a = 0.54, \ b = 4.44, \ c = 8.01, \ d = -9.10. \tag{3.52}$$

A fitting with the same functional form is also performed for the $\mathbb{Z}_2$ singlet extension model as discussed in Sec. 2.3. An interesting observation is that the fitting coefficients for the $\mathbb{Z}_2$ singlet extension model and DarkCPV model are of comparable orders, indicating universal correlation patterns of α_n-v_w and α_n-v_n/T_n across the singlet scalar extensions of the SM. However, the upper bound of α_n allowing for deflagration/hybrid bubbles in the DarkCPV model ($\sim 10^{-3}$) is found to be one-order-of-magnitude smaller than that in the $\mathbb{Z}_2$ singlet extension model ($\sim 10^{-2}$). This significant model dependence highlights the importance of a careful treatment of the fluid profiles and wall velocity for each model.

3.3.2 Baryon number generation and its v_w dependence

The wall velocities obtained in the previous section for the DarkCPV model are in the range $\sim 0.5 - 0.7$, which are much higher than the commonly assumed value $v_w \sim 0.1$ for EWBG calculations, see, e.g. [87, 90, 96]. Accordingly, the non-local baryon number generation based on the diffusion mechanism has to be re-examined for wall velocities in this range. In this section, we compare different computational frameworks for the baryon number generation and examine their validity depending on the range of v_w. We then present the numerical results in the DarkCPV model, demonstrating distinct behaviors for the baryon asymmetry in the proximity of the real value of v_w.

In non-local EWBG, which relies on CP-violating particle reflecting off the bubble wall, the behavior of the BAU under an increasing wall velocity has been long believed to involve two competing effects. On the one hand, a faster wall velocity allows reflected particles to

diffuse back into the bubble wall more quickly, reducing the window in which the sphaleron process can convert the CP asymmetry into baryon asymmetry, and thus suppressing the BAU. On the other hand, higher wall velocity enhances the scattering rate between the plasma particles and the bubble wall, producing a larger CP asymmetry and thereby increasing the BAU. A detailed understanding of the dependency of BAU on v_w requires solving the transport equation accurately in the wall frame.

Two commonly used frameworks have been developed to formulate the transport equation: the semi-classical approach under the WKB approximation [97–102], and the VEV-insertion approximation (VIA) method [103–107]. The essential difference between these two methods lies in their calculations of the CP-violating source term that enters the transport equation governing the distribution of particle number densities near the bubble wall. The VIA method treats the CP-violating mass term induced by the bubble wall as a perturbation that flips chirality, and calculates the source term to leading order in the mass insertion. Although originally calculations based on the VIA approximation seemed to accommodate EWBG for a large number of models, more recent studies have shown pathologies that call into question its validity [108, 109]. Further studies are needed to understand if future improvements in the VIA approximation could lead to reliable results. The semi-classical method, which will be used throughout this work, describes the interaction of the bubble wall as a semi-classical force in the WKB approximation. This approach is only valid in the thick wall regime, where the particle's de Broglie wavelength ($\sim T^{-1}$) is much smaller than the wall width L_w[3].

Earlier calculations for the baryon number generation using the semi-classical method by Cline, Joyce, and Kainulainen [101] and by Fromme and Huber [102] assumed $v_w \ll 1$ and truncated the transport equation to the leading order of v_w. We will refer to this framework as the leading order (L.O.) approximation. More recently, computations by Cline

3. The real L_w can be computed from first principles and has been done for the $\mathbb{Z}_2$ model in Ref. [82]. Given the similarity in the range for v_w for the $\mathbb{Z}_2$ and the DarkCPV models, we shall assume that the wall thickness is in a similar range as in the $\mathbb{Z}_2$ case ($L_w \sim 5/T$). We leave a first-principle calculation of L_w for the DarkCPV model for future work.

and Kainulainen [110] that keep the full v_w dependence uncover a significantly different behavior of the baryon number as a function of v_w. We will refer to this all orders calculation as the full treatment. In this section, we compute the baryon asymmetry generated in the DarkCPV model using the full treatment of v_w. We find striking differences between these results and those obtained using the L.O. v_w approximation, which is only valid for small v_w[4]. Detailed formulations of these two treatments are provided in Appendix B.1.

EWBG in the DarkCPV model was introduced in Sec. 3.1 and is recapped here. At the time of EWPT, the chiral fermion χ gains a spatially varying complex mass via coupling to the complex singlet scalar field profile as,

$$M_\chi = m_0 + |\lambda_c| \exp(i[\theta + \arg(S)])|S| \,. \tag{3.53}$$

This complex mass breaks CP symmetry, hence the chiral fermions $\chi_L, \bar{\chi}_L$ (and their charge conjugates $\bar{\chi}_R, \chi_R$) scatter off the bubble wall at different rates, creating a chiral asymmetry. To transfer this chiral asymmetry to the SM, we gauge the lepton number to $U(1)_l$ with the gauge boson Z', and assign lepton numbers to χ and S, such that χ and the SM leptons are connected via the Z' portal. The transferred chiral asymmetry in SM leptons will be turned into a net baryon asymmetry by the sphaleron.

The chiral asymmetry carried by χ is quantified by the CP-odd chemical potential $\mu_o(z) = \mu_{\chi L} - \mu_{\bar{\chi} L} = -(\mu_{\chi R} - \mu_{\bar{\chi} R})$, where the second equality follows from charge conjugation symmetry. The profile of $\mu_o(z)$ can be solved from the transport equation Eq. (B.12) with the CP-odd source terms[5]. In our model, the dark fermion only directly couples to the complex scalar S (generating the mass M_χ) and the gauge boson Z'. The gauge coupling is strongly constrained by the experimental bounds from LEP and dark matter

4. A comparison of the L.O. and full treatments has also been performed in Ref. [110].

5. The relaxation method behaves the best in solving Eq. (B.12) numerically and thus is adopted here, as discussed in Ref. [110]. Shooting method, Runge-Kutta, or BDF all tend to be unstable.

direct detection (DD), and is negligible compared to the Yukawa coupling. Therefore, we will consider the chirality flipping term generated by the mass M_χ to be the only collision term in the transport equation for $\chi_{L,R}$, which can be computed following [107]. Here, we take the approximation provided in [111] and write the collision term as[6]:

$$\Gamma_m(z) \simeq \frac{3}{\pi^2}\frac{|M_\chi(z)|^2}{T^2}\gamma_{\rm th}, \tag{3.54}$$

where $\gamma_{\rm th}$ is the thermal width[7] of the fermion in the plasma, and is computed as [98, 118, 119]:

$$\gamma_{\rm th} \simeq \frac{1}{16}\alpha_\lambda T\,, \tag{3.55}$$

where $\alpha_\lambda = |\lambda_c|^2/(4\pi)$. Here we again omit the gauge boson contribution to the thermal width.

The chiral asymmetry computed above is transferred to the SM as follows. The chiral asymmetry of χ implies a net $U(1)_l$ charge density determined by the different charges carried by the left and right-handed components,

$$\rho_l(z) = \frac{1}{3}N_g T_n^2 \mu_o(z). \tag{3.56}$$

Next, a long-range Coulomb-like potential of the Z' can be generated by this net charge, i.e.

$$\langle Z_0'(z)\rangle = \frac{g'}{2M_{Z'}}\int_{-\infty}^{\infty} dz'\rho_l(z')\exp(-M_{Z'}|z-z'|). \tag{3.57}$$

This potential acts effectively as a chemical potential $\Delta\mu = g'\langle Z_0'(z)\rangle$, sourcing a chiral

6. Note that the collision term provided in those references is defined for the Boltzmann equation in terms of the particle number density n, which is widely used in the VIA formalism. Eq. (3.54) is for the Boltzmann equation in terms of chemical potential. The relation between them is reviewed in Ref. [112].

7. This is also known as the damping rate of quasiparticles in the thermal plasma, which basically refers to the rate of the decoherence of thermally dressed particles. This thermal effect played an important role in EWBG in the minimal SM, see [103, 113–117].

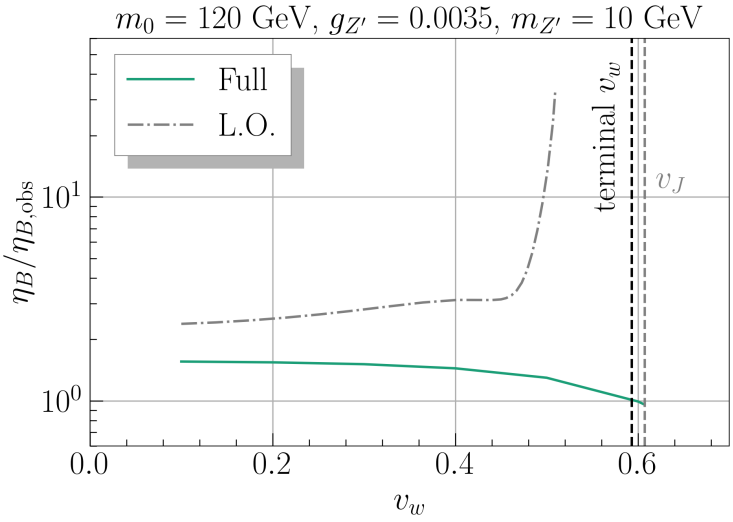


Figure 3.7: Baryon number to photon ratio η_B normalized to the observed value $\eta_{B,\mathrm{obs}}$ as a function of v_w in the DarkCPV model. The terminal v_w obtained using the entropy conservation approach is labeled by the black dashed line. The gray dashed line denotes the Jouguet velocity. The green solid curve shows the result of the all orders calculation, retaining full v_w-dependence. The gray dot-dashed line is the result of the L.O. approximation, which truncates the transport equation at leading order in v_w and so is valid only for small $v_w \ll 1$. This approximation introduces an unphysical divergence when $v_w \sim 0.5$ crosses the sound speed. Clearly, the all orders treatment is necessary in such a regime.

asymmetry in the SM lepton sector with its equilibrium value given by,

$$\Delta n_{L_L}^{EQ}(z) = \frac{2N_g T_n^2}{3} g' \langle Z_0'(z) \rangle. \tag{3.58}$$

This asymmetry biases the electroweak sphaleron to generate net lepton number, and thus net baryon number as,

$$\Delta n_B = \Delta n_{L_L} = \frac{\Gamma_{\mathrm{sph}}}{v_w \gamma_w} \int_0^\infty dz\, \Delta n_{L_L}^{EQ}(z) \exp(-\frac{\Gamma_{\mathrm{sph}} z}{v_w \gamma_w}), \tag{3.59}$$

with $\Gamma_{\mathrm{sph}} \simeq 10^{-6} T_n$. This baryon number behaves as $g^2/M_{Z'}^2$. Note that the γ_w factor appearing in this expression is the result of boosting the wall frame back into the cosmic frame, as shown in Ref. [110]. This factor is ignored in methods taking the L.O. small v_w limit.

Fig. 3.7 shows the produced baryon number asymmetry normalized to the observed value $\eta_{B,\mathrm{obs}} \equiv n_{B,\mathrm{obs}}/s \simeq 8.7 \times 10^{-11}$ [6] as a function of v_w calculated with the full and L.O. frameworks. The benchmark point for this plot is chosen to be $m_a = 10\,\mathrm{GeV}$, $m_s = 70\,\mathrm{GeV}$, $m_0 = 120\,\mathrm{GeV}$, $|\lambda_c| = 0.3$, $\theta = -0.25$, $v_S' = 1048.04\,\mathrm{GeV}$, $\lambda_{SH} = 9.38 \times 10^{-3}$, which leads to a hybrid bubble wall. We choose $g_{Z'} = 0.0035$ to avoid the LEP bound for Z' boson search [87, 90, 120–122] as well as to ensure the BAU at the terminal v_w assumes the observed value. The terminal velocity obtained from the entropy conservation approach is $v_w \approx 0.6$ as shown by the black dashed line in the plot.

Meanwhile, the BAU is not plotted for detonation bubble walls ($v_w > v_J$) in Fig. 3.7 for the following reasons. First, by definition, detonation has all the fluid perturbations falling behind the wall, as a result, the functions modeling the departure from equilibrium may be discontinuous at the wall, which was not carefully modeled in our calculational framework. Second, detonation bubble walls may collide with each other before reaching the ultra-relativistic regime (i.e. percolation may occur before the end of acceleration). Current understanding within this community for percolation is based on a static wall velocity [123]. This may have significant impacts on the produced baryon number. Based on these two points, theories for bubble percolation and baryogenesis for accelerating detonation walls remain as open questions.

Fig. 3.7 has profound implications for the impact of v_w on the computation of the BAU. In the range near the terminal v_w, some early methods keeping only the leading-order terms of v_w cannot accurately compute BAU. We show the result of the L.O. approximation of Ref. [101] as an example, which features a singularity at v_w around 0.5, similarly to Ref. [102]. Clearly for such velocities, one requires a method which keeps the full v_w dependence. Our all orders treatment is shown to behave smoothly in the deflagration/hybrid regime. Furthermore, due to the qualitative difference between deflagration/hybrid and detonation bubbles for BAU calculations as discussed in the previous paragraph, it is of vital importance to distinguish

the fluid profiles from the first principles.

The benchmark point chosen in Fig. 3.7 passes all bounds except those from the direct direction (DD) of DM-nucleon scattering [124]. The relevant scattering cross section for DD is generated at the one-loop level and can be found in Ref. [87, 122]. These can easily be circumvented in a few different ways. One option is to allow the Z' boson to have a kinetic mixing with the photon. Such a mixing does not alter the generated baryon number [90, 122], but it produces an additional diagram contributing to the DM-nucleon scattering cross section. By properly choosing the sign and size of the mixing parameter, the new diagram can cancel the loop-level diagrams so that the DD bound is avoided. For the benchmark used in Fig. 3.7, the required size of mixing is roughly $\epsilon e \sim 4 \times 10^{-4}$. Another option is to introduce soft $U(1)$ breaking Majorana mass terms $\delta_L \chi_L \chi_L$ and $\delta_R \chi_R \chi_R$ with $\delta_{L,R} \ll m_0$. The mass eigenstates then have a small mass splitting $\Delta m \simeq (\delta_L + \delta_R)/2$ and their vector current coupling with the Z' boson becomes off-diagonal. The vector-current DM-nucleon cross section is thus inelastic and kinematically suppressed by the mass splitting, and DD bound can be avoided for $\Delta m \simeq O(200 \text{ keV})$ [125, 126]. For original references of this idea, see Ref. [127, 128]. The axial-vector current, on the other hand, provides a suppressed cross section in the non-relativistic limit. See, for example, Ref. [129].

3.3.3 Gravitational Waves

First-order phase transitions proceed via bubble nucleation and source tensor perturbations[8] — and therefore gravitational waves (GWs) — through bubble collisions, sound waves, and turbulence [131–133]. During the initial bubble collision stage, mergers of true vacuum bubbles break spherical symmetry, allowing the gradient energy of the scalar field to source GWs [134, 135]. This stage completes quickly, but can be the dominant GW source for

8. Tensor perturbations produced in a strong first-order phase transition may also lead to observable B-mode polarization in the CMB, particularly for late-time or supercooled transitions [130]. This can offer a complimentary signature of this scenario.

strong, vacuum energy-dominated transitions, which are typically associated with significant supercooling and "runaway" bubble walls.

Long after the initial bubble collisions have completed, shells of fluid kinetic energy continue to propagate through the plasma and collide, acting as an additional, much longer-lasting source of GWs. Fluid perturbations can be decomposed into longitudinal (compressional) and transverse (rotational) components, which source sound waves and magnetohydrodynamic (MHD) turbulence, respectively [136–141]. Numerical simulations reveal that for intermediate strength phase transitions, compressional waves dominate over rotational waves [142]. Thus, sound waves are usually considered to be the dominant source of GWs for thermal transitions, and have been extensively studied for various models [79, 82, 143–148].

It is convenient to decompose the energy density in GWs, as quantified by the spectral density parameter

$$\Omega_{\rm GW} \equiv \frac{1}{\rho_{\rm tot}} \frac{d\rho_{\rm GW}}{d\ln k}\,, \tag{3.60}$$

into contributions from each of these three sources

$$\Omega_{\rm GW} = \Omega_\phi + \Omega_{\rm sw} + \Omega_{\rm tur}\,, \tag{3.61}$$

with Ω_ϕ corresponding to bubble collisions, $\Omega_{\rm sw}$ to sound waves, and $\Omega_{\rm tur}$ to MHD turbulence[9]. As previously alluded to, the relative contribution from each of these components depends sensitively on the transition strength, as quantified by the parameter α_n defined in Eq. (2.34), as well as the bubble wall velocity v_w. The detailed calculations of the GW power spectrum from each source are reviewed in Appendix B.2.

Using this machinery, we show in Fig. 3.8 the GW spectrum for the DarkCPV model using the data in Fig. 3.6. For the deflagration/hybrid walls, the true v_w as shown in Fig. 3.6(c) is

9. It has recently been shown that particle production from bubble-bubble collision can act as an additional source of GWs [149]. This source is non-negligible only in vacuum or supercooled phase transitions, similarly to the scalar field contribution.

used, while for the detonation walls, we take $v_w = 1$. We observe a positive correlation between the amplitude of GW signals and v_w — as one might expect, the detonation walls generally produce stronger GW signals than the deflagration/hybrid walls, and deflagration/hybrid walls with higher v_w generally produce stronger GW signals than those with lower v_w. We also observe a negative correlation between the amplitude and the peak frequency of the spectrum, reflecting the negative correlation of the peak frequency with v_w, as can be seen from Eqs. (B.21) and (B.26).

Deflagration/hybrid bubbles in the DarkCPV model occur only for very small $\alpha_n \lesssim 4 \times 10^{-3}$, as shown in the upper right panel of Fig. 3.6. As a consequence of these small α_n and the fact that $\Omega_{\rm GW} \sim (\frac{\alpha_n}{1+\alpha_n})^2$, the GW signal from the deflagration/hybrid transitions of this model are below the sensitivities of all proposed experiments shown in Fig. 3.8. Thus, the observation of a GW signature, if interpreted in the context of the DarkCPV model, would be indicative of a detonation solution and therefore potentially incompatible with a successful baryogenesis in this model. We emphasize that the GW spectra from first-order phase transitions are highly model-dependent, since the upper bound of α_n permitting deflagration/hybrid solutions depends sensitively on the particle content and model details, as discussed in Sec. 3.3.1. The situation may be more optimistic for other models for which the deflagration/hybrid solution class admits larger α_n, such that a GW signal would be compatible with EWBG.

3.4 Summary

In this chapter we focus on a novel mechanism for electroweak baryogenesis, where the new required source for CP violation resides in a dark sector. Introducing dark CP violation for a successful EWBG evades the stringent constraints imposed by measurements of electron and neutron electric dipole moments. This new EWBG mechanism involves a new fermionic particle χ and a complex scalar S in the dark sector that together can generate a non-vanishing

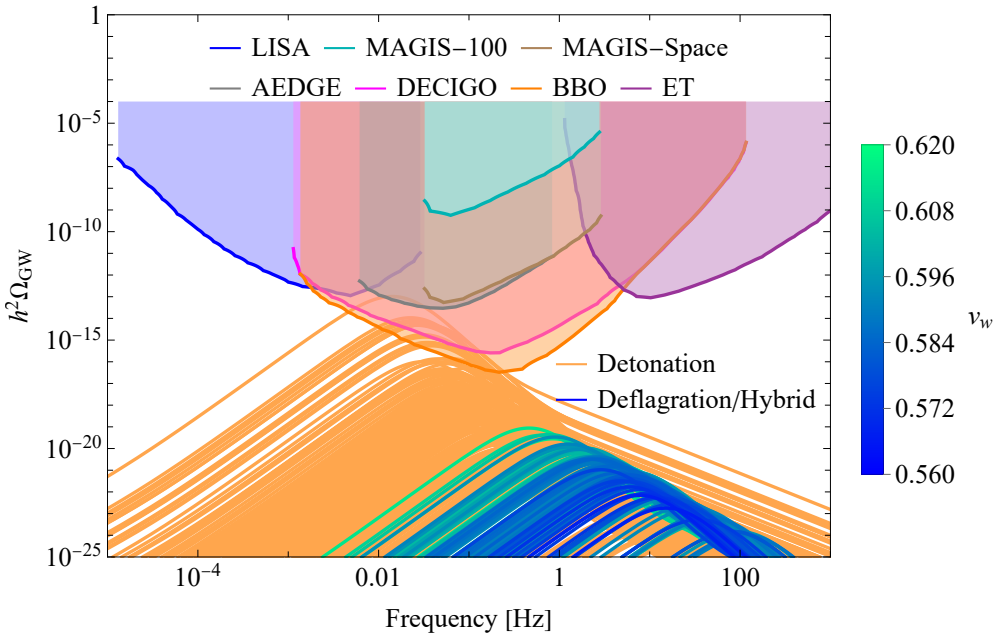


Figure 3.8: GW spectrum for the DarkCPV model, with v_w depicted by the color gradient. Orange curves are detonation bubbles.

CPV source. The global lepton number symmetry $U(1)_l$, with $l = e + \mu + \tau$, needs to be promoted to gauge symmetry, with the associated Z' gauge boson that acts as a portal to transfer the CPV source from the dark sector to the SM sector. More in detail, as the Universe undergoes a strong first order phase transition from an EW preserving vacuum to the EW breaking one, the singlet vev is changing along the bubble wall and generates a varying non-vanishing imaginary component for the dark fermion mass, that creates a CPV induced non-zero chiral asymmetry for the dark fermion χ . This chiral asymmetry is transferred to a chiral asymmetry in the SM lepton sector via the Z' portal. The EW sphaleron process in the SM can convert the chiral asymmetry in the SM lepton sector to baryon asymmetry which will be preserved once entering the bubble of EW breaking vacuum. The Higgs portal, connecting the SM sector with the dark sector via its interactions with the singlet complex scalar, allows for a SFOEWPT. Interestingly enough, the fermionic particle χ introduced can also serve as a dark matter candidate. In [86], the generated baryon asymmetry at the EWPT was calculated, assuming a sufficiently strong EWPT and that nucleation takes place.

Here we perform a meticulous analysis of the phase transition dynamics.

Exploring the phase transitions, we find distinct thermal histories for the scalar sector: The Yukawa coupling between χ and S, together with the bare mass for χ, breaks the Z_2 symmetry ($S \to -S$) explicitly at tree level and introduces a tadpole term for S at finite temperature. This generically leads to stationary points with non-vanishing vev of S at high temperatures. Later on, the Universe goes through a one-step SFOEWPT to converge to the EW symmetry breaking vacuum. The EWPT proceeding in this way is generically strong due to the barrier between the two vacua induced by the quartic coupling between the complex singlet and the SM Higgs boson. We derive two zero temperature boundary conditions to secure that the potential is bounded from below and the EW breaking vacuum is the global minimum. Furthermore, we derive two necessary conditions to achieve SFOEWPT and successful nucleation. The parameter space constrained analytically agrees well with that found by numerical calculations using `CosmoTransitions`.

Once we identify the parameter space with successful SFOEWPT, nucleation and dark matter relic abundance for the dark fermion, we proceed to compute the bubble wall velocities using the method developed in Sec. 2.2.5. We study the parameter dependencies of v_w, and the correlations among v_w and two common measures of the phase transition strength, α_n and v_n/T_n. We also study the implications of v_w for baryogenesis and the GW signal. We review the calculation of the BAU in different computational frameworks, commenting on their applicability given the value of v_w. In particular, the treatment based on truncating the transport equations at leading order in v_w is determined to be unreliable for realistic values of v_w in this model. This indicates that one should first carefully determine v_w from the first principles before choosing a BAU computation framework. The GW signal is another observable which depends sensitively on both the wall velocity v_w and the transition strength α_n. We find that in the DarkCPV model, deflagration/hybrid solutions occur only for very small $\alpha_n \lesssim 4 \times 10^{-3}$. Consequently, the GW signal, which scales as $(\frac{\alpha_n}{1+\alpha_n})^2$, is beyond the

sensitivities of current and projected GW detectors for this class of solutions. Detonation solutions, on the other hand, may yield a detectable GW signal, but would not necessarily be compatible with a successful baryogenesis.

CHAPTER 4

TOWARDS REAL-TIME SIMULATION OF BARYOGENESIS

Among the Sakharov conditions that must be satisfied by baryogenesis mechanisms, departure from thermal equilibrium is realized by different cosmological processes. For high-scale baryogenesis, such as grand unified theory baryogenesis [150] or leptogenesis [151], the baryon asymmetry arises at high temperatures from out-of-equilibrium decays of heavy particles whose rates fall below the Hubble expansion rate. For a low-scale baryogenesis, such as electroweak baryogenesis (EWBG), the departure from equilibrium is caused by a strong first-order phase transition. To effectively address the out-of-equilibrium dynamics in baryogenesis, approximations are applied at multiple stages of the theoretical calculations, introducing significant uncertainties to the predictions of the baryon asymmetry [110, 152–156] and the associated observables, such as the gravitational waves emitted from phase transitions [87, 132, 157, 158].

As quantum technology advances, the possibility of achieving fault-tolerant quantum computing systems becomes increasingly attractive and may lead to transformative tools for tackling real-time dynamics in particle physics. Studies exploring this area are consistently emerging; see review articles [159–162]. Examples include particle scattering problems which are hard to solve by perturbation theory [163–166], parton shower studies considering quantum interference [167–169]. Real-time simulations of out-of-equilibrium dynamics on a quantum computer may well emerge as the best computational tool for a deeper understanding of the evolution of our Universe. Although realistic large-scale quantum simulations are still limited by resources, classical simulations with tensor network methods have enabled real-time studies of scattering phenomenon [170–174], as well as dynamics of bubble-wall collisions [173, 174] in $1 + 1$ dimensions. Tensor network methods exploit the fact that physically relevant states occupy only a small corner of the exponentially large Hilbert space. In particular, the ground states of the gapped 1+1 dimensional lattice systems can be efficiently approximated by

matrix product states (MPS) [175, 176]. This insight underlies powerful algorithms such as the density matrix renormalization group (DMRG) [177, 178], which enable efficient computation of ground states and even real-time dynamics in such systems.

In this chapter, focusing on the dynamics of EWBG, we first discuss the limitations of conventional non-real-time calculations, highlighting the importance of real-time simulations. We then present a prototype real-time simulation of the CP violation process in EWBG, demonstrating the feasibility of studying the real-time dynamics of baryogenesis using technologies available today or in the near future. This is based on our work [179]. We conclude the chapter with an outlook on extending this prototype study toward simulations of the full dynamics of baryogenesis.

4.1 Limitations of conventional calculations for EWBG

The electroweak baryogenesis mechanism has been discussed in detail in the previous chapters, and is summarized here for the readers' convenience. During the first-order electroweak phase transition, bubbles of true vacuum form, as the Higgs field acquires a VEV, and fermions become massive. In the presence of CP violation, particles and antiparticles are redistributed among different chiral states in the collisions with the bubble wall, resulting in a nonvanishing chiral asymmetry. This asymmetry is then converted into net baryon number through the nonperturbative sphaleron process active in the symmetric phase, outside the bubble wall. The net baryon number generated in front of the bubble wall is subsequently transported into the broken phase as the bubble expands. If the phase transition is sufficiently strong, the sphalerons become inactive, due to the Boltzmann suppression controlled by the Higgs VEV, and the baryon asymmetry is preserved.

The nonequilibrium processes described above are most accurately formulated as real-time dynamics governed by a time-dependent Hamiltonian. However, solving such dynamics is intractable with classical computational resources because of the exponentially large Hilbert

space. One therefore introduces approximations that reduce the real-time problem to a static one, which can then be studied analytically and numerically. To understand the approximation that can be made, we recall the equivalence of the Hamiltonian formalism and the Lagrangian formalism on computing the probability for an initial field configuration $|\phi_a(\mathbf{x})\rangle$ to transform into a final configuration $|\phi_b(\mathbf{x})\rangle$ after time T:

$$\langle\phi_b(\mathbf{x})|e^{-i\int_0^T dt\, H}|\phi_a(\mathbf{x})\rangle = \int \mathcal{D}\phi \exp\left[i\int_0^T dt \int d^3\mathbf{x}\,\mathcal{L}\right], \tag{4.1}$$

where the path integral $\int \mathcal{D}\phi$ is over the field space bounded by $\phi(0,\mathbf{x}) = \phi_a(\mathbf{x})$ and $\phi(T,\mathbf{x}) = \phi_b(\mathbf{x})$. The exponential factor on the right hand side of Eq. (4.1) can be rewritten in terms of the Euclidean time $t_E \equiv -it$ as

$$\exp\left[-\int_0^{iT} dt_E \int d^3\mathbf{x}\,\mathcal{L}\right] \equiv \exp\left[-S_E\right]. \tag{4.2}$$

Therefore, the path integral in the Lagrangian formalism can be evaluated by Monte Carlo sampling over the field configurations weighted by e^{-S_E}, as was done in the early-days lattice simulations of EWPT [17–28]. However, this approach is well-defined only when the Euclidean action S_E is real, which is not generally the case[1]. Thermal equilibrium provides one such scenario where S_E is real. This follows from the Kubo-Martin-Schwinger (KMS) relation [60, 61] that enforces periodicity in Euclidean time with period equal to the inverse temperature β, allowing the Euclidean time integral to be restricted to the interval $[0,\beta]$. Assuming a time-independent Lagrangian, the Euclidean action then factorizes into temporal and spatial parts, $S_E = \beta S_3$. This simplification is the starting point for the perturbative calculations of the bubble nucleation rates as discussed in Sec. 2.1.2. Hence, the conventional calculations for nucleation rate based on Lagrangian formalism, either perturbatively or nonperturbatively, are restricted to the assumption of thermal equilibrium, which is in clear

1. Complex S_E would give rise to the well-known sign problem [180, 181].

contradiction to the nonequilibrium nature of first-order EWPT.

Another important source of uncertainties arises from the determination of the chiral asymmetry generated from fermion-bubble scattering. The relevant dynamics is commonly calculated with semiclassical methods [101, 182], or VEV-insertion approximation (VIA) [103, 104, 183]. Both approaches have limitations. Semiclassical methods only apply to walls with thickness much larger than the de Broglie wavelength of the particle, where the impact of the bubble wall can be approximated by a classical force. VIA evaluates the asymmetry generation with reflection and transmission coefficients, which are only defined in the asymptotic regions away from the scattering point and thus do not capture the instantaneous asymmetry generated near the scattering point. Moreover, the calculations of the reflection and transmission coefficients are currently limited to perturbative regimes. The real-time simulation to be presented in the next subsection provides the first nonperturbative results on the asymmetry generation over the space throughout the scattering process.

4.2 Prototype study: Real-time simulation of CP violation in electroweak baryogenesis

A prototype of chiral asymmetry generation in EWBG is a Dirac fermion ψ coupled to a complex scalar field that undergoes a first-order phase transition, from the phase that preserves electroweak symmetry to the one that breaks it. Bubbles of the true vacuum of the scalar field nucleate and expand, and the massless fermions outside the bubble scatter off the wall. In this work, we consider the rest frame of the bubble wall, where its effect on the fermions can be described by a complex mass term $m(x) = |m(x)|e^{i\theta(x)\gamma^5}$, where we have $|m(x)| = 0$ in the region outside the bubble (symmetric phase s) and a nonvanishing mass $|m(x)| \neq 0$ inside the bubble (broken phase b). Such mass term can be induced by the Yukawa coupling of the fermion to a complex scalar field in the presence of a physical complex phase; see its realization in, e.g., the two Higgs doublet model in Refs. [14, 98, 184].

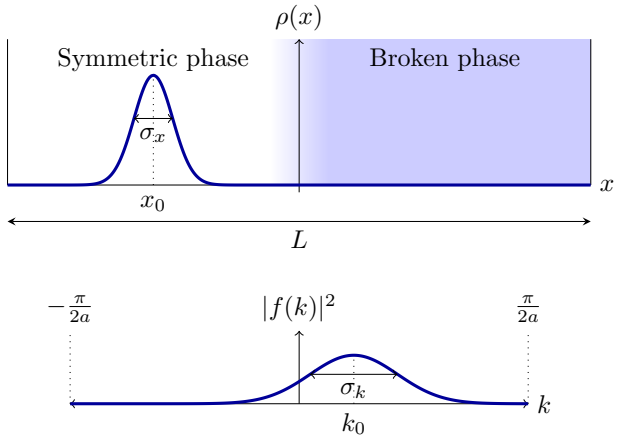


Figure 4.1: Schematic for our simulations of fermion-bubble scattering. *Top*: local charge density for a fermion (or antifermion) wave packet in position space. The region around $x = 0$ with the color gradient represents the bubble wall. *Bottom:* the wave packet in momentum space.

The Hamiltonian in $d + 1$ (even) spacetime dimensions of the fermion interacting with a static bubble wall is

$$H = \int d^d x \, \bar{\psi} \left[-i\gamma^j \partial_j + |m(x)| e^{i\theta(x)\gamma_5} \right] \psi, \tag{4.3}$$

with $j = 1, \ldots, d$. Dynamical scalar fields can also be incorporated in this framework (see, for example, recent studies of bubble-wall collisions [173, 174]), which we leave for future work.

The presence of a complex mass with $\theta(x) \neq 0$ makes the scattering process qualitatively different from the case of a bubble-wall profile with $\theta(x) = 0$. This is because a complex mass term generically breaks certain discrete symmetries relating particles and antiparticles. A nontrivial profile for $\theta(x)$ breaks CP symmetry in $3 + 1$ dimensions. With varying $\theta(x)$, fermions of a certain chirality will scatter differently from their CP conjugates.

Thus, one can measure changes of the chiral charge density $j^0_A = \bar{\psi}\gamma^0\gamma^5\psi$ to quantify the effects of CP violation in scattering. Since j^0_A is CP odd, an initially CP symmetric state would have a vanishing chiral charge density. With CP-violating interactions, j^0_A would generically become nonzero after scattering. This net chiral charge density subsequently

creates a chemical potential that enables the electroweak sphaleron to generate more baryons than antibaryons.

Can we study this process of CP asymmetry generation nonperturbatively? While a thorough quantitative study of this problem for the Standard Model is beyond the reach of all current classical or quantum resources, in this work we start an investigation of how we might study this with future quantum hardware. To do so, we consider the problem of fermion-bubble collisions in a $1+1$-dimensional setting. In $1+1$ dimensions, the complex mass term breaks charge conjugation C (but preserves CP), allowing for chiral asymmetry generation since j^0_A is odd under C.[2] With the replacement of CP by charge conjugation C, the discussion of measuring asymmetry generation in the previous paragraph for $(3+1)$ dimensions can be applied to $(1+1)$ dimensions.

The scattering process relevant for generating the asymmetry near the bubble wall is that a Weyl fermion (or its C-conjugate antifermion) in the symmetric phase moves toward the bubble wall and scatters off. To develop a formalism for a lattice simulation of this process, let us first describe our setup in the continuum with an infinite volume.

4.2.1 Simulation setup in the continuum and infinite volume

Let $|\Omega\rangle$ be the ground state of the Hamiltonian in Eq. (4.3). We take the static bubble-wall profile $m(x)$ to be centered at $x_w = 0$ with a wall width L_w such that $m(x) \to 0$ as $x \ll -L_w$ and $m(x) \to m_0$ for $x \gg L_w$. We take the physical volume to be infinite for this discussion.

With $\psi(x)$, $\psi^\dagger(x)$ denoting Dirac fields, we define the creation operators $\psi^\dagger_{k\alpha}$ and the annihilation operators $\psi_{k\alpha}$ for particles ($\alpha = +$) and antiparticles ($\alpha = -$),

$$\psi(x) = \int \frac{dk}{2\pi} \frac{1}{\sqrt{2\epsilon_k}} \left(\psi_{k+} u_k e^{-ikx} + \psi^\dagger_{k-} v_k e^{+ikx} \right), \tag{4.4}$$

2. For a discussion of the charge-conjugation C and parity P symmetries in arbitrary spacetime dimensions, see Appendix C.1.

where u_k and v_k are the positive and negative energy eigenfunctions of the massless Dirac Hamiltonian with energy $\epsilon_k = \pm|k|$. For a momentum-space wave packet $f(k)$, we define wave packet states

$$|f_\pm\rangle = \int dk\, f(k)\psi^\dagger_{k\pm}\,|\Omega\rangle\,. \tag{4.5}$$

Normalization of the wave packet states $\langle f_\pm|f_\pm\rangle = 1$ requires $\int dk\,|f(k)|^2 = 1/(2\pi)$. If the wave packet $f(k)$ is nonvanishing only for $k > 0$, then the states $|f_\pm\rangle$ describe a particle or antiparticle wave packet moving in the positive x direction. We note that the states $|f_\pm\rangle$ are conjugates of each other under charge-conjugation symmetry C that exchange particles and antiparticles,

$$\mathrm{C} : \psi^\dagger_{k+} \leftrightarrow \psi^\dagger_{k-}, \tag{4.6}$$

$$|f_\pm\rangle = \mathrm{C}\,|f_\mp\rangle\,. \tag{4.7}$$

See Appendix C.1 for a more in-depth discussion of charge conjugation.

As shown in Fig. 4.1, we take $f(k)$ to be a Gaussian wave packet localized in momentum space at $k = k_0 > 0$ with width σ_k, and localized in position space at $x = x_0 < 0$ with width $\sigma_x = 1/(2\sigma_k)$,

$$f(k; k_0, \sigma_k, x_0) = \frac{1}{(2\pi)^{3/4}\sqrt{\sigma_k}} e^{-ikx_0} e^{-(k-k_0)^2/(4\sigma_k^2)}. \tag{4.8}$$

We need to choose $\sigma_x \ll |x_0|$ to ensure that the wave packet is located deep inside the massless phase, away from the bubble wall. Furthermore, we need to choose $\sigma_k \ll k_0$ to make sure that there are no left-moving modes (modes with negative k). With this, $|f_+\rangle$ and $|f_-\rangle$ are right-moving, left-chiral ($\gamma_5 = -1$) Weyl fermion and antifermion states, respectively.

Taking the initial state at time $t = 0$ to be either the particle or the antiparticle wave

packet

$$|\Psi_\pm(0)\rangle = |f_\pm\rangle\,, \tag{4.9}$$

we turn on time evolution, obtaining the state $|\Psi_\pm(t)\rangle = e^{-iHt}\,|\Psi_\pm(0)\rangle$ after a time t. As the wave packet moves toward the bubble wall with velocity $v = 1$, it scatters off the bubble wall at time $t \sim |x_0|$. Part of the wave packet is reflected back, whereas the rest is transmitted across the bubble wall into the massive phase. After a sufficiently long time, the (reflected and transmitted) wave packets are sufficiently far from the bubble wall. We can then measure some observables quantifying the asymmetry between how the particle $|f_+\rangle$ and antiparticle $|f_-\rangle$ wave packets are scattered. This would be a measure of the C asymmetry generated during the interactions of the fermions with the bubble wall.

4.2.2 Observables

Breaking of C by the bubble wall implies that the particles scatter differently than the corresponding antiparticles. Therefore, we need to probe the C-asymmetry in the S-matrix for the fermion-bubble scattering.

Schematically, the S-matrix for elastic fermion-bubble scattering, $S_\alpha(k, k')$ ($\alpha = \pm 1$ for fermion/antifermion), governs how a single-particle momentum eigenstate in the far past $t \to -\infty$,

$$|k\alpha\rangle_{-\infty} = \psi^\dagger_{k\alpha}\,|\Omega\rangle\,, \tag{4.10}$$

transforms into $|k\alpha\rangle_{+\infty} = \lim_{t\to+\infty} e^{-iHt}\,|k\alpha\rangle_{-\infty}$ in the far future $t \to +\infty$,

$$|k\alpha\rangle_{-\infty} \xrightarrow[\text{scattering}]{} |k\alpha\rangle_{+\infty} = \int dk'\; S_\alpha(k, k')\,|k'\alpha\rangle_{-\infty}\,. \tag{4.11}$$

Elastic scattering implies that

$$S_\alpha(k,k') = R_\alpha(k)\delta(k+k') + T_\alpha(k)\delta(k'-k_T), \tag{4.12}$$

where $k_T = \sqrt{k^2 - m^2}$ is the transmitted momentum in the massive phase, and $R_\alpha(k)$ and $T_\alpha(k)$ are the complex reflection and transmission coefficients, respectively. Thus,

$$|k\alpha\rangle_{+\infty} = R_\alpha(k)\,|-k\alpha\rangle_{-\infty} + T_\alpha(k)\,|k_T\alpha\rangle_{-\infty} \tag{4.13}$$

A localized wave packet $|f_\alpha\rangle_{-\infty} \equiv \int dk f(k)\,|k\alpha\rangle_{-\infty}$ in the far past transforms into $|f_\alpha\rangle_{+\infty}$ in the far future,

$$\begin{aligned} |f_\alpha\rangle_{+\infty} &= \int dk\, f(k)\left[R_\alpha(k)\,|-k\alpha\rangle_{-\infty} + T_\alpha(k)\,|k_T\alpha\rangle_{-\infty}\right] \\ &= |f_{R\alpha}\rangle_{+\infty} + |f_{T\alpha}\rangle_{+\infty} \end{aligned} \tag{4.14}$$

with

$$|f_{R\alpha}\rangle_{+\infty} = \int dk\, R_\alpha(k) f(k)\,|-k\,\alpha\rangle_{-\infty}\,, \tag{4.15}$$

$$|f_{T\alpha}\rangle_{+\infty} = \int dk\, T_\alpha(k) f(k)\,|k_T\,\alpha\rangle_{-\infty}\,. \tag{4.16}$$

Let us consider just the reflected wave packet. The reflection coefficient $R_\alpha(k) = |R_\alpha(k)|e^{-i\phi_\alpha(k)}$ characterizes the reflected wave packet completely. The C-asymmetry can appear in both the magnitude $|R_\alpha(k)|$ and the phase $\phi_\alpha(k)$. In a lattice simulation, we would like to be able to measure both of these. Therefore, we define two observables that measure (i) "magnitude asymmetry" and (ii) "phase asymmetry".

Magnitude asymmetry

Let $j^\mu(x) = \bar{\psi}(x)\gamma^\mu\psi(x)$ be the current for the vector $U(1)$ symmetry, such that the local charge density at time t is

$$\rho_\pm(x,t) = \langle \Psi_\pm(t)|j^0(x)|\Psi_\pm(t)\rangle\,. \tag{4.17}$$

The total charge in the symmetric phase $x < 0$ is then

$$\mathcal{Q}_{t,\pm} \equiv \int_{-\infty}^{0} dx\, \rho_\pm(x,t). \tag{4.18}$$

Since the initial wave packet is completely localized in the symmetric region, $\mathcal{Q}_{0,\pm} = \pm 1$ at $t = 0$. At large times, this is related to the reflection magnitudes using Eqs. (4.4) and (4.15)[3]:

$$\mathcal{Q}_{\infty,\pm} = \int_{-\infty}^{\infty} dx\ \langle f_{R\pm}|j^0(x)|f_{R\pm}\rangle_{+\infty} \tag{4.19}$$

$$= \pm \int_{-\infty}^{\infty} dk\, |R_\pm(k)|^2 |f(k)|^2. \tag{4.20}$$

Therefore, a convenient measure of the magnitude asymmetry is simply the sum over the particle and antiparticle states $\mathcal{Q}_t = \mathcal{Q}_{t,+} + \mathcal{Q}_{t,-}$, such that in the limit $t \to \infty$, we get

$$\mathcal{Q}_\infty = \mathcal{Q}_{\infty,+} + \mathcal{Q}_{\infty,-} \tag{4.21}$$

$$= \int_{-\infty}^{\infty} dk\ \left[|R_+(k)|^2 - |R_-(k)|^2\right] |f(k)|^2. \tag{4.22}$$

3. This can be seen by writing $\mathcal{Q}_{\infty,\pm} = \int_{-\infty}^{0} dx\ \langle f_{R\pm}|j^0(x)|f_{R\pm}\rangle$, noting that the integration limits can be extended to the entire space because $|f_{R\pm}\rangle$ vanishes outside the symmetric region anyway.

We note that in the limit $\sigma_k/k_0 \to 0$ as the wave packet becomes infinitely peaked at $k = k_0$, the observable $\mathcal{Q}_{\infty,\pm}$ measures the reflection coefficients $|R_\pm(k_0)|^2$,

$$\mathcal{Q}_{\infty,\pm} \to \pm|R_\pm(k_0)|^2 \quad \text{as} \quad \frac{\sigma_k}{k_0} \to 0. \tag{4.23}$$

Phase asymmetry

While the above observable captures any C-asymmetry in the magnitude $|R_\pm(k)|$, asymmetry will also lie in the phase $\phi_\pm(k) = \arg R_\pm(k)$. As we will see in our lattice simulations, this becomes especially important when the fractional C-asymmetry in magnitude $\frac{|R_+|^2-|R_-|^2}{|R_+|^2+|R_-|^2}$ is too small to be detected within numerical uncertainties. In that case, there may still be a significant asymmetry in the phase.

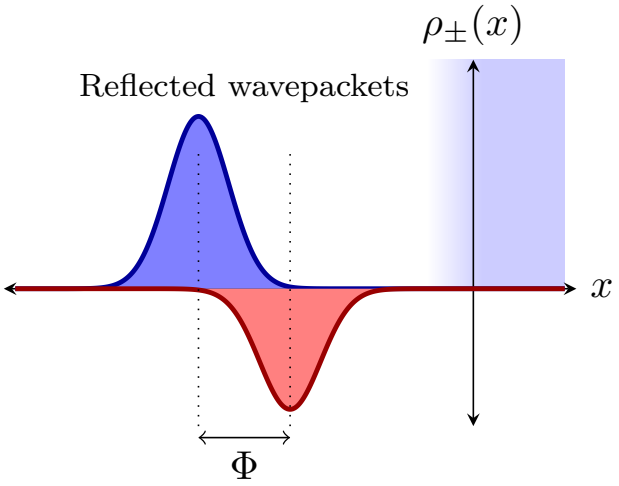


Figure 4.2: The phase-asymmetry observable Φ [Eq. (4.26)] captures the relative spatial displacement between the particle and antiparticle wave packets, while the magnitude asymmetry $\mathcal{Q}_\infty$ [Eq. (4.21)] captures the asymmetry between the total amount of charge reflected. In this picture of the local charge densities $\rho_\pm(x)$ for the particle (blue) and antiparticle (red) wave packets, Φ is the distance between the peaks of the Gaussian wave packets, and $\mathcal{Q}_\infty$ is the sum of (signed) areas enclosed by the wave packets.

An observable that is sensitive to the phase of $R_\pm(k)$ is the spatial displacement of the reflected wave packets, shown schematically in Fig. 4.2. We provide a more careful explanation

in Appendix C.2, but the essential idea of this observable can be simply understood as follows. For a relativistic Gaussian wave packet sharply peaked around $k = k_0$, a given k wave transforms after reflection as

$$e^{ik(x-t)} \to |R_\alpha(k)|\, e^{-ik[x+t]-i\phi_\alpha(k)} \tag{4.24}$$

$$\approx |R_\alpha(k)|\, e^{-ik[x+t+\phi'_\alpha(k_0)]} \tag{4.25}$$

where we expand the phase $\phi_\alpha(k)$ about $k = k_0$ as $\phi_\alpha(k) = \phi_\alpha(k_0) + (k - k_0)\phi'_\alpha(k_0) + O(k^2)$ for $\alpha = \pm$, and drop the k-independent phase $\phi_\alpha(k_0)$. We see that the reflected wave at a given time t gets displaced by an amount $\phi'_\alpha(k_0)$ relative to the case with a trivial phase shift $\phi_\alpha(k) = 0$. Therefore, we may use the difference in the displacement of the sharply peaked Gaussian wave packets for the particle and antiparticle after reflection as a measure of the phase asymmetry:

$$\Phi = \phi'_+(k_0) - \phi'_-(k_0). \tag{4.26}$$

Assuming that the reflected wave packet is itself well approximated by a Gaussian, we can relate Φ to the correlation between the charge densities $\rho_\pm(x,t)$ [defined in Eq. (4.17)]. At large times $t \to \infty$, we find

$$\lim_{t\to\infty} \int_{-\infty}^{0} dx\, \rho_+(x,t)\rho_-(x,t) = -Ae^{-B\Phi^2} \tag{4.27}$$

for certain constants A, B independent of Φ, where the integration limits ensure that only the reflected wave packets contribute. This relation motivates us to define a new (time-dependent) phase-asymmetry observable,

$$\tilde{\Phi}(t) = \sqrt{-\frac{1}{B(t)} \log\left(-\frac{1}{A(t)} \int_{-\infty}^{0} dx\, \rho_+(x,t)\rho_-(x,t)\right)}, \tag{4.28}$$

where $A(t), B(t)$ are now time-dependent functions that do not depend on cross-correlations of $\rho_\pm$. In the limit $t \to \infty$, we get $\tilde{\Phi}(t) \to \Phi$ of Eq. (4.26). See Appendix C.2 for a more detailed discussion of this observable, including the definitions of $A(t), B(t)$.

4.2.3 Mass profiles

To complete the description of our simulations, we need to specify the mass profiles used for the bubble wall $m(x)$. For EWBG calculations, a commonly used mass profile is of the hyperbolic form [185], given by

$$\begin{aligned} |m(x)| &= \frac{m_0}{2}\left[1 + \tanh(x/L_w)\right], \\ \theta(x) &= \frac{\theta_0}{2}\left[1 + \tanh(x/L_w)\right], \end{aligned} \tag{4.29}$$

where L_w is the width of the bubble wall. The parameter θ_0 controls the degree of C violation. In this work, we consider two cases.

First, we consider a real mass profile, $\theta_0 = 0$ with no C violation. The Dirac equation in this case is, in fact, analytically solvable [186] and thus serves as a benchmark for our lattice simulations. The reflection coefficient $|R_+(k)|^2 = |R_-(k)|^2$ is [186]

$$|R_\pm(k)|^2 = \begin{cases} \frac{\sin\left[\frac{\pi}{2}(\beta'-\beta+\xi)\right]\sin\left[\frac{\pi}{2}(\beta'-\beta-\xi)\right]}{\sin\left[\frac{\pi}{2}(\beta'+\beta+\xi)\right]\sin\left[\frac{\pi}{2}(\beta'+\beta-\xi)\right]}, & k > m_0 \\ 1, & k \le m_0 \end{cases}, \tag{4.30}$$

where $\beta' = i\sqrt{\epsilon^2 - \xi^2}$, $\beta = i\epsilon$, with the dimensionless quantities $\epsilon \equiv kL_w$, $\xi \equiv m_0 L_w$. As there is no C symmetry breaking, the asymmetry observables should vanish: $\mathcal{Q}_\infty = 0$ and $\Phi = 0$.

We then consider the nontrivial case of a complex mass with $\theta_0 \neq 0$, where no analytical solution is available. A complex mass term produces an asymmetry in the reflected particle

and antiparticle wave packets. The goal of this work is to show the above mentioned asymmetry observables can be computed using real-time simulations.

4.2.4 Lattice Simulations

We now translate the continuum setup described in the previous subsections to the lattice to enable a nonperturbative study of C-asymmetry generation during fermion-bubble collisions. We then describe the results of the simulations performed using MPS [187].

Hamiltonian

Staggered fermions [188] provide a convenient doubler-free lattice formulation for a Dirac fermion in $1+1$ dimensions by mapping the two spinor components of the Dirac field $\psi(x)$ in Eq. (4.3) to the odd and even sites. On a N-site (N even) chain with open boundary conditions (OBC), the staggered fermion Hamiltonian is

$$\begin{aligned}\hat{H} = &\sum_{n=1}^{N-1} i\left[\frac{1}{2} + (-1)^n |m_n| \sin\theta_n\right](\chi_{n+1}^\dagger \chi_n - \chi_n^\dagger \chi_{n+1}) \\ &- \sum_{n=1}^{N} (-1)^n |m_n| \cos\theta_n \, \chi_n^\dagger \chi_n,\end{aligned} \tag{4.31}$$

where χ_n are 1-component complex fermion fields satisfying $\{\chi_i^\dagger, \chi_j\} = \delta_{ij}$.

We use $m_n \equiv am(an - aN_c)$ and $\theta_n \equiv \theta(an - aN_c)$ as discretizations of the mass profile given in Eq. (4.29), where $N_c = (N+1)/2$ is the center of the bubble wall. The symmetric phase can thus be identified as the half space of sites n with $1 \le n \le N/2$ and the broken phase as the other half with $N/2 + 1 \le n \le N$.

Initial state and time evolution

We use DMRG to compute the ground state $|\Omega\rangle$ [177, 189]. Despite the vanishing mass gap in the symmetric phase, we find that DMRG converges well for the system sizes considered in this work.

Let $\hat{\psi}^\dagger_{k\alpha}$ be the creation operators on the lattice for particles ($\alpha = +$) and antiparticles ($\alpha = -$) with momentum k for the staggered fermion Hamiltonian in Eq. (4.31). (See Appendix C.3 for precise definitions on the lattice.) Strictly speaking, lattice momenta k are not well defined in OBC. However, we define the single-particle momentum eigenstates in periodic boundary conditions (PBC) and assume that the volumes are large enough such that the errors are negligible. We study the finite-size effects in more detail in Appendix C.4.

In analogy with the continuum formalism discussed in the previous section, we define the wave packet initial states

$$|\Psi_\pm(0)\rangle = |f_\pm\rangle = \mathcal{N} \sum_k f(k) \hat{\psi}^\dagger_{k\pm} |\Omega\rangle \tag{4.32}$$

where $\mathcal{N}$ is the normalization constant such that $\langle f_\pm | f_\pm \rangle = 1$, and k runs over lattice momenta in PBC, $k = -\pi/2 + 2\pi j/N$ for $j = 1, \ldots, N/2$. We place the center of the wave packet at $n_0 = N/4$ to have minimal overlap with the bubble wall and the lattice boundary. The exact construction of the wave packet is specified in Appendix C.3.

The state $|\Psi_\pm(t)\rangle$ is then obtained by time evolution with the Hamiltonian in Eq. (4.31). The real-time evolution can be computed using a simple second-order Trotter scheme as described in Appendix C.3.

Choice of parameters

In the continuum theory, the mass m_0 of the fermion in the broken phase is the natural physical scale. Therefore, in the following, we report all quantities in physical units of m_0.

We fix the lattice volume to be $L = 28$ and the wall width to be $L_w = 0.6$ for all simulations in this work. We perform time evolution for a total time $T = L$. For this, we use a Suzuki-Trotter scheme with the step size fixed at $\tau = 0.05$, which is much smaller than the inverse of the momentum resolution $\Delta k = 2\pi/L \approx 0.22$. We find that the Trotter errors are negligible compared to finite-size and lattice artifacts, so we do not perform $\tau \to 0$ extrapolations.

One of the most challenging aspects of these simulations is that we need the wave packet to be localized in both position and momentum space. This results in the presence of multiple scales that need to fit in the box. The initial Gaussian wave packet is characterized by the physical value of the central momentum k_0, the momentum width σ_k, the central position x_0, and the spatial width $\sigma_x = 1/(2\sigma_k)$. With the bubble wall located at $x = 0$, localization of the initial wave packet in position space implies

$$0 \ll |x_0 \pm \sigma_x| \ll \frac{L}{2}. \tag{4.33}$$

On the other hand, we need the wave packet to also be sufficiently localized in momentum space to avoid lattice artifacts from large momenta and to avoid the presence of negative-momentum (left-moving) modes,

$$0 \ll |k_0 \pm \sigma_k| \ll \frac{\pi}{2a}. \tag{4.34}$$

We take $x_0 = -L/4$ so that the initial wave packet has a minimal overlap with the left boundary at $x = -L/2$ and the bubble wall at $x = 0$. Noting that $\sigma_x \sigma_k = 1/2$, the above inequalities can be satisfied if we choose the wave packet momentum-space parameters k_0, σ_k such that

$$\frac{\pi}{2a} \gg k_0 \gg \sigma_k \gg \frac{2}{L}. \tag{4.35}$$

Getting a clean separation of all these scales is a numerical challenge for any lattice simulation. In particular, for a fixed σ_k, we expect there to be increased systematic errors as we make k_0 too small ($k_0 \lesssim \sigma_k$), as well as when k_0 becomes large ($k_0 \gtrsim \pi/2a$).

We vary the lattice spacing a in the range $\{\frac{1}{8}, \frac{1}{6}, \frac{1}{5}, \frac{1}{4}\}$ for a continuum limit extrapolation. This corresponds to a lattice size $N = L/a$ varying in the range $N = 112, \ldots, 224$. The largest lattice spacing we have is thus $a = 0.25$. Therefore, Eq. (4.35) requires that $6.28 \gg k_0 \gg \sigma_k \gg 0.07$. Ideally, we would like σ_k to be as small as possible to allow maximum variation in k_0. However, we are also limited by the resolution in momentum space $\Delta k = 2\pi/L \approx 0.22$. So we take $\sigma_k = 0.5 \approx 2\Delta k$ and keep it fixed for all simulations.[4]

Observable (i) magnitude asymmetry

Defining the local charge density of the states $|\Psi_\pm(t)\rangle$,

$$\rho_{n,\pm}(t) = \langle \Psi_\pm(t)|\hat{j}^0_n|\Psi_\pm(t)\rangle - \langle \Omega|\hat{j}^0_n|\Omega\rangle \,, \tag{4.36}$$

where we subtract the vacuum contribution to reduce lattice artifacts, we define the total charge in the symmetric phase on the lattice as the lattice analog of Eq. (4.18),

$$\hat{\mathcal{Q}}_{t,\pm} = \sum_{n=1}^{N} w_n \rho_{n,\pm}(t) \tag{4.37}$$

where $\hat{j}^0_n = \chi^\dagger_n \chi n$ is the $U(1)$ charge density on the lattice at site n, and w_n is a suitably chosen "smeared" step function which vanishes deep in the broken phase $w_n = 0$ for $n \gg N_c$ and is unity in the symmetric phase: $w_n = 1$ for $n \ll N_c$. A smooth w_n reduces contributions close to the wall, thereby reducing lattice artifacts. For the measurement of the magnitude

4. For a study of finite-volume effects, see Appendix C.4.

asymmetry, we choose w_n to be the Sigmoid function,

$$w_n = \left[\exp\left(\frac{n-(N_c-n_w)}{0.1\,n_w}\right)+1\right]^{-1}, \tag{4.38}$$

where $n_w = L_w/a$ is the wall width in lattice unit.

The magnitude-asymmetry observable on the lattice is then

$$\hat{\mathcal{Q}}_t = \hat{\mathcal{Q}}_{t,+} + \hat{\mathcal{Q}}_{t,-} \tag{4.39}$$

In the infinite-volume limit, $\hat{\mathcal{Q}}_t$ saturates to the total reflected charge $\hat{\mathcal{Q}}_\infty$ as $t \to \infty$. However, this is not the case in a finite box, and therefore we need to choose an appropriate time window to measure this observable with minimal finite-size errors. The finite-size effects will be minimized when the reflected wave packet has minimal overlap with the bubble wall. Since the wave packet in the symmetric region travels with a velocity $v = 1$, and the wave packet is initially located at the center of the symmetric region, we choose to measure the observable in the window $t \in (\Delta t)_{\mathcal{Q}} \equiv (3L/4, L)$. This is when the reflected wave packet is expected to hit the left boundary and return to its starting position. We use the mean value of $\hat{\mathcal{Q}}_t$ in the window $(\Delta t)_{\mathcal{Q}}$ as the measurement and use the standard deviation of $\hat{\mathcal{Q}}_t$ over the time window $(\Delta t)_{\mathcal{Q}}$ as an estimate of the systematic errors due to finite volume. [See Fig. 4.3(a) for an illustration of the time window $(\Delta t)_{\mathcal{Q}}$, which is highlighted as a yellow band.]

Observable (ii) phase asymmetry

We use a naive discretization of the phase-asymmetry observable $\tilde{\Phi}(t)$ in Eq. (4.28) given by

$$\hat{\Phi}_t = \sqrt{-\frac{1}{B(t)}\log\left[-\frac{1}{A(t)}\sum_{n=1}^{N} a^{-1} w'_n \rho_{n,+}(t)\rho_{n,-}(t)\right]}, \tag{4.40}$$

where w'_n is again a suitably chosen smearing function that vanishes in the broken phase. We choose w'_n to be a double-sided sigmoid function to suppress the boundary effects from both the bubble wall and the lattice boundary (see discussion in the next paragraph),

$$w'_n = w_n \left[\exp\left(-\frac{n - n_w}{0.1\, n_w} \right) + 1 \right]^{-1}, \tag{4.41}$$

with w_n given by Eq. (4.38). See the discussion following Eq. (C.27) for the expressions of $A(t)$ and $B(t)$ on the lattice.

The choice of a suitable time window $(\Delta t)_\Phi$ to measure the phase asymmetry is more subtle than for the magnitude asymmetry. This is because while the magnitude asymmetry only depends on the total charge reflected back, the phase asymmetry assumes that the wave packets are Gaussian. When there is significant overlap with either the bubble wall or lattice boundary, the shape of the wave packet cannot be approximated as a Gaussian anymore. However, if the wave packet is sufficiently away from both boundaries, $\hat{\Phi}_t$ becomes independent of t. Thus, we choose the window $(\Delta t)_\Phi$ by looking for a plateau in $\hat{\Phi}_t$. We find that an optimal time window is approximately $(\Delta t)_\Phi \equiv (0.5L, 0.6L)$ for the choice of parameters considered in this work [see Fig. 4.5(b) for an illustration of $(\Delta t)_\Phi$, highlighted as a yellow band]. This is consistent with our expectation that the reflected wave packet is in the center of the symmetric region, and therefore is maximally away from the bubble wall and lattice boundary, at approximately $t = L/2$. We use the mean value in this window as the measured asymptotic value $\hat{\Phi}_\infty$ and the standard deviation as a measure of systematic errors from the finite volume.

4.2.5 Simulation results: real mass ($\theta_0 = 0$)

We first consider a fermion that scatters off a bubble wall given by a real mass profile $\theta_0 = 0$. When $\theta_0 = 0$, the Hamiltonian preserves C and therefore the particle and antiparticle wave

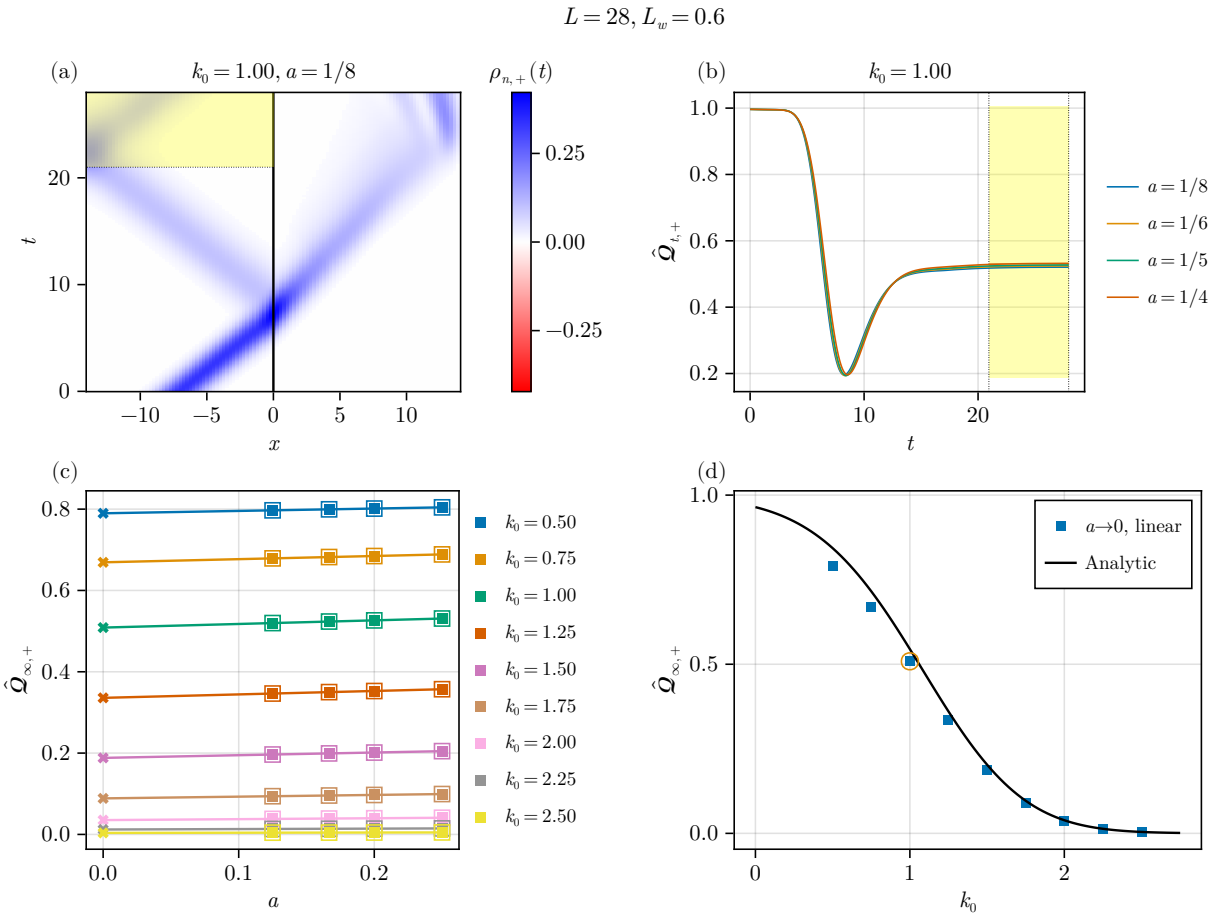


Figure 4.3: Simulation results for a fermion wave packet with $\sigma_k = 0.5$ scattering off a real mass profile with wall width $L_w = 0.6$ in a lattice box of size $L = 28$. (a) Evolution of the particle number density over the lattice for $k_0 = 1.0$ and $a = 1/8$. (b) Particle number in the symmetric phase $\hat{\mathcal{Q}}_{t,+}$ as function of time at different lattice spacings. The vertical dotted line shows the time $t = 3T/4$. The yellow highlighted band in (a) and (b) shows the time window $(\Delta t)_{\mathcal{Q}}$ used for the asymptotic value $\hat{\mathcal{Q}}_{\infty,+}$. (c) Continuum limit extrapolations for $\hat{\mathcal{Q}}_{\infty,+}$ using linear fit for various values k_0. The measurement errors are too small to be visible on this scale. (d) Continuum limit of $\hat{\mathcal{Q}}_{\infty,+}$ as a function of k_0, compared with the analytic prediction (black line) $R_f(k_0)$ [Eq. (4.42)]. The result for $k_0 = 1$, corresponding to (a) and (b), is highlighted by a yellow circle.

packets propagate identically. We therefore only consider the particle wave packet. For the real mass profile in Eq. (4.29), we have an analytic computation of the reflection coefficient [Eq. (4.30)]. Therefore, this computation serves as an important benchmark for the validation and estimation of systematic uncertainties when we look at C-asymmetry generation with a complex mass in Sec. 4.2.6.

Figure 4.3 shows the results of the simulation for a total time of $T = L = 28$. In Fig. 4.3(a), we illustrate the time evolution of a particle wave packet prepared with $k_0 = 1.0, \sigma_k = 0.5$ at the lattice spacing $a = 1/8$, where the color gradient indicates the particle number density $\rho_{n,+}(t)$. The fermion wave packet moves toward the bubble wall with a constant velocity $v = 1$ until it hits the bubble wall at $t \sim L/4 = 7$. Part of the wave packet is reflected back into the symmetric phase, while the rest is transmitted across into the massive phase. Around $t \sim 3L/4 = 21$, the reflected wave packet hits the lattice boundary and reflects again. During this simulation, we measure the total charge in the symmetric phase $\hat{\mathcal{Q}}_{t,+}$ as a function of time t to keep track of the reflected wave packet.

In Fig. 4.3(b), we show the behavior of $\hat{\mathcal{Q}}_{t,+}$ for the same $k_0 = 1.0$ for various lattice spacings a. The initial value of $\hat{\mathcal{Q}}_{t,+} = 1$ is maintained until the wave packet hits the bubble wall. After the reflection is complete, $\hat{\mathcal{Q}}_{t,+}$ approaches an asymptotic value $\hat{\mathcal{Q}}_{\infty,+} < 1$. The yellow highlighted band marks the window of time $(\Delta t)_{\mathcal{Q}}$ that we use to obtain the asymptotic value $\hat{\mathcal{Q}}_{\infty,+}$. The variation in this time window is a measure of the finite-volume effects. We then take the measured value $\hat{\mathcal{Q}}_{\infty,+}$ as a function of a and extrapolate to $a \to 0$. Even though the asymptotic value of $\hat{\mathcal{Q}}_{t,+}$ does not depend on the boundary for the definition of $\hat{\mathcal{Q}}_{t,+}$—that is, the convention of w_n in Eq. (4.38)—we would like to point out that the dip structure of $\hat{\mathcal{Q}}_{t,+}$ near the scattering region in Fig. 4.3(b) does depend on it. If the boundary for $\hat{\mathcal{Q}}_{t,+}$ was pushed deep into the broken phase by setting $w_n = 1$ for $n < N_c + n_w$ and $w_n = 0$ for $n > N_c + n_w$, the result would be a monotonic decrease in $\hat{\mathcal{Q}}_{t,+}$ toward its asymptotic value as a function of t.

The continuum limit extrapolation for $\hat{\mathcal{Q}}_{\infty,+}$ is shown in Fig. 4.3(c) for k in the range of $[0.5, 2.5]$ in steps of 0.25. We find that a two-parameter linear fit (shown by a solid line) works well. The uncertainties from the variation of the observable in the time window are too small to be seen on this scale.

Finally, we show a comparison between the lattice simulations and the analytic predictions for $\hat{\mathcal{Q}}_{\infty,+}$ as a function of the wave packet momentum k_0 in Fig. 4.3(d). The continuum-extrapolated values of $\hat{\mathcal{Q}}_{\infty,+}$ are shown by filled squares. The continuum, infinite-volume, analytic prediction (shown by a solid line) is computed using $|R_+(k)|^2$ from Eq. (4.30) with the wave packet $f(k; k_0, \sigma_k, x_0)$ in Eq. (4.8) as

$$R_f(k_0) = \int_0^\infty dk \; |R_+(k) f(k; k_0, \sigma_k, x_0)|^2, \tag{4.42}$$

where we set $\sigma_k = 0.5$ for the incoming wave packet, and the above expression is independent of x_0. We observe a good agreement between the lattice and the analytic predictions. However, compared to the error bars from the continuum limit fits, which are too small to be visible on the plot, the deviation between the lattice and analytic results is much larger. We observe larger deviations with respect to the error bars for smaller k_0, which is expected from a consideration of scale separation. At a fixed $\sigma_k = 0.5$, the small momentum $k_0 \sim \sigma_k$ invalidates the scale separation of Eq. (4.35). This results in a shape distortion of the wave packet away from a Gaussian, since we do not allow negative k modes in the wave packet. Ideally, we could make σ_k smaller, but that would require a larger physical volume to fit a wider wave packet in position space. So, the disagreement at lower momentum is a systematic error from finite-volume effects.

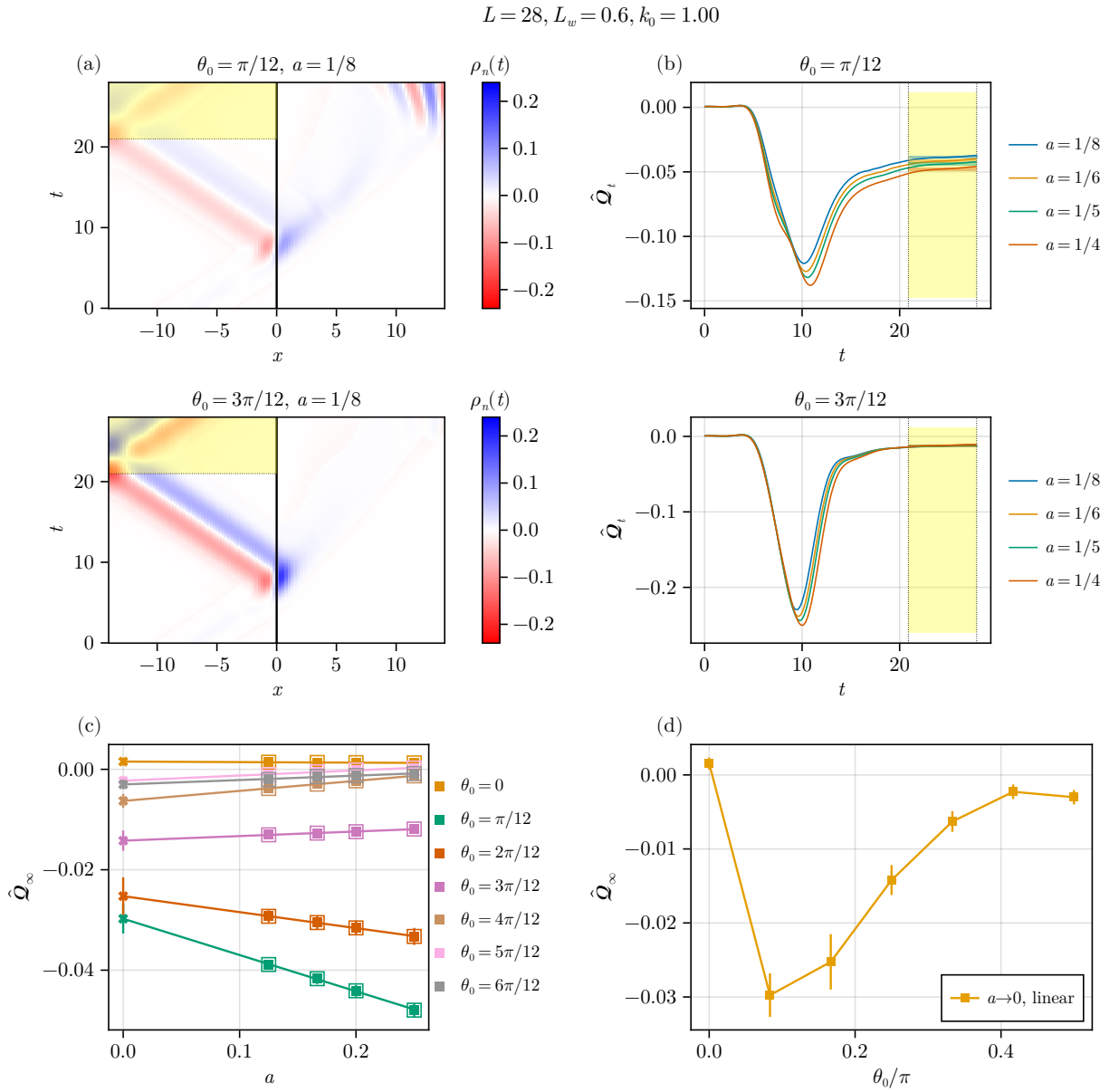


Figure 4.4: Magnitude asymmetry as a measure of C-asymmetry generated during fermion and antifermion scattering with a complex mass profile for fixed wave packet with $k_0 = 2\sigma_k = 1.0$ and physical volume of $L = 28$. For two parameters $\theta_0 = \pi/12, 3\pi/12$, (a) shows the net charge density in spacetime and (b) the evolution of the net charge density in the symmetric phase $\hat{\mathcal{Q}}_t$ at different lattice spacings a. The yellow band marks the time window $(\Delta t)_{\mathcal{Q}}$ used to measure the asymptotic value $\hat{\mathcal{Q}}_\infty$ and estimate the systematic uncertainties, as described in Sec. 4.2.4. (c) Continuum limit extrapolations for $\hat{\mathcal{Q}}_\infty$ using linear fit for various values of θ_0. The errors on the measurements are too small to be seen on this scale, and the 1σ errors from the fitting are shown for the extrapolated $a \to 0$ points. (d) Finally, $\hat{\mathcal{Q}}_\infty$ as function of θ_0. The error bars are 1σ uncertainties computed in $a \to 0$ fits of (c).

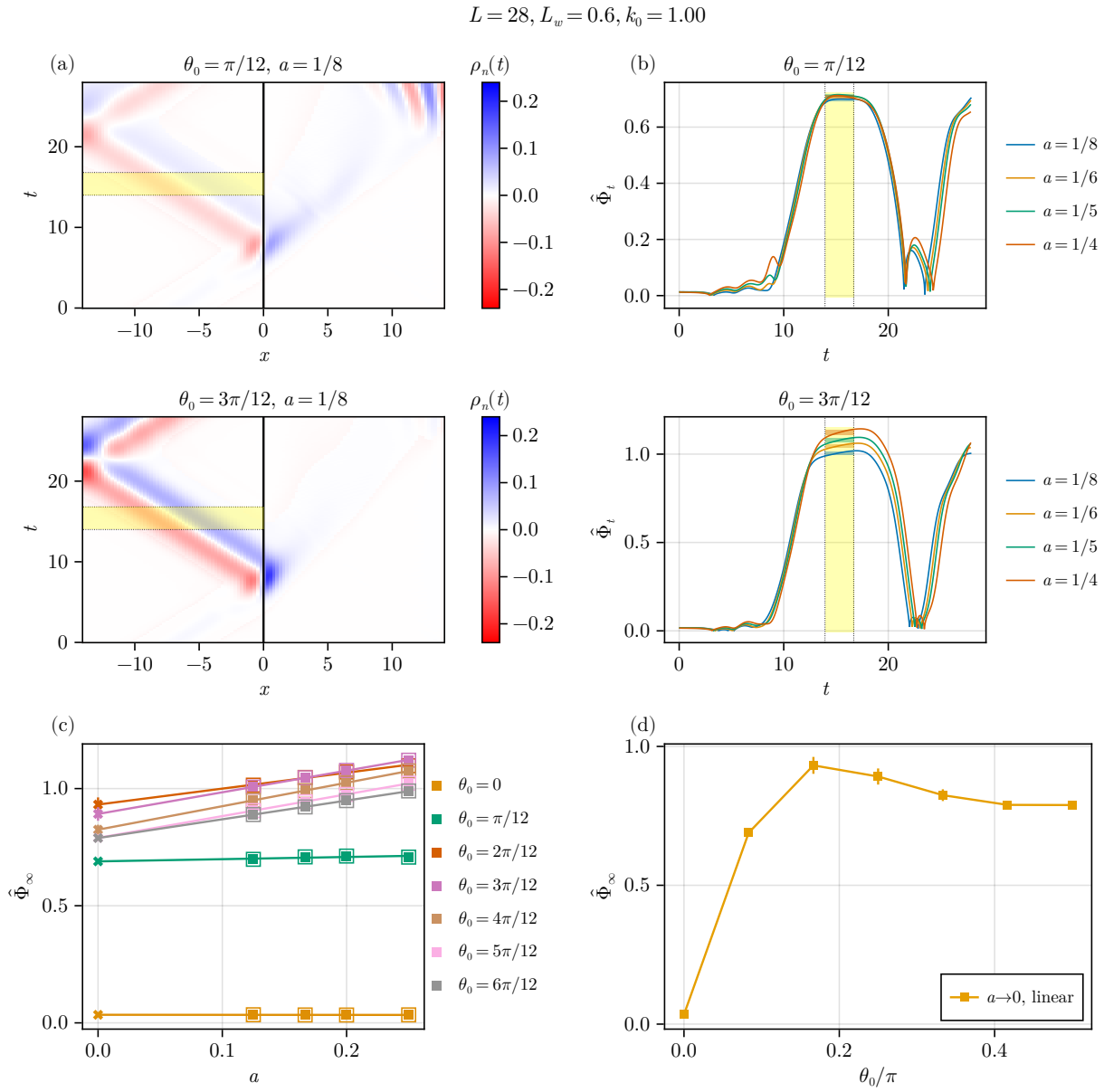


Figure 4.5: Phase asymmetry as a measure of C-asymmetry generated during fermion and antifermion scattering with a complex mass profile for fixed wave packet with $k_0 = 2\sigma_k = 1.0$ and physical volume of $L = 28$. For two parameters $\theta_0 = \pi/12, 3\pi/12$, (a) shows the net charge density in spacetime and (b) the evolution of the phase asymmetry in the symmetric phase $\hat{\Phi}_t$ at different lattice spacings a. The yellow band marks the time window $(\Delta t)_\Phi$ used to measure the asymptotic value $\hat{\Phi}_\infty$ and estimate the systematic uncertainties. (c) Continuum limit extrapolations for $\hat{\Phi}_\infty$ using linear fit for various values of θ_0. The errors from the measurements and the 1σ errors from the fitting are shown for the finite a points and the extrapolated $a \to 0$ point, respectively. (d) Finally, $\hat{\Phi}_\infty$ as function of θ_0. The error bars are the 1σ uncertainties computed in $a \to 0$ fits of (c).

4.2.6 Simulation results: complex mass ($\theta_0 \neq 0$)

Having validated our methods with an estimate of the expected uncertainties, we now proceed to the nontrivial case of a complex mass profile where a genuine C-asymmetry generation may be observed.

For studying the C-asymmetry, we independently simulate the particle and antiparticle scattering processes and combine the results. We can equivalently formulate our discussion in terms of the time evolution of a completely mixed state $\rho_0 = \sum_{\alpha=\pm} |f_\alpha\rangle \langle f_\alpha|$ of the C-conjugate pair of wave packet states $|f_\pm\rangle$. As this initial mixed state is symmetric under C, observables that are not invariant under C can be used to measure the generation of C-asymmetry in collision. However, for efficiency of the tensor network algorithms, we perform separate simulations for the C-conjugate pure states $|f_\pm\rangle$.

We would like to study the asymmetry generation for the mass profile Eq. (4.29) as a function of θ_0. For these simulations, we vary θ_0 in the range $[0, \pi/2]$ in steps of $\pi/12$. The wave packet parameters are fixed to $k_0 = 2\sigma_k = 1.0$. All other parameters are as before. We now describe the results for both the magnitude and phase-asymmetry observables.

Magnitude asymmetry

The results for the magnitude asymmetry are shown in Fig. 4.4. In Figs. 4.4(a) and 4.4(b), we focus on two values of θ_0 for illustration $\theta_0 = \pi/12, 3\pi/12$. In Fig. 4.4(a), we show the net local charge density,

$$\rho_n(t) \equiv \rho_{n,+}(t) + \rho_{n,-}(t), \tag{4.43}$$

for lattice spacing $a = 1/8$. For both θ_0s, the C-asymmetry can be clearly seen from the nonvanishing $\rho_n(t)$. In Fig. 4.4(b), we plot the time evolution of the magnitude-asymmetry observable $\hat{\mathcal{Q}}_t$ [Eq. (4.39)], measuring the net charge in the symmetric region, for various

lattice spacings a. The total charge in the symmetric region $\hat{\mathcal{Q}}_t$ is zero at $t = 0$, since the initial wave packet states are C conjugates of each other.[5] After an initial period of no change, the wave packet scatters from the bubble wall around $t \sim 7$, where we see a large dip in $\hat{\mathcal{Q}}_t$. Around $t \sim 21$, the reflected wave packet has minimal overlap with the bubble wall, and therefore $\hat{\mathcal{Q}}_t$ begins to saturate. The yellow band therefore marks the time window $(\Delta t)_{\mathcal{Q}}$ which we used to define the asymptotic value $\hat{\mathcal{Q}}_\infty$, as discussed previously.

Fig. 4.4(c) shows the continuum limit $a \to 0$ extrapolation of $\hat{\mathcal{Q}}_\infty$ for the entire range of θ_0. We find that a linear fit works well. The errors in the measurements are too small to be visible, but the error of the linear fit $a \to 0$ can be seen on the $a = 0$ axis. We observe that for $\theta_0 = 0$, the central value of $\hat{\mathcal{Q}}_\infty$, which is expected to be zero, is comparable to the systematic errors of the initial state preparation as we studied in Appendix C.4.1. Interestingly, we find that the lattice artifacts, and therefore the total systematic errors as shown in Fig. 4.4(d), are larger for intermediate θ_0 values.

Finally, we show the continuum-extrapolated magnitude asymmetry $\hat{\mathcal{Q}}_\infty$ as a function of θ_0 in Fig. 4.4(d). While these results establish $\hat{\mathcal{Q}}_\infty$ as an easily measurable observable quantifying the C-asymmetry generated during the fermion-bubble collision, they also demonstrate a clear limitation of this observable. At large θ_0, $\hat{\mathcal{Q}}_\infty$ is small simply because of the strong reflection but not because the asymmetry itself is small. Because both the particle and the antiparticle are completely reflected, the net reflected charge is almost zero. But the local charge density plot in Fig. 4.4(a) clearly shows a large asymmetry in the relative displacement of the particle and antiparticle wave packets even for the larger $\theta_0 = 3\pi/12$. This demonstrates that when the reflection coefficient approaches unity, $|R_\alpha(k_0)|^2 \approx 1$, magnitude asymmetry no longer serves as an effective measure of C-asymmetry. Consequently, we turn our attention to the phase asymmetry in $R_\alpha(k_0)$ in what follows.

5. The initial wave packet states are actually not exact C conjugates of each other in the presence of a complex mass due to a finite wave packet width, which introduces a small systematic error from the overlap of the initial wave packet with the bubble wall. We examine this in Appendix C.4.1.

Phase asymmetry

We now look at the phase-asymmetry observable $\hat{\Phi}_t$ defined in Eq. (4.40), with the results shown in Fig. 4.5. Figure 4.5(a) shows the same net local charge density $\rho_n(t)$ as previously shown in Fig. 4.4. However, the time window $(\Delta t)_\Phi$ over which $\hat{\Phi}_\infty$ is measured is different, shown as a yellow band in Fig. 4.5(a). The reason for this can be seen from Fig. 4.5(b), where we plot $\hat{\Phi}_t$ as a function of t for various lattice spacings a. Our definition of $\hat{\Phi}_\infty$ assumes a Gaussian wave packet, which is valid only when the reflected wave packet is sufficiently far from any boundaries. The presence of a plateau in Fig. 4.5(b) shows that the yellow band is a reasonable choice for $(\Delta t)_\Phi$. In the limit of $L/\sigma_x \to \infty$, Fig. 4.5(b) would be completely flat in this time window. Therefore, any variation in this window is a finite-volume effect.

In Fig. 4.5(c), we show the continuum limit extrapolation $a \to 0$ for $\hat{\Phi}_\infty$ for various θ_0. Again, we find that a linear extrapolation works well. The dependence of phase asymmetry $\hat{\Phi}_\infty$ (in the $a \to 0$ limit) on the parameter θ_0 is shown in Fig. 4.5(d). At $\theta_0 = 0$, we observe a small nonvanishing $\hat{\Phi}_\infty$ which is again comparable to the systematic errors in $\hat{\Phi}_\infty$ from initial state preparation, as discussed in Appendix C.4.1. For large θ_0, the phase-asymmetry observable reveals a significant C-asymmetry, which could not be detected by the magnitude-asymmetry observable.

The behavior of the instantaneous charge asymmetry in Fig. 4.5(a), shown by the nonvanishing $\rho_n(t)$, in real time near the wall, merits particular attention. In EWBG, $SU(2)$ sphalerons active in the symmetric phase can convert the analogous CP asymmetry in 3+1 dimensions to baryon asymmetry. As the bubble expands, the baryon asymmetry generated near the wall penetrates into the broken phase, where it remains preserved when electroweak sphalerons become inactive for a sufficiently strong phase transition. This suggests that the instantaneous CP asymmetry generated at the collision point near the wall may play a crucial role in explaining the observed baryon asymmetry of the Universe, necessitating careful consideration in future nonperturbative studies.

4.3 Discussion and outlooks

Motivated by the goal of a fully nonperturbative quantum simulation of baryon-number asymmetry generation during EWBG, we initiated the study of C-asymmetry generation during fermion-bubble collisions in 1+1 dimensions. Although quantum technologies evolve and a full-scale simulation of EWBG remains beyond immediate reach, tensor network methods provide an extremely useful way to prototype future quantum simulations in lower dimensions.

In this first study, we explored a toy model consisting of free fermions moving in the rest frame of a bubble wall modeled as a complex mass profile. The particle and antiparticle wave packets reflect off the bubble wall differently, which is the source of the C-asymmetry generated on the symmetric side. Emphasizing the need to carefully design real-time observables that can capture the C-asymmetry, we proposed two observables constructed from local charge densities of the final states. The first is the magnitude asymmetry, which measures the total net charge in the symmetric phase after scattering, and the second is the phase asymmetry, which measures the relative spatial displacement between particle and antiparticle wave packets. In regimes of strong reflection, which occur at large C-violating phase θ_0, the simplest observable, the magnitude asymmetry, is too small, comparable to systematic errors, thereby creating a signal-to-noise ratio problem. We observe a strong asymmetry in the relative displacement of the wave packets in real time, which can be successfully captured by the phase-asymmetry observable. This observable does not suffer from the signal-to-noise problem afflicting the magnitude asymmetry, although it does require a careful choice of measurement time window due to strong boundary effects.

While this work employs classical tensor network simulations exclusively, a natural extension would be quantum simulations on actual hardware. This would necessitate wave packet state preparation, time evolution, and measurement of asymmetry observables. Quantum simulation of fermionic wave packet scattering is, fortunately, an active research area [163–

166, 190–194]. These methods apply directly to our scenario although hardware limitations prevent C-asymmetry studies on quantum hardware from being quantitative, restricting us to tensor networks in 1+1d for the present work. Ultimately, realistic simulations in higher dimensions would require large-scale quantum simulations.

Beyond applications to early-Universe dynamics, our methods for computing phase asymmetry could be broadly relevant for nonperturbative computations of scattering amplitudes in quantum field theories, as an alternative to the Lüscher method [195] used in lattice quantum chromodynamics. Exploring such applications in the context of two-particle scattering on quantum computers remains an important direction. Our phase-asymmetry observable is closely related to the time-delay measurement of Ref. [196], though their approach differs fundamentally from ours.

We have shown that lattice methods can compute a *quantitative* measure of C-asymmetry generation in a 1+1-dimensional toy model of baryogenesis, demonstrating how real-time simulations can quantitatively probe nonequilibrium phenomena. We focus on a phenomenologically relevant measure of C-asymmetry often computed using traditional analytic methods without systematically improvable uncertainties. Real-time lattice simulations instead supplement them by computing such observables in a controlled manner. We emphasize that although we compute the asymmetry away from the bubble walls, where reflection coefficients are well defined, the methods are also applicable for computing the asymmetry closer to the bubble wall, which could in fact be the relevant quantity for precise estimates of baryon asymmetry in the broken phase.

There is no in-principle obstruction to also including thermal effects within the simulation itself, which would complement the analytic approaches which use diffusion equations. In the context of early-Universe dynamics, Refs. [173, 174] studied the scattering of dynamical bubble walls (without fermions) using tensor networks. Combining their techniques with ours provides a natural pathway to study asymmetry generation in the presence of dynamical

bubble walls. Including sphaleron processes is an important step toward a more complete model for baryogenesis. The minimal change to our model which would allow this would be the addition of a $U(1)$ gauge field and a complex scalar field, resulting in the 1+1d Abelian Higgs model coupled to dynamical fermions [197]. Our work serves as a starting point for investigating ingredients such as sphalerons converting chiral asymmetry to baryon-number asymmetry, dynamical bubble walls, thermal effects, and particle transport, preparing us for a fully nonperturbative *ab initio* simulation of baryogenesis.

CHAPTER 5

POST-SPHALERON BARYOGENESIS AND DETECTION

As reviewed in Chapter 1, post-sphaleron baryogenesis provides a mechanism for generating the baryon asymmetry below the electroweak scale through baryon-number-violating (BNV) interactions beyond the Standard Model. Such interactions are often assumed to arise only at or above the grand unification scale, largely due to the null results from experimental searches for proton decay, which render them inaccessible to direct collider probes. However, it has been recognized by Steven Weinberg in 1980 that certain patterns of baryon and lepton number violation can parametrically suppress proton decay rates by multiple powers of the heavy resonance masses [198]. This opens the possibility that current bounds on the proton lifetime remain compatible with BNV physics at significantly lower energy scales. Models of post-sphaleron baryogenesis based on such low-scale BNV interactions are therefore of considerable phenomenological interest, as they may be testable at the LHC and future collider experiments.

In this chapter, we construct a model featuring baryon number violation by one unit and lepton number violation by three units, and demonstrate that, despite stringent proton decay constraints, the masses of the new states can lie at the TeV scale. We then develop a baryogenesis scenario in which this framework provides the required source of baryon number violation. Finally, we propose dedicated search strategies for this model at the LHC and the HL-LHC. This study is based on our recent work [51].

5.1 Baryon and lepton number violation at low energy scale

The conservation of baryon (B) and lepton (L) number in the observed interactions of elementary particles is an established experimental fact. From a theoretical point of view, however, this raises many questions as there are no fundamental principles at play behind

the existence of either of these global symmetries. Moreover, there are many reasons to consider them to be accidental effects, valid only up to the roughly 10 TeV energy scale that has been directly accessed so far in experiments. For example, it is predicted that global symmetries are explicitly broken by quantum gravitational effects [199–201]. The validity of this argument in the absence of an experimentally verified quantum theory of gravity is an open question. Yet, based on robust theoretical foundations and experimental observations, there are compelling arguments in favour of a more complete theory of nature with additional elementary particles whose interactions violate either *or both* B and L. Namely, baryon number violation is one of three necessary conditions for realizing *baryogenesis* [10], and lepton number violation is common in mechanisms that generate neutrino masses, which are necessary to explain the observed flavour oscillations in the neutrino sector [202–204].

The most distinctive prediction of most theories with Baryon Number Violation (BNV) is, of course, that the proton — or a bound neutron — should decay. This is the subject of a rich experimental program, with modes such as $p \to \pi_0\, e^+/\mu^+$ and $p \to K^+\overline{\nu}$ having been extensively searched for and, so far, not observed [45–49]. A variety of more exotic nucleon decay modes have also been considered — see [205] for a summary — but, even in these channels, experiments have yet to identify conclusive evidence for BNV. These null results put stringent constraints on the masses of new particles that violate B and L, potentially pushing them to values above 10^{15} GeV, a characteristic scale of Grand Unified Theories (GUTs) [206–208].

In light of this, one might be tempted to associate any BNV interaction with very high energy scales, inaccessible to even the most optimistic of future collider experiments. There is, however, one caveat to these conclusions: GUT theories typically violate B and L by one unit each, keeping the difference, $B - L$, as a conserved quantity. This in turn induces low energy BNV operators at dimension six. Given a measured proton lifetime of τ_P years, one

can argue by naive dimensional analysis that the scale associated with BNV is roughly

$$M_{\text{BNV}} \sim \left(5000 \times \frac{\tau_P}{10^{32}\ \text{yrs}}\right)^{\frac{1}{4}} \times 10^{15}\ \text{GeV},$$

where we take the proton mass to be 1 GeV for simplicity and neglect phase space factors.

It has, however, been shown that if instead of $B - L$, the underlying theory of nature[1] conserves a more general linear combination $B + aL$, a $\in \mathbb{Q}$, the BNV effective operator is generated at a dimension higher than six [198, 209]. This causes a suppression of proton-decay-inducing operators by multiple powers of M_{BNV}. In fact, for such a low energy effective operator of dimension $d > 6$ and a corresponding proton lifetime τ_P,

$$M_{\text{BNV}} \sim \left(5000 \times \frac{\tau_P}{10^{32}\ \text{yrs}}\right)^{\frac{1}{4}} \times \left(10^{15}\right)^{\frac{4}{2d-8}}\ \text{GeV},$$

once again neglecting phase space factors and taking the proton mass to be 1 GeV. From this estimate, for sufficiently high d, the mass scale of new particles involved in BNV interactions can lie significantly below the GUT scale. As an example, $d = 11$ sets $M_{\text{BNV}} \approx 10$ TeV, within reach of current or near-term future collider experiments such as the Large Hadron Collider (LHC) and its upcoming High Luminosity (HL) upgrade.

For such theories, where M_{BNV} is low enough to lie within the reach of the LHC or other near-term future colliders, the new resonances responsible for the BNV interactions can be physically produced, and the ultraviolet (UV) complete model can be directly probed. As we will demonstrate in the following with a specific model, the collider probe can be even more powerful than the experiments that probe proton decay directly, if the proton decay rate predicted from the model is beyond the reach of even upcoming experiments like Hyper-Kamiokande (Hyper-K) [210]. Complementary to the collider search, the new particles

1. Perhaps, more accurately, an intermediate version of it valid for energies above the electroweak scale but below that of Grand Unification.

in the UV complete model can also be probed by low energy precision experiments, as they will generally have B and L conserving couplings to the known elementary particles of nature.

Such experiments include searching for flavour violation in the quark and leptonic sectors, measuring rates of rare meson decays, and measuring the anomalous magnetic moments of leptons. The results to date from these experiments have yielded very stringent constraints on the parameter space of the UV model, which must be taken into account when analyzing the collider search for the new particles.

In this chapter, we will illustrate the points made above using a theory that violates B and L by one and three units, respectively, but conserves $B - L/3$,[2] or

$$\Delta B = \frac{1}{3}\Delta L = -1.$$

In this scenario the proton is predicted to decay into three anti-leptons,

$$p \to e^+/\mu^+\overline{\nu\nu},$$

a process for which the Super-Kamiokande (Super-K) experiment has searched. No evidence of this decay was found, setting a lower limit on the proton lifetime of $\tau_P > 1.7 \times 10^{32}$ years if the charged anti-lepton is a positron and $\tau_P > 2.2 \times 10^{32}$ years if it is an anti-muon [211]. We find that the proton decay rate for this model implies a bound of roughly $M_{\rm BNV} > 1$ TeV, opening up the possibility of studying this model at the LHC. Our study shares many similarities with the analysis of [212].

Relevant to the theme of this thesis, the model being considered can provide a natural explanation of the baryon asymmetry of the universe, in a mechanism similar to the post-sphaleron baryogenesis developed in [50, 213]. A novel feature of this mechanism is that it

2. The conserved $B - L/3$ global symmetry is anomalous, but since we make no attempt to gauge it, this poses no serious implications for the model itself.

Particle	SU(3)	$\mathbf{SU(2)_L}$	$\mathbf{U(1)_Y}$	$\mathbf{U(1)_B}$	$\mathbf{U(1)_L}$
χ_{uu}	**3**	**1**	$-\frac{4}{3}$	$-\frac{2}{3}$	0
χ_{LQ}	**3**	**1**	$-\frac{1}{3}$	$\frac{1}{3}$	$+1$
χ_{LL}	**1**	**1**	$+1$	0	-2

Table 5.1: Quantum Numbers of the three new scalars of the $B - L/3$ conserving model considered in this work.

utilizes the new high-dimensional BNV interaction for the baryon number generation, instead of the electroweak sphaleron that is known to be the only BNV source in the Standard Model and is commonly used in baryogenesis mechanisms. To avoid the generated baryon asymmetry being washed out by electroweak sphalerons, we choose an appropriate mass scale for the participating particles such that the baryogenesis is only effective when the electroweak sphalerons have become inactive. This can be easily achieved thanks to the suppression from the high dimensionality of the BNV interaction. The baryogenesis process also has to violate CP symmetry according to the Sakharov's conditions [10], which can be induced purely from the CP violations in the quark and leptonic sectors of the Standard Model, and hence can be directly constrained by future neutrino precision measurements.

5.2 Model and effective operators

We add three new scalar fields to the Standard Model (SM). The first is a diquark, χ_{uu}, that couples two quarks and arises in the context of Grand Unification models based on the E_6 [214] or Pati-Salam [207, 215] gauge groups. In our theory, it couples two right handed up-type quarks of different generations,

$$\mathcal{L}_{uu} = y_{uu}^{ij} \epsilon^{c_1 c_2 c_3} \overline{u}^c_{ic_1} P_R u_{jc_3} \chi_{uuc_2} + \text{h.c.} \tag{5.1}$$

In the equation above i and j label quark flavours, $i \neq j$ due to fermionic statistics, and the c indices label QCD color. The second particle we add is a leptoquark, χ_{LQ}, also common in

many GUT theories — particularly the ones based on $SU(5)$ [216] or $SO(10)$ [217]. These theories predict many different types of leptoquarks, but we will only employ one and couple it to a left-handed quark and a left-handed lepton,

$$\mathcal{L}_{LQ} = y_{LQ}^{ij*}\epsilon^{\alpha\beta}\ \overline{Q}^{c}_{\alpha i c_1}\chi^{\dagger c_1}_{LQ}L_{\beta j} + \text{ h.c.} \tag{5.2}$$

$$= y_{LQ}^{ij*}\ \overline{u}^{c}_{i c_1}P_L l_j \chi^{\dagger c_1}_{LQ} - y_{LQ}^{ij*}\ \overline{d}^{c}_{i c_1}P_L \nu_j \chi^{\dagger c_1}_{LQ} + \text{ h.c,} \tag{5.3}$$

where Q, L are the SM left-handed $SU(2)_L$ quark and lepton doublets correspondingly, and α, β are the weak isospin indices. Finally, we add a Zee-Babu [218, 219] singly charged dilepton singlet, χ_{LL}, coupling two left handed leptons of different generations (once again due to fermion statistics),

$$\mathcal{L}_{LL} = y_{LL}^{ij}\ \epsilon^{\alpha\beta}\overline{L}^{c}_{\alpha i}\chi_{LL}L_{\beta j} + \text{ h.c.} \tag{5.4}$$

$$= y_{LL}^{ij}\ \overline{\nu}^{c}_{i}P_L l_j \chi_{LL} - y_{LL}^{ij}\ \overline{l}^{c}_{i}P_L \nu_j \chi_{LL} + \text{ h.c.} \tag{5.5}$$

This naturally brings up the question of neutrino masses, which can be achieved in exactly the same manner as the Zee-Babu mechanism, i.e., by introducing either a doubly charged scalar or a second Higgs doublet to our model — we leave this for a dedicated future study. In general, the Yukawa couplings in Equations (5.1)–(5.4) can be complex numbers, which may lead to interesting CP violation phenomena. We will focus on real Yukawa couplings in the mass basis for this work.

Since these Yukawa interactions represent a *hard* breaking of B and L, we must assign quantum numbers to the new scalars such that both global symmetries are conserved, as listed in Table 5.1.

So far, nothing about this model is different from other works that have studied these scalars individually [218–223], aside from assigning them the correct quantum numbers to enforce B and L conservation. Therefore, these *cannot* induce BNV interactions, even at loop

level. To achieve BNV, we introduce the *only* baryon and lepton number violating interaction of this model, one that occurs in the scalar sector:

$$\mathcal{L}_{\rm BNV} = \Lambda_{\rm BNV}\ \chi^\dagger_{LQ}\chi_{uu}\chi_{LL} + \text{ h.c.} \tag{5.6}$$

This trilinear interaction breaks B and L softly but conserves $B - L/3$. It is worthwhile to take a brief detour from our presentation of this model and speculate a little on the origins of this term. A motivating possibility, from the point of view of baryogenesis that we will discuss later, is that it arises from the interaction of the three χs with a complex SM singlet scalar field Φ that acquires a vacuum expectation value (VEV),

$$\lambda \langle\Phi\rangle\, \chi^\dagger_{LQ}\chi_{uu}\chi_{LL} \to \Lambda_{\rm BNV}\, \chi^\dagger_{LQ}\chi_{uu}\chi_{LL},$$

where λ is a dimensionless coupling constant. Since Φ is a complex scalar field, it is always possible to rotate away the B and L violation in this interaction if the latter is not fixed by any other interaction. The theory then violates B and L spontaneously after Φ acquires a vacuum expectation value, while still preserving $B - L/3$. This, of course, implies the existence of a massless Goldstone boson that could, for example, add an extra source of radiation which over-closes the universe. To remedy this situation, we can make the global symmetry associated with Φ only approximate, for example by adding a cubic interaction term of the form $(\Phi^*\Phi)\Phi$ to the Lagrangian. Then, one can use the phase rotation to fix either the cubic self-interactions of Φ or its interactions with the χs, but not *both*. For example, using the phase rotation to make the quartic interaction with the χs baryon number conserving effectively assigns to Φ a baryon and a lepton number that is then softly broken by its cubic self-interactions. Spontaneous symmetry breaking then results in the appearance of a pseudo-Goldstone boson carrying both B and L with interactions with the SM that are potentially weak enough to make it a dark matter candidate. We leave a dedicated study of

these interesting cosmological scenarios to future work.

We close this presentation of our model by mentioning the low energy effective operators that can be derived from these interactions and are important phenomenologically. Of special interest is the one responsible for BNV, which appears at dimension nine,

$$\mathcal{O}_9^{\rm BNV} = \frac{c_9}{M_{\rm BNV}^5}\overline{Q}^c_{i\beta}L_{j\alpha}\overline{u}^c_k P_R u_l \overline{L}^c_{m\gamma}L_{n\delta}\epsilon^{\alpha\beta}\epsilon^{\gamma\delta}, \tag{5.7}$$

where

$$M_{\rm BNV}^5 = \frac{\left(m_{\chi_{LQ}} m_{\chi_{uu}} m_{\chi_{LL}}\right)^2}{\Lambda_{\rm BNV}} \quad \text{and} \quad c_9 = y^{ij}_{LQ} y^{kl}_{uu} y^{mn}_{LL} \tag{5.8}$$

is the Wilson coefficient, i, j, k, l, m, n and $\alpha, \beta, \gamma, \delta$ are the flavour and $SU(2)$ indices respectively, and we have suppressed colour labels for clarity. Since the two right handed up-type quarks resulting from integrating out the diquark have to be of different generations, at least one of them has to be either a charm or a top quark, which kinematically forbids proton decay at tree level but allows it at one-loop through flavour violation in charged current interactions, as discussed in Appendix D.1.

5.3 Baryogenesis model

Baryogenesis within our BNV model can be realized through a mechanism similar to the post-sphaleron baryogenesis mechanism developed in [50, 213]. Here we consider the scenario where $\Lambda_{\rm BNV}$ is set by the vacuum expectation value of a complex scalar field Φ as discussed in Sec. 5.2. After the spontaneous symmetry breaking of B and L, the real part of Φ — denoted as Φ_r — acquires a mass m_{Φ_r} which can be $\mathcal{O}(100)\,\text{GeV}$. The decay of Φ_r can generate baryon asymmetry if the Sakharov's conditions are satisfied:

1. Baryon number violation

2. Out of thermal equilibrium

3. C, CP violation

The first condition is apparently satisfied since the only decay channel of Φ_r to the SM fermions is mediated by the BNV operator of our model as shown in Fig. 5.1. The second and third conditions can also be naturally satisfied as discussed below.

The out-of-thermal-equilibrium condition involves comparing the decay rate of Φ_r to the expansion rate of the universe H. At a temperature below m_{Φ_r}, the six-body decay rate for $\Phi_r \to 3L + Q + 2u_R$ mediated by the new scalar fields is independent of the temperature and is estimated to be [224]:

$$\begin{aligned}\Gamma_r =& \Gamma(\Phi_r \to 6f) + \Gamma(\Phi_r \to 6\bar{f}) \\ \simeq& \frac{c_{ps}^4}{3^6}\left(\frac{1}{8\pi}\right)^9 \frac{N_c}{2S}\left(\frac{m_{\Phi_r}^{13}}{m_{\chi_{LL}}^4 m_{\chi_{LQ}}^4 m_{\chi_{uu}}^4}\right) \\ & \cdot |\lambda|^2 \,\mathrm{Tr}(y_{LL}^\dagger y_{LL})\,\mathrm{Tr}(y_{LQ}^\dagger y_{LQ})\,\mathrm{Tr}(y_{uu}^\dagger y_{uu}),\end{aligned} \tag{5.9}$$

where c_{ps} is a scale factor for the phase space integral estimation and is taken to be 0.8, $N_c = 6$ is the color factor, and $S = 1$ is the phase space symmetry factor for the decay process being considered. λ is a dimensionless coupling constant that couples Φ to the three χ fields. For the following estimations, we set $\lambda = 1$, and the scalar masses to be $m_{\chi_{uu}} = 3.5$ TeV, $m_{\chi_{LQ}} = m_{\chi_{LL}} = 1.5$ TeV, which are compatible with the proton decay bounds. The Yukawa couplings are set to be the following values that saturate the baryon number conserving

bounds (see detailed discussion of the existing experimental constraints in Appendix. D.1.):

$$y_{uu} = \begin{pmatrix} 0 & 0.25 & 0.12 \\ -0.25 & 0 & 0.12 \\ -0.12 & -0.12 & 0 \end{pmatrix}, \quad y_{LL} = \begin{pmatrix} 0 & 0.125 & 10^{-3} \\ -0.125 & 0 & 0.325 \\ -10^{-3} & -0.325 & 0 \end{pmatrix},$$
$$y_{LQ} = \begin{pmatrix} 0.397 & 0 & 0 \\ 0 & 0.949 & 0 \\ 0 & 1 & 1 \end{pmatrix}. \tag{5.10}$$

We adopt the parameterization $\Phi = \langle\Phi\rangle + (\Phi_r + iG)/\sqrt{2}$ so that the factor 2 from summing over the CP-conjugate processes is compensated by the extra factor from $1/\sqrt{2}$. For $m_{\Phi_r} \sim \mathcal{O}(100)\,\text{GeV}$ and $m_\chi \sim \mathcal{O}(\text{TeV})$, Γ_r is much lower than the Hubble rate $H(T) = 1.66 g_*^{1/2} T^2/M_{Pl}$ at the temperature $T = m_{\Phi_r}$. Hence, the decay of Φ_r is negligible until the temperature drops to T_d at which $\Gamma_r = H(T_d)$. When it finally starts to decay at around T_d, Φ_r is already far out of equilibrium, satisfying the out-of-equilibrium condition of baryogenesis. We find that for $m_{\Phi_r} < 1\,\text{TeV}$, $T_d \lesssim 3.4\,\text{GeV}$ is well below the electroweak scale $T_{\text{EW}} \approx 100\,\text{GeV}$, hence the electroweak sphalerons have been deactivated at the time of Φ_r decay and would not wash out the generated baryon asymmetry. Requiring the decay to occur prior to the QCD phase transition: $T_d > \Lambda_{\text{QCD}} \approx 200\,\text{MeV}$, m_{Φ_r} is constrained above a lower bound at $m_{\Phi_r}^{\min} \approx 647\,\text{GeV}$. The out-of-equilibrium decay of Φ_r would produce entropy that would dilute the baryon asymmetry. The dilution factor is given by $\eta \approx [1 + m_{\Phi_r}/(g_* T_d)]^{-1}$ [225], which varies in the range of $0.03 \lesssim \eta \lesssim 0.26$ for $m_{\Phi_r}^{\min} < m_{\Phi_r} < 1\,\text{TeV}$.

CP violation can be induced from the interference of the tree and one-loop-level diagrams shown in Fig. 5.1. In this work, we only consider the interference of the tree-level diagram with the W-loop correction to the χ_{LQ} vertex as shown in the middle panel of Fig. 5.1, which has an appealing feature of depending solely on the CP violations in the quark and

lepton sectors of the Standard Model[34]. The χ_{LL}–exchange diagram shown in the right panel of Fig. 5.1 is also a possible CP violation source if considering complex Yukawa couplings, while it does not contribute with the real Yukawa couplings considered in this work. The CP asymmetry quantified by the ratio of the difference in the decay rates of the CP conjugate processes to the sum of them is found to be:

$$\begin{aligned}\epsilon_{\rm CP} &\equiv \frac{\Gamma(\Phi_r \to 6f) - \Gamma(\Phi_r^* \to 6\bar{f})}{\Gamma(\Phi_r \to 6f) + \Gamma(\Phi_r^* \to 6\bar{f})} \\ &\simeq \frac{g_W^2}{4\pi {\rm Tr}[y_{LQ}^\dagger y_{LQ}]} \left(\frac{m_t^2}{\langle s \rangle - m_t^2} + \frac{m_t^2}{\langle s \rangle} \right) \log\left(1 + \frac{\langle s \rangle - m_t^2}{m_W^2} \right) {\rm Im}[y_{LQ}^\dagger U^T y_{LQ} V]_{33} \,, \quad (5.11)\end{aligned}$$

where $\langle s \rangle$ is the thermal average of the squared total energy of $L_{\gamma k}$ and $Q_{\delta l}$ in their center-of-mass frame, which can be estimated as $\langle s \rangle \approx (2 \cdot m_{\Phi_r}/6)^2 = m_{\Phi_r}^2/9$. $U \equiv V_L^l V_L^{\nu\dagger}$ is the PMNS matrix of the lepton sector [226–228], and $V \equiv V_L^u V_L^{d\dagger}$ is the CKM matrix of the quark sector [229–231]. The V_L^f matrices are defined such that the mass matrix of the fermion of flavor f is diagonalized as $M_{\rm diag}^f = V_L^f Y^f V_R^{f\dagger}(v/\sqrt{2})$. Note that in the kinematic calculation leading to Eq. (5.11), we ignore the masses of all the fermions except for the top quark. In this limit, the total contribution from the channels involving only the light fermions vanishes when summing over the flavor and $SU(2)_L$ indices of the intermediate and final states. The only nonvanishing contribution comes from the channels involving a top quark. We note that the massless limit is only taken for the evaluations of the phase space integrals, since the PMNS and CKM matrices are not well-defined in this limit. Including the fermion masses only introduces a small correction of $\mathcal{O}(m_f^2/m_t^2)$ to the kinematic factor.

The PMNS matrix remains loosely constrained, so are the CP asymmetry and the baryon

3. There is another possible W-loop correction to the χ_{LL} vertex, which, however, has real coupling factor in the interference term due to the antisymmetric structure of y_{LL}. Hence it does not contribute to CP asymmetry.

4. The W-loop correction on the wavefunctions of the outgoing particles would also contribute to CP asymmetry. This contribution, however, was found to be subdominant to the vertex correction [50, 213], and thus is not considered in the present work.

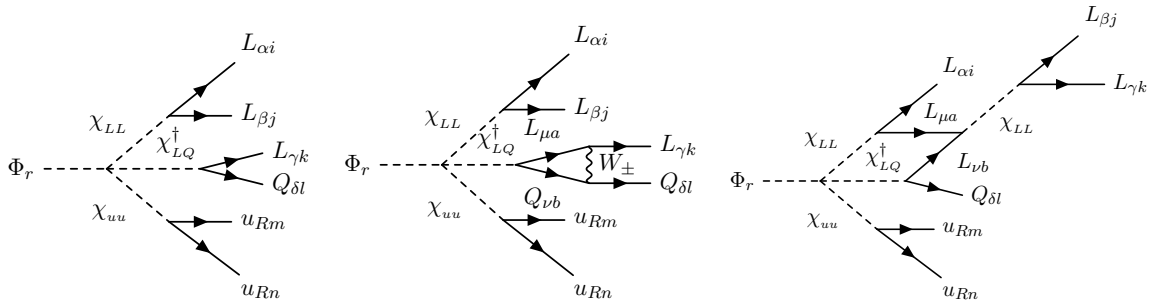


Figure 5.1: Tree and one-loop diagrams of Φ_r decay that would interfere and violate CP symmetry. We use $i, j, k, ...$ for the flavour indices, and $\alpha, \beta, \gamma, ...$ for the $SU(2)_L$ indices.

asymmetry $\eta_B \sim \epsilon_{CP} \cdot \eta$ generated from the presented mechanism. Hence the observed baryon asymmetry $\eta_B^{\text{obs}} \sim 10^{-10}$ can be accommodated in a large parameter space of our model at present, and will be directly constrained by the future neutrino precision measurements.

5.4 Baryon Number Violation at the LHC and HL-LHC

The fact that the new particles introduced by our model can be as light as $\mathcal{O}$(TeV) raises the interesting possibility that our model can be probed at the LHC and, subsequently, HL-LHC. LHC searches for BNV, particularly in the top sector [232], have been conducted in the past — see, for example, [233]. However, we have not been able to identify a previous search with signatures that are optimized to our model, due in part to its specificity. We therefore propose a dedicated search that offers the opportunity to test it both with current data at the LHC and at the upcoming HL-LHC.

Our proposal is based, at the parton level, on the Feynman diagram shown in Figure (5.2). The diquark is produced on-shell via the annihilation process $uc \to \chi^\dagger_{uu}$ and decays to the leptoquark $\chi^\dagger_{LQ}$ and the dilepton singlet χ_{LL}. These in turn decay to an anti-top quark and an anti-muon $\bar{t}\mu^+$, and an anti-muon and an anti-neutrino $\mu^+\bar{\nu}_\tau$:

$$uc \to \chi^\dagger_{uu} \to \chi^\dagger_{LQ}\chi_{LL} \to \bar{t}\mu^+\mu^+\bar{\nu}_\tau. \tag{5.12}$$

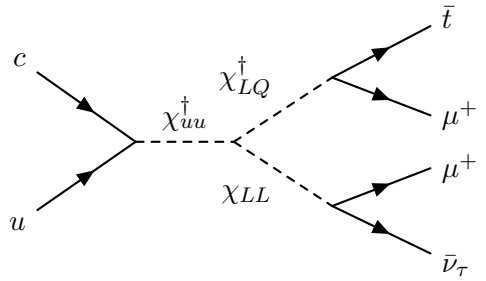


Figure 5.2: Parton level description of the distinctive hadron collider signature we propose for our model. An up and a charm quark from the protons annihilate to produce a diquark, a process which benefits from an s channel enhancement. It then decays to a leptoquark and a dilepton singlet. These in turn decay to an anti-top quark and an anti-muon, and an anti-muon and an anti-neutrino. The anti-top in the final state makes it possible to identify the charge — and hence baryon number of the outgoing particle and establish that baryon number violation by one unit, $\Delta\mathrm{B} = -1$, has occurred. However, due to the anti-neutrino in the final state, it is not possible to identify whether lepton number has bee violated by one, $\Delta\mathrm{L} = -1$, or three, $\Delta\mathrm{L} = -3$, units.

A similar process with two anti-τ leptons instead of two anti-muons is possible and, taking existing constraints into account, has a similar cross-section to the process we consider. The CP conjugate of these processes, while being potentially within reach of the LHC, are one order of magnitude suppressed compared to these ones due to the lower anti-quark content of the proton and will not be considered further. We also note in passing that even though the LHC is insensitive to neutrino flavours, due to existing constraints described in Appendix D.1, the dilepton singlet decay to $e^+\overline{\nu}_\mu$ or $\mu^+\overline{\nu}_e$ is more suppressed.

Having an anti-top quark in the final state makes it easier to reconstruct the baryon number of the final states and ascertain that BNV by one unit occurred, $\Delta B = -1$. Particle and charge identification of the anti-top quark requires leptonic decay of the associated W-boson. While leptonic decay adds another missing particle to the final state, the charged lepton and b-jet separation will be small since the anti-top quark should be boosted [234]. Full kinematic reconstruction of the anti-top quark is then not necessary, as only the particle and charge identification is needed to reconstruct the baryon number. If full reconstruction of the anti-top quark is necessary, then hadronic decay of the W-boson can be used at the

expense of reconstructing the baryon number of the final state. We leave the full details of the requirements of anti-top quark reconstruction for a proper experimental analysis of our model. On the other hand, due to the anti-neutrino in the final state, lepton number cannot be fully reconstructed and its violation is determined to be either $\Delta L = -1$ or $\Delta L = -3$. Interestingly, one can reconstruct the lepton number of the dilepton singlet from the

$$pp \to W^* \to e^- \mu^- \chi_{LL},\ \chi_{LL} \to \mu^+ \overline{\nu}_\tau,$$

process and its CP conjugate version by making use of the fact that the original W vertex must have zero lepton number. This can help identify the correct $\Delta L = -3$ violation for the BNV process, but, unfortunately, we find that existing constraints predict a cross-section for this process that is too small to yield a statistically significant number of events at the HL-LHC.

The signature we propose shares many similarities with previous same-sign dilepton searches performed by both the ATLAS [235] and CMS [236] experiments. While these same-sign dilepton searches could in principle probe our model, we expect that requiring the anti-top quark will make existing searches less efficient at probing the model parameter space, since the existing searches require only 2 or more jets without the use of top-tagging. We therefore suggest a dedicated search strategy, using existing same-sign dilepton searches as inspiration for kinematic cuts and background determination. We adopt the main sources of background events considered in these works, listed here:

1. Non-prompt leptons which can be suppressed by a large transverse momentum cut,

$\sigma \times$ **BR (pb)**	**Signal BP1**	**Signal BP2**	$t\bar{t}W$
Before cuts	8.3×10^{-4}	3.6×10^{-5}	2.7×10^{-3}
Basic cuts	5.5×10^{-4}	2.5×10^{-5}	5.2×10^{-6}

Table 5.2: Cut flow of the signal at each benchmark point (BP) and dominant SM background $t\bar{t}W$. The cuts applied are given in Eq. (5.13).

$p_T > 25$ GeV on each lepton in the di-lepton pair together with a rapidity cut $|\eta_\ell| < 2.5$.

2. The dominant SM process mimicking our signal is $pp \to t\bar{t}W^+$, with the top and W decaying to two anti-muons. This process comes with an additional b jet not present in our signal and can be further suppressed using a jet veto that we do not consider here.

3. Another process that can potentially contribute is $pp \to WZj, Z \to \mu^+\mu^-$ when the jet is misidentified as an anti-top quark and the outgoing muon is not detected and therefore considered as missing energy. We have found that, assuming a conservative jet and lepton misidentification[5] probability of 10% each, this background is sub-dominant.

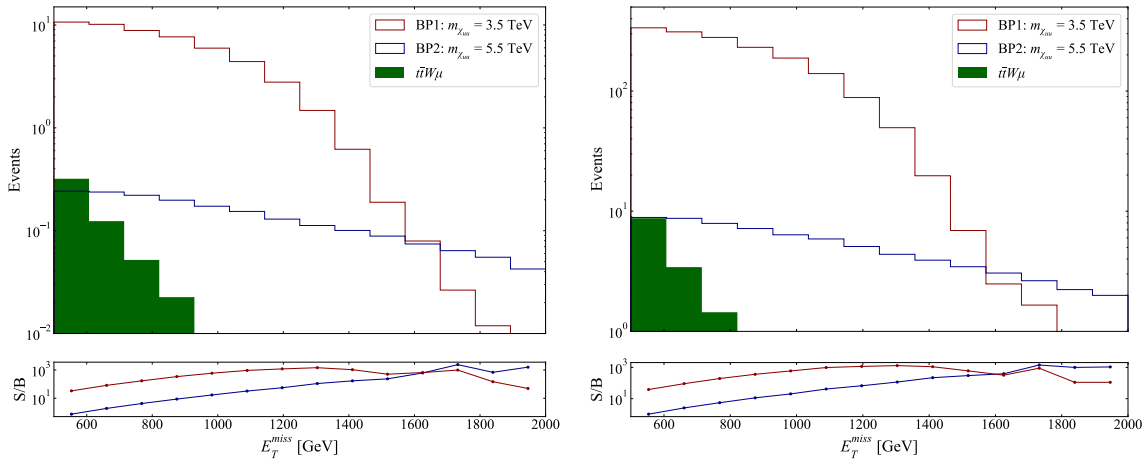
4. The most important cut in terms of background suppression is on the missing energy. We set $E_T^{\rm miss} > 500$ GeV, which is higher than that considered in [236]. Our choice of higher $E_T^{\rm miss}$ is motivated by the fact that the missing energy in our process is carried by a single outgoing anti-neutrino produced from the two-body decay of a TeV mass dilepton singlet and is therefore naturally peaked at very high energies compared to SM neutrinos. The latter are produced mainly from W boson decays and therefore peak at lower energies, making this $E_T^{\rm miss}$ cut particularly effective at suppressing SM backgrounds while not affecting signal events in a significant way.

We define the basic selection cuts as follows:

$$p_{T,\ell} > 25 \text{ GeV}, \ |\eta_{\ell,j,b,t}| < 2.5, \ E_T^{\rm miss} > 500 \text{ GeV}. \tag{5.13}$$

As an illustrative example, we consider two benchmark points, with diquark masses $m_{\chi_{uu}} = 3.5$ TeV (BP1) and $m_{\chi_{uu}} = 5.5$ TeV (BP2). The Yukawa couplings are chosen to be the values given in Eq. (5.10). We conventionally pick the upper triangular entries of the anti-symmetric matrices to be positive and set the scalar masses to be $m_{\chi_{LQ}} = m_{\chi_{LL}} = 1.5$ TeV and $\Lambda_{\rm BNV}$

5. More appropriately non-identification for the lepton.



(a) LHC Run 2: $\sqrt{s} = 13$ TeV, $\mathcal{L} = 139$ fb^{-1} (b) HL-LHC: $\sqrt{s} = 14$ TeV, $\mathcal{L} = 3000$ fb^{-1}

Figure 5.3: Missing transverse energy distributions for signal and background events for the current LHC and HL-LHC cases. The signal to background ratios for each bin are given in the subplots.

= 10 TeV. We simulate the process shown in Figure (5.2) using `MadGraph5_aMC@NLO` [237] for the LHC and for its HL upgrade. The cross sections for the signal at two benchmark points, at $\sqrt{s} = 14$ TeV as well as the main background before and after our chosen cuts are shown in Table 5.2.

In Fig. 5.3 we show the resulting event distributions for the missing transverse energies in our chosen final states. We find that for $m_{\chi uu} \in [3.5 \text{ TeV}, 5.5 \text{ TeV}]$, the predicted number of signal events is significantly in excess of the background events coming mainly from $t\bar{t}W$, highlighting the potential of the LHC and HL-LHC to probe this region of parameter space. Therefore, an ideal target search for our model even using current LHC data is to look for an excess of missing transverse energy in the $\bar{t}\mu^+\mu^+$ final state. The reach of the HL-LHC in probing our model (green) is shown in Fig. 5.4 for our benchmark discussed previously, but varying the scalar diquark mass and Yukawa coupling to up quark and charm quark. We also show, on the same figure, existing dijet constraints (blue) and several contours for the proton lifetime that are all well above 10^{35} years, to illustrate that to probe our model, proton decay experiments are sub-optimal compared to collider experiments.

5.5 Summary

In this chapter, we introduce a model for baryon number violation by one unit and lepton number violation by three units that adds three new scalars, a diquark, a leptoquark, and a dilepton singlet, to the SM. We show that limits from proton decay fix the masses of these new scalars to be $\mathcal{O}$(TeV), which opens opportunities to probe this model using both low energy precision and collider experiments. On this note, we propose a dedicated search for this model that can be done with both currently available data at the LHC and upcoming ones at the HL-LHC.

A post-sphaleron baryogenesis model is constructed based on the proposed BNV interaction. The out-of-equilibrium condition can be easily satisfied due to the strong suppression of the decay rate from the high dimensionality of the BNV operator, resulting in a decay temperature

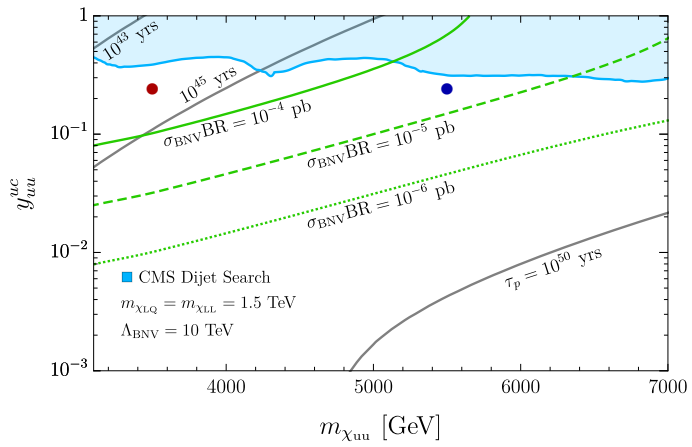


Figure 5.4: Parameter space showing existing constraints (blue), proton lifetime contours (dark gray contours), and BNV cross sections at $\sqrt{s} = 14$ TeV observable at the HL-LHC (green) while varying the scalar diquark mass and Yukawa coupling to up quark and charm quark. The shaded blue region is ruled out by existing dijet searches at the LHC [2, 3]. The proton lifetimes in this region span from $\tau_p \gtrsim 10^{43}$ years, well above the current Super-K bound ($\sim 10^{32}$ years) and projected Hyper-K bound ($\sim 10^{35}$ years). The green contours show the BNV cross section times branching ratio for the final state of Eq. (5.12) after applying the cuts of Eq. (5.13). They correspond to 10^{-4} pb (solid), 10^{-5} pb (dashed), and 10^{-6} pb (dotted), accessible at the (HL-)LHC. The solid contour corresponds to $\mathcal{O}(300)$ events with HL-LHC luminosity $\mathcal{L} = 3 \times 10^6$ pb^{-1}. The dark red and dark blue circles represent the benchmark points shown in Fig. 5.3.

much lower than the mass of the decaying particle. If the decaying particle is lighter than 1 TeV, the decay temperature is well below the electroweak scale, thus preventing the washout by the electroweak sphalerons. The other condition, CP violation, can be induced purely from the CP violation in the quark and lepton sectors of the Standard Model via the interference of the tree and the W-exchanged one-loop diagrams. This indicates that the baryogenesis mechanism based on our model can be directly constrained by future measurements of the lepton sector CP violation.

APPENDIX A

APPENDICES FOR CHAPTER 2

A.1 Out-of-Equilibrium Bubble Wall

This section reviews the bubble wall dynamics for a general out-of-equilibrium fluid, complementing the treatment in Sec. 2.2. The starting point is again EMT conservation Eq. (2.8), but with the more general expression for the fluid EMT given by Eq. (2.10). Focusing on a single-component fluid for simplicity, we decompose the distribution function into equilibrium and out-of-equilibrium contributions:

$$f(k,z) = f^{\rm eq}(k,z) + f^{\rm out}(k,z)\,. \tag{A.1}$$

Correspondingly, the fluid EMT can also be decomposed as

$$T_f^{\mu\nu} = T_{f,\,\rm LTE}^{\mu\nu} + T_{f,\,\rm out}^{\mu\nu}\,, \tag{A.2}$$

where

$$T_{f,\,\rm out}^{\mu\nu} = \int \frac{d^3k}{(2\pi)^3}\frac{k^\mu k^\nu}{2E_k} f^{\rm out}(k,z)\,. \tag{A.3}$$

Recall that the equilibrium contribution to $T_f^{\mu\nu}$ could equivalently be expressed in the perfect fluid form of Eq. (2.15). Similarly, one can always perform a decomposition of $T_{f\,\rm out}^{\mu\nu}$ into a linear combination of Lorentz covariant pieces,

$$T_{f,\,\rm out}^{\mu\nu} = T_{f,\,\rm out}^{(\eta)}\eta^{\mu\nu} + T_{f,\,\rm out}^{(u)}u^\mu u^\nu + T_{f,\,\rm out}^{(\bar u)}\bar u^\mu \bar u^\nu + T_{f,\,\rm out}^{(u\bar u)}(u^\mu \bar u^\nu + \bar u^\mu u^\nu)\,, \tag{A.4}$$

where

$$T_{f,\,\rm out}^{(\eta)} = \int \frac{d^3k}{(2\pi)^3}\frac{1}{2E_k}\left(m^2 + (k_\mu \bar u^\mu)^2 - (k_\mu u^\mu)^2\right) f^{\rm out}(k,z)\,. \tag{A.5}$$

The explicit forms of $T^{(u)}_{f,\,\mathrm{out}}$, $T^{(\bar{u})}_{f,\,\mathrm{out}}$, and $T^{(u\bar{u})}_{f,\,\mathrm{out}}$ will not be important for what follows, and can be found in Ref. [1].

The equilibrium contribution to the divergence, $\partial_\mu T^{\mu\nu}_{f,\mathrm{LTE}}$, was derived in Sec. 2.2 and is given by Eq. (2.16). It can be combined with the scalar field divergence of Eq. (2.17) and the out-of-equilibrium contribution to give the following conservation law:

$$\begin{aligned}\partial^\nu\phi\left(\Box\phi+\frac{\partial V_{\mathrm{eff}}}{\partial\phi}+\frac{\partial T^{(\eta)}_{f,\,\mathrm{out}}}{\partial\phi}\right)+\partial_\mu(wu^\mu u^\nu)-s\partial^\nu T \\ +\partial_\mu\left(T^{(u)}_{f,\,\mathrm{out}}u^\mu u^\nu+T^{(\bar{u})}_{f,\,\mathrm{out}}\bar{u}^\mu\bar{u}^\nu+T^{(u\bar{u})}_{f,\,\mathrm{out}}(u^\mu\bar{u}^\nu+\bar{u}^\mu u^\nu)\right)=0\,,\end{aligned} \tag{A.6}$$

The quantity in parentheses must vanish independently, giving the following effective EOM for the scalar field

$$\Box\phi+\frac{\partial V_{\mathrm{eff}}}{\partial\phi}+\frac{\partial T^{(\eta)}_{f,\,\mathrm{out}}}{\partial\phi}=0\,. \tag{A.7}$$

Noting that only the term $\propto m^2$ in Eq. (A.5) is ϕ-dependent, this simplifies to

$$\Box\phi+\frac{\partial V_{\mathrm{eff}}}{\partial\phi}+\frac{\partial m^2}{\partial\phi}\int\frac{d^3k}{(2\pi)^3}\frac{1}{2E_k}f^{\mathrm{out}}(k,z)=0\,. \tag{A.8}$$

A.1.1 Dynamics of the Expanding Bubble

Consider now an isolated, spherically symmetric bubble of true vacuum that has nucleated in the false vacuum and is expanding radially outwards, as in Fig. A.2. This expansion is the result of a competition between the driving pressure from the energy released in the phase transition and backreaction from the plasma in the form of a frictive pressure on the wall. If the friction exerted by the plasma on the wall is sufficient to balance the driving force, the wall quickly reaches the terminal velocity v_w. If not, the bubble wall continues to accelerate towards ultra-relativistic velocities.

In order to work out expressions that will allow us to discriminate between the two cases,

we work in the *instantaneous*[1] wall rest frame, in which all the quantities are functions of z. Our starting point is the scalar equation of motion of Eq. (A.8) (generalized to multiple species). Multiplying both sides by $(\partial_z\phi)$ and integrating over the wall, we find

$$\int dz\,(\partial_z\phi)\left(\ddot{\phi}+\frac{\partial V_0}{\partial\phi}+\sum_i n_i\frac{dm_i^2}{d\phi}\int\frac{d^3k}{(2\pi)^3}\frac{1}{2E_i}f_i(k,z)\right)=0\,, \tag{A.9}$$

where we have used the fact that $\int dz\,(\partial_z\phi)(\partial_z^2\phi)=\frac{1}{2}\int dz\,\partial_z\left[(\partial_z\phi)^2\right]=0$ is a total derivative and $\partial_z\phi$ vanishes away from the wall in order to eliminate the would-be second term. The left-most term is related to the wall's acceleration and may be identified with the net pressure, which we define as

$$\begin{aligned}\mathcal{P}_{\rm net}&\equiv\int dz(\partial_z\phi)\ddot{\phi}\\&=-\int dz(\partial_z\phi)\left(\frac{\partial V_0}{\partial\phi}+\sum_i n_i\frac{dm_i^2}{d\phi}\int\frac{d^3k}{(2\pi)^3}\frac{1}{2E_i}f_i(k,x)\right)\,.\end{aligned} \tag{A.10}$$

The condition for a stationary wall is that the net pressure vanishes, $\mathcal{P}_{\rm net}=0$. Note that we follow the sign convention of Ref. [1, 68, 238], for which a negative $\mathcal{P}_{\rm net}$ is associated with an accelerating wall.

It is instructive to decompose $\mathcal{P}_{\rm net}$ as the difference between friction and driving pressure,

$$\mathcal{P}_{\rm net}=\mathcal{P}_{\rm fric}-\mathcal{P}_{\rm drive}\,. \tag{A.11}$$

We identify[2] the driving pressure with the difference in the zero-temperature potential between

1. Because we allow the acceleration to be non-zero here, we cannot define a global wall rest frame. Nevertheless, we can still define an *instantaneous* wall rest frame.

2. Note that this decomposition is not unique, and various authors may have different conventions.

the symmetric and broken phases,

$$\mathcal{P}_{\rm drive} = \int dz\,(\partial_z\phi)\frac{\partial V_0}{\partial\phi} = \Delta V_0\,, \tag{A.12}$$

which is purely determined by the zero-temperature scalar potential. The remaining term is then identified as the friction caused by the plasma,

$$\mathcal{P}_{\rm fric} = -\int dz\,(\partial_z\phi)\sum_i n_i\frac{dm_i^2}{d\phi}\int\frac{d^3k}{(2\pi)^3}\frac{1}{2E_k}f_i(k,x). \tag{A.13}$$

A negative $\mathcal{P}_{\rm net}$ implies $\mathcal{P}_{\rm drive} > \mathcal{P}_{\rm fric}$, corresponding to an accelerating wall. Typically, this acceleration continues until the pressures balance and $\mathcal{P}_{\rm net} = 0$, at which point the wall assumes steady state motion at the terminal velocity v_w. As we will see in the following subsection, the friction, and thus the net pressure, peaks at the Jouguet velocity v_J. If the friction at this peak is not strong enough to balance the driving pressure, $\mathcal{P}_{\rm fric} < \mathcal{P}_{\rm drive}$ at v_J, the wall will accelerate beyond v_J and enter the detonation regime. In this regime, the LTE contribution to the friction is negligible, since the plasma is at rest in front of the bubble wall. The bubble wall will keep accelerating to the ultra-relativistic regime, where the pressure receives further contributions from the emission of soft radiation, and will finally reach a terminal velocity [66, 239, 240].

One may observe from Eq. (A.13) that $\mathcal{P}_{\rm fric}$ receives contributions only from those particles with ϕ-dependent masses coupling directly to the wall. This, however, is not the full picture, given that the distribution function for a given species depends on interactions with *all* the particles in the plasma. Even if a particle does not couple directly to ϕ, it may still contribute to $\mathcal{P}_{\rm fric}$ provided that it interacts sufficiently strongly with a particle which does couple directly to the wall. Following Ref. [68], we refer to those particles that couple directly to the wall and have ϕ-dependent masses "active" particles, and those that couple indirectly through their interactions with active particles "passive" particles. Active particles always contribute

to the effective degrees of freedom of the plasma, while passive particles should only be counted if their interactions are sufficiently rapid that the active particles can communicate to them the influence of the wall on a time scale much faster than the phase transition itself. A natural condition for passive particles to count towards the degrees of freedom is then

$$\Gamma = n \langle \sigma v \rangle \gg \beta \,, \tag{A.14}$$

where Γ is the interaction rate for the relevant scatterings that help to maintain the passive species in kinetic equilibrium with the plasma and β is the inverse duration of the phase transition. Passive particles that fail to satisfy this criterion are essentially transparent to the wall. Note that all SM particles are either "active" or have a large enough interaction rate with the wall, and so their particle degrees of freedom contribute to V_{eff}.

A.1.2 Wall Velocity and Thickness from EOM

The bubble wall velocity v_w enters the expression of the net pressure Eq. (A.10) as a parameter, and can be solved for by requiring $\mathcal{P}_{\text{net}} = 0$. In addition to v_w, $\mathcal{P}_{\text{net}}$ also depends on the scalar field profile across the space, which can be parameterized by, e.g., the wall width L_ϕ. More equations are needed to solve for the field profile parameters, which can be constructed as moment equations of the scalar field EOM Eq. (A.8). A general out-of-equilibrium calculation is performed in [1] for the first-order EWPT occurring from the $\mathbb{Z}_2$-symmetric real singlet extension model. In the following, we will review the calculations in [1] in the LTE approximation, and compare them to the entropy conservation approach discussed in Sec. 2.2.5. Readers are referred to the original work for the case including out-of-equilibrium contribution. This section adopts the $\mathbb{Z}_2$-symmetric singlet scalar extension model described in Sec. 2.3 as an example, and the discussions can be easily generalized to more complicated models.

In such a model model, both h and S obey analogous EOMs, given by Eq. (A.8). For convenience, we define the left-hand side of these equations as $E_{h,S}$. In the wall frame and assuming LTE, these are

$$E_h \equiv -\partial_z^2 h + \frac{\partial V_{\text{eff}}}{\partial h} = 0\,, \tag{A.15a}$$

$$E_S \equiv -\partial_z^2 S + \frac{\partial V_{\text{eff}}}{\partial S} = 0\,, \tag{A.15b}$$

where the finite-temperature effective potential $V_{\text{eff}}(h, S; T)$ receives contributions from both h and S. A simple Ansatz for the field profiles solving these equations is

$$h(z) = \frac{h_0}{2}\left(1 - \tanh\left(\frac{z}{L_h}\right)\right)\,, \tag{A.16a}$$

$$S(z) = \frac{S_0}{2}\left(1 + \tanh\left(\frac{z}{L_S} + \delta_S\right)\right)\,, \tag{A.16b}$$

where L_h and L_S are the wall widths and δ_S is the offset between the two wall centers, all of which are constants once the walls have reached the terminal velocity. The vacuum expectation values h_0 and S_0, on the other hand, are generically functions of the asymptotic plasma temperatures $T_\pm$, which in turn depend on v_w.

The temperature itself also smoothly changes from T_- to T_+ across $-\infty < z < \infty$. The EMT conservation along z can be used to determine the temperature profile $T(z)$. In the wall frame, it can be written as (under LTE):

$$\begin{aligned} T^{30} &= w\gamma^2 v = c_1 \\ T^{33} &= \frac{1}{2}\left((\partial_z h)^2 + (\partial_z S)^2\right) - V_{\text{eff}}(h(z), S(z), T(z)) + w\gamma^2 v^2 = c_2\,, \end{aligned} \tag{A.17}$$

where c_1 and c_2 are constants that can be directly determined from $v_\pm$ and $T_\pm$. Combining

these two equations to eliminate v, one arrives at

$$\frac{1}{2}\left((\partial_z h)^2 + (\partial_z S)^2\right) - V_{\text{eff}}(h(z), S(z), T(z)) - \frac{1}{2}w + \frac{1}{2}\sqrt{4c_1^2 + w^2} - c_2 = 0\,. \tag{A.18}$$

With this equation, the temperature $T(z)$ can be solved directly, using the scalar field profile given in Eq. (A.16).

All the above discussions depend on parameters L_h, L_s and δs. We can solve for the values of these parameters by taking moments of E_h and E_S and demanding that they vanish. Two convenient choices are the pressures $\mathcal{P}_{h,S}$ and pressure gradients $\mathcal{G}_{h,S}$ associated to each field [1, 238]. As in Eq. (A.10), we can define the net pressures on the walls

$$\mathcal{P}_h(v_w, L_h, L_S, \delta_S) = -\int dz(\partial_z h)E_h\,, \tag{A.19a}$$

$$\mathcal{P}_S(v_w, L_h, L_S, \delta_S) = -\int dz(\partial_z S)E_S\,. \tag{A.19b}$$

These quantities are well-suited to determine v_w, since the walls reach their steady state when the net pressures on each of them vanish, $\mathcal{P}_{h,\,S} = 0$. Additionally, the requirement $\mathcal{P}_h = \mathcal{P}_S$ ensures constant offset between the walls, and can be used to solve for δ_S. The net pressure gradients on the walls are

$$\mathcal{G}_h(v_w, L_h, L_S, \delta_S) = \int dz\,(\partial_z h)\left(\frac{2h}{h_0} - 1\right)E_h\,, \tag{A.20a}$$

$$\mathcal{G}_S(v_w, L_h, L_S, \delta_S) = \int dz\,(\partial_z S)\left(\frac{2S}{S_0} - 1\right)E_S\,. \tag{A.20b}$$

A non-vanishing pressure gradient $\mathcal{G}_{h,S}$ would lead to the compression or stretching of the wall, and so demanding that these moments vanish allows us to determine the constant wall

widths $L_{h,S}$. A final steady state solution thus requires

$$(\mathcal{P}_h + \mathcal{P}_S) = (\mathcal{P}_h - \mathcal{P}_S) = \mathcal{G}_h = \mathcal{G}_S = 0\,. \tag{A.21}$$

We can use these conditions to solve for the wall velocity v_w following the algorithm of CL. Since the framework to find out v_J, solving for $v_\pm$ and $T_\pm$, and iterate over v_w is essentially the same as that in Sec. 2.2.5, we only present how to compute $P_{\rm tot}$ for a given v_w. The algorithm is

1. Determining $c_{1,2}$ with $T_\pm$ and $v_\pm$ from Eq. (A.17)[3].
2. Design a function to solve for $T(z)$ as a function of L_h, L_s, δs, using the $c_{1,2}$ and Eq. (A.18).
3. Given $T(z)$, compute $\mathcal{P}_{h,S}$ and $\mathcal{G}_{h,S}$ as in Eqs. (A.19) and (A.20) as a function of L_h, L_s, δs.
4. Demand $(\mathcal{P}_h - \mathcal{P}_S) = \mathcal{G}_h = \mathcal{G}_S = 0$ and solve for L_h, L_S, and δ_S.
5. Calculate $\mathcal{P}_{\rm tot}(v_w)$ using the solutions for $\{L_h, L_S, \delta_S\}$.

	scalar EOM	Entropy conservation
Condition 1, 2	Matching conditions between v_+ and v_- (Eq. (2.23a) and Eq. (2.23b))	
Condition 3	Scalar field EOM Eq. (A.8)	Entropy conservation Eq. (2.28)
Advantages	Can go beyond LTE Can output wall width	Fast Numerically stable
Disadvantages	Slow Numerical instabilities	Cannot go beyond LTE Cannot compute wall widths

Table A.1: Summary of different algorithms to solve for the wall velocity.

The left panel of Fig. A.1 shows the $P_{\rm tot}$ as a function of v_w. The benchmark chosen for this plot is $m_S = 66.14$ GeV, $\lambda_{SH} = 0.79$, $\lambda_S = 1$. The friction opposing bubble

3. Theoretically, input T_- and v_- should give the same result as T_+ and v_+. However, we found it numerically more stable to start from v_- and T_- and solve for $T(z)$ from $-\infty$ to $+\infty$.

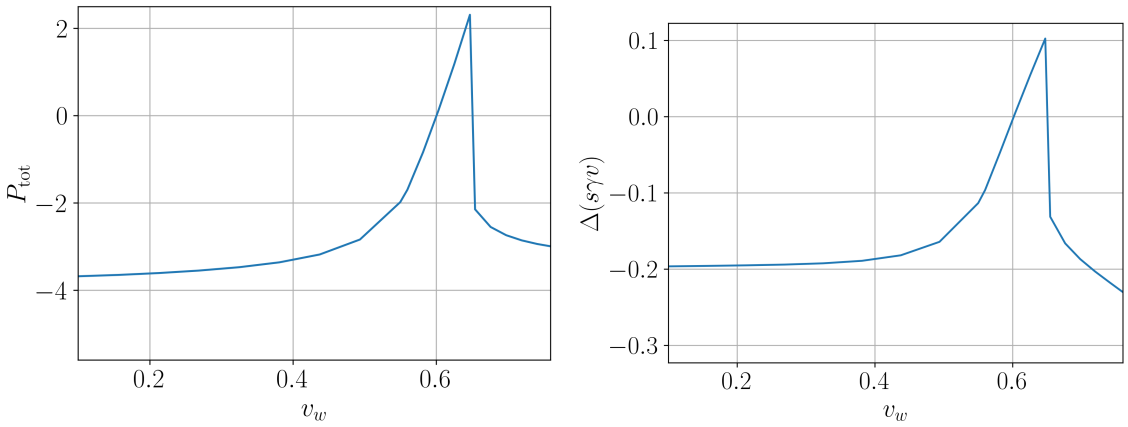


Figure A.1: Left: Total pressure on the wall $\mathcal{P}_{\rm tot}$ as a function of v_w in arbitrary units. Right: Entropy difference $\Delta(s\gamma v)$ between plasmas on either side of the wall (arbitrary units). Note that both display qualitatively identical behavior and cross zero at the same value of v_w. We do not plot v_w up to 1 since LTE is not justified in that range.

expansion comes mainly from the heated plasma in front of the wall — a phenomenon known as "hydrodynamic obstruction" [1, 65]. This is a purely equilibrium effect which appears whenever there is a shock wave preceding the wall (i.e., in the deflagration and hybrid regimes). As one increases v_w, the total pressure also begins increasing from its initial negative value. (Recall that we have defined a negative $\mathcal{P}$ to correspond to an accelerating wall.) After passing the Jougeut velocity v_J, $\mathcal{P}_{\rm tot}$ drops sharply since the heated plasma front disappears. Thus, there should be a sharp peak in $\mathcal{P}_{\rm tot}$ at $v_w = v_J$, as is indeed the case in Fig. A.1.

The right panel of Fig. A.1 shows the $\Delta(s\gamma v)$ using the same parameter point (which is the same plot in Fig. 2.2) for the comparison between the approaches of the scalar EOM and entropy conservation. We observe that the curves in these two panels have a similar shape and reach zero at an identical v_w, indicating the equivalence between the two approaches. The entropy conservation approach significantly reduces computation time and minimizes numerical instability, as it eliminates the need to solve for $T(z)$ and (L_h, L_S, δ_S). For models with additional scalar fields, requiring even more free parameters to solve the wall profile, the entropy conservation method is even more advantageous. We summarize the scalar EOM and entropy conservation approaches in Table A.1.

A.2 Free Energy

The central quantity governing the thermodynamics of the phase transition is the free energy density $\mathcal{F}$, which recieves contributions from both the scalar field and fluid $\mathcal{F} = \mathcal{F}_\phi + \mathcal{F}_f$. The free energy of the fluid is equivalent to the finite temperature contribution to the effective potential $\mathcal{F}_f = V_T$ and is computed as the sum of the free energies of the thermalized particle constituents,

$$\mathcal{F}_f = \sum_B n_B \mathcal{F}_B + \sum_F n_F \mathcal{F}_F \,, \tag{A.22}$$

with $n_{B/F}$ the number of degrees of freedom per species. In order for a particle to count towards the degrees of freedom, it should either couple directly to the wall or interact sufficiently strongly with particles coupling directly to the wall. See Eq. (A.14) of Appendix A.1.1 for a precise formulation of this condition and related discussion. We remark that all SM particles trivially satisfy this condition at the electroweak scale. To compute this explicitly, recall that the free energy density of a single bosonic degree of freedom with field-dependent effective mass m is

$$\mathcal{F}_B = T \int \frac{d^3k}{(2\pi)^3} \ln\left(1 - e^{-E_k/T}\right) \equiv T^4 J_B\left(\frac{m}{T}\right) \,, \tag{A.23}$$

where we have defined the bosonic thermal function J_B. Similarly for a fermionic degree of freedom,

$$\mathcal{F}_F = -T \int \frac{d^3k}{(2\pi)^3} \ln\left(1 + e^{-E_k/T}\right) \equiv T^4 J_F\left(\frac{m}{T}\right) \,, \tag{A.24}$$

with J_F the fermionic thermal function. These admit the following high temperature expansions

$$\mathcal{F}_B \simeq -\frac{\pi^2}{90}T^4 + \frac{1}{24}m^2T^2 - \frac{1}{12\pi}m^3T - \frac{1}{32\pi^2}m^4\left[\ln\left(\frac{me^{\gamma_E}}{4\pi T}\right) - \frac{3}{4}\right] \,, \tag{A.25a}$$

$$\mathcal{F}_F \simeq -\frac{7}{8}\frac{\pi^2}{90}T^4 + \frac{1}{48}m^2T^2 - \frac{1}{32\pi^2}m^4\left[\ln\left(\frac{me^{\gamma_E}}{\pi T}\right) - \frac{3}{4}\right]. \tag{A.25b}$$

The free energy in the high temperature approximation can then be expressed as

$$\mathcal{F}_f = -\frac{\pi^2}{90}g_\star T^4 + \frac{T^2}{24}\left(\sum n_B m_B^2 + \frac{1}{2}\sum_F n_F m_F^2\right) - \frac{T}{12\pi}\sum n_B m_B^3\,, \tag{A.26}$$

where $g_\star = \sum_B n_B + \frac{7}{8}\sum_F n_F$ is the effective number of degrees of freedom and we have neglected higher order terms for simplicity. The free energy density for the scalar field, meanwhile, is simply the zero-temperature potential[4]

$$\mathcal{F}_\phi = V_0\,. \tag{A.27}$$

The total free energy density for the scalar-fluid system is then the finite-temperature effective potential

$$\mathcal{F} = V_0 + V_T \equiv V_{\rm eff}\,, \tag{A.28}$$

which takes the schematic form

$$V_{\rm eff} = V_0 - \frac{\pi^2}{90}g_\star T^4 + \frac{T^2}{24}\left(\sum n_B m_B^2 + \frac{1}{2}\sum_F n_F m_F^2\right) - \frac{T}{12\pi}\sum n_B m_B^3 + ... \tag{A.29}$$

Accurate predictions of phase transition parameters therefore depend on an accurate determination of $V_{\rm eff}$. For practical reasons, the finite-temperature effective potential is often computed in perturbation theory, though there are a number of theoretical uncertainties associated with a perturbative calculation [241–243]. Among them, the finite temperature perturbative expansion breaks down at high temperatures when infrared bosonic modes become highly occupied. This generically necessitates the resummation of large thermal

4. The zero-temperature potential includes both the tree-level piece and the zero-temperature loop-level corrections, $V_0 = V_{\rm tree} + V_0^{\rm loop}$.

corrections to the effective potential [56–59].

A.3 Reference Frames

This appendix section provides a more detailed explanation of the two main reference frames that are used in Sec. 2.2. Namely, we will consider the rest frame of the bubble center, which we will refer to as the "cosmic frame", and the rest frame of the bubble wall, which we will call the "wall frame". Both frames are depicted in Fig. A.2.

Cosmic Frame

In the cosmic frame, the spherical symmetry and lack of characteristic scale motivate us to introduce the dimensionless coordinate $\xi \equiv R/t$, where R is the distance as measured from the center of the bubble and t is the time since nucleation. A fluid element at the point described by ξ in the wave profile has velocity $v(\xi)$, and so in the cosmic frame (in spherical coordinates) we parameterize the fluid 4-velocity $u^\mu_{\rm cf}$ and the 4-velocity orthogonal to the flow $\bar{u}^\mu_{\rm cf}$ as

$$u^\mu_{\rm cf}(\xi) = \gamma_{\rm cf}(\xi)\big(1, 0, 0, v_{\rm cf}(\xi)\big)\,, \quad \bar{u}^\mu_{\rm cf}(\xi) = \gamma_{\rm cf}(\xi)\big(v_{\rm cf}(\xi), 0, 0, 1\big)\,, \tag{A.30}$$

where $\gamma(\xi) = 1/\sqrt{1 - v_{\rm cf}(\xi)^2}$ is the Lorentz factor and $v_{\rm cf}(\xi)$ is the fluid velocity in the cosmic frame.

We presume that the wall quickly[5] accelerates to its terminal velocity v_w, after which it undergoes steady-state expansion at v_w. The wall is then located at $\xi_w = v_w$ in this coordinate system, and we label the fluid outside and inside the wall by ξ_+ and ξ_-, respectively, with $\xi_+ > \xi_w$ and $\xi_- < \xi_w$. We denote the scalar field values on either side of the wall by $\phi_\pm$,

5. Though the initial period of acceleration is short relative to the duration of the phase transition, it is nevertheless important, as demonstrated by the numerical simulations of [69]. It would be valuable to develop an analytic description of this period.

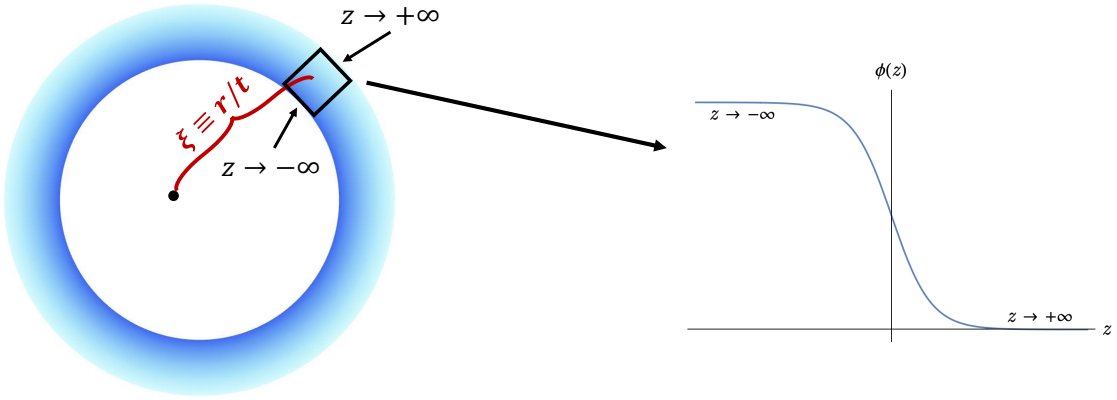


Figure A.2: The two main reference frames and their coordinate systems. The left panel shows a spherically symmetric bubble expanding radially outwards in the cosmic frame, with $\xi = r/t$ labeling an arbitrary point in the wave profile. The bubble wall itself is shown in blue; note the thickness has been greatly exaggerated for illustrative purposes. The gradient represents how the scalar profile interpolates between false and true vacua, as shown more explicitly in the right panel as a function of z, the wall frame coordinate.

which satisfy

$$\left.\frac{\partial V_{\text{eff}}}{\partial \phi}\right|_{\phi_\pm, T_\pm} = 0\,, \quad V_{\text{eff}}(\phi_-, T_-) < V_{\text{eff}}(\phi_+, T_+)\,, \tag{A.31}$$

consistent with the true, broken vacuum lying in the bubble interior and the false, symmetric vacuum outside. The bubble wall is the region interpolating between these two local minima, and is often modeled with a tanh profile; see Fig. A.2. The bubble wall width is typically very small compared with the radius, motivating us to work in the thin wall approximation while in the cosmic frame.

Wall Frame

In other contexts, it will be more convenient to work in the wall's rest frame, where all quantities are time-independent. It is always possible to define such a frame when the bubble wall moves with constant velocity v_w. A sufficiently large bubble can be approximated as locally planar, and without loss of generality, we take the wall to be at $z = 0$ and consider expansion in the $+z$-direction from the perspective of the cosmic frame, such that the fluid

velocity is in the $-z$-direction. The broken and symmetric phases are found in the limits $z \to -\infty$ and $z \to +\infty$, respectively; see Fig. A.2. We parameterize the fluid 4-velocity $u^\mu_{\rm wf}$ and the 4-velocity orthogonal to the flow $\bar{u}^\mu_{\rm wf}$ as

$$u^\mu_{\rm wf}(z) = \gamma(z)\big(1, 0, 0, -v_{\rm wf}(z)\big)\,, \quad \bar{u}^\mu_{\rm wf}(z) = \gamma(z)\big(v_{\rm wf}(z), 0, 0, -1\big)\,, \tag{A.32}$$

where we have introduced the minus sign so that $v_{\rm wf} \geq 0$ is non-negative. For future reference, we also define the asymptotic values of the velocity in the symmetric and broken phases, $v_+ \equiv v_{\rm wf}(z \to +\infty)$ and $v_- \equiv v_{\rm wf}(z \to -\infty)$.

A.4 Relativistic Fluid Equations

The matching conditions derived in Sec. 2.2.2 will turn out to be sufficient to solve for the bubble wall velocity in the case of detonation profiles (see Sec. 2.2.4). However, for deflagration and hybrid profiles — which feature a shock front preceding the bubble wall — we need a bit more information to fully characterize the relativistic velocity and temperature profiles. Again, our starting point will be energy-momentum conservation.

The total energy-momentum tensor is given by the sum of Eqs. (2.9) and (2.15). We work in the cosmic frame away from the wall, where the gradient energy of the scalar field vanishes. In this region, the conservation law $\partial_\mu T^{\mu\nu} = 0$ reads

$$\partial_\mu(w u^\mu_{\rm cf}) u^\nu_{\rm cf} + w u^\mu_{\rm cf}(\partial_\mu u^\nu_{\rm cf}) - \partial^\nu p = 0\,. \tag{A.33}$$

Projecting along the flow by contracting both sides with the fluid 4-velocity $u^{\rm cf}_\nu$ defined in Eq. (A.30), we find

$$\partial_\mu(w u^\mu_{\rm cf}) = u^\nu_{\rm cf}\partial_\nu p\,, \tag{A.34}$$

where we have used the property $u_\nu \partial_\mu u^\nu = 0$. If we instead project orthogonal to the flow

by contracting with the space-like vector $\bar{u}^{\rm cf}_\nu$, we find

$$w u^\mu_{\rm cf} \bar{u}^\nu_{\rm cf} \partial_\mu u^{\rm cf}_\nu = \bar{u}^\nu_{\rm cf} \partial_\nu p \,. \tag{A.35}$$

Expressing the gradient contractions in terms of partial derivatives with respect to ξ via $u^\mu_{\rm cf}\partial_\mu = -\frac{\gamma_{\rm cf}}{t}(\xi - v_{\rm cf})\partial_\xi$ and $\bar{u}^\mu_{\rm cf}\partial_\mu = \frac{\gamma_{\rm cf}}{t}(1-\xi v_{\rm cf})\partial_\xi$, Eqs. (A.34) and (A.35) can be re-written as

$$\left(\frac{\xi - v_{\rm cf}}{w}\right)\frac{\partial e}{\partial \xi} = 2\frac{v_{\rm cf}}{\xi} + \left(1 - \gamma^2_{\rm cf} v_{\rm cf}(\xi - v_{\rm cf})\right)\frac{\partial v_{\rm cf}}{\partial \xi}\,, \tag{A.36a}$$

$$\left(\frac{1 - v_{\rm cf}\,\xi}{w}\right)\frac{\partial p}{\partial \xi} = \gamma^2_{\rm cf}(\xi - v_{\rm cf})\frac{\partial v_{\rm cf}}{\partial \xi}\,. \tag{A.36b}$$

Finally, these equations can condensed into a single expression by invoking the plasma sound speed c_s^2 defined in Eq. (2.37). Thus we arrive at [1, 64]

$$2\frac{v_{\rm cf}(\xi)}{\xi} = \gamma^2_{\rm cf}(1 - v_{\rm cf}(\xi)\,\xi)\left(\frac{\mathfrak{v}(\xi, v_{\rm cf}(\xi))^2}{c_s^2(\xi)} - 1\right)\frac{\partial v_{\rm cf}(\xi)}{\partial \xi}\,, \tag{A.37a}$$

$$\frac{\partial T}{\partial \xi} = T\gamma^2_{\rm cf}\mathfrak{v}(\xi, v_{\rm cf})\frac{\partial v_{\rm cf}}{\partial \xi}\,. \tag{A.37b}$$

Specifically, Eq. (A.37a) is nothing but Eq. (2.38). These are the master equations for the relativistic velocity and temperature profiles, respectively, and generically need to be solved numerically. The numerical solution is typically easier with recasting these equations in parametric form [64]

$$\begin{aligned}
\frac{dv}{d\tau} &= 2vc_s^2(1-v^2)(1-\xi v)\,,\\
\frac{d\xi}{d\tau} &= \xi\left((\xi - v)^2 - c_s^2(1-\xi v)\right)\,,\\
\frac{dT}{d\tau} &= \partial_\xi T\frac{d\xi}{d\tau}\,.
\end{aligned} \tag{A.38}$$

APPENDIX B

APPENDICES FOR CHAPTER 3

B.1 Baryon Number Calculation

The starting point for calculating baryon number generation in EWBG is to solve for the particle number distribution near the bubble wall governed by the Boltzmann equation. In the rest frame of the bubble wall, focusing on the region near the wall where the curvature of the bubble wall can be ignored, the Boltzmann equation reduces to a one-dimensional form along the direction perpendicular to the wall (z):

$$\left(v_g\partial_z + F_z\partial_{k_z}\right) f_i = C_i[f_i, f_j, ...], \tag{B.1}$$

where we have introduced the group velocity and force in the z direction as, $v_g \equiv \dot{z}$ and $F_z \equiv \dot{k_z}$, respectively. $C_i[f_i, f_j, ...]$ is the collision term depending on various particle species. For a fermion with CP-violating complex mass term $m(z) = |m(z)|e^{i\theta(z)\gamma^5}$, taking the WKB approximation, these quantities are given by:

$$v_g = (\partial_{k_c} E_w)_z \equiv \frac{k_z}{E_w}, \tag{B.2}$$

$$F_z = -\frac{(|m|^2)'}{2E_w} + ss_{k_0}\frac{\left(|m|^2\theta'\right)'}{2E_w E_{wz}}, \tag{B.3}$$

where E_w is the conserved energy in the wall frame, and $E_{wz}^2 \equiv E_w^2 - (k_x^2 + k_y^2)$. Throughout this work, we use $'$ to denote ∂_z for all quantities other than the particle distribution function f. The derivative on f will be defined later. The first equality of Eq. (B.2) follows from the classical Hamiltonian equation for the WKB wave packet, with k_c being the canonical momentum. The second equality of Eq. (B.2) can be taken as the definition of the kinetic momentum in the z direction–k_z. The CP violation effect is induced by the second term

of F_z, with $ss_{k_0} = -1$ for the left-handed fermion with $k_z > 0$, and $ss_{k_0} = +1$ for its CP conjugate–the right-handed anti-fermion. In presence of a spatially varying phase profile $\theta(z)$, E_w is given by the physical momentum as,

$$E_w \approx E_0 - ss_{k_0}\frac{|m|^2\theta'}{2E_0E_z} \equiv E_0 + ss_{k_0}\Delta E, \tag{B.4}$$

$$\text{with} \quad E_0 \equiv \sqrt{\mathbf{k}^2 + m^2}, \quad E_z \equiv \sqrt{k_z^2 + m^2}. \tag{B.5}$$

This is analogous to the conserved energy of a charged particle in an electromagnetic field. Substitute these into Eq. (B.2) and Eq. (B.3) and keep the leading-order terms in spatial derivative, we get

$$v_g \approx \frac{k_z}{E_0}\left(1 + ss_{k_0}\frac{|m|^2\theta'}{2E_0^2E_z}\right), \tag{B.6}$$

$$F_z \approx -\frac{(|m|^2)'}{2E_0} + ss_{k_0}\left[\frac{(|m|^2\theta')'}{2E_0E_z} - \frac{|m|^2(|m|^2)'\theta'}{4E_0^3E_z}\right]. \tag{B.7}$$

It is difficult to solve the Boltzmann equation directly in the presence of the collision term, which is a non-local integral over the phase space. To proceed, one usually needs to take an ansatz. The methods to be reviewed and compared here, i.e. the leading order (L.O.) approximation and all orders full treatment, are based on the ansatz of a perturbed equilibrium distribution boosted to the wall frame,

$$f = \frac{1}{e^{\beta[\gamma_w(E_w + v_w k_z) - \mu(z)]} \pm 1} + \delta f(k, z). \tag{B.8}$$

Here $\gamma_w = 1/\sqrt{1 - v_w^2}$ is the Lorentz boost factor. In this ansatz, the departure from chemical equilibrium is encoded in $\mu(z)$, and the departure from kinetic equilibrium is encoded in $\delta f(k, z)$, which satisfies the following condition so that it does not affect the local particle

density

$$\int d^3k\, \delta f = 0. \tag{B.9}$$

The problem then reduces to solving the differential equation for μ and δf, which is non-linear and hard to solve upon substituting Eq. (B.8) into the Boltzmann equation. To proceed, one could expand over μ and δf, and keep the linear terms, as detailed in Appendix F of [52]. In the following, we compare two linearization schemes that keep different orders of v_w in the coefficients[1].

One way to solve the linearized differential equation is to take moments over momentum space, weighting by 1 and k_z/E_0 respectively. This gives two independent moment equations for two variables, the chemical potential μ, and a new variable $u \equiv \langle \frac{k_z}{E_0} \delta f \rangle$, with the angle bracket defined as

$$\langle X \rangle \equiv \frac{\int d^3k\, X}{\int d^3k\, f_0'}\,. \tag{B.10}$$

Here f_0 is the equilibrium distribution boosted to the wall frame. In the full treatment, the relativistic Lorentz boosting is retained, and the distribution function f_0 is given by

$$f_{0w} = \frac{1}{e^{\beta\gamma_w(E_0 + v_w k_z)} \pm 1}\,. \tag{B.11}$$

Correspondingly, $f'_{0w} = \partial f_{0w}/\partial(\gamma_w E_0)$. The moment equations can be written in the matrix form as

$$A\omega' + B\omega = S + C\,, \tag{B.12}$$

with $\omega = (\mu, u)^T$, which in general can be decomposed into the CP-even and CP-odd contributions as $(\mu, u) = (\mu_e, u_e) + s_{k_0}(\mu_o, u_o)$. The transport equations for the CP-even

1. Note that there is another commonly employed ansatz modeling the out-of-equilibrium distribution in a perfect fluid form [244, 245], predicting a singularity at the sound speed; whether this singularity is physical or not is under debate. In this work, however, we focus on the ansatz in Eq. (B.8).

and CP-odd components decouple after linearization as discussed in Appendix F of [52]. In this section, we focus on the transport equation for the CP-odd terms, which is relevant for baryogenesis. In the all orders treatment that keeps the full dependence on v_w, the matrices of the derivative coefficients A, the linear coefficients B, the source terms S, and the collision terms C take the following forms

$$
\begin{aligned}
A &= \begin{pmatrix} -D_1 & 1 \\ -D_2 & -v_w \end{pmatrix}, \quad B = (|m|^2)' \begin{pmatrix} v_w\gamma_w Q_1 & 0 \\ v_w\gamma_w Q_2 & \bar{R} \end{pmatrix}, \\
S &= \begin{pmatrix} S_1 \\ S_2 \end{pmatrix}, \quad \text{with} \quad S_\ell \equiv v_w\gamma_w \left[(|m|^2\theta')' Q_\ell^{8o} - (|m|^2)'|m|^2\theta' Q_\ell^{9o} \right], \\
C &= \begin{pmatrix} C_1 \\ -\Gamma_i^{\rm tot} u - v_w C_1 \end{pmatrix}, \quad \text{with} \quad C_1 = K_0 \sum_c \Gamma_i^c \sum_j s_j^c \frac{\mu_j^c}{T} \,.
\end{aligned}
\tag{B.13}
$$

Here, Γ_i^c and $\Gamma_i^{\rm tot}$ are the inelastic interaction rates for species i in channel c and in total, respectively, where $s_j^c = +1(-1)$ if the species j is in the initial (final) state in channel c. The coefficients appearing in the moment equations above are given by,

$$
\begin{aligned}
&D_\ell \equiv \langle \left(\frac{k_z}{E_0}\right)^\ell f'_{0w} \rangle, \quad Q_\ell \equiv \langle \left(\frac{k_z^{\ell-1}}{2E_0^\ell}\right) f''_{0w} \rangle, \quad \bar{R} = \frac{\int d^3k \, \left(\frac{1}{2k_z E_0}\right) f_{0w}}{\int d^3k \, f_{0w}}, \\
&Q_\ell^{8o} \equiv \langle \frac{s_k k_z^{\ell-1}}{2E_0^\ell E_z} f'_{0w} \rangle, \quad Q_\ell^{9o} \equiv \langle \frac{s_k k_z^{\ell-1}}{2E_0^{\ell+1} E_z} \left(\frac{1}{E_0} f'_{0w} - \gamma_w f''_{0w} \right) \rangle, \quad K_0 \equiv -\frac{\int d^3k f_{0w}}{\int d^3k f'_{0w}} \,,
\end{aligned}
\tag{B.14}
$$

where $s_k = \text{sign}(k_z)$ denotes the sign of the z-direction momentum. The source terms for the CP-odd transport equation describe the CP-violating effects for the left-handed particles, which are non-vanishing only for non-trivial θ'.

Eqs. (B.12) and (B.13) are the final equations to solve in the all orders treatment. Note that these equations have no singularity in v_w and behave smoothly for all $0 < v_w < 1$. In

contrast, earlier methods assuming small wall velocity which took only the leading order term in an expansion in v_w frequently encounter singular behavior at $v_w < 1$. The origin of this singularity is discussed in more details in Appendix F of [52]. To summarize, in the L.O. approximation, the Lorentz transformation is approximated as the Galilean transformation at small v_w, such that $f_0^{\text{L.O.}} = (e^{\beta E_0} \pm 1)^{-1}$. The derivative coefficient matrix A, the source term S, and the collision term C are given by,

$$A_{\text{L.O.}} = \begin{pmatrix} -v_w & 1 \\ -\langle \frac{k_z^2}{E_0^2} f_0' \rangle & v_w \end{pmatrix}, \quad B_{\text{L.O.}} = \mathbf{0},$$
$$S_{\text{L.O.}} = \begin{pmatrix} 0 \\ -v_w \langle \frac{k_z}{E_0} F_z f_0' \rangle \end{pmatrix}, \quad C_{\text{L.O.}} = \begin{pmatrix} K_0 \sum_c \Gamma_i^c \sum_j s_j^c \frac{\mu_j^c}{T} \\ -\Gamma_i^{\text{tot}} u \end{pmatrix}. \tag{B.15}$$

Here, K_0 is the normalization factor defined in Eq. (B.14) with f_{0w} replaced by $f_0^{\text{L.O.}}$. The force F_z in the source term for the CP-odd transport equation should be the CP-violating part, $F_z = F_o \approx s\left(|m|^2\theta'\right)'/(2E_0E_z)$ (ignoring the second term of Eq. (F.5) in [52] contributed by ΔE). One can check that indeed these L.O. coefficients are the low v_w limits of the full coefficients given by Eq. (B.13). Since only the leading order of v_w is kept, this framework is not expected to perform well at larger v_w. This expectation is borne out in the numerical results of Sec. 3.3.2.

B.2 Gravitational Wave Spectrum from different sources

B.2.1 Scalar Field Contribution

When a bubble nucleates, a portion of the vacuum energy is transformed into the gradient energy of the scalar whose interpolating profile defines the bubble wall. Once spherical symmetry is broken by bubble collision, this gradient energy can source GWs. For details, we refer the reader to Ref. [246], which computes the GW spectrum semi-analytically from first

principles by evaluating the 2-point function of the scalar stress-energy tensor. The resulting GW spectrum takes the form

$$\Omega_\phi h^2 = 1.67 \times 10^{-5} \left(\frac{\kappa_\phi\, \alpha_n}{1+\alpha_n}\right)^2 \left(\frac{H}{\beta}\right)^2 \left(\frac{100}{g_*}\right)^{1/3} \Delta_{\rm peak} S \tag{B.16}$$

with coefficients

$$\begin{aligned}
\Delta_{\rm peak} &= \left(\frac{0.48 v_w^3}{1+5.3v_w^2+5v_w^4}\right), \\
S &= \left(0.064\left(\frac{f}{f_{\rm env}}\right)^{-3} + (1-0.064-0.48)\left(\frac{f}{f_{\rm env}}\right)^{-1} + 0.48\left(\frac{f}{f_{\rm env}}\right)\right)^{-1}, \\
f_{\rm env} &= 16.5 \times 10^{-9}{\rm Hz} \left(\frac{0.35}{1+0.069v_w+0.69v_w^4}\right)\left(\frac{\beta}{H}\right)\left(\frac{T}{100}\right)\left(\frac{g_*}{100}\right)^{1/6}.
\end{aligned} \tag{B.17}$$

Here, β/H describes the ratio of the Hubble timescale H^{-1} to the duration of the phase transition β^{-1} and can be evaluated as

$$\frac{\beta}{H} = T\frac{d(S_3/T)}{dT}\bigg|_{T_n}, \tag{B.18}$$

where S_3 is the three-dimensional Euclidean action. The coefficient κ_ϕ characterizes the fraction of released energy which goes into bubble gradient energy, and is believed to behave as [133, 247]

$$\kappa_\phi = \frac{E_{\rm wall}}{E_{\rm vac}} \propto \frac{\gamma w}{R} \tag{B.19}$$

where R is the bubble radius at the time of bubble collision, and $E_{\rm wall}$ and $E_{\rm vac}$ represent the energy carried by the bubble wall and released from the phase transition, respectively.[2] As the bubble wall expands, this fraction is suppressed by R, making the produced GW signal

2. In the presence of the plasma, $E_{\rm vac}$ may be replaced by a more proper quantity that reflects the total released energy, but the dependency on R does not change.

negligible unless the wall continues to accelerate, allowing an increasing γ_w to compensate for the growing R.

Whether or not the bubble wall can keep accelerating depends on its interactions with the plasma. It was once believed that once α_n exceeded some critical value, the bubble wall would accelerate without bound, becoming a "runaway" bubble [248]. Working under the LTE approximation, detonation solutions naively seem to result in runaway bubbles, since there is no friction force to stop the bubble from accelerating. It has recently been realized, however, that an additional source of frictive pressure in the form of the emission of soft radiation as particles cross the bubble wall becomes important in the ultra-relativistic regime, growing with increasing γ_w [66]. Whether this pressure behaves as $\mathcal{P} \propto \gamma_w^2$ [239] or $\mathcal{P} \propto \gamma_w$ [240] remains under debate. Nevertheless, the consensus is that the pressure grows sufficiently quickly as the wall accelerates into the ultra-relativistic regime that it will ultimately reach a terminal[3] velocity. That is, so long as a thermal plasma is present, no runaway bubble wall can appear, and thus the GW contribution from the bubble collision stage is negligible. Only for strongly supercooled phase transitions, for which expansion significantly dilutes the plasma, can this source dominate. Since this is not the case for the DarkCPV model in our parameter space of interest, we omit the bubble collision contribution to the total GW signal in Fig. 3.8.

B.2.2 Sound Waves

Long after the initial bubble collisions have completed, fluid sound shells ("sound waves") continue to collide and merge. This provides an additional source of GWs, which is actually the dominant contribution for most thermal transitions. The GW spectrum from this source

3. In the case of detonations, it is also possible that bubble walls may collide with one another before reaching the terminal velocity. To our knowledge, this scenario has not been investigated in the literature, though some papers have provided preliminary estimates [247].

takes the form [132, 133, 136–138, 142, 249, 250]

$$\Omega_{\rm sw}h^2 = 2.65\times10^{-6}\left(\frac{\kappa_{\rm sw}\,\alpha_n}{1+\alpha_n}\right)^2\left(\frac{H}{\beta}\right)\left(\frac{100}{g_*}\right)^{1/3}(H\tau_{\rm sw})\,v_w\left(\frac{f}{f_{\rm sw}}\right)^3\left(\frac{7}{4+3(f/f_{\rm sw})^2}\right)^{7/2}, \tag{B.20}$$

the sound wave peak frequency $f_{\rm sw}$ set by

$$f_{\rm sw} = 1.9\times10^{-5}\,{\rm Hz}\left(\frac{1}{v_w}\right)\left(\frac{\beta}{H}\right)\left(\frac{g_*(T_n)}{100}\right)^{1/6}\left(\frac{T_n}{100\ {\rm GeV}}\right). \tag{B.21}$$

The "time duration suppression factor" $H\tau_{\rm sw}$, describing the ratio of the sound wave formation timescale $\tau_{\rm sw}$ to the expansion timescale H^{-1}, has been applied in various approximations in the recent literature [82, 123, 133, 148, 249–251]. Here we choose the approximation in Ref. [123, 148, 250],

$$H\tau_{\rm sw} = \min\left(1, (8\pi)^{1/3}\left(\frac{\max(v_w,c_s)}{\beta/H}\right)\left(\frac{4}{3}\frac{1+\alpha_n}{\kappa_{\rm sw}\alpha_n}\right)^{1/2}\right). \tag{B.22}$$

The fraction of released energy which goes into sound waves, $\kappa_{\rm sw}$, is in principle calculable from the fluid velocity profile $v(\xi)$. Ref. [64] provides a good numerical fit as a function of α_n in their Appendix A, which we reproduce here:

$$\begin{aligned}
\kappa_{v_w\lesssim c_s} =& \frac{c_s^{11/5}\kappa_A\kappa_B}{(c_s^{11/5}-v_w^{11/5})\kappa_B + v_w c_s^{6/5}\kappa_A},\\
\kappa_{c_s<v_w<v_J} =& \kappa_B + (v_w-c_s)\delta\kappa + \frac{(v_w-c_s)^3}{(v_J-c_s)^3}\left(\kappa_C-\kappa_B-(v_J-c_s)\delta\kappa\right),\\
\kappa_{v_w\to1} =& \frac{\alpha_n}{0.73+0.083\sqrt{\alpha_n}+\alpha_n},
\end{aligned} \tag{B.23}$$

where

$$\kappa_A = v_w^{6/5} \frac{6.9\alpha_n}{1.36 - 0.037\sqrt{\alpha_n} + \alpha_n}\,, \quad \kappa_B = \frac{\alpha_n^{2/5}}{0.017 + (0.997 + \alpha_n)^{2/5}},$$
$$\kappa_C = \frac{\sqrt{\alpha_n}}{0.135 + \sqrt{0.98 + \alpha_n}}\,, \quad \delta\kappa = -0.9 \log \frac{\sqrt{\alpha_n}}{1 + \sqrt{\alpha_n}}\,. \tag{B.24}$$

We comment that the above numerical fit was based on the range $0.001 < \alpha_n < 10$, which is consistent with the range of α_n explored in our current work.

B.2.3 Magnetohydrodynamic Turbulence

If the timescale $\tau_{\rm sw}$ is shorter than the Hubble time, $H\tau_{\rm sw} < 1$, MHD turbulence can form [136–138, 142]. In general, the contribution from MHD must be determined through numerical simulations [252]. From modeling Kolmogorov-type turbulence [132, 133, 140], though, it is expected that the parameter dependency can be expressed as

$$\Omega_{\rm tur}h^2 = 3.35 \times 10^{-4} \left(\frac{\kappa_{\rm turb}\,\alpha_n}{1+\alpha_n}\right)^{3/2} \left(\frac{H}{\beta}\right) \left(\frac{100}{g_*}\right)^{1/3} v_w S_{\rm turb}\,, \tag{B.25}$$

where

$$S_{\rm turb} = \frac{(f/f_{\rm turb})^3}{(1 + (f/f_{\rm turb}))^{11/3}(1 + 8\pi f/h_*)}\,,$$
$$f_{\rm turb} = 2.7 \times 10^{-5}\,{\rm Hz} \left(\frac{1}{v_w}\right) \left(\frac{\beta}{H}\right) \left(\frac{g_*(T_n)}{100}\right)^{1/6} \left(\frac{T_n}{100\ {\rm GeV}}\right)\,,$$
$$h_* = 16.5 \times 10^{-6}\,{\rm Hz} \left(\frac{g_*(T_n)}{100}\right)^{1/6} \left(\frac{T_n}{100\ {\rm GeV}}\right)\,. \tag{B.26}$$

The coefficient $\kappa_{\rm tur}$ describes the fraction of vacuum energy that is transformed into MHD turbulence, and is estimated to be between $(0.05 - 0.1)\kappa_{\rm sw}$ for thermal phase transitions. We assume $\kappa_{\rm turb} = 0.05\kappa_{\rm sw}$ in this work.

APPENDIX C

APPENDICES FOR CHAPTER 4

C.1 Symmetries

In this appendix, we discuss the symmetries of the staggered fermions formulation and their dynamics.

C.1.1 Continuum

Parity

The massless Dirac fermion in even spacetime dimensions has a parity symmetry P. We define this to be a symmetry which flips the sign of all the spatial coordinates. Under P, we have

$$\mathrm{P}: \begin{cases} \psi(t,x) \to \kappa\gamma_0\psi(t,-x) \\ \bar{\psi}(t,x) \to \bar{\psi}(t,-x)(\kappa\gamma_0)^\dagger \end{cases} \tag{C.1}$$

where $\kappa = 1$ or $\kappa = i$ such that $(\kappa\gamma_0)^2 = 1$, so that this is valid of any choice of signature, either Minkowski or Euclidean. One can check that this is always a symmetry of the fermion kinetic term, but not necessarily for a mass term. A general fermion bilinear transforms under parity as

$$\overline{\psi}\Gamma\psi \xrightarrow{\mathrm{P}} \overline{\psi}\gamma_0^{-1}\Gamma\gamma_0\psi. \tag{C.2}$$

Charge-conjugation

There are actually two definitions of charge conjugation since any charge-conjugation symmetry can be transformed into another by a discrete chiral transformation. To define the charge-

conjugation symmetry C, we first define unitary matrices C_ϵ ($\epsilon = \pm$), such that

$$C_\epsilon \gamma_\mu C_\epsilon^{-1} = \epsilon(\gamma_\mu)^T \quad (\epsilon = \pm) \tag{C.3}$$

$$C_\epsilon \gamma_5 C_\epsilon^{-1} = \eta_5 (\gamma_5)^T, \tag{C.4}$$

for the Clifford algebra in even spacetime dimensions D. These matrices can be defined in any even dimension, and we refer the reader to Ref. [253] for a detailed pedagogical discussion.[1] The action of C_ϵ on the "fifth" γ matrix depends on the dimension, with $\eta_5 = (-1)^{\frac{D}{2}}$. With this definition, a charge-conjugation symmetry C acts on a Dirac field operator $\psi(x)$ as

$$\mathrm{C}_\epsilon : \begin{cases} \psi \to C_\epsilon \overline{\psi}^T = C_\epsilon (\gamma^0)^T \psi^* \\ \bar{\psi} \to \epsilon \psi^T C_\epsilon^{-1} \end{cases} \tag{C.5}$$

where we used Eq. (C.3) to obtain the action on $\bar{\psi}$. We can check that either choice of $\epsilon = \pm$ leads to a symmetry of the fermion kinetic term, since it transforms as

$$\overline{\psi}\gamma^\mu \partial_\mu \psi \xrightarrow{\mathrm{C}_\epsilon} \epsilon \overline{\psi}(C_\epsilon^{-1}\gamma^\mu C_\epsilon)^T \partial_\mu \psi = \overline{\psi}\gamma^\mu \partial_\mu \psi. \tag{C.6}$$

On the other hand, a fermion mass term may not be invariant under this symmetry. A general fermion bilinear transforms as

$$\overline{\psi}\Gamma\psi \xrightarrow{\mathrm{C}_\epsilon} \overline{\psi}(-\epsilon C_\epsilon^{-1}\Gamma C_\epsilon)^T \psi. \tag{C.7}$$

The transformation of various mass bilinears $\overline{\psi}\Gamma\psi$ for the C_ϵ symmetry is given in Table C.1.

We note that the C-conjugation on a Weyl fermion flips its chirality in 3+1d but not in 1+1d. Let ψ be a right-chiral ($\gamma_5 = +1$) Weyl fermion field. Right chirality of ψ implies that

1. In Ref. [253] the C_+, C_- matrices are referred to as T and C matrices, respectively.

Γ	1	γ^5	γ^μ	$\gamma^\mu\gamma^5$
C_ϵ	$-\epsilon$	$-\epsilon\eta_5$	-1	η_5
P	1	-1	$(-1)^\mu$	$-(-1)^\mu$

Table C.1: Charge-conjugation C_ϵ and parity P transformation properties of various fermion bilinears $\overline{\psi}\Gamma\psi$. The two definitions of charge conjugation correspond to $\epsilon = \pm$, as defined in Eqs. (C.3) and (C.5). The action of charge conjugation on γ_5 depends on the dimension and is given by $\eta_5 = (-1)^{\frac{D}{2}}$ in D spacetime dimensions. We use the notation where $(-1)^\mu = 1$ for $\mu = 0$ and -1 otherwise.

$\gamma_5\psi = +\psi$, which upon charge conjugation implies

$$\psi_c = C(\gamma^0)^T\gamma_5^*\psi^* = -\eta_5\gamma_5\psi_c, \tag{C.8}$$

where we used $\gamma_5^T = \gamma_5^*$. Therefore, we find that $\gamma_5\psi_c = -\eta_5\psi_c$. In 3+1d with $\eta_5 = 1$, chirality flips under C. However, this is different in 1+1d with $\eta_5 = -1$: the C-conjugate of a left-chiral ($\gamma_5 = -1$), right-moving Weyl fermion in $1+1$d is a left-chiral, right-moving Weyl antifermion.

C.1.2 Lattice

Charge conjugation

In 1+1 dimensions (mostly minus signature) with the basis choice $\gamma_0, \gamma_1, \gamma_5 = \sigma_3, i\sigma_2, \sigma_1$, we obtain the $C_\pm$ matrices,

$$C_+ = \sigma_3, \quad C_- = \sigma_2, \tag{C.9}$$

which lead to the following action of charge-conjugation $\mathrm{C}_\pm$ on the continuum Dirac fermion fields:

$$\begin{aligned} \mathrm{C}_+ : &\quad \psi \to C_+ \gamma_0^T \psi^* = \psi^* \\ \mathrm{C}_- : &\quad \psi \to C_- \gamma_0^T \psi^* = i\sigma_1 \psi^*. \end{aligned} \tag{C.10}$$

In the staggered fermion formulation, the action in Eq. (C.10) implies that C_+ is an on-site symmetry, while C_- mixes with translations,

$$\mathrm{C}_+ : \quad \chi_n \to \chi_n^\dagger \tag{C.11}$$

$$\mathrm{C}_- : \quad \chi_n \to i\chi_{n+1}^\dagger \tag{C.12}$$

One can check that, with the above definitions, the transformations for $\mathrm{C}_\pm$ in Table C.1 are satisfied on the 1+1-dimensional lattice for our discretization of the complex mass term as in Eq. (4.31).

C.2 Phase asymmetry for Gaussian wave packets

In this appendix, we show how the phase asymmetry can be computed from the charge densities under the assumption of Gaussian wave packets.

Phase asymmetry in the continuum

We begin with the incident wave function at $t \to -\infty$,

$$\varphi_0(x,t) = \int dk\, f(k; k_0, \sigma_k)\, e^{ik(x-t)}, \tag{C.13}$$

where $f(k;k_0,\sigma_k) = \mathcal{N}(\sigma_k)\, e^{-(k-k_0)^2/(4\sigma_k^2)}$, with $\mathcal{N}(\sigma_k) \equiv \left[(2\pi)^{3/4}\sqrt{\sigma_k}\right]^{-1}$, such that $\int dk\, |f(k)|^2 = 1/(2\pi)$. With the reflection coefficient defined as $R(k) \equiv e^{-r(k)}e^{-i\phi(k)}$, the reflected wave function as $t \to \infty$ can be written as

$$\begin{aligned}
\varphi_r(x,t) &= \int dk\, R(k)\, f(k;k_0,\sigma_k)\, e^{-ik(x+t)} \\
&= \int dk\, \left[e^{-r(k)}\, f(k;k_0,\sigma_k)\right]\, e^{-ik(x+t)-i\phi(k)} \\
&= \mathcal{N}(\sigma_k) \int dk\, e^{-g(k)}\, e^{-ik(x+t)-i\phi(k)}.
\end{aligned} \tag{C.14}$$

The peak of the momentum-space wave function of the reflected wave packet is determined by the minimum of the exponential factor $g(k) \equiv r(k) + (k-k_0)^2/(4\sigma_k^2)$ at $\overline{k_0}$, which satisfies the following equation:

$$0 = g'(\overline{k_0}) = r'(\overline{k_0}) + \frac{\overline{k_0} - k_0}{2\sigma_k^2}. \tag{C.15}$$

To further simplify Eq. (C.14), we expand $g(k)$ and $\phi(k)$ around $\overline{k_0}$ and keep only the leading-order terms,

$$g(k) \approx g(\overline{k_0}) + \frac{1}{2}\left[r''(\overline{k_0}) + \frac{1}{2\sigma_k^2}\right](k-\overline{k_0})^2, \tag{C.16}$$

$$\phi(k) \approx \phi(\overline{k_0}) + \phi'(\overline{k_0})(k-\overline{k_0}). \tag{C.17}$$

Substitute these expansions into Eq. (C.14), and define

$$\frac{1}{4\overline{\sigma_k}^2} \equiv \frac{1}{2}\left[r''(\overline{k_0}) + \frac{1}{2\sigma_k^2}\right], \tag{C.18}$$

$$\overline{f}(k;\overline{k_0},\overline{\sigma_k}) \equiv \mathcal{N}(\overline{\sigma_k})\, e^{-(k-\overline{k_0})^2/(4\overline{\sigma_k}^2)}, \tag{C.19}$$

we get

$$\varphi_r(x,t) \approx e^{-g(\overline{k_0})-i\zeta}\sqrt{\frac{\overline{\sigma_k}}{\sigma_k}}\int dk\,\overline{f}(k;\overline{k_0},\overline{\sigma_k})\,e^{-ik\left[x+t+\phi'(\overline{k_0})\right]}, \tag{C.20}$$

with $\zeta \equiv \phi(\overline{k_0}) - \phi'(\overline{k_0})\overline{k_0}$. The reflected particle number density after a sufficiently long time is

$$\begin{aligned}\rho_r(x,t) &= |\varphi_r(x,t)|^2 &\text{(C.21)}\\ &= \sqrt{\frac{2}{\pi}}\,e^{-2g(\overline{k_0})}\frac{\overline{\sigma_k}^2}{\sigma_k}\,e^{-\left[x+t+\phi'(\overline{k_0})\right]^2/(2\overline{\sigma_x}^2)}\\ &= \frac{\overline{\sigma_k}}{\sigma_k}e^{-2g(\overline{k_0})}N_{\overline{\sigma_x}}(x+t;\phi'(\overline{k_0})) &\text{(C.22)}\end{aligned}$$

with

$$\overline{\sigma_x} \equiv \frac{1}{2\overline{\sigma_k}}, \tag{C.23}$$

where we have used the notation $N_\sigma(x;\mu)$ to denote a normalized Gaussian with width σ and center μ. Eq. (C.22) shows that the reflected wave is an unnormalized Gaussian with amplitude reduced and the central position shifted to $\phi'(\bar{k}_0)$. For later use, we note that

$$\int dx\ \rho_r(x,t) = \frac{\overline{\sigma_k}}{\sigma_k}e^{-2g(\overline{k_0})}, \tag{C.24}$$

$$\int dx\,\rho_r(x,t)^2 = \frac{\overline{\sigma_k}}{\sqrt{\pi}}\left[\int dx\,\rho_r(x,t)\right]^2. \tag{C.25}$$

In the case of charge symmetry breaking, the particle and antiparticle have different reflection amplitude $r_\pm(k)$ and phase $\phi_\pm(k)$. The difference in the reflection amplitude can be measured by the reflected charge in the symmetric phase, which, according to Eq. (C.24), is determined by $r_\pm(k)$. To measure the difference in the phase, we calculate the product of

the particle and antiparticle number densities and find it to be related to the phase difference:

$$-\int_{-\infty}^{0} dx\, \rho_+\, \rho_- = A\, e^{-B\Phi^2} \tag{C.26}$$

where

$$\begin{aligned}
\Phi &\equiv \phi'(\overline{k_0}_+) - \phi'(\overline{k_0}_-), \\
A &= \sqrt{\frac{2}{\pi}} \frac{\overline{\sigma_k}_+^2\, \overline{\sigma_k}_-^2}{\sigma_k^2 \sqrt{\overline{\sigma_k}_+^2 + \overline{\sigma_k}_-^2}}\, e^{-2\left[g(\overline{k_0}_+) + g(\overline{k_0}_-)\right]}, \\
B &= \frac{2\overline{\sigma_k}_+^2\, \overline{\sigma_k}_-^2}{\overline{\sigma_k}_+^2 + \overline{\sigma_k}_-^2}.
\end{aligned} \tag{C.27}$$

From this we can define a new observable for the phase shift as

$$\Phi = \sqrt{-\frac{1}{B} \ln\left[-\frac{\int_{-\infty}^{0} dx\ \rho_+\, \rho_-}{A}\right]}. \tag{C.28}$$

Phase asymmetry on the lattice

On the lattice, $\overline{\sigma_k}_\pm$ and $e^{-2g(\overline{k_0}_\pm)}$ can be measured from the discrete version of Eq. (C.24) and Eq. (C.25) as follows:

$$\begin{aligned}
\overline{\sigma_k}_\pm &= \frac{\sqrt{\pi}}{a} \frac{\sum_n (\rho_\pm^n)^2}{\left(\sum_n \rho_\pm^n\right)^2}, \\
e^{-2g(\overline{k_0}_\pm)} &= \frac{\sigma_k}{\overline{\sigma_k}_\pm} \sum_n \rho_\pm^n.
\end{aligned} \tag{C.29}$$

With these quantities, one can calculate the coefficients A and B. The cross term can be measured as

$$\int_{-\infty}^{0} dx\, \rho_+ \rho_- \to \frac{1}{a} \sum_n w_n'\, \rho_+^n \rho_-^n, \tag{C.30}$$

with the weight function w'_n picking up only the charge density in the symmetric phase. This can then be used to calculate the phase shift observable using Eq. (C.28).

Some useful identities

The product of two normalized Gaussians is an (unnormalized) Gaussian:

$$N_{\sigma_1}(x;\mu_1)N_{\sigma_2}(x;\mu_2) = N_{\frac{\sigma_1\sigma_2}{\overline{\sigma}}}(\mu_1-\mu_2;0)N_{\overline{\sigma}}(x;\overline{\mu}) \tag{C.31}$$

with

$$\overline{\sigma} = \sqrt{\frac{\sigma_1^2\sigma_2^2}{\sigma_1^2+\sigma_2^2}}, \qquad \overline{\mu} = \frac{\mu_1\sigma_1^2+\mu_2\sigma_2^2}{\sigma_1^2+\sigma_2^2} \tag{C.32}$$

In particular, to compute the square of a Gaussian, we can set $\sigma_1 = \sigma_2 = \sigma$ and $\mu_1 = \mu_2 = \mu$ to get

$$N_\sigma(x;\mu)^2 = N_{\sigma\sqrt{2}}(0;0)N_{\frac{\sigma}{\sqrt{2}}}(x;\mu) = \frac{1}{2\sigma\sqrt{\pi}}N_{\frac{\sigma}{\sqrt{2}}}(x;\mu) \tag{C.33}$$

C.3 Wave packets on the lattice and time evolution

We prepare the initial wave packet as a superposition of plane waves defined on the full lattice in the absence of the bubble wall. Taking PBC, the Fourier transform takes the following form on the lattice for the staggered fermion:

$$\zeta_k = \begin{bmatrix}\zeta_1\\ \zeta_2\end{bmatrix}_k \equiv \frac{1}{\sqrt{N/2}}\sum_{j=1}^{N/2}\begin{bmatrix}\chi_{2j-1}\,e^{-i(2j-1)k}\\ \chi_{2j}\,e^{-i2jk}\end{bmatrix}, \tag{C.34}$$

The momentum modes satisfying PBC take the discrete values $k = -\frac{\pi}{2} + \frac{2\pi j}{N}$, $j = 1, 2, ..., N/2$. This leads to the lattice Hamiltonian given by

$$\hat{H}_{\text{PBC}} = \sum_k \zeta_k^\dagger \begin{pmatrix} 0 & \sin k \\ \sin k & 0 \end{pmatrix} \zeta_k. \tag{C.35}$$

We define $(c_k, d_{-k}^\dagger)^T \equiv V_k \zeta_k^T$, with V_k given by

$$V_k = \frac{1}{\sqrt{2}} \begin{pmatrix} 1 & \text{sign}(k) \\ -\text{sign}(k) & 1 \end{pmatrix}, \tag{C.36}$$

the Hamiltonian can be diagonalized as

$$\begin{aligned} \hat{H}_{\text{PBC}} &= \sum_k \epsilon_k \left(c_k^\dagger c_k - d_{-k} d_{-k}^\dagger \right) \\ &= \sum_k \epsilon_k \left(c_k^\dagger c_k + d_{-k}^\dagger d_{-k} \right) + \text{const}, \end{aligned} \tag{C.37}$$

with $\epsilon_k = |\sin k|$. $c_k^\dagger$ and $d_k^\dagger$ can be expressed in terms of the position space operators as

$$c_k^\dagger = \frac{1}{\sqrt{N}} \sum_{n=1}^{N} e^{ikn} \left[\Pi_{n0} + \text{sign}(k) \Pi_{n1} \right] \chi_n^\dagger, \tag{C.38}$$

$$d_k^\dagger = \frac{1}{\sqrt{N}} \sum_{n=1}^{N} e^{ikn} \left[\Pi_{n1} + \text{sign}(k) \Pi_{n0} \right] \chi_n, \tag{C.39}$$

where

$$\Pi_{nl} \equiv \frac{1 - (-1)^{n+l}}{2}, \quad l \in \{0, 1\}. \tag{C.40}$$

When acting on the vacuum, $\hat{\psi}_{k+}^\dagger \equiv c_k^\dagger$ and $\hat{\psi}_{k-}^\dagger \equiv d_k^\dagger$ create particle and antiparticle excitations with $P^\mu = (\epsilon_k, k)$. We can then construct the creation operators for the fermion

($C^\dagger$) and antifermion ($D^\dagger$) wave packets:

$$C^\dagger = \sum_k \hat{\psi}^\dagger_{k+} f_k = \sum_n \chi^\dagger_n \varphi_{n+}, \tag{C.41}$$

$$D^\dagger = \sum_k \hat{\psi}^\dagger_{k-} f_k = \sum_n \chi_n \varphi_{n-}, \tag{C.42}$$

with

$$\varphi_{n+} = \frac{1}{\sqrt{N}} \sum_k f_k e^{ikn} \left[\Pi_{n0} + \mathrm{sign}(k)\Pi_{n1}\right], \tag{C.43}$$

$$\varphi_{n-} = \frac{1}{\sqrt{N}} \sum_k f_k e^{ikn} \left[\Pi_{n1} + \mathrm{sign}(k)\Pi_{n0}\right]. \tag{C.44}$$

The initial wave packet $||\rangle\, \Psi_\pm(0) >$ is thus prepared by applying Eq. (C.41) or Eq. (C.42) to the ground state of the Hamiltonian in Eq. (4.31).

Time evolution

Staggered fermions in 1+1 dimensions can be mapped to a one-dimensional spin chain by Jordan-Wigner transformation [254],

$$\chi_n = \left(\prod_{s<n} i\sigma^z_s\right) \sigma^+_n, \qquad \chi^\dagger_n = \left(\prod_{s<n} -i\sigma^z_s\right) \sigma^-_n, \tag{C.45}$$

which ensures anti-commutation relations between different lattice sites. This leads to the following Hamiltonian:

$$\hat{H} = \sum_{n=1}^{N-1} h_{n,n+1} + h_N, \tag{C.46}$$

with $h_N = (-1)^{N+1}|m_N|\cos\theta_N \sigma_N^- \sigma_N^+$ and

$$h_{n,n+1} = \left[\frac{1}{2} + (-1)^n |m_n| \sin\theta_n\right](\sigma_{n+1}^- \sigma_n^+ + \sigma_n^- \sigma_{n+1}^+) - (-1)^n |m_n| \cos\theta_n \sigma_n^- \sigma_n^+. \tag{C.47}$$

The time evolution of this Hamiltonian can be efficiently implemented by Trotter decomposition. For our simulation, we employ second-order Trotterization [255]:

$$e^{-i\hat{H}\hat{\tau}} \approx e^{-ih_{1,2}\hat{\tau}/2} e^{-ih_{2,3}\hat{\tau}/2} \cdots e^{-ih_{N-1,N}\hat{\tau}/2} e^{-ih_N\hat{\tau}} e^{-ih_{N-1,N}\hat{\tau}/2} \cdots e^{-ih_{2,3}\hat{\tau}/2} e^{-ih_{1,2}\hat{\tau}/2} + \mathcal{O}(\hat{\tau}^3), \tag{C.48}$$

where $\hat{\tau} = \tau/a$ is the Trotter step in lattice units. The error for each time step is $\mathcal{O}(N\hat{\tau}^3)$ for Trotterizing H into N pairs of non-commuting terms. For total evolution time T, there are $N_t = T/\tau$ Trotter steps, thus the total error is $\mathcal{O}(NN_t\hat{\tau}^3)$.

A note on boundary conditions and momentum truncation. To ensure that the wave packet moves toward the bubble wall and avoids scattering with the lattice boundary in the direction opposite to the bubble, we truncate away the nonpositive k modes from the wave packet. This truncation will distort the wave packet from a perfect Gaussian shape, which will cause errors in measuring local observables. For $\theta_0 = 0$, where we can compare with exact analytic results, we find these truncation errors to be negligible. When $\theta_0 \neq 0$, where we study the asymmetry generation, we choose $k_0 \geq 2\sigma_k$ to ensure that the negative modes lie beyond $2\sigma_k$ from k_0, thereby diminishing the Gaussian shape distortion.

C.4 Systematic Uncertainties

In the simulations presented in Figs. 4.3–4.5, we fix the physical volume to $L = 28$ and extrapolate to the continuum limit $a \to 0$. In this appendix, we investigate the systematic

uncertainties associated with the finite-volume effects, which could be a dominant source of errors. We vary lattice spacing in the range $a \in \{\frac{1}{8}, \frac{1}{6}, \frac{1}{5}, \frac{1}{4}\}$ and physical volume $L \in \{20, 24, 28\}$.

C.4.1 Charge asymmetry of the initial state

We first check the charge asymmetry of the initial state consisting of the particle and antiparticle wave packets by measuring the magnitude asymmetry and phase asymmetry in the symmetric phase at $t = 0$, $\hat{\mathcal{Q}}_0$ and $\hat{\Phi}_0$. Using the same hyperbolic complex mass profile as in Figs. 4.4 and 4.5, we prepare the initial state and measure $\hat{\mathcal{Q}}_0$ and $\hat{\Phi}_0$. Since the wave packets have not yet interacted with the bubble wall, the θ_0 dependence of the initial state is expected to be very weak. In Figs. C.1 and C.2, we show as an example for $\theta_0 = \pi/3$, the measured values of $\hat{\mathcal{Q}}_0$ and $\hat{\Phi}_0$ at various lattice spacings and physical volumes. With these results, we first perform a linear fit of the two observables as a function of the lattice spacings a and extrapolate to the continuum limit $a \to 0$, as shown in the left panels of Figs. C.1 and C.2. We then perform a linear fit of the continuum limits as a function of the inverse physical volumes $1/L$ and extrapolate to the infinite-volume limit $1/L \to 0$, as shown in the right panels of Figs. C.1 and C.2. The extrapolation results are the "$\times$" points in the plots, with the error bars showing 1σ fitting errors. The deviation of the extrapolation results from zero quantifies the systematic uncertainties in the initial state preparation. These uncertainties can come from a charge-conjugation symmetry [C_- defined in Eq. (C.12)] breaking inherent to staggered fermions and finite-volume effects caused by the wave packet leaking into the broken phase where charge-conjugation symmetry is broken.

C.4.2 Asymmetry generation from scattering with step-function complex mass profile

We also investigate the systematic uncertainties associated with the scattering. For this investigation, we take the mass profile to be a step function for both magnitude and phase:

$$|m(x)| = \begin{cases} 0 & x \leq 0 \\ m_0 & x > 0 \end{cases}, \quad \theta(x) = \begin{cases} 0 & x \leq 0 \\ \theta_0 & x > 0 \end{cases}. \tag{C.49}$$

The complex phase of this profile, although nonvanishing in the broken phase, can be rotated away by a field redefinition without breaking other symmetries. Therefore, no asymmetry is expected to be generated in this case. Any deviation from zero for the asymmetry observables $\hat{\mathcal{Q}}_\infty$ and $\hat{\Phi}_\infty$ is thus a measure of systematic errors. In the following, we show the results for step-function mass profile with $m_0 = 1$ and θ_0 varying in the range $[0, \pi/2]$. With the results for various a and L, we first extrapolate to the continuum $a \to 0$ for each fixed L. Then to study finite-volume effects, we perform an infinite-volume extrapolation using a linear fit.

In Fig. C.3, we show the continuum limits at the largest physical volume $L = 28$, as well as the infinite-volume extrapolations of $\hat{\mathcal{Q}}_\infty$ and $\hat{\Phi}_\infty$, where the error bars represent 1σ errors from the infinite-volume linear fits. As expected from a step-function profile, the absolute values of $\hat{\mathcal{Q}}_\infty$ and $\hat{\Phi}_\infty$ are close to zero for $L = 28$. The measured magnitude asymmetry is of the order $\hat{\mathcal{Q}}_\infty \sim 10^{-3}$ while the phase asymmetry is $\hat{\Phi}_\infty \sim 10^{-2}$. This therefore provides an approximate measure of the absolute errors in our studies of the complex mass profile in Sec. 4.2.6. We expect that the nonvanishing asymmetry is likely due to finite-volume effects. Looking at the infinite-volume results in Fig. C.3, we observe that a simple linear $1/L \to 0$ extrapolation is not under control, sometimes leading to larger uncertainties compared to the continuum limit results at $L = 28$. Therefore, in this work, we work with a fixed physical volume of $L = 28$ and leave a more systematic analysis of the finite-volume effects for future

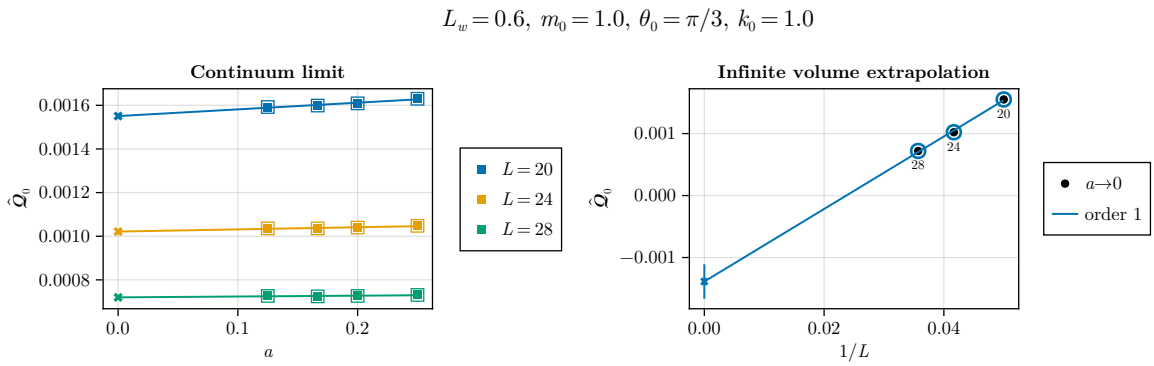


Figure C.1: Magnitude asymmetry of the initial state $\hat{\mathcal{Q}}_0$ for various lattice spacings and physical volumes. The mass profile is chosen to be the same one used for Figs. 4.4 and 4.5, with $\theta_0 = \pi/3$. For each physical volume L, we calculate the continuum limits by fitting $\hat{\mathcal{Q}}_0$ as a linear function of the lattice spacings a and extrapolating to $a = 0$. The continuum limits are then fitted as a linear function of the inverse lattice volume $1/L$ and extrapolated to the infinite-volume limit $1/L \to 0$. The deviation of the infinite-volume limit of $\hat{\mathcal{Q}}_0$ from zero measures the systematic uncertainty of the charge asymmetry in the initial state.

work.

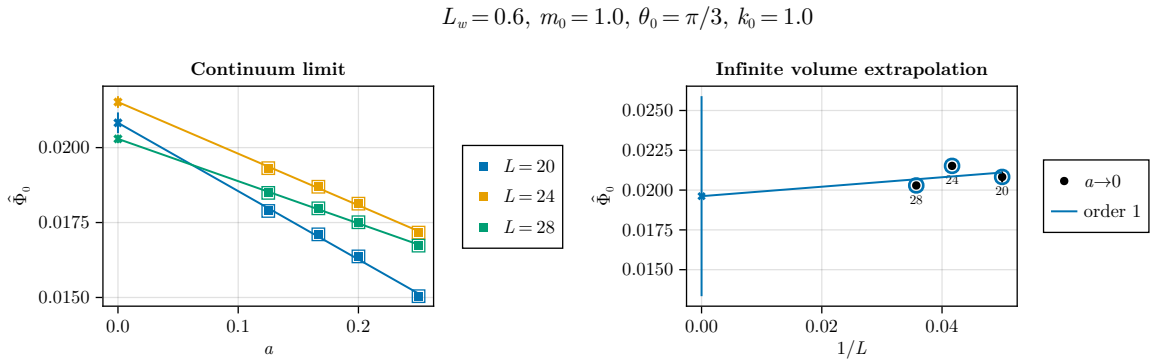


Figure C.2: Same as Fig. C.1 but for the phase asymmetry $\hat{\Phi}_0$ of the initial state.

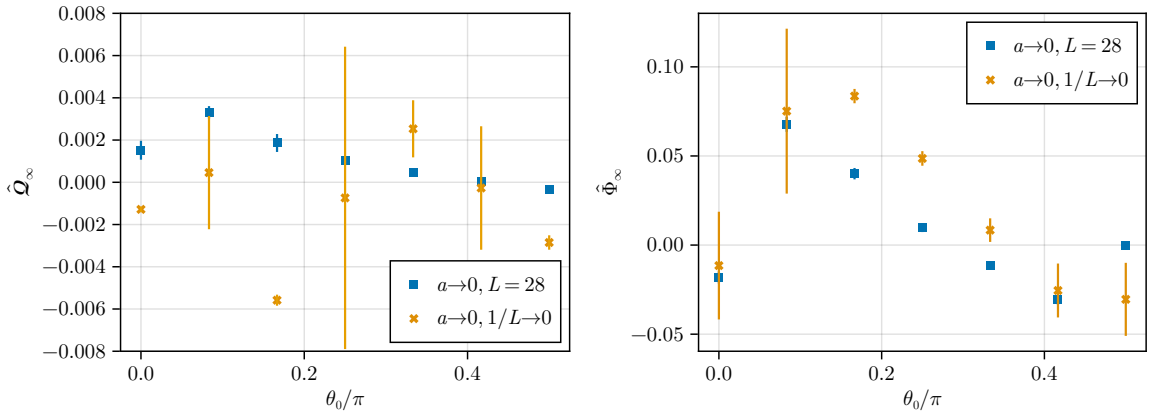


Figure C.3: The continuum limits at the largest physical volume $L = 28$ and the infinite-volume limits of $\hat{\mathcal{Q}}_\infty$ and $\hat{\Phi}_\infty$ generated from scattering with the step mass profiles with $m_0 = 1$ and θ_0 varying in the range $[0, \pi/2]$. The error bars represent the 1σ fitting errors.

APPENDIX D

APPENDICES FOR CHAPTER 5

D.1 Existing constraints

In this section, we consider the phenomenology of the BNV model introduced in Sec. 5.2. Since our focus is on baryon number violation, the starting point is naturally proton decay: it sets the scale at which new resonances should appear and guides the choice of experiment to test them, if any are available at all. In our case, this exercise will show that the scale in question is $\mathcal{O}(\text{TeV})$, which opens up a variety of low energy probes of this model that we then survey before discussing their implications on the predicted proton lifetime in our model.

D.1.1 Proton Decay

Let us begin our precise evaluation of the proton decay rate, focusing on important conceptual ideas here and leaving out the calculation details (interested readers can find the details in Appendix B of [51]). There are two relevant Feynman diagrams for the $p \to \overline{\nu\nu} e^+/\mu^+$ process, as shown in Figure (D.1). If the outgoing antineutrino flavours $l = m$, each of the diagrams will have a companion with the antineutrino momenta interchanged, $k_1 \leftrightarrow k_2$. To proceed, we split the amplitude as

$$\mathcal{M}_{p\to\bar{l}\overline{\nu\nu}} = \mathcal{M}^q_{p\to\bar{l}\overline{\nu\nu}} + \mathcal{M}^l_{p\to\bar{l}\overline{\nu\nu}}, \tag{D.1}$$

corresponding to the amplitudes for the left and right panels of Figure (D.1) respectively. These two diagrams carry a relative minus sign between them due to the antisymmetric contraction of $SU(2)$ indices in leptoquark-fermions interactions, causing destructive interference.

The amplitudes are proportional to two quark masses corresponding to the two chirality flips expected from an effective operator analysis [198]. The first of these is from an off-shell

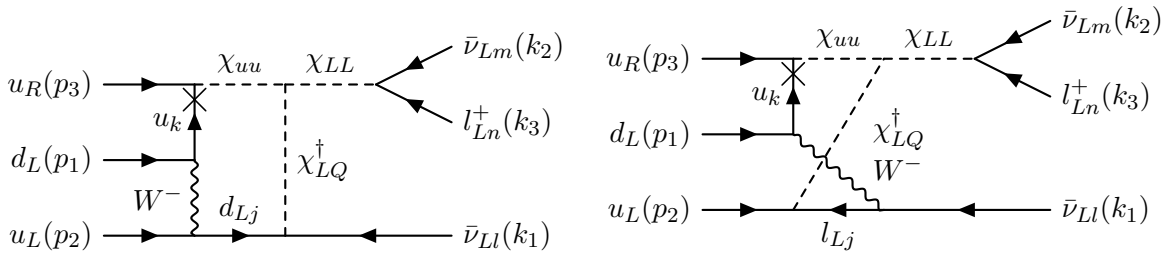


Figure D.1: Feynman diagrams for loop level proton decay, where j, k, l, m, n are flavour indices. A chirality flip along the u_k propagator is necessary to ensure the correct chirality on both vertices, which is induced by a mass insertion denoted by the $\times$. When the two antineutrinos are of the same flavour, $l = m$, each of these diagrams has a companion with $k_1 \leftrightarrow k_2$. On the upper panel, the W boson couples an incoming up quark and a virtual down type quark of flavour j. On the lower panel it couples an outgoing antineutrino and a virtual lepton of flavour j. Because of the $SU(2)$ index contraction of the leptoquark couplings, these two diagrams carry a relative minus sign between them and interfere destructively.

charm or top quark interacting with an up quark from the proton. Since this involves a diquark vertex, these are all right handed. However, the c or t must also attach to a left-handed d quark from the proton, so a chirality flip is required, as indicated by the cross in Figure (D.1). The second chirality flip occurs from the vector nature of the loop integral, which introduces factors of momentum "slashed" that can then be applied to quark fields — this is discussed in detail in Appendix B of [51]. Importantly, for the second chirality flip, the only non-zero contribution introduces a factor of the up quark mass, but we do not take it to be that of a free up quark as, in this case, it is the valence quark of a proton. Instead, we use the constituent quark mass [256, 257], which we denote by m_u^*, and set to one third the proton mass,[1]

$$m_u^* \simeq m_P/3.$$

It can be checked by explicit computation that with equal scalar masses and Yukawa couplings all set to unity, the existing limits on $p \to \overline{\nu\nu} e^+/\mu^+$ set a lower bound of about 1 TeV on the masses of the new scalar fields, well below the GUT scale and within reach of the LHC. This

1. The precise value, the determination of which requires detailed lattice calculations, has no appreciable effect on the proton decay rate.

lower bound, however, may be further weakened by the constraints from the baryon number conserving probes of the new scalars, which will be discussed in the following subsection.

D.1.2 Baryon Number Conserving Constraints

Let us now discuss the relevant baryon number conserving (BNC) constraints on the new scalar fields. A novel feature of our model is that there are some processes for which the leptoquark and the dilepton contribute together at the amplitude level. For example, measurements of the anomalous magnetic moment of leptons are sensitive to contributions from both of them. However, due to the maximally chiral nature of the Yukawas in our model, these are suppressed by $m_l^2/(m_{\chi_j} m_{\chi_k})$ [258], with $j,k = LL, LQ$, hence for $\mathcal{O}$(TeV) masses, these constraints are easily satisfied. A much stronger probe comes from their contributions to the decay of a muon into an electron and a photon, $\mu \to e\gamma$. This process has a predicted SM rate that renders it unobservable for all practical purposes and can therefore serve as a background-free and sensitive probe of new physics. Expressions for the $\mu \to e\gamma$ decay rate from theories with only one leptoquark or only one dilepton singlet have been computed in [222, 258, 259]. Making the simplifying assumption that $m_{\rm SM}/m_\chi \ll 1$, where $m_{\rm SM}$ is the mass of *any* SM fermion and m_χ is the mass of the dilepton singlet or leptoquark, the branching ratio for this decay mode can be written as

$$\begin{aligned}\mathrm{Br}_{\mu\to e\gamma} = 12\pi\alpha_{EM} \times \left(\frac{1}{m^2_{\chi_{LQ}} G_F}\right)^2 \times \\ \left[N_c^2 \left(\frac{Q_{LQ}}{4} - \frac{1}{6}\right) \sum_{j=1}^{3} y^{*\mu j}_{LQ} y^{ej}_{LQ} + \frac{m^2_{\chi_{LQ}}}{m^2_{\chi_{LL}}} \left(\frac{Q_{LL}}{4} - \frac{1}{6}\right) y^{*e\tau}_{LL} y^{\mu\tau}_{LL}\right]^2 , \end{aligned} \tag{D.2}$$

where $Q_{LQ} = -1/3$ and $Q_{LL} = +1$ are the electromagnetic charges of the leptoquark and the dilepton respectively, and $N_c = 3$ is the colour factor. From this expression, it can be checked that if the Yukawa couplings of the leptoquark and/or the dilepton to muons and

electrons are set to unity, the combined limit of

$$\mathrm{Br}_{\mu\to e\gamma} < 3\times 10^{-13}$$

reported by the MEG [260] and MEG II [261] experiments, requires these two scalars to be heavier than $\mathcal{O}(10)$ TeV. We note that the lowest order diagram for the $\mu \to e\gamma$ process via the dilepton singlet must involve a τ neutrino that couples to both μ and e. To accommodate this stringent constraint, we set $y^{e\tau}_{LL} = 10^{-3}$ for the benchmark used for the collider simulation and baryogenesis estimation in Chapter 5, allowing for $m_{\chi_{LL}} \sim \mathcal{O}(\mathrm{TeV})$. For the leptoquark, we assume that they couple diagonally across the lepton and quark families, except for the top quark for which we allow, in addition to its coupling to the τ lepton, an $\mathcal{O}(1)$ coupling to the muons. This choice of parameters prohibits lepton flavour violation at tree level and satisfies the above mentioned limit on the $\mu \to e\gamma$ branching fraction.[2] This is also a common choice in the LHC searches for leptoquark [262–264].

Next, we discuss the remaining constraints on the leptoquark χ_{LQ}. The tree-level interactions between the leptoquark and the fermions produce dimension six low energy effective operators such as

$$\mathcal{L}_{\text{eff}} = \frac{c_{ijkm}}{m^2_{\chi_{LQ}}} \left(\overline{u}^i_L \gamma^\mu d^j_L\right) \left(\bar{l}^k_L \gamma_\mu \nu^m_L\right),$$

that contribute to leptonic and semi-leptonic meson decays as well as τ lepton decays. In the expression above, i, j and k, m label quark and lepton flavours respectively, and c_{ijkm} is the Wilson coefficient that results from integrating out the leptoquark. There are stringent limits on these effective operators from rare meson decays, an up to date review of which can be found in [4], which we summarize in Table D.1. For the remainder of this work, we focus on those with preferential couplings to the third generation quarks and/or leptons, particularly

2. We note the rather uninteresting possibility that fine tuning between the sum of leptoquark Yukawas and that of the dilepton singlet to the τ generation in the limit of nearly degenerate scalar masses can lead to cancellations that provide a further avenue to avoid the stringent constraints from observed limits on the rate for the $\mu \to e\gamma$ process. However, we choose not to chase that particular ambulance in this work.

Yukawa Coupling	Limits
y_{LQ}^{ue}	$y_{LQ}^{ue} < 0.3\ (m_{\chi_{LQ}}/\text{TeV})$
$y_{LQ}^{c\mu}$	$y_{LQ}^{c\mu} < 0.8\ (m_{\chi_{LQ}}/\text{TeV})$

Table D.1: Summary of existing constraints on the leptoquark reproduced from [4]. Cross-generational couplings of light quarks to light leptons are set to zero to avoid lepton flavour violation constraints such as the $\mu \to e\gamma$ process discussed previously. Top quark couplings to the muon and τ leptons are set to unity while that to the electrons is set to zero for consistency with $\mu \to e\gamma$ limits. See the text for more details.

the top quark. In contrast to the leptoquark couplings to the lighter quarks, those to the top quark can only be efficiently probed through their decay to top quarks at the LHC. Such leptoquarks can be produced in pairs via gluon fusion, a channel that is independent of any Yukawa couplings (the production part) and has been searched for by both the ATLAS and CMS experiments [262, 263]. In particular, the ATLAS experiment set a limit of 1.48 TeV, 1.47 TeV, and 1.43 TeV for scalar leptoquarks decaying to a top quark and an electron, a top quark and a muon, and a top quark and a τ lepton respectively [262, 264] with unit Yukawa couplings.

Yukawa Coupling	Limits
$y_{LL}^{e\mu}$	$y_{LL}^{e\mu} < 0.08\ (m_{\chi_{LL}}/\text{TeV})$
$y_{LL}^{\mu\tau}$	$\sqrt{\lvert\lvert y_{LL}^{\mu\tau}\rvert^2 - \lvert y_{LL}^{e\mu}\rvert^2\rvert} < 0.2\ (m_{\chi_{LL}}/\text{TeV})$
$y_{LL}^{e\tau}$	$y_{LL}^{e\tau} < 0.001$. See $\mu \to e\gamma$ for details.

Table D.2: Summary of existing constraints on the dilepton singlet from [5]. See the text for more details.

Then, we have the dilepton singlet χ_{LL}. This scalar field *necessarily* violates lepton flavor at tree level, making it particularly sensitive to experiments searching for lepton flavor violation or testing lepton flavour universality, particularly in τ decays. Using measurements of leptonic vs. hadronic universality in meson decays and e/μ universality in τ decays reported in [265], the authors of [5] obtained limits on $y_{LL}^{e\mu}$ and $y_{LL}^{\mu\tau}$, respectively. We list these limits and the limits from $\mu \to e\gamma$ in Table D.2 for convenience. For the benchmark used for collider simulation, we set $y_{LL}^{\mu\tau} = 0.325$ to saturate the lepton universality limit, while also satisfying

$\mu \to e\gamma$.

Finally, we discuss the constraints on χ_{uu}. There are 3 Yukawa couplings, y^{uc}_{uu}, y^{ut}_{uu} and y^{ct}_{uu}. For the latter two, there are constraints from the $\Delta F = 2$ processes from flavour physics, particularly $D_0 \to \overline{D}_0$ mixing. As explained in [221], such processes occur at the one-loop level and, due to the chirality and anti-symmetric nature of the couplings, necessarily involve a box diagram of two diquarks and two top quarks. The authors of [220, 221] find particularly tight constraints on the up-top and charm-top Yukawas,

$$|y^{ut}_{uu} y^{ct}_{uu}| \times \frac{m_{\chi_{uu}}}{\text{TeV}} \leq 1.5 \times 10^{-2}. \tag{D.3}$$

These bounds do not affect the main production channel for diquarks at the LHC, the s-channel process $u\ c \to \chi^{\dagger}_{uu}$, but favor dijet final states instead of top and jet ones. The former has been searched for by both the ATLAS and CMS experiments [2, 3], providing strong constraints on χ_{uu} that are relevant to our model. These constraints, however, would be weakened by the extra BNV decay mode $\chi^{\dagger}_{uu} \to \chi^{\dagger}_{LL}\chi_{LQ}$ if it is kinematically allowed. We will apply the dijet constraints to our studies of collider phenomenology to be discussed in the next section. For diquark masses above 3 TeV, Yukawa couplings $|y^{uc}_{uu}| = 0.25$ are allowed by existing dijet searches, and we adopt this benchmark for the calculations in Chapter 5.

REFERENCES

[1] Benoit Laurent and James M. Cline. First principles determination of bubble wall velocity. *Phys. Rev. D*, 106(2):023501, 2022. doi:10.1103/PhysRevD.106.023501.

[2] Search for New Phenomena in Dijet Events using 139 fb^{-1} of pp collisions at $\sqrt{s} =$ 13TeV collected with the ATLAS Detector. Technical report, CERN, Geneva, 2019. URL https://cds.cern.ch/record/2668385.

[3] Albert M Sirunyan et al. Search for high mass dijet resonances with a new background prediction method in proton-proton collisions at $\sqrt{s} = 13$ TeV. *JHEP*, 05:033, 2020. doi:10.1007/JHEP05(2020)033.

[4] S. Navas et al. Review of particle physics. *Phys. Rev. D*, 110(3):030001, 2024. doi:10.1103/PhysRevD.110.030001.

[5] Juan Herrero-Garcia, Miguel Nebot, Nuria Rius, and Arcadi Santamaria. The Zee–Babu model revisited in the light of new data. *Nucl. Phys. B*, 885:542–570, 2014. doi:10.1016/j.nuclphysb.2014.06.001.

[6] N. Aghanim et al. Planck 2018 results. VI. Cosmological parameters. *Astron. Astrophys.*, 641:A6, 2020. doi:10.1051/0004-6361/201833910. [Erratum: Astron.Astrophys. 652, C4 (2021)].

[7] Brian D. Fields, Keith A. Olive, Tsung-Han Yeh, and Charles Young. Big-Bang Nucleosynthesis after Planck. *JCAP*, 03:010, 2020. doi:10.1088/1475-7516/2020/03/010. [Erratum: JCAP 11, E02 (2020)].

[8] Dietrich Bodeker and Wilfried Buchmuller. Baryogenesis from the weak scale to the grand unification scale. *Rev. Mod. Phys.*, 93(3):035004, 2021. doi:10.1103/RevModPhys.93.035004.

[9] Tsung-Han Yeh, Keith A. Olive, Brian D. Fields, Erik Aver, Richard W. Pogge, Noah S. J. Rogers, Evan D. Skillman, and Miqaela K. Weller. The LBT $Y_{\rm p}$ Project V: Cosmological Implications of a New Determination of Primordial ^{4}He. 1 2026.

[10] A. D. Sakharov. Violation of CP Invariance, C asymmetry, and baryon asymmetry of the universe. *Pisma Zh. Eksp. Teor. Fiz.*, 5:32–35, 1967. doi:10.1070/PU1991v034n05ABEH002497.

[11] Gerard 't Hooft. Symmetry Breaking Through Bell-Jackiw Anomalies. *Phys. Rev. Lett.*, 37:8–11, 1976. doi:10.1103/PhysRevLett.37.8.

[12] C. Jarlskog. Commutator of the quark mass matrices in the standard electroweak model and a measure of maximal cp nonconservation. *Phys. Rev. Lett.*, 55:1039, 1985.

[13] C. Jarlskog. A basis independent formulation of the connection between quark mass matrices, cp violation and experiment. *Z. Phys. C*, 29:491, 1985.

[14] James M. Cline. Baryogenesis. In *Les Houches Summer School - Session 86: Particle Physics and Cosmology: The Fabric of Spacetime*, 9 2006.

[15] V.A. Kuzmin, V.A. Rubakov, and M.E. Shaposhnikov. On anomalous electroweak baryon-number non-conservation in the early universe. *Physics Letters B*, 155(1):36 – 42, 1985. ISSN 0370-2693. doi:https://doi.org/10.1016/0370-2693(85)91028-7. URL http://www.sciencedirect.com/science/article/pii/0370269385910287.

[16] Andrew G. Cohen, David B. Kaplan, and Ann E. Nelson. Weak scale baryogenesis. *Physics Letters B*, 245(3):561 – 564, 1990. ISSN 0370-2693. doi:https://doi.org/10.1016/0370-2693(90)90690-8. URL http://www.sciencedirect.com/science/article/pii/0370269390906908.

[17] K. Kajantie, K. Rummukainen, and Mikhail E. Shaposhnikov. A Lattice Monte Carlo

study of the hot electroweak phase transition. *Nucl. Phys. B*, 407:356–372, 1993. doi:10.1016/0550-3213(93)90062-T.

[18] K. Farakos, K. Kajantie, K. Rummukainen, and Mikhail E. Shaposhnikov. The Electroweak phase transition at m(H) approximately = m(W). *Phys. Lett. B*, 336: 494–501, 1994. doi:10.1016/0370-2693(94)90563-0.

[19] Karl Jansen. Status of the Finite Temperature Electroweak Phase Transition on the Lattice. *Nuclear Physics B - Proceedings Supplements*, 47:196–211, 1996. doi:10.1016/0920-5632(96)00045-X.

[20] K. Kajantie, M. Laine, K. Rummukainen, and Mikhail E. Shaposhnikov. The Electroweak phase transition: A Nonperturbative analysis. *Nucl. Phys. B*, 466:189–258, 1996. doi:10.1016/0550-3213(96)00052-1.

[21] K. Rummukainen. Finite T Electroweak Phase Transition on the Lattice. *Nuclear Physics B - Proceedings Supplements*, 53:30–42, 1997. doi:10.1016/S0920-5632(96)00597-X.

[22] K. Kajantie, M. Laine, K. Rummukainen, and Mikhail E. Shaposhnikov. Is there a hot electroweak phase transition at $m_H \gtrsim m_W$? *Phys. Rev. Lett.*, 77:2887–2890, 1996. doi:10.1103/PhysRevLett.77.2887.

[23] M. Gurtler, Ernst-Michael Ilgenfritz, and A. Schiller. Where the electroweak phase transition ends. *Phys. Rev. D*, 56:3888–3895, 1997. doi:10.1103/PhysRevD.56.3888.

[24] F. Csikor, Z. Fodor, and J. Heitger. Endpoint of the hot electroweak phase transition. *Phys. Rev. Lett.*, 82:21–24, 1999. doi:10.1103/PhysRevLett.82.21.

[25] M. Laine and K. Rummukainen. A Strong electroweak phase transition up to m(H) is about 105-GeV. *Phys. Rev. Lett.*, 80:5259–5262, 1998. doi:10.1103/PhysRevLett.80.5259.

[26] M. Laine and K. Rummukainen. The MSSM Electroweak Phase Transition on the Lattice. *Nuclear Physics B*, 535:423–457, 1998. doi:10.1016/S0550-3213(98)00530-6.

[27] K. Rummukainen, M. Tsypin, K. Kajantie, M. Laine, and Mikhail E. Shaposhnikov. The Universality class of the electroweak theory. *Nucl. Phys. B*, 532:283–314, 1998. doi:10.1016/S0550-3213(98)00494-5.

[28] Z. Fodor. Electroweak Phase Transitions. *Nuclear Physics B - Proceedings Supplements*, 83–84:121–125, 2000. doi:10.1016/S0920-5632(00)91603-7.

[29] J. R. Espinosa and M. Quiros. The Electroweak phase transition with a singlet. *Phys. Lett. B*, 305:98–105, 1993. doi:10.1016/0370-2693(93)91111-Y.

[30] Massimo Pietroni. The Electroweak phase transition in a nonminimal supersymmetric model. *Nucl. Phys. B*, 402:27–45, 1993. doi:10.1016/0550-3213(93)90635-3.

[31] M. Carena, M. Quiros, and C. E. M. Wagner. Opening the window for electroweak baryogenesis. *Phys. Lett. B*, 380:81–91, 1996.

[32] C. Grojean, G. Servant, and J. D. Wells. First order electroweak phase transition in the standard model with a low cutoff. *Phys. Rev. D*, 71:036001, 2005.

[33] Stefano Profumo, Michael J. Ramsey-Musolf, and Gabe Shaughnessy. Singlet Higgs phenomenology and the electroweak phase transition. *JHEP*, 08:010, 2007. doi:10.1088/1126-6708/2007/08/010.

[34] A. Noble and M. Perelstein. Higgs self-coupling as a probe of the electroweak phase transition. *Phys. Rev. D*, 78:063518, 2008.

[35] G. C. Dorsch, S. J. Huber, and J. M. No. A strong electroweak phase transition in the 2hdm. *JHEP*, 1310:029, 2013.

[36] P. Basler, M. Krause, M. Muhlleitner, J. Wittbrodt, and A. Wlotzka. Strong First Order Electroweak Phase Transition in the CP-Conserving 2HDM Revisited. *JHEP*, 02:121, 2017. doi:10.1007/JHEP02(2017)121.

[37] David Curtin, Patrick Meade, and Chiu-Tien Yu. Testing Electroweak Baryogenesis with Future Colliders. *JHEP*, 11:127, 2014. doi:10.1007/JHEP11(2014)127.

[38] D. E. Morrissey and M. J. Ramsey-Musolf. Electroweak baryogenesis. *New J. Phys.*, 14:125003, 2012.

[39] M. Fukugita and T. Yanagida. Baryogenesis without grand unification. *Phys. Lett. B*, 174:45–47, 1986. doi:10.1016/0370-2693(86)91126-3.

[40] L. Covi, E. Roulet, and F. Vissani. Cp violating decays in leptogenesis scenarios. *Phys. Lett. B*, 384:169–174, 1996.

[41] A. Pilaftsis. Cp violation and baryogenesis due to heavy majorana neutrinos. *Phys. Rev. D*, 56:5431–5451, 1997.

[42] W. Buchmuller, P. Di Bari, and M. Plumacher. Leptogenesis for pedestrians. *Annals Phys.*, 315:305–351, 2005.

[43] G. F. Giudice, A. Notari, M. Raidal, A. Riotto, and A. Strumia. Towards a complete theory of thermal leptogenesis in the sm and mssm. *Nucl. Phys. B*, 685:89–149, 2004.

[44] S. Davidson, E. Nardi, and Y. Nir. Leptogenesis. *Phys. Rept.*, 466:105–177, 2008.

[45] A. Takenaka et al. Search for proton decay via $p \to e^+\pi^0$ and $p \to \mu^+\pi^0$ with an enlarged fiducial volume in Super-Kamiokande I-IV. *Phys. Rev. D*, 102(11):112011, 2020. doi:10.1103/PhysRevD.102.112011.

[46] C. McGrew et al. Search for nucleon decay using the IMB-3 detector. *Phys. Rev. D*, 59:052004, 1999. doi:10.1103/PhysRevD.59.052004.

[47] K. S. Hirata et al. Experimental Limits on Nucleon Lifetime for Lepton + Meson Decay Modes. *Phys. Lett. B*, 220:308–316, 1989. doi:10.1016/0370-2693(89)90058-0.

[48] K. Abe et al. Search for proton decay via $p \to \nu K^+$ using 260 kiloton·year data of Super-Kamiokande. *Phys. Rev. D*, 90(7):072005, 2014. doi:10.1103/PhysRevD.90.072005.

[49] K. Kobayashi et al. Search for nucleon decay via modes favored by supersymmetric grand unification models in Super-Kamiokande-I. *Phys. Rev. D*, 72:052007, 2005. doi:10.1103/PhysRevD.72.052007.

[50] K. S. Babu, R. N. Mohapatra, and S. Nasri. Post-Sphaleron Baryogenesis. *Phys. Rev. Lett.*, 97:131301, 2006. doi:10.1103/PhysRevLett.97.131301.

[51] Amit Bhoonah, Francis Burk, Da Liu, Tong Ou, and Deepak Sathyan. A Baryon and Lepton Number Violation Model Testable at the LHC. 8 2025.

[52] Marcela Carena, Aurora Ireland, Tong Ou, and Isaac R. Wang. The discriminant power of bubble wall velocities: gravitational waves and electroweak baryogenesis. *JHEP*, 09: 175, 2025. doi:10.1007/JHEP09(2025)175.

[53] David Curtin, Patrick Meade, and Harikrishnan Ramani. Thermal resummation and phase transitions. *The European Physical Journal C*, 78(9):1–29, 2018.

[54] J. R. Espinosa, M. Quiros, and F. Zwirner. On the nature of the electroweak phase transition. *Phys. Lett. B*, 314:206–216, 1993. doi:10.1016/0370-2693(93)90450-V.

[55] Mariano Quiros. Finite temperature field theory and phase transitions. *Proceedings, Summer school in high-energy physics and cosmology: Trieste, Italy*, 1999:187–259, 1998.

[56] Rajesh R. Parwani. Resummation in a hot scalar field theory. *Phys. Rev. D*, 45:4695, 1992. doi:10.1103/PhysRevD.45.4695. [Erratum: Phys.Rev.D 48, 5965 (1993)].

[57] Peter Brockway Arnold and Olivier Espinosa. The Effective potential and first order phase transitions: Beyond leading-order. *Phys. Rev. D*, 47:3546, 1993. doi:10.1103/PhysRevD.47.3546. [Erratum: Phys.Rev.D 50, 6662 (1994)].

[58] Henning Bahl, Marcela Carena, Aurora Ireland, and Carlos E. M. Wagner. Improved thermal resummation for multi-field potentials. *JHEP*, 09:153, 2024. doi:10.1007/JHEP09(2024)153.

[59] Pedro Bittar, Subhojit Roy, and Carlos E. M. Wagner. Self Consistent Thermal Resummation: A Case Study of the Phase Transition in 2HDM. 4 2025.

[60] Ryogo Kubo. Statistical-mechanical theory of irreversible processes. i. general theory and simple applications to magnetic and conduction problems. *Journal of the Physical Society of Japan*, 12(6):570–586, 1957. doi:10.1143/JPSJ.12.570.

[61] Paul C. Martin and Julian Schwinger. Theory of many-particle systems. i. *Physical Review*, 115(6):1342–1373, 1959. doi:10.1103/PhysRev.115.1342.

[62] Shyam Balaji, Michael Spannowsky, and Carlos Tamarit. Cosmological bubble friction in local equilibrium. *JCAP*, 03:051, 2021. doi:10.1088/1475-7516/2021/03/051.

[63] Wen-Yuan Ai, Bjorn Garbrecht, and Carlos Tamarit. Bubble wall velocities in local equilibrium. *JCAP*, 03(03):015, 2022. doi:10.1088/1475-7516/2022/03/015.

[64] Jose R. Espinosa, Thomas Konstandin, Jose M. No, and Geraldine Servant. Energy Budget of Cosmological First-order Phase Transitions. *JCAP*, 06:028, 2010. doi:10.1088/1475-7516/2010/06/028.

[65] Thomas Konstandin and Jose M. No. Hydrodynamic obstruction to bubble expansion. *JCAP*, 02:008, 2011. doi:10.1088/1475-7516/2011/02/008.

[66] Dietrich Bodeker and Guy D. Moore. Electroweak Bubble Wall Speed Limit. *JCAP*, 05:025, 2017. doi:10.1088/1475-7516/2017/05/025.

[67] Wen-Yuan Ai, Benoit Laurent, and Jorinde van de Vis. Model-independent bubble wall velocities in local thermal equilibrium. *JCAP*, 07:002, 2023. doi:10.1088/1475-7516/2023/07/002.

[68] Wen-Yuan Ai, Xander Nagels, and Miguel Vanvlasselaer. Criterion for ultra-fast bubble walls: the impact of hydrodynamic obstruction. *JCAP*, 03:037, 2024. doi:10.1088/1475-7516/2024/03/037.

[69] Tomasz Krajewski, Marek Lewicki, and Mateusz Zych. Bubble-wall velocity in local thermal equilibrium: hydrodynamical simulations vs analytical treatment. *JHEP*, 05: 011, 2024. doi:10.1007/JHEP05(2024)011.

[70] Tomasz Krajewski, Marek Lewicki, Ignacy Nałęcz, and Mateusz Zych. Steady-state bubbles beyond local thermal equilibrium. *JHEP*, 06:118, 2025. doi:10.1007/JHEP06(2025)118.

[71] John McDonald. Electroweak baryogenesis and dark matter via a gauge singlet scalar. *Phys. Lett. B*, 323:339–346, 1994. doi:10.1016/0370-2693(94)91229-7.

[72] Jarny Choi and R. R. Volkas. Real Higgs singlet and the electroweak phase transition in the Standard Model. *Phys. Lett.*, B317:385–391, 1993. doi:10.1016/0370-2693(93)91013-D.

[73] Jose Ramon Espinosa and Mariano Quiros. Novel Effects in Electroweak Breaking from a Hidden Sector. *Phys. Rev. D*, 76:076004, 2007. doi:10.1103/PhysRevD.76.076004.

[74] Jose R. Espinosa, Thomas Konstandin, and Francesco Riva. Strong Electroweak Phase Transitions in the Standard Model with a Singlet. *Nucl. Phys. B*, 854:592–630, 2012. doi:10.1016/j.nuclphysb.2011.09.010.

[75] James M. Cline, Kimmo Kainulainen, Pat Scott, and Christoph Weniger. Update on scalar singlet dark matter. *Phys. Rev. D*, 88:055025, 2013. doi:10.1103/PhysRevD.88.055025. [Erratum: Phys.Rev.D 92, 039906 (2015)].

[76] P. H. Damgaard, A. Haarr, D. O'Connell, and A. Tranberg. Effective Field Theory and Electroweak Baryogenesis in the Singlet-Extended Standard Model. *JHEP*, 02:107, 2016. doi:10.1007/JHEP02(2016)107.

[77] Gowri Kurup and Maxim Perelstein. Dynamics of Electroweak Phase Transition In Singlet-Scalar Extension of the Standard Model. *Phys. Rev. D*, 96(1):015036, 2017. doi:10.1103/PhysRevD.96.015036.

[78] Cheng-Wei Chiang, Yen-Ting Li, and Eibun Senaha. Revisiting electroweak phase transition in the standard model with a real singlet scalar. *Phys. Lett. B*, 789:154–159, 2019. doi:10.1016/j.physletb.2018.12.017.

[79] Marcela Carena, Zhen Liu, and Yikun Wang. Electroweak phase transition with spontaneous Z_2-breaking. *JHEP*, 08:107, 2020. doi:10.1007/JHEP08(2020)107.

[80] Avi Friedlander, Ian Banta, James M. Cline, and David Tucker-Smith. Wall speed and shape in singlet-assisted strong electroweak phase transitions. *Phys. Rev. D*, 103(5): 055020, 2021. doi:10.1103/PhysRevD.103.055020.

[81] Pouya Asadi, Eric David Kramer, Eric Kuflik, Gregory W. Ridgway, Tracy R. Slatyer, and Juri Smirnov. Thermal squeezeout of dark matter. *Phys. Rev. D*, 104(9):095013, 2021. doi:10.1103/PhysRevD.104.095013.

[82] James M. Cline, Avi Friedlander, Dong-Ming He, Kimmo Kainulainen, Benoit Laurent, and David Tucker-Smith. Baryogenesis and gravity waves from a UV-completed electroweak phase transition. *Phys. Rev. D*, 103(12):123529, 2021. doi:10.1103/PhysRevD.103.123529.

[83] Vitaly Andreev and NR Hutzler. Improved limit on the electric dipole moment of the electron. *Nature*, 562(7727):355–360, 2018.

[84] J. Baron, W. C. Campbell, D. DeMille, J. M. Doyle, G. Gabrielse, Y. V. Gurevich, P. W. Hess, N. R. Hutzler, E. Kirilov, I. Kozyryev, B. R. O'Leary, C. D. Panda, M. F. Parsons, E. S. Petrik, B. Spaun, A. C. Vutha, and A. D. West. Order of magnitude smaller limit on the electric dipole moment of the electron. *Science*, 343 (6168):269–272, 2014. ISSN 0036-8075. doi:10.1126/science.1248213. URL https://science.sciencemag.org/content/343/6168/269.

[85] Marcela Carena, Mariano Quirós, and Yue Zhang. Electroweak baryogenesis from dark-sector c p violation. *Physical Review Letters*, 122(20):201802, 2019.

[86] Marcela Carena, Mariano Quirós, and Yue Zhang. Dark c p violation and gauged lepton or baryon number for electroweak baryogenesis. *Physical Review D*, 101(5):055014, 2020.

[87] Marcela Carena, Ying-Ying Li, Tong Ou, and Yikun Wang. Anatomy of the electroweak phase transition for dark sector induced baryogenesis. *JHEP*, 02:139, 2023. doi:10.1007/JHEP02(2023)139.

[88] Pavel Fileviez Perez and Mark B. Wise. Breaking Local Baryon and Lepton Number at the TeV Scale. *JHEP*, 08:068, 2011. doi:10.1007/JHEP08(2011)068.

[89] Michael Duerr, Pavel Fileviez Perez, and Mark B. Wise. Gauge Theory for Baryon and Lepton Numbers with Leptoquarks. *Phys. Rev. Lett.*, 110:231801, 2013. doi:10.1103/PhysRevLett.110.231801.

[90] Marcela Carena, Mariano Quirós, and Yue Zhang. Dark CP violation and gauged lepton or baryon number for electroweak baryogenesis. *Phys. Rev. D*, 101(5):055014, 2020. doi:10.1103/PhysRevD.101.055014.

[91] Diego Restrepo, Andrés Rivera, and Walter Tangarife. Dirac dark matter, neutrino masses, and dark baryogenesis. *Phys. Rev. D*, 106(5):055021, 2022. doi:10.1103/PhysRevD.106.055021.

[92] Pavel Fileviez Perez, Sebastian Ohmer, and Hiren H. Patel. Minimal Theory for Lepto-Baryons. *Phys. Lett. B*, 735:283–287, 2014. doi:10.1016/j.physletb.2014.06.057.

[93] Pavel Fileviez Pérez, Clara Murgui, and Alexis D. Plascencia. Neutrino-Dark Matter Connections in Gauge Theories. *Phys. Rev. D*, 100(3):035041, 2019. doi:10.1103/PhysRevD.100.035041.

[94] Jonathan Kozaczuk, Michael J. Ramsey-Musolf, and Jessie Shelton. Exotic Higgs boson decays and the electroweak phase transition. *Phys. Rev. D*, 101(11):115035, 2020. doi:10.1103/PhysRevD.101.115035.

[95] Carroll L Wainwright. Cosmotransitions: computing cosmological phase transition temperatures and bubble profiles with multiple fields. *Computer Physics Communications*, 183(9):2006–2013, 2012.

[96] Bohdan Grzadkowski and Da Huang. Spontaneous CP-Violating Electroweak Baryogenesis and Dark Matter from a Complex Singlet Scalar. *JHEP*, 08:135, 2018. doi:10.1007/JHEP08(2018)135.

[97] Michael Joyce, Tomislav Prokopec, and Neil Turok. Efficient electroweak baryogenesis from lepton transport. *Phys. Lett. B*, 338:269–275, 1994. doi:10.1016/0370-2693(94)91377-3.

[98] Michael Joyce, Tomislav Prokopec, and Neil Turok. Nonlocal electroweak baryogenesis. Part 1: Thin wall regime. *Phys. Rev. D*, 53:2930–2957, 1996. doi:10.1103/PhysRevD.53.2930.

[99] Michael Joyce, Tomislav Prokopec, and Neil Turok. Nonlocal electroweak baryogenesis. Part 2: The Classical regime. *Phys. Rev. D*, 53:2958–2980, 1996. doi:10.1103/PhysRevD.53.2958.

[100] James M. Cline, Kimmo Kainulainen, and Axel P. Vischer. Dynamics of two Higgs doublet CP violation and baryogenesis at the electroweak phase transition. *Phys. Rev. D*, 54:2451–2472, 1996. doi:10.1103/PhysRevD.54.2451.

[101] James M. Cline, Michael Joyce, and Kimmo Kainulainen. Supersymmetric electroweak baryogenesis. *JHEP*, 07:018, 2000. doi:10.1088/1126-6708/2000/07/018.

[102] Lars Fromme and Stephan J. Huber. Top transport in electroweak baryogenesis. *JHEP*, 03:049, 2007. doi:10.1088/1126-6708/2007/03/049.

[103] Patrick Huet and Eric Sather. Electroweak Baryogenesis and Standard Model CP Violation. *Physical Review D*, 51:379–394, 1995. doi:10.1103/PhysRevD.51.379.

[104] Patrick Huet and Ann E. Nelson. Electroweak baryogenesis in supersymmetric models. *Phys. Rev. D*, 53:4578–4597, 1996. doi:10.1103/PhysRevD.53.4578.

[105] Antonio Riotto. Towards a nonequilibrium quantum field theory approach to electroweak baryogenesis. *Phys. Rev. D*, 53:5834–5841, 1996. doi:10.1103/PhysRevD.53.5834.

[106] A. Riotto. The More relaxed supersymmetric electroweak baryogenesis. *Phys. Rev. D*, 58:095009, 1998. doi:10.1103/PhysRevD.58.095009.

[107] Christopher Lee, Vincenzo Cirigliano, and Michael J. Ramsey-Musolf. Resonant relaxation in electroweak baryogenesis. *Phys. Rev. D*, 71:075010, 2005. doi:10.1103/PhysRevD.71.075010.

[108] Kimmo Kainulainen. CP-violating transport theory for electroweak baryogenesis with thermal corrections. *JCAP*, 11(11):042, 2021. doi:10.1088/1475-7516/2021/11/042.

[109] Marieke Postma, Jorinde van de Vis, and Graham White. Resummation and cancellation of the VIA source in electroweak baryogenesis. *JHEP*, 12:121, 2022. doi:10.1007/JHEP12(2022)121.

[110] James M. Cline and Kimmo Kainulainen. Electroweak baryogenesis at high bubble wall velocities. *Phys. Rev. D*, 101(6):063525, 2020. doi:10.1103/PhysRevD.101.063525.

[111] Kohei Kamada and Andrew J. Long. Baryogenesis from decaying magnetic helicity. *Phys. Rev. D*, 94(6):063501, 2016. doi:10.1103/PhysRevD.94.063501.

[112] James M. Cline and Benoit Laurent. Electroweak baryogenesis from light fermion sources: A critical study. *Phys. Rev. D*, 104(8):083507, 2021. doi:10.1103/PhysRevD.104.083507.

[113] Glennys R. Farrar and M. E. Shaposhnikov. Baryon asymmetry of the universe in the standard electroweak theory. *Phys. Rev. D*, 50:774, 1994. doi:10.1103/PhysRevD.50.774.

[114] Glennys R. Farrar and M. E. Shaposhnikov. Baryon asymmetry of the universe in the minimal Standard Model. *Phys. Rev. Lett.*, 70:2833–2836, 1993. doi:10.1103/PhysRevLett.70.2833. [Erratum: Phys.Rev.Lett. 71, 210 (1993)].

[115] M. B. Gavela, P. Hernández, J. Orloff, and O. Pène. Standard Model CP-violation and Baryon asymmetry. *Modern Physics Letters A*, 09:795–809, 1994. doi:10.1142/S0217732394000629.

[116] M. B. Gavela, P. Hernandez, J. Orloff, O. Pène, and C. Quimbay. Standard Model CP-violation and Baryon asymmetry Part II: Finite Temperature. *Nuclear Physics B*, 430:382–426, 1994. doi:10.1016/0550-3213(94)00410-2.

[117] M. B. Gavela, P. Hernández, J. Orloff, and O. Pène. Standard Model Baryogenesis. *arXiv:hep-ph/9407403*, 1994.

[118] Eric Braaten and Robert D. Pisarski. Calculation of the quark damping rate in hot QCD. *Phys. Rev. D*, 46:1829–1834, 1992. doi:10.1103/PhysRevD.46.1829.

[119] M. H. Thoma. Damping of a Yukawa fermion at finite temperature. *Z. Phys. C*, 66: 491–494, 1995. doi:10.1007/BF01556376.

[120] Marcela Carena, Alejandro Daleo, Bogdan A. Dobrescu, and Timothy M. P. Tait. Z' gauge bosons at the Tevatron. *Phys. Rev. D*, 70:093009, 2004. doi:10.1103/PhysRevD.70.093009.

[121] Yu Seon Jeong, C. S. Kim, and Hye-Sung Lee. Constraints on the $U(1)_L$ gauge boson in a wide mass range. *Int. J. Mod. Phys. A*, 31(11):1650059, 2016. doi:10.1142/S0217751X16500597.

[122] Marcela Carena, Mariano Quirós, and Yue Zhang. Electroweak Baryogenesis from Dark-Sector CP Violation. *Phys. Rev. Lett.*, 122(20):201802, 2019. doi:10.1103/PhysRevLett.122.201802.

[123] John Ellis, Marek Lewicki, and José Miguel No. On the Maximal Strength of a First-Order Electroweak Phase Transition and its Gravitational Wave Signal. *JCAP*, 04:003, 2019. doi:10.1088/1475-7516/2019/04/003.

[124] J. Aalbers et al. Dark Matter Search Results from 4.2 Tonne-Years of Exposure of the LUX-ZEPLIN (LZ) Experiment. 10 2024.

[125] Rebecca Krall and Matthew Reece. Last Electroweak WIMP Standing: Pseudo-Dirac Higgsino Status and Compact Stars as Future Probes. *Chin. Phys. C*, 42(4):043105, 2018. doi:10.1088/1674-1137/42/4/043105.

[126] Joshua Eby, Patrick J. Fox, Roni Harnik, and Graham D. Kribs. Luminous Signals of Inelastic Dark Matter in Large Detectors. *JHEP*, 09:115, 2019. doi:10.1007/JHEP09(2019)115.

[127] David Tucker-Smith and Neal Weiner. Inelastic dark matter. *Phys. Rev. D*, 64:043502, 2001. doi:10.1103/PhysRevD.64.043502.

[128] Lawrence J. Hall, Takeo Moroi, and Hitoshi Murayama. Sneutrino cold dark matter with lepton number violation. *Phys. Lett. B*, 424:305–312, 1998. doi:10.1016/S0370-2693(98)00196-8.

[129] Jason Kumar and Danny Marfatia. Matrix element analyses of dark matter scattering and annihilation. *Phys. Rev. D*, 88(1):014035, 2013. doi:10.1103/PhysRevD.88.014035.

[130] Kylar Greene, Aurora Ireland, Gordan Krnjaic, and Yuhsin Tsai. Observable CMB Tensor Modes from Cosmological Phase Transitions. 10 2024.

[131] Marc Kamionkowski, Arthur Kosowsky, and Michael S. Turner. Gravitational radiation from first order phase transitions. *Phys. Rev. D*, 49:2837–2851, 1994. doi:10.1103/PhysRevD.49.2837.

[132] Chiara Caprini et al. Science with the space-based interferometer eLISA. II: Gravitational waves from cosmological phase transitions. *JCAP*, 04:001, 2016. doi:10.1088/1475-7516/2016/04/001.

[133] David J. Weir. Gravitational waves from a first order electroweak phase transition: a brief review. *Phil. Trans. Roy. Soc. Lond. A*, 376(2114):20170126, 2018. doi:10.1098/rsta.2017.0126. [Erratum: Phil.Trans.Roy.Soc.Lond.A 381, 20230212 (2023)].

[134] S. W. Hawking, I. G. Moss, and J. M. Stewart. Bubble Collisions in the Very Early Universe. *Phys. Rev. D*, 26:2681, 1982. doi:10.1103/PhysRevD.26.2681.

[135] Arthur Kosowsky and Michael S. Turner. Gravitational radiation from colliding vacuum bubbles: envelope approximation to many bubble collisions. *Phys. Rev. D*, 47:4372–4391, 1993. doi:10.1103/PhysRevD.47.4372.

[136] Mark Hindmarsh, Stephan J. Huber, Kari Rummukainen, and David J. Weir. Numerical simulations of acoustically generated gravitational waves at a first order phase transition. *Phys. Rev. D*, 92(12):123009, 2015. doi:10.1103/PhysRevD.92.123009.

[137] Mark Hindmarsh. Sound shell model for acoustic gravitational wave production at a first-order phase transition in the early Universe. *Phys. Rev. Lett.*, 120(7):071301, 2018. doi:10.1103/PhysRevLett.120.071301.

[138] Mark Hindmarsh, Stephan J. Huber, Kari Rummukainen, and David J. Weir. Shape of the acoustic gravitational wave power spectrum from a first order phase transition. *Phys. Rev. D*, 96(10):103520, 2017. doi:10.1103/PhysRevD.96.103520. [Erratum: Phys.Rev.D 101, 089902 (2020)].

[139] Chiara Caprini and Ruth Durrer. Gravitational waves from stochastic relativistic sources: Primordial turbulence and magnetic fields. *Phys. Rev. D*, 74:063521, Sep 2006. doi:10.1103/PhysRevD.74.063521. URL https://link.aps.org/doi/10.1103/PhysRevD.74.063521.

[140] Chiara Caprini, Ruth Durrer, and Geraldine Servant. The stochastic gravitational wave background from turbulence and magnetic fields generated by a first-order phase transition. *JCAP*, 12:024, 2009. doi:10.1088/1475-7516/2009/12/024.

[141] Pierre Auclair, Chiara Caprini, Daniel Cutting, Mark Hindmarsh, Kari Rummukainen, Danièle A. Steer, and David J. Weir. Generation of gravitational waves from freely decaying turbulence. *JCAP*, 09:029, 2022. doi:10.1088/1475-7516/2022/09/029.

[142] Mark Hindmarsh, Stephan J. Huber, Kari Rummukainen, and David J. Weir. Gravitational waves from the sound of a first order phase transition. *Phys. Rev. Lett.*, 112: 041301, 2014. doi:10.1103/PhysRevLett.112.041301.

[143] Iason Baldes and Géraldine Servant. High scale electroweak phase transition: baryogenesis \& symmetry non-restoration. *JHEP*, 10:053, 2018. doi:10.1007/JHEP10(2018)053.

[144] Eleanor Hall, Thomas Konstandin, Robert McGehee, Hitoshi Murayama, and Géraldine Servant. Baryogenesis From a Dark First-Order Phase Transition. *JHEP*, 04:042, 2020. doi:10.1007/JHEP04(2020)042.

[145] Eleanor Hall, Thomas Konstandin, Robert McGehee, and Hitoshi Murayama. Asymmetric matter from a dark first-order phase transition. *Phys. Rev. D*, 107(5):055011, 2023. doi:10.1103/PhysRevD.107.055011.

[146] Ke-Pan Xie, Ligong Bian, and Yongcheng Wu. Electroweak baryogenesis and gravitational waves in a composite Higgs model with high dimensional fermion representations. *JHEP*, 12:047, 2020. doi:10.1007/JHEP12(2020)047.

[147] Ke-Pan Xie. Lepton-mediated electroweak baryogenesis, gravitational waves and the 4τ final state at the collider. *JHEP*, 02:090, 2021. doi:10.1007/JHEP02(2021)090. [Erratum: JHEP 8, 052 (2022)].

[148] Kohei Fujikura, Keisuke Harigaya, Yuichiro Nakai, and Isaac R. Wang. Electroweak-like baryogenesis with new chiral matter. *JHEP*, 07:224, 2021. doi:10.1007/JHEP07(2021)224. [Erratum: JHEP 12, 192 (2021), Erratum: JHEP 1, 156 (2022), Erratum: JHEP 01, 156 (2022)].

[149] Keisuke Inomata, Marc Kamionkowski, Kentaro Kasai, and Bibhushan Shakya. Gravitational Waves from Particles Produced from Bubble Collisions in First-Order Phase Transitions. 12 2024.

[150] Dimitri V. Nanopoulos and Steven Weinberg. Mechanisms for Cosmological Baryon Production. *Phys. Rev. D*, 20:2484, 1979. doi:10.1103/PhysRevD.20.2484.

[151] Motohiko Yoshimura. Origin of Cosmological Baryon Asymmetry. *Phys. Lett. B*, 88: 294–298, 1979. doi:10.1016/0370-2693(79)90471-4.

[152] Andrei D. Linde. Infrared Problem in Thermodynamics of the Yang-Mills Gas. *Phys. Lett. B*, 96:289–292, 1980. doi:10.1016/0370-2693(80)90769-8.

[153] Andrew G. Cohen, D. B. Kaplan, and A. E. Nelson. Progress in electroweak baryogenesis. *Ann. Rev. Nucl. Part. Sci.*, 43:27–70, 1993. doi:10.1146/annurev.ns.43.120193.000331.

[154] David Curtin, Patrick Meade, and Harikrishnan Ramani. Thermal Resummation and Phase Transitions. *Eur. Phys. J. C*, 78(9):787, 2018. doi:10.1140/epjc/s10052-018-6268-0.

[155] Sebastian Baum, Marcela Carena, Nausheen R. Shah, Carlos E. M. Wagner, and Yikun Wang. Nucleation is more than critical: A case study of the electroweak phase transition in the NmsSm. *JHEP*, 03:055, 2021. doi:10.1007/JHEP03(2021)055.

[156] Lauri Niemi, Michael J. Ramsey-Musolf, and Guotao Xia. Nonperturbative study of the electroweak phase transition in the real scalar singlet extended standard model. *Phys. Rev. D*, 110(11):115016, 2024. doi:10.1103/PhysRevD.110.115016.

[157] Chiara Caprini et al. Detecting gravitational waves from cosmological phase transitions with LisA: an update. *JCAP*, 03:024, 2020. doi:10.1088/1475-7516/2020/03/024.

[158] Huai-Ke Guo, Kuver Sinha, Daniel Vagie, and Graham White. Phase Transitions in an Expanding Universe: Stochastic Gravitational Waves in Standard and Non-Standard Histories. *JCAP*, 01:001, 2021. doi:10.1088/1475-7516/2021/01/001.

[159] Christian W. Bauer et al. Quantum Simulation for High-Energy Physics. *PRX Quantum*, 4(2):027001, 2023. doi:10.1103/PRXQuantum.4.027001.

[160] Alberto Di Meglio et al. Quantum Computing for High-Energy Physics: State of the Art and Challenges. *PRX Quantum*, 5(3):037001, 2024. doi:10.1103/PRXQuantum.5.037001.

[161] Christian W. Bauer, Zohreh Davoudi, Natalie Klco, and Martin J. Savage. Quantum simulation of fundamental particles and forces. *Nature Rev. Phys.*, 5(7):420–432, 2023. doi:10.1038/s42254-023-00599-8.

[162] Yaquan Fang, Christina Gao, Ying-Ying Li, Jing Shu, Yusheng Wu, Hongxi Xing, Bin Xu, Lailin Xu, and Chen Zhou. Quantum Frontiers in High Energy Physics, 11 2024.

[163] Stephen P. Jordan, Keith S. M. Lee, and John Preskill. Quantum Computation of Scattering in Scalar Quantum Field Theories. *Quant. Inf. Comput.*, 14:1014–1080, 2014.

[164] Yahui Chai, Arianna Crippa, Karl Jansen, Stefan Kühn, Vincent R. Pascuzzi, Francesco Tacchino, and Ivano Tavernelli. Fermionic wave packet scattering: a quantum computing approach. *Quantum*, 9:1638, 2025. doi:10.22331/q-2025-02-19-1638.

[165] Elizabeth R. Bennewitz et al. Simulating Meson Scattering on Spin Quantum Simulators, 3 2024.

[166] Roland C. Farrell, Marc Illa, Anthony N. Ciavarella, and Martin J. Savage. Quantum simulations of hadron dynamics in the Schwinger model using 112 qubits. *Phys. Rev. D*, 109(11):114510, 2024. doi:10.1103/PhysRevD.109.114510.

[167] Christian W. Bauer, Wibe A. de Jong, Benjamin Nachman, and Davide Provasoli. Quantum Algorithm for High Energy Physics Simulations. *Phys. Rev. Lett.*, 126(6): 062001, 2021. doi:10.1103/PhysRevLett.126.062001.

[168] Khadeejah Bepari, Sarah Malik, Michael Spannowsky, and Simon Williams. Quantum walk approach to simulating parton showers. *Phys. Rev. D*, 106(5):056002, 2022. doi:10.1103/PhysRevD.106.056002.

[169] Christian W. Bauer, So Chigusa, and Masahito Yamazaki. Quantum parton shower with kinematics. *Phys. Rev. A*, 109(3):032432, 2024. doi:10.1103/PhysRevA.109.032432.

[170] Maarten Van Damme, Laurens Vanderstraeten, Jacopo De Nardis, Jutho Haegeman, and Frank Verstraete. Real-time scattering of interacting quasiparticles in quantum spin chains. *Phys. Rev. Res.*, 3:013078, Jan 2021. doi:10.1103/PhysRevResearch.3.013078. URL https://link.aps.org/doi/10.1103/PhysRevResearch.3.013078.

[171] Marco Rigobello, Simone Notarnicola, Giuseppe Magnifico, and Simone Montangero. Entanglement generation in (1+1)D qEd scattering processes. *Phys. Rev. D*, 104(11): 114501, 2021. doi:10.1103/PhysRevD.104.114501.

[172] Irene Papaefstathiou, Johannes Knolle, and Mari Carmen Bañuls. Real-time scattering in the lattice Schwinger model. *Phys. Rev. D*, 111(1):014504, 2025. doi:10.1103/PhysRevD.111.014504.

[173] Ashley Milsted, Junyu Liu, John Preskill, and Guifre Vidal. Collisions of false-vacuum bubble walls in a quantum spin chain. *PRX Quantum*, 3(2), April 2022. ISSN 2691-3399. doi:10.1103/PRXQuantum.3.020316. URL http://arxiv.org/abs/2012.07243.

[174] Raghav G. Jha, Ashley Milsted, Dominik Neuenfeld, John Preskill, and Pedro Vieira. Real-Time Scattering in Ising Field Theory using Matrix Product States, 11 2024.

[175] M. B. Hastings. An area law for one-dimensional quantum systems. *J. Stat. Mech.*, 0708:P08024, 2007. doi:10.1088/1742-5468/2007/08/P08024.

[176] G. Vidal. Efficient simulation of one-dimensional quantum many-body systems. *Phys. Rev. Lett.*, 93:040502, 2004. doi:10.1103/PhysRevLett.93.040502.

[177] Steven R. White. Density matrix formulation for quantum renormalization groups. *Phys. Rev. Lett.*, 69(19):2863, 1992.

[178] U. Schollwöck. The density-matrix renormalization group. *Rev. Mod. Phys.*, 77(1): 259–315, April 2005. doi:10.1103/RevModPhys.77.259. URL https://link.aps.org/doi/10.1103/RevModPhys.77.259.

[179] Marcela Carena, Ying-Ying Li, Tong Ou, and Hersh Singh. Real-time simulation of asymmetry generation in fermion-bubble collisions. *Phys. Rev. D*, 113(1):014502, 2026. doi:10.1103/nphy-2y8q.

[180] Philippe de Forcrand. Simulating qcd at finite density. *PoS*, LAT2009:010, 2009. doi:10.22323/1.091.0010.

[181] Gert Aarts. Introductory lectures on lattice qcd at nonzero baryon number. *Journal of Physics: Conference Series*, 706:022004, 2016. doi:10.1088/1742-6596/706/2/022004.

[182] Michael Joyce, Tomislav Prokopec, and Neil Turok. Electroweak baryogenesis from a classical force. *Phys. Rev. Lett.*, 75:1695–1698, 1995. doi:10.1103/PhysRevLett.75.1695. [Erratum: Phys.Rev.Lett. 75, 3375 (1995)].

[183] Patrick Huet and Ann E. Nelson. CP violation and electroweak baryogenesis in extensions of the standard model. *Phys. Lett. B*, 355:229–235, 1995. doi:10.1016/0370-2693(95)00674-A.

[184] Lars Fromme, Stephan J. Huber, and Michael Seniuch. Baryogenesis in the two-Higgs doublet model. *JHEP*, 11:038, 2006. doi:10.1088/1126-6708/2006/11/038.

[185] Alejandro Ayala, Jamal Jalilian-Marian, Larry D. McLerran, and Axel P. Vischer. Scattering in the presence of electroweak phase transition bubble walls. *Phys. Rev. D*, 49:5559–5570, 1994. doi:10.1103/PhysRevD.49.5559.

[186] Koichi Funakubo, Akira Kakuto, Shochiro Otsuki, Kazunori Takenaga, and Fumihiko Toyoda. Fermion scattering off Cp violating electroweak bubble wall. *Phys. Rev. D*, 50: 1105–1117, 1994. doi:10.1103/PhysRevD.50.1105.

[187] Matthew Fishman, Steven R. White, and E. Miles Stoudenmire. The Itensor Software Library for Tensor Network Calculations. *SciPost Phys. Codeb.*, 2022:4, 2022. doi:10.21468/SciPostPhysCodeb.4.

[188] John B. Kogut and Leonard Susskind. Hamiltonian Formulation of Wilson's Lattice Gauge Theories. *Phys. Rev. D*, 11:395–408, 1975. doi:10.1103/PhysRevD.11.395.

[189] Ulrich Schollwöck. The density-matrix renormalization group in the age of matrix product states. *Annals of Physics*, 326(1):96–192, January 2011. ISSN 0003-4916. doi:10.1016/j.aop.2010.09.012. URL http://www.sciencedirect.com/science/article/pii/S0003491610001752.

[190] Nikita A. Zemlevskiy. Scalable quantum simulations of scattering in scalar field theory on 120 qubits. *Phys. Rev. D*, 112(3):034502, 2025. doi:10.1103/qr72-51v1.

[191] Stephen P. Jordan, Keith S. M. Lee, and John Preskill. Quantum Algorithms for Fermionic Quantum Field Theories, apr 2014. URL http://arxiv.org/abs/1404.7115.

[192] Roland C. Farrell, Marc Illa, and Martin J. Savage. Steps toward quantum simulations of hadronization and energy loss in dense matter. *Phys. Rev. C*, 111(1):015202, 2025. doi:10.1103/PhysRevC.111.015202.

[193] Yanting Cheng, Shang Liu, Wei Zheng, Pengfei Zhang, and Hui Zhai. Tunable Confinement-Deconfinement Transition in an Ultracold-Atom Quantum Simulator. *PRX Quantum*, 3(4):040317, 2022. doi:10.1103/PRXQuantum.3.040317.

[194] Ron Belyansky, Seth Whitsitt, Niklas Mueller, Ali Fahimniya, Elizabeth R. Bennewitz, Zohreh Davoudi, and Alexey V. Gorshkov. High-Energy Collision of Quarks and Mesons in the Schwinger Model: From Tensor Networks to Circuit QED. *Phys. Rev. Lett.*, 132 (9):091903, 2024. doi:10.1103/PhysRevLett.132.091903.

[195] Martin Lüscher. Two-particle states on a torus and their relation to the scattering matrix. *Nuclear Physics B*, 354(2):531–578, May 1991. ISSN 0550-3213. doi:10.1016/0550-3213(91)90366-6. URL http://www.sciencedirect.com/science/article/pii/0550321391903666.

[196] Erik Gustafson, Yingyue Zhu, Patrick Dreher, Norbert M. Linke, and Yannick Meurice. Real-time quantum calculations of phase shifts using wave packet time delays. *Phys. Rev. D*, 104(5):054507, sep 2021. ISSN 2470-0010, 2470-0029. doi:10.1103/PhysRevD.104.054507. URL http://arxiv.org/abs/2103.06848.

[197] D. Yu. Grigoriev, V. A. Rubakov, and M. E. Shaposhnikov. Topological transitions at finite temperatures: A real time numerical approach. *Nuclear Physics B*, 326(3): 737–757, November 1989. ISSN 0550-3213. doi:10.1016/0550-3213(89)90553-1. URL https://www.sciencedirect.com/science/article/pii/0550321389905531.

[198] Steven Weinberg. Varieties of Baryon and Lepton Nonconservation. *Phys. Rev. D*, 22: 1694, 1980. doi:10.1103/PhysRevD.22.1694.

[199] L. F. Abbott and Mark B. Wise. Wormholes and Global Symmetries. *Nucl. Phys. B*, 325:687–704, 1989. doi:10.1016/0550-3213(89)90503-8.

[200] Renata Kallosh, Andrei D. Linde, Dmitri A. Linde, and Leonard Susskind. Gravity and global symmetries. *Phys. Rev. D*, 52:912–935, 1995. doi:10.1103/PhysRevD.52.912.

[201] Ki-Myeong Lee. Wormholes and Goldstone Bosons. *Phys. Rev. Lett.*, 61:263–266, 1988. doi:10.1103/PhysRevLett.61.263.

[202] Raymond Davis, Jr., Don S. Harmer, and Kenneth C. Hoffman. Search for neutrinos from the sun. *Phys. Rev. Lett.*, 20:1205–1209, 1968. doi:10.1103/PhysRevLett.20.1205.

[203] Y. Fukuda et al. Evidence for oscillation of atmospheric neutrinos. *Phys. Rev. Lett.*, 81:1562–1567, 1998. doi:10.1103/PhysRevLett.81.1562.

[204] Q. R. Ahmad et al. Measurement of the rate of $\nu_e + d \rightarrow p + p + e^-$ interactions produced by ^{8}B solar neutrinos at the Sudbury Neutrino Observatory. *Phys. Rev. Lett.*, 87:071301, 2001. doi:10.1103/PhysRevLett.87.071301.

[205] Julian Heeck and Volodymyr Takhistov. Inclusive Nucleon Decay Searches as a Frontier of Baryon Number Violation. *Phys. Rev. D*, 101(1):015005, 2020. doi:10.1103/PhysRevD.101.015005.

[206] H. Georgi and S. L. Glashow. Unity of All Elementary Particle Forces. *Phys. Rev. Lett.*, 32:438–441, 1974. doi:10.1103/PhysRevLett.32.438.

[207] Jogesh C. Pati and Abdus Salam. Lepton Number as the Fourth Color. *Phys. Rev. D*, 10:275–289, 1974. doi:10.1103/PhysRevD.10.275. [Erratum: Phys.Rev.D 11, 703–703 (1975)].

[208] Harald Fritzsch and Peter Minkowski. Unified Interactions of Leptons and Hadrons. *Annals Phys.*, 93:193–266, 1975. doi:10.1016/0003-4916(75)90211-0.

[209] Frank Wilczek and A. Zee. Operator Analysis of Nucleon Decay. *Phys. Rev. Lett.*, 43: 1571–1573, 1979. doi:10.1103/PhysRevLett.43.1571.

[210] K. Abe et al. Hyper-Kamiokande Design Report. 5 2018.

[211] V. Takhistov et al. Search for Trilepton Nucleon Decay via $p \rightarrow e^+\nu\nu$ and $p \rightarrow \mu^+\nu\nu$ in the Super-Kamiokande Experiment. *Phys. Rev. Lett.*, 113(10):101801, 2014. doi:10.1103/PhysRevLett.113.101801.

[212] Renato M. Fonseca, Martin Hirsch, and Rahul Srivastava. $\Delta L = 3$ processes: Proton decay and the LHC. *Phys. Rev. D*, 97(7):075026, 2018. doi:10.1103/PhysRevD.97.075026.

[213] K. S. Babu, P. S. Bhupal Dev, Elaine C. F. S. Fortes, and R. N. Mohapatra. Post-

Sphaleron Baryogenesis and an Upper Limit on the Neutron-Antineutron Oscillation Time. *Phys. Rev. D*, 87(11):115019, 2013. doi:10.1103/PhysRevD.87.115019.

[214] JoAnne L. Hewett and Thomas G. Rizzo. Low-Energy Phenomenology of Superstring Inspired E(6) Models. *Phys. Rept.*, 183:193, 1989. doi:10.1016/0370-1573(89)90071-9.

[215] R. N. Mohapatra, Nobuchika Okada, and Hai-Bo Yu. Diquark Higgs at LHC. *Phys. Rev. D*, 77:011701, 2008. doi:10.1103/PhysRevD.77.011701.

[216] W. Buchmuller and D. Wyler. Constraints on SU(5) Type Leptoquarks. *Phys. Lett. B*, 177:377–382, 1986. doi:10.1016/0370-2693(86)90771-9.

[217] Goran Senjanovic and Aleksandar Sokorac. Light Leptoquarks in SO(10). *Z. Phys. C*, 20:255, 1983. doi:10.1007/BF01574858.

[218] A. Zee. A Theory of Lepton Number Violation, Neutrino Majorana Mass, and Oscillation. *Phys. Lett. B*, 93:389, 1980. doi:10.1016/0370-2693(80)90349-4. [Erratum: Phys.Lett.B 95, 461 (1980)].

[219] K. S. Babu. Model of 'Calculable' Majorana Neutrino Masses. *Phys. Lett. B*, 203: 132–136, 1988. doi:10.1016/0370-2693(88)91584-5.

[220] Bruna Pascual-Dias, Pratishruti Saha, and David London. LHC Constraints on Scalar Diquarks. *JHEP*, 07:144, 2020. doi:10.1007/JHEP07(2020)144.

[221] Gian Francesco Giudice, Ben Gripaios, and Raman Sundrum. Flavourful Production at Hadron Colliders. *JHEP*, 08:055, 2011. doi:10.1007/JHEP08(2011)055.

[222] I. Doršner, S. Fajfer, A. Greljo, J. F. Kamenik, and N. Košnik. Physics of leptoquarks in precision experiments and at particle colliders. *Phys. Rept.*, 641:1–68, 2016. doi:10.1016/j.physrep.2016.06.001.

[223] Andreas Crivellin and Luc Schnell. Complete Lagrangian and set of Feynman rules for scalar leptoquarks. *Comput. Phys. Commun.*, 271:108188, 2022. doi:10.1016/j.cpc.2021.108188.

[224] Johan Alwall, Claude Duhr, Benjamin Fuks, Olivier Mattelaer, Deniz Gizem Öztürk, and Chia-Hsien Shen. Computing decay rates for new physics theories with FeynRules and MadGraph 5_aMC@NLO. *Comput. Phys. Commun.*, 197:312–323, 2015. doi:10.1016/j.cpc.2015.08.031.

[225] M. A. Luty. Baryogenesis via leptogenesis. *Phys. Rev. D*, 45:455–465, 1992. doi:10.1103/PhysRevD.45.455.

[226] M.C. Gonzalez-Garcia and M. Yokoyama. https://pdg.lbl.gov/2024/reviews/rpp2024-rev-neutrino-mixing.pdf. [Accessed 25-08-2025].

[227] B. Pontecorvo. Inverse Beta Processes and Nonconservation of Lepton Charge. *Sov. Phys. JETP*, 7:172–173, 1958.

[228] Ziro Maki, Masami Nakagawa, and Shoichi Sakata. Remarks on the unified model of elementary particles. *Prog. Theor. Phys.*, 28:870–880, 1962. doi:10.1143/PTP.28.870.

[229] A. Ceccucci, Z. Ligeti, and Y. Sakai. https://pdg.lbl.gov/2019/reviews/rpp2019-rev-ckm-matrix.pdf. [Accessed 20-08-2025].

[230] Nicola Cabibbo. Unitary Symmetry and Leptonic Decays. *Phys. Rev. Lett.*, 10:531–533, 1963. doi:10.1103/PhysRevLett.10.531.

[231] Makoto Kobayashi and Toshihide Maskawa. CP Violation in the Renormalizable Theory of Weak Interaction. *Prog. Theor. Phys.*, 49:652–657, 1973. doi:10.1143/PTP.49.652.

[232] Zhe Dong, Gauthier Durieux, Jean-Marc Gerard, Tao Han, and Fabio Maltoni.

Baryon number violation at the LHC: the top option. *Phys. Rev. D*, 85:016006, 2012. doi:10.1103/PhysRevD.85.016006.

[233] Aram Hayrapetyan et al. Search for baryon number violation in top quark production and decay using proton-proton collisions at $\sqrt{s} = 13$ TeV. *Phys. Rev. Lett.*, 132:241802, 2024. doi:10.1103/PhysRevLett.132.241802.

[234] Keith Rehermann and Brock Tweedie. Efficient Identification of Boosted Semileptonic Top Quarks at the LHC. *JHEP*, 03:059, 2011. doi:10.1007/JHEP03(2011)059.

[235] Georges Aad et al. Inclusive search for same-sign dilepton signatures in pp collisions at $\sqrt{s} = 7$ TeV with the ATLAS detector. *JHEP*, 10:107, 2011. doi:10.1007/JHEP10(2011)107.

[236] Vardan Khachatryan et al. Search for new physics in same-sign dilepton events in proton–proton collisions at $\sqrt{s} = 13\,\text{TeV}$. *Eur. Phys. J. C*, 76(8):439, 2016. doi:10.1140/epjc/s10052-016-4261-z.

[237] J. Alwall, R. Frederix, S. Frixione, V. Hirschi, F. Maltoni, O. Mattelaer, H. S. Shao, T. Stelzer, P. Torrielli, and M. Zaro. The automated computation of tree-level and next-to-leading order differential cross sections, and their matching to parton shower simulations. *JHEP*, 07:079, 2014. doi:10.1007/JHEP07(2014)079.

[238] Thomas Konstandin, Germano Nardini, and Ingo Rues. From Boltzmann equations to steady wall velocities. *JCAP*, 09:028, 2014. doi:10.1088/1475-7516/2014/09/028.

[239] Stefan Höche, Jonathan Kozaczuk, Andrew J. Long, Jessica Turner, and Yikun Wang. Towards an all-orders calculation of the electroweak bubble wall velocity. *JCAP*, 03: 009, 2021. doi:10.1088/1475-7516/2021/03/009.

[240] Yann Gouttenoire, Ryusuke Jinno, and Filippo Sala. Friction pressure on relativistic bubble walls. *JHEP*, 05:004, 2022. doi:10.1007/JHEP05(2022)004.

[241] Djuna Croon, Oliver Gould, Philipp Schicho, Tuomas V. I. Tenkanen, and Graham White. Theoretical uncertainties for cosmological first-order phase transitions. *JHEP*, 04:055, 2021. doi:10.1007/JHEP04(2021)055.

[242] Mikael Chala, Juan Carlos Criado, Luis Gil, and Javier López Miras. Higher-order-operator corrections to phase-transition parameters in dimensional reduction. *JHEP*, 10:025, 2024. doi:10.1007/JHEP10(2024)025.

[243] Mikael Chala and Guilherme Guedes. The High-Temperature Limit of the SM(EFT). 3 2025.

[244] Guy D. Moore and Tomislav Prokopec. How fast can the wall move? A Study of the electroweak phase transition dynamics. *Phys. Rev. D*, 52:7182–7204, 1995. doi:10.1103/PhysRevD.52.7182.

[245] Glauber C. Dorsch, Stephan J. Huber, and Thomas Konstandin. A sonic boom in bubble wall friction. *JCAP*, 04(04):010, 2022. doi:10.1088/1475-7516/2022/04/010.

[246] Ryusuke Jinno and Masahiro Takimoto. Gravitational waves from bubble collisions: An analytic derivation. *Phys. Rev. D*, 95(2):024009, 2017. doi:10.1103/PhysRevD.95.024009.

[247] Wen-Yuan Ai, Malcolm Fairbairn, Ken Mimasu, and Tevong You. Non-thermal production of heavy vector dark matter from relativistic bubble walls. 6 2024.

[248] Dietrich Bodeker and Guy D. Moore. Can electroweak bubble walls run away? *JCAP*, 05:009, 2009. doi:10.1088/1475-7516/2009/05/009.

[249] John Ellis, Marek Lewicki, and José Miguel No. Gravitational waves from first-order cosmological phase transitions: lifetime of the sound wave source. *JCAP*, 07:050, 2020. doi:10.1088/1475-7516/2020/07/050.

[250] Chiara Caprini, Ryusuke Jinno, Marek Lewicki, Eric Madge, Marco Merchand, Germano Nardini, Mauro Pieroni, Alberto Roper Pol, and Ville Vaskonen. Gravitational waves from first-order phase transitions in LISA: reconstruction pipeline and physics interpretation. *JCAP*, 10:020, 2024. doi:10.1088/1475-7516/2024/10/020.

[251] Daniel Cutting, Mark Hindmarsh, and David J. Weir. Vorticity, kinetic energy, and suppressed gravitational wave production in strong first order phase transitions. *Phys. Rev. Lett.*, 125(2):021302, 2020. doi:10.1103/PhysRevLett.125.021302.

[252] Alberto Roper Pol, Sayan Mandal, Axel Brandenburg, Tina Kahniashvili, and Arthur Kosowsky. Numerical simulations of gravitational waves from early-universe turbulence. *Phys. Rev. D*, 102(8):083512, 2020. doi:10.1103/PhysRevD.102.083512.

[253] Michael Stone. Gamma matrices, Majorana fermions, and discrete symmetries in Minkowski and Euclidean signature. *J. Phys. A*, 55(20):205401, 2022. doi:10.1088/1751-8121/ac61b7.

[254] Subir Sachdev. *Quantum Phase Transitions*. Cambridge University Press, 4 2011. ISBN 978-0-511-97376-5. doi:10.1017/cbo9780511973765.

[255] Naomichi Hatano and Masuo Suzuki. Finding Exponential Product Formulas of Higher Orders. *Lect. Notes Phys.*, 679:37, 2005. doi:10.1007/11526216_2.

[256] Martin Lavelle and David McMullan. Constituent quarks from QCD. *Phys. Rept.*, 279: 1–65, 1997. doi:10.1016/S0370-1573(96)00019-1.

[257] S. Navas et al. Review of particle physics. *Phys. Rev. D*, 110(3):030001, 2024. doi:10.1103/PhysRevD.110.030001.

[258] Innes Bigaran and Raymond R. Volkas. Getting chirality right: Single scalar leptoquark solutions to the $(g-2)_{e,\mu}$ puzzle. *Phys. Rev. D*, 102(7):075037, 2020. doi:10.1103/PhysRevD.102.075037.

[259] G. C. McLaughlin and J. N. Ng. A Study of the charged scalar in the Zee model. *Phys. Lett. B*, 455:224–230, 1999. doi:10.1016/S0370-2693(99)00490-6.

[260] A. M. Baldini et al. Search for the lepton flavour violating decay $\mu^+ \to e^+\gamma$ with the full dataset of the MEG experiment. *Eur. Phys. J. C*, 76(8):434, 2016. doi:10.1140/epjc/s10052-016-4271-x.

[261] K. Afanaciev et al. A search for $\mu^+ \to e^+\gamma$ with the first dataset of the MEG II experiment. *Eur. Phys. J. C*, 84(3):216, 2024. doi:10.1140/epjc/s10052-024-12416-2. [Erratum: Eur.Phys.J.C 84, 1042 (2024)].

[262] Georges Aad et al. Search for pair production of third-generation scalar leptoquarks decaying into a top quark and a τ-lepton in pp collisions at $\sqrt{s} = 13$ TeV with the ATLAS detector. *JHEP*, 06:179, 2021. doi:10.1007/JHEP06(2021)179.

[263] Armen Tumasyan et al. Inclusive nonresonant multilepton probes of new phenomena at $\sqrt{s}$=13 TeV. *Phys. Rev. D*, 105(11):112007, 2022. doi:10.1103/PhysRevD.105.112007.

[264] Georges Aad et al. Search for pair production of scalar leptoquarks decaying into first- or second-generation leptons and top quarks in proton–proton collisions at $\sqrt{s} = 13$ TeV with the ATLAS detector. *Eur. Phys. J. C*, 81(4):313, 2021. doi:10.1140/epjc/s10052-021-09009-8.

[265] Antonio Pich. Precision Tau Physics. *Prog. Part. Nucl. Phys.*, 75:41–85, 2014. doi:10.1016/j.ppnp.2013.11.002.